

# Smart Platform for Low-Cost MEMS Sensors – Pressure, Flow and Thermal Conductivity



**Ethan Gardner**

Department of Engineering

University of Cambridge

This dissertation is submitted for the degree of

*Doctor of Philosophy*

Robinson College

March 2020



## Declaration

I hereby declare that except where specific reference is made to the work of others, the contents of this dissertation are original and have not been submitted in whole or in part for consideration for any other degree or qualification in this, or any other university. This dissertation is my own work and contains nothing which is the outcome of work done in collaboration with others, except as specified in the text and Acknowledgements. This dissertation contains fewer than 65,000 words including appendices, bibliography, footnotes, tables and equations and has fewer than 150 figures.

ETHAN GARDNER

March 2020



# Abstract

## Smart Platform for Low-Cost MEMS Sensors — Pressure, Flow and Thermal Conductivity

**I**N a technological world that is trending towards smart and autonomous engineering, the collection of quality data is of unrivalled importance. This has led to a huge market demand for the development of low-cost, small and accurate sensors and thus has resulted in significant research into sensors, with the aim of advancing the price/performance ratio in commercial solutions. Micro Electro Mechanical Systems (MEMS) have recently offered an attractive solution to miniaturise and drastically improve the performance of sensors. In this thesis, MEMS technology is exploited to create a multi-sensor technology platform that is used to fabricate several sensing technologies.

Piezo-resistive and piezo-electronic pressure sensors are designed, fabricated and tested. Different doping profiles, stress-engineered structures and electronic devices for pressure transduction are investigated, with focus on their sensitivity and non-linearity. A ring is fabricated in the metal layer around the circumference of the membrane that alleviates the effects of over/under etching. This is achieved by creating a new rigid edge of the membrane in the metal layer, which has tighter fabrication tolerances. A piezo-MOSFET is developed and shown to have greater sensitivity than similar state-of-the-art devices.

Flow sensors based on a heated tungsten wire are designed, fabricated, tested and substantiated with numerical modelling. Calorimetric and anemometric driving modes are optimised with regards to device structure. Thermodiodes are also used as the temperature transduction devices and are compared to the traditional resistor method and showed to be preferable when further miniaturising the sensor.

Thermal conductivity gas sensors based on a heated tungsten resistor are designed, tested and substantiated with numerical modelling. Holes through the membrane are used to improve the sensitivity to measuring carbon dioxide by 270%. Asymmetric holes are utilised to prove a novel method of measuring thermal conductivity in a calorimetric method. Designs improving this new concept are outlined and substantiated with analytical and numerical models.

Linear statistical methods and artificial neural networks are used to differentiate flow rate and gas concentration using three on-membrane resistors. With membrane holes, the discrimination between gases in the presence of flow is improved. Neural networks provide a viable solution and show an increase in the accuracy of both flow rate and gas concentration.

The main objective of the work in this thesis was to develop low-cost, low-power, small devices capable of high-volume production and monolithic integration using a single smart technology platform for fabrication. The smart technology platform was used to create pressure sensors, flow sensors and thermal conductivity gas sensors. Within each sensing technology, proof-of-concepts and optimisations have been carried out in order to maximise performance whilst using the low-cost, high-volume fabrication process, ultimately helping towards smart and autonomous engineering solutions driven by data.

## Dissemination

PARTS of this work have been included in patent applications, published in the scientific literature and presented at international conferences, all of which are listed below:

### Patents

#### **Filed:**

1. Florin Udrea, Andrea De Luca, Claudio Falco, **Ethan Gardner**, Syed Zeeshan Ali. “Thermal Fluid Flow Sensor”. (US 16/658711). [Flow sensors + membrane holes]
2. Andrea De Luca, Cerdin Lee, Tim Butler, **Ethan Gardner**, Florin Udrea. “Sensor Assembly”. (US 16/658718) [Sensor package with gel]
3. Syed Zeeshan Ali, Andrea De Luca, Cerdin Lee, **Ethan Gardner**, Tim Butler, Florin Udrea. “Flow Sensor Package”. (US 16/658725). [Chip level packaging]
4. Andrea De Luca, **Ethan Gardner**, Syed Zeeshan Ali, Florin Udrea. “Flow Sensor”. (GB 1915213.1). [Sensor with perpendicular hotwires]
5. Andrea De Luca, **Ethan Gardner**, Syed Zeeshan Ali, Florin Udrea. “Flow Sensor Assembly”. (GB1915211.5). [Assembly with inhomogeneous cross-section]

**Filing with Marks and Clerk:**

1. Andrea De Luca, **Ethan Gardner**, Syed Zeeshan Ali, Florin Udrea. “Flow Sensor”. [Metal ring structure for flow and pressure sensors]
2. **Ethan Gardner**, Andrea De Luca, Syed Zeeshan Ali, Cerdin Lee, Florin Udrea. “Flow Sensor Packaging”. [Vortex guiding structures]

**Journal Articles**

1. **E. L. W. Gardner**, Timothy A. Vincent, RG Jones, JW Gardner, J Coull, Andrea De Luca and Florin Udrea, "MEMS Thermal Flow Sensors—An Accuracy Investigation," in IEEE Sensors Journal, vol. 19, no. 8, pp. 2991-2998, 15 April, 2019.
2. **E. L. W. Gardner**, A. De Luca, J. Philippe, D. Dragomirescu and F. Udrea, "Thin-Film MOSFET-Based Pressure Sensor," in IEEE Sensors Letters, vol. 3, no. 7, pp. 1-4, July 2019.
3. **E. L. W. Gardner**, Timothy A. Vincent, Andrea De Luca and Florin Udrea, “CMOS MEMS Flow Sensor with Membrane Holes for Enhanced Gas Discrimination,” in Preparation for IEEE Sensors Letters.
4. **E. L. W. Gardner**, Timothy A. Vincent, Andrea De Luca and Florin Udrea, “Simultaneous Flow and Thermal Conductivity Sensing on a Single Chip Using Artificial Neural Networks,” in IEEE Sensors Journal, vol. 20, no. 9, pp. 4985-4991, 1 May, 2020.
5. **E. L. W. Gardner**, Claudio Zuliani, Timothy A. Vincent, Andrea De Luca and Florin Udrea, “A Handheld Flow-Compensated Breathalyser Module,” in preparation for IEEE Sensors Letters.



6. **E. L. W. Gardner** and Florin Udrea, "Micromachined Thermal Gas Sensors - A Review," in preparation for Sensors and Actuators B: Chemical.
7. C. Zuliani, J. Luque, C. Falco, **E. L. W Gardner**, A. de Luca, T.A Vincent, S. Tripathy, Z. Ali and F. Udrea, "Flow Compensated Gas Sensing Array for Improved Performances in Breath-Analysis Applications," "Flow Compensated Gas Sensing Array for Improved Performances in Breath-Analysis Applications," in IEEE Sensors Letters, vol. 4, no. 3, pp. 1-4, March 2020.
8. G. Loubet, A. Takacs, **E. Gardner**, A. De Luca, F. Udrea, and D. Dragomirescu, "LoRaWAN Battery-Free Wireless Sensors Network Designed for Structural Health Monitoring in the Construction Domain," Sensors, vol. 19, no. 7, p. 1510, Mar. 2019.

### **Conference Publications**

1. **E. L. W. Gardner**, A. De Luca and F. Udrea, "2D and 3D thermal flow sensor modelling — A comparative analysis," 2017 International Semiconductor Conference (CAS), Sinaia, Romania, 2017, pp. 197-200.
2. **Gardner, E.L.**; Luca, A.D.; Falco, C.; Udrea, F. "Geometrical Optimisation of Diode-Based Calorimetric Thermal Flow Sensors through Multiphysics Finite Element Modelling," Proceedings 2017, 1, 280.
3. **E. L. W. Gardner**, T. A. Vincent, A. D. Luca and F. Udrea, "Comparison of Thermo-Resistive and Thermo-Electronic Transduction Methods in Thermal Flow Sensors," 2019 20th International Conference on Solid-State Sensors, Actuators and Microsystems & Eurosensors XXXIII (TRANSDUCERS & EUROSENSORS XXXIII), Berlin, Germany, 2019, pp. 2084-2087.

4. **E. L. W. Gardner**, Timothy A. Vincent, RG Jones, JW Gardner, Andrea De Luca and Florin Udrea, "Thermal Conductivity Sensor with Isolating Membrane Holes," 2019 20th International Conference on Solid-State Sensors, Actuators and Microsystems (TRANSDUCERS), Montreal
5. De Luca, C. Falco, **E. L. W. Gardner**, J. D. Coull and F. Udrea, "Diode-based CMOS MEMS thermal flow sensors," 2017 19th International Conference on Solid-State Sensors, Actuators and Microsystems (TRANSDUCERS), Kaohsiung, 2017, pp. 2211-2214.
6. Falco, C.; **E. L. W. Gardner**; Luca, A.D.; André, N.; Francis, L.A.; Udrea, F. Membrane Deflection and Stress in Thermal Flow Sensors. Proceedings 2018, 2, 1089.
7. G. Loubet, **E. L. W. Gardner**, A. Takacs, A. D. Luca, F. Udrea, and D. Dragomirescu, "Wirelessly Powered and Battery-Free LoRaWAN Wireless Sensing Nodes Designed for Communicating Reinforced Concrete," Structural Health Monitoring 2019.

## Acknowledgements

ALL my gratitude must be expressed to Professor Florin Udrea for providing me with this wonderful opportunity to be a PhD student in his group, and for his excellent guidance in whichever direction I chose to go. I would also like to express my deepest thanks to Dr Andrea De Luca, who consistently offered his wealth of knowledge and helped me navigate the field of microelectronics. I would also like to thank Flusso Ltd., who offered me financial support and exposure to the exciting nature of start-up companies and a special mention must go to Dr Tim Vincent for the technical support and supply of interesting conversations. I thank all the members of the High Voltage Microelectronics & Sensors (HVMS) group for welcoming me into Cambridge and always being happy to offer help in their areas of expertise. A huge thanks must be given to Professor Daniela Dragomirescu and the entire MINC team at the CNRS-LAAS in Toulouse. I spent a fantastic six months using the expertise and equipment in their department and received an unforgettable welcome to Toulouse and to French culture. Merci à tous !

To my parents, grandparents, and sister I would like to give you all my heartfelt gratitude for your never faulting encouragement and support. During my time in Cambridge I have made an incredible network of interesting, thoughtful and talented friends, thank you for making my time here unforgettable. Last on this page but first in my thoughts, my deepest thanks go to my loving and supportive partner, Amy Chodorowski, who provides unending inspiration.



# Table of Contents

	Page
List of Figures	xix
List of Tables	xxxi
<b>1 Introduction</b>	<b>1</b>
1.1 THESIS MOTIVATION . . . . .	1
1.2 CMOS-MEMS SMART SENSING PLATFORM . . . . .	2
1.2.1 INTRODUCTION TO MICROMACHINING TECHNOLOGY . . . . .	2
1.2.2 OVERVIEW OF CMOS-MEMS . . . . .	3
1.2.3 SILICON-ON-INSULATOR (SOI) TECHNOLOGY . . . . .	5
1.2.4 SMART TECHNOLOGY PLATFORM . . . . .	6
1.3 MEMS SENSING APPLICATIONS . . . . .	9
1.3.1 OVERVIEW . . . . .	9

1.3.2	MECHANICAL SENSORS . . . . .	11
1.3.3	THERMAL SENSORS . . . . .	14
1.4	THESIS OUTLINE . . . . .	17
<b>2</b>	<b>Pressure Sensing</b>	<b>19</b>
2.1	INTRODUCTION . . . . .	19
2.2	PIEZO-RESISTIVE MEMS PRESSURE SENSORS . . . . .	31
2.2.1	DESIGN AND FABRICATION DETAILS . . . . .	31
2.2.2	EXPERIMENTAL . . . . .	36
2.2.3	DISCUSSION . . . . .	40
2.2.4	SUMMARY . . . . .	47
2.3	PIEZO-JUNCTION MEMS PRESSURE SENSORS . . . . .	48
2.3.1	DESIGN AND FABRICATION DETAILS . . . . .	48
2.3.2	EXPERIMENTAL . . . . .	51
2.3.3	DISCUSSION . . . . .	52
<b>3</b>	<b>Flow Sensing</b>	<b>67</b>
3.1	INTRODUCTION . . . . .	67
3.2	DESIGN AND FABRICATION DETAILS . . . . .	75
3.3	NUMERICAL MODEL . . . . .	80

---

3.4	EXPERIMENTAL . . . . .	84
3.4.1	ELECTRO-THERMAL CHARACTERISATION . . . . .	84
3.4.2	FLOW CHARACTERISATION . . . . .	85
3.5	OPTIMISATION OF CMOS MEMS FLOW SENSORS . . . . .	87
3.5.1	2-D vs 3-D NUMERICAL MODELLING . . . . .	87
3.5.2	CALORIMETRIC FLOW SENSOR OPTIMISATION . . . . .	94
3.5.3	ANEMOMETRIC FLOW SENSOR OPTIMISATION . . . . .	97
3.5.4	THERMO-DIODE TEMPERATURE SENSING . . . . .	105
3.6	SUMMARY . . . . .	108
<b>4</b>	<b>Thermal Conductivity Sensing</b>	<b>111</b>
4.1	INTRODUCTION . . . . .	111
4.2	DESIGN AND FABRICATION DETAILS . . . . .	120
4.3	EXPERIMENTAL . . . . .	122
4.4	DISCUSSION . . . . .	124
4.4.1	SYMMETRIC MEMBRANE HOLES . . . . .	124
4.4.2	ASYMMETRIC MEMBRANE HOLES . . . . .	127
4.5	NUMERICAL MODELLING . . . . .	131
4.6	SUMMARY . . . . .	137

---

<b>5</b>	<b>Dual Flow and Thermal Conductivity Sensing</b>	<b>139</b>
5.1	INTRODUCTION . . . . .	139
5.2	EXPERIMENTAL . . . . .	143
5.2.1	SENSOR DESIGN & FABRICATION . . . . .	143
5.2.2	MEASURING SETUP & TESTING PROTOCOL . . . . .	145
5.2.3	LINEAR STATISTICAL METHODS . . . . .	146
5.2.4	NETWORK ARCHITECTURE . . . . .	147
5.3	DISCUSSION . . . . .	148
5.3.1	RESPONSE TO FLOW & THERMAL CONDUCTIVITY . . . . .	148
5.3.2	DATA PRE-PROCESSING . . . . .	149
5.3.3	LINEAR STATISTICAL METHODS . . . . .	151
5.3.4	IMPLEMENTATION OF ARTIFICIAL NEURAL NETWORKS . . . . .	152
5.4	SUMMARY . . . . .	157
<b>6</b>	<b>Conclusions &amp; Further Work</b>	<b>159</b>
6.1	PREFACE . . . . .	159
6.2	GENERAL CONCLUSIONS . . . . .	160
6.3	GENERAL FURTHER WORK . . . . .	161
6.4	PRESSURE SENSORS . . . . .	162



---

6.4.1	CONCLUSIONS . . . . .	162
6.4.2	FURTHER WORK . . . . .	164
6.5	FLOW SENSORS . . . . .	165
6.5.1	CONCLUSIONS . . . . .	165
6.5.2	FURTHER WORK . . . . .	166
6.6	THERMAL CONDUCTIVITY SENSORS . . . . .	167
6.6.1	CONCLUSIONS . . . . .	167
6.6.2	FURTHER WORK . . . . .	168
6.7	MULTI-PARAMETER SENSORS . . . . .	170
6.7.1	CONCLUSIONS . . . . .	170
6.7.2	FURTHER WORK . . . . .	171
	<b>References</b>	<b>175</b>
	<b>Appendix A BreathFit</b>	<b>197</b>
A.1	Introduction . . . . .	197
A.2	Design and Fabrication Details . . . . .	198
A.2.1	Combo Sensor . . . . .	198
A.2.2	Housing . . . . .	200
A.3	Conclusions . . . . .	204



# List of Figures

1.1	Schematic cross-section of the available layers in the membrane stack fabrication process. LTO is low temperature oxide. . . . .	8
1.2	Flow chart representing sensor design through to the various investigated sensors, that are all created from the same smart technology platform. . . . .	9
1.3	Classification of MEMS sensors by the energy domain that the sensor measurand principally works in. . . . .	11
1.4	Different MEMS-based mechanical sensors and some of the various applications they can be used for. . . . .	13
1.5	Different MEMS-based thermal sensors and some of the various applications they can be used for (SMA is Shape Memory Alloy). 15	
2.1	A diagram illustrating the working principle of an optical MEMS pressure sensor. . . . .	22
2.2	A diagram illustrating the working principle of a resonating beam MEMS pressure sensor. . . . .	22

---

2.3	A diagram illustrating the working principle of a thin-film MEMs capacitive pressure sensor. . . . .	23
2.4	Schematic cross-section of a simple diffused n-type piezo-resistor. . . . .	25
2.5	A cross-section showing structure and deformation of a typical piezo-resistor. . . . .	26
2.6	A flow chart defining the working principle of a typical piezo-resistor. . . . .	26
2.7	A top view showing the location of the piezo-resistors and the Wheatstone bridge circuit diagram. . . . .	27
2.8	Optical micrograph of the fabricated sensor (Pr 09). Inset - detailed view of a fabricated diffused resistor (Pr 01). . . . .	32
2.9	Cross-section of the pressure sensor illustrating the position of the piezo-resistors within the membrane. . . . .	32
2.10	Cross-section diagram of the piezo resistor from device Pr 01. . . . .	33
2.11	Optical micrograph of Pr 09, illustrating the implementation of the metal ring. . . . .	34
2.12	Optical micrograph of Pr 12, illustrating the implementation of the metal tracks without the addition of silicon. . . . .	34
2.13	Picture of silicon substrate with sensors hermetically attached and cured. . . . .	37
2.14	The membrane deflection measured before and after the attaching process. . . . .	38

---

2.15	The voltage difference between -200 mBar and -300 mBar for both increasing and decreasing pressure to illustrate the membrane snapping. . . . .	39
2.16	Voltage difference output for the designs with different doping layers. . . . .	40
2.17	Deflection measured from the profilometer for the three designs with different membrane size at zero pressure difference. The dots represent the experimental data points and the line is an interpolation. . . . .	41
2.18	Voltage difference output for the change in pressure difference for the three designs with varying membrane size. . . . .	42
2.19	Voltage difference output for the designs investigating the effect of the metal ring. . . . .	44
2.20	Voltage difference output for the two structural designs of metal tracks and no membrane silicon. . . . .	46
2.21	Micrograph of device Pr A. The crystallographic orientation of pMOSFET is [110] and follows the x-axis, whereas the nMOSFET is [100] and follows the y-axis. . . . .	50
2.22	Schematic of n-channel piezo-MOSFET where p-Si denotes p-doped silicon. . . . .	50
2.23	Schematic of a piezo-diode. . . . .	51
2.24	Schematic showing the operation of the MOSFET pressure sensor for Wheatstone bridge operation. . . . .	55

2.25	Schematic showing the operation of the MOSFET pressure sensor for the equivalent circuit as piezo resistances. N.B. $V_G$ was held constant for all 4 MOSFETs. . . . .	55
2.26	The characteristic curves of the pMOSFET. . . . .	56
2.27	The characteristic curves of the nMOSFET. . . . .	57
2.28	The drain current against gate voltage for calculating the threshold voltage. . . . .	57
2.29	The change in voltage output with the evolution of pressure for the pMOSFET design with varying drain voltage. . . . .	58
2.30	The change in voltage output with the evolution of pressure for the nMOSFET design with varying drain voltage. . . . .	59
2.31	The change in voltage output with the evolution of pressure for the pMOSFET design with varying gate voltage. . . . .	59
2.32	The change in voltage output with the evolution of pressure for the nMOSFET design with varying gate voltage. . . . .	60
2.33	I-V curves for the 2 piezo-diodes where dashed lines are on-membrane diodes and solid lines are on-substrate diodes. . . . .	61
2.34	The voltage output of the Wheatstone bridge with the evolution of pressure for the piezo-diode designs. . . . .	64
3.1	Diagrammatic representation of the three main operation modes for a thermal flow sensor. . . . .	72

---

3.2	Optical micrograph of MEMS flow sensor with multiple heaters (FL 01) – die dimensions of 1.6 mm by 1.6 mm. The dotted black line represents the square with rounded corners membrane shape. . . . .	77
3.3	Cross-section of sensor along cut point X-X that is depicted in Figure 3.2 (not to scale) The tungsten heater connects to tracks within the same metal layer in the membrane which are connected to the surrounding pads. . . . .	78
3.4	Temperature distribution across the membrane. . . . .	82
3.5	Temperature distribution across the membrane and heater, parallel to the direction of flow. This temperature distribution is for no flow and is therefore symmetric. . . . .	83
3.6	Temperature distribution along the heater, perpendicular to the direction of flow. . . . .	83
3.7	Photograph of a thermal flow sensor wedge bonded on a DIL8 package with the cavities full of a cured transparent photopolymer. . . . .	85
3.8	Pictures of the experimental setup. . . . .	86
3.9	A block diagram representation of the experimental setup, for flow sensor measurements only the compressed air was used. . . . .	86
3.10	A snapshot 2D simulation result with air flowing above the sensor. A thermal contour plot as well as velocity colour mapping are presented along with arrows indicating the flow velocity profile. The colour map goes from highest velocity at red to zero velocity at dark blue. . . . .	88

3.11	A snapshot 3D simulation result with air flowing above the sensor. A thermal contour plot as well as surface temperature distributions are presented along with arrows indicating the flow velocity profile. . . . .	89
3.12	Temperature reached by the heater for specified power input. . .	90
3.13	Temperature profile along the line X-X from Figure 3.2 for no flow ( $\tau_w = 0$ Pa) and flow ( $\tau_w = 1$ Pa). Heater location is set at zero with each direction extended to the edge of the membrane, temperature after this (through the substrate) is negligibly close to ambient. . . . .	91
3.14	Temperature difference output as a function of wall shear stress for anemometric approach. Voltage standard deviation measurements are converted to temperature and added to the experimental plot. . . . .	93
3.15	Temperature difference output as a function of wall shear stress for calorimetric approach at 400 $\mu\text{m}$ either side of the heater. . .	93
3.16	The evolution of temperature difference against wall shear stress for the calorimetric method at the two distances of 100 $\mu\text{m}$ and 200 $\mu\text{m}$ from the central heater. . . . .	95
3.17	Temperature output as a function of diode distance from central heater for varying wall shear stress, the dotted line bisects each flow rate at its point of highest sensitivity. . . . .	95
3.18	Optimum diode distance for varying wall shear stress at 4 different heater lengths where the legend refers to the heater length. .	97



---

3.19	Thermal colour plot of numerical simulation showing the difference in heated region shape for heater lengths 200 $\mu\text{m}$ (left) and 800 $\mu\text{m}$ (right). The temperature legend is in degrees Celsius and applies to both sides of the figure. . . . .	98
3.20	Experimental voltage drop change measured across the resistor in 2-wire configuration. . . . .	100
3.21	Percentage accuracy of the flow rate reading measured in 2-wire configuration for all the sensors with varying resistor geometries.	102
3.22	Direction and proportional magnitude of air velocity in stagnant flow for (top) Fl 02, (middle) Fl 04 and (bottom) Fl 05. The red segment schematically represents position and length of the heating element. The scale bar legend is in degrees Celsius and applies to all three scenarios. . . . .	104
3.23	Experimental forward bias voltage against temperature for the long (Fl 11) and short (Fl 12) diode at three different driving currents (1 $\mu\text{A}$ , 10 $\mu\text{A}$ and 100 $\mu\text{A}$ ). . . . .	106
3.24	Experimental voltage drop change measured across the diode for small and large designs. The original design of 5 short diodes in series is also shown as a reference. . . . .	107
3.25	The accuracy calculated for each flow rate. The purple lines represent Fl 02, orange Fl 03 and green Fl 04. Solid lines are for 2-wire (2w) resistance measurements, dashed for 4-wire (4w) resistance measurements and dotted for diode (D) measurements.	108
4.1	An illustration of the working principle behind the thermal conductivity detector. . . . .	117

- 
- 4.2 Optical micrograph of one of the sensor chips – die dimensions of 2.0 mm  $\times$  2.0 mm. . . . . 120
- 4.3 Cross-section of sensor along cut point A-A that is depicted in Figure 4.2 (not to scale). . . . . 121
- 4.4 A photograph of the sensor packaged in a DIL8 base and attached to the 3D printed lid, containing barbs for connected to the inlet and outlet of the gas testing system. . . . . 123
- 4.5 Electrothermal efficiency for the three investigated symmetric designs. . . . . 125
- 4.6 The voltage response of the central resistor with the evolution of CO<sub>2</sub> concentration. . . . . 126
- 4.7 The difference in voltage between the two RTDs plotted against percentage CO<sub>2</sub> in air. . . . . 128
- 4.8 Top schematic of ‘asymmetric holes’ sensor with two different designs for membrane hole location. Blue dotted lines represent the location of the membrane holes. Electrical resistor symbols have been added to represent the Thermal Resistance (TR) between the heater and the RTDs. . . . . 129
- 4.9 Electrically equivalent circuit of the heat transfer through the membrane. . . . . 129
- 4.10 Geometry created for the numerical model with the inclusion of holes. Inset - 3D isometric detailed view of circled section showing fabrication layers. . . . . 132

---

4.11	The mesh used in the numerical model for the design with holes where the colour legend illustrates mesh size in metres. . . . .	132
4.12	Simulation results of the temperature profile across the sensor for the original design (design 1) and the improved design (design 2) in both air and CO <sub>2</sub> . . . . .	133
4.13	A graphical depiction of the three membrane holes investigated where small, medium and large holes are denoted by red, blue and green respectively. . . . .	135
4.14	Temperature reached by the heater for the experiment and simulation. . . . .	135
5.1	A chart showing the development of the top impacting factors on the global MEMS market from 2019 to 2026, trends are taken from [1]. . . . .	140
5.2	Optical micrograph of the investigated sensor chips – die dimensions of 2.0 mm ×2.0 mm. . . . .	144
5.3	A cross-section of the layer technology used in fabrication for the design with membrane holes. . . . .	144
5.4	A diagram of the 3-layer network incorporated for 3 inputs and 2 outputs fully connected with 10 neurons in the hidden layer. .	147
5.5	The discrimination between air and 20% CO <sub>2</sub> after being normalised by base resistance for the designs with double holes and without holes for the central resistor. . . . .	149

5.6	The discrimination between air and 20% CO <sub>2</sub> after being normalised by base resistance for the designs with double holes and without holes for the downstream resistor. . . . .	150
5.7	The discrimination between air and 20% CO <sub>2</sub> after being normalised by base resistance for the designs with double holes and without holes for the upstream resistor. . . . .	150
5.8	The observed responses of the experiment against the fitted responses from PLSR and PCR linear correlation methods. . . .	152
5.9	The output values from the neural network compared against the target values from experimental data for the design with no holes. . . . .	154
5.10	The output values from the neural network compared against the target values from experimental data for the design with holes.	154
6.1	Optical micrograph showing an example of a fabricated design with asymmetric membrane holes for optimising sensitivity. . . .	169
6.2	Optical micrograph showing an example of a second fabricated design with asymmetric membrane holes for optimising sensitivity.	170
6.3	A design idea for both thermal conductivity and flow measurement using perpendicular wires. . . . .	172
6.4	An optical micrograph of a sensor with a heater for flow measurements and piezo-resistive pressure sensitive elements. . . . .	173
A.1	Optical micrograph of the combo sensor that embeds three metal oxide sensors and one flow sensor. . . . .	199

---

A.2	The dependence of gas sensor response on the flow rate. . . . .	200
A.3	3D CAD models of each individual component and assembly of the housing that embeds the electronics and the sensor in an air-tight handheld system. . . . .	201
A.4	A picture of the 3D printed housing assembly, also illustrating how it is connected to the gas rig for testing. . . . .	201
A.5	Simulation results showing the velocity through the bypass system where flow is going from right to left. . . . .	202
A.6	Experimental set-up for bypass characterisation. The air first flows inside the big pipe, where it interacts with the first flow sensor, and then fed inside the bypass, collected by the small pipe and redirected on top of the second sensor. . . . .	202
A.7	Response comparison from the two sensors, inside the main pipe exposed to slow flow (blue line) and inside the bypass with high flow allowed by the MFCs . . . . .	203



# List of Tables

1.1	Comparison between the materials that are commonly used for the metal layer within CMOS MEMS sensors. . . . .	7
1.2	A summary of the benefits and drawbacks of the most common temperature detectors. . . . .	16
2.1	A summation of fields where pressure sensors need to be used alongside some applications they are used within. . . . .	20
2.2	Advantages and disadvantages of the main transduction methods used in pressure sensors. . . . .	24
2.3	Current commercial pressure sensors with their price and working range. . . . .	29
2.4	A summary of all the investigated pressure sensor designs and their pertinent design parameters. . . . .	35
2.5	Summary of all the investigated piezo-junction pressure sensor designs and their pertinent design parameters. . . . .	49
2.6	Table showing current technologies and their sensitivities. . . . .	65

---

3.1	A summation of fields where flow sensors need to be used alongside some parameters that need to be specifically measured. . . .	68
3.2	The main advantages and disadvantages of the three main operating modes used for thermal flow sensors. . . . .	72
3.3	A summary of current commercial thermal gas flow sensors that operate in a similar flow rate range to the designed flow sensor in this thesis. . . . .	76
3.4	A summary of all the investigated flow sensor designs and their pertinent design parameters where Sq. w/ RC stands for square with rounded corners. . . . .	79
3.5	Electrothermal efficiency of the different designs flow sensor designs driven in anemometric mode. . . . .	99
4.1	A comparison between the gas sensing technologies with their relative advantages and disadvantages. . . . .	114
4.2	The thermal conductivity values of common gases. . . . .	118
4.3	Electrothermal efficiency and relative percentage increase with the addition of isolating membrane holes. . . . .	127
4.4	The sensitivity and improvement of the designs extracted from the power-temperature relationship. . . . .	136
5.1	Table showing the results of testing the trained network 1 for the design with no holes. . . . .	156
5.2	Table showing the results of testing the trained network 1 for the design with holes. . . . .	156



# Chapter 1

## Introduction

### 1.1 Thesis Motivation

THROUGHOUT the world there are an abundance of situations that require close monitoring and control. With the development of sensors, both industry and consumables can be revolutionised to change the way in which we live. This has resulted in a large commercial demand for sensors with a high performance/price ratio, highlighting the prime motivation behind this thesis: *market demand*.

A sensor is a device that is used to measure a property from the surrounding environment such as pressure, position, temperature or acceleration among many others. This property can then be relayed to the user, or a system can be implemented that automatically responds with a designed feedback. In this globally technological world, sensors are the axiom of system performance. They are essential to provide useful and accurate data in order to achieve the desired outcome in the increasingly smart, connected and autonomous world.

## 1.2 CMOS-MEMS Smart Sensing Platform

### 1.2.1 Introduction to Micromachining Technology

The acronym MEMS stands for Micro Electro Mechanical Systems, which was coined in the United States in the 1980s and the MEMS industry was kick-started off the back of the discovery of silicon micromachining fabrication techniques. With the advent of micromachining technologies, sensors have become miniaturised whilst also dramatically improving their sensitivity, power consumption, cost, temporal accuracy and reliability. There are currently four major classes of micromachining that are bulk, surface, epi-micromachining and LIGA-micromachining (Lithographie, Galvanoformung, Abformung [Lithography, Electroplating, and Moulding]), however the latter is very expensive and incompatible with microelectronics so is rarely used for the commercial fabrication of low-cost micro sensors and is thus disregarded here.

Surface micromachining builds MEMS through thin-film deposition and etching of layers over a substrate. This allows the fabrication of mechanical and electronic components on the same substrate, which can be made from cheaper materials such as glass or plastic. In opposition to this, bulk micromachining defines its structures by selectively etching structures inside a substrate, allowing the etching to be independent of crystal orientation and dependant on the etchant. Bulk micromachining is inherently more reproducible due to the well-defined material properties of single-crystal silicon as opposed to polycrystalline and amorphous thin-films.

More recently, to try and counter-act the disadvantages of both these methods by using techniques from both, epi-micromachining was developed, which is where front-side bulk micromachining is used with wet or dry etching. Bulk micromachining is a reality when it comes to commercially viable MEMS

sensors due to the number of available foundries producing off the shelf products that are extremely attractive for price and performance.

In the most general form, MEMS consist of mechanical micro-structures, micro-sensors, micro-actuators and micro-electronics, all integrated into the same device. The micro-sensors detect a change in the system's environment by measuring mechanical, thermal, magnetic, chemical or electromagnetic phenomena. The micro-electronics process this information and then the micro-actuators react and create a measurable change correlated to the environmental change.

Finally, a report on the global sensor market showed that MEMS accounted for 73% of the 9.3 billion US dollar semiconductor sensor market in 2018 and also 47% of the 42.1 billion total sensor units to be shipped [2] and is set to rise by around 12%. This shows why research into the advancement of MEMS based sensors is crucial, and only set to get a larger commercial attraction in the future.

MEMS devices are very small, with their micro-structures often being micron dimensioned with nanosized grains. However, MEMS is not just the miniaturisation of mechanical components, and can be considered a misleading term as many MEMS devices do not contain any mechanical parts. MEMS can be considered as a manufacturing technology that can be used for creating complex devices and systems as well as their integrated electronics.

### 1.2.2 Overview of CMOS-MEMS

MEMS sensors all convert a non-electrical input into an electric output, which must then be processed to attain valuable information from the sensor. When MEMS sensors are fabricated with the standardised Complementary Metal Oxide Semiconductor (CMOS) processes, the resulting devices are known as

CMOS MEMS. Over the last 30 years, considerable effort has been made to achieve MEMS sensors that can be incorporated into the CMOS process. The employment of standard CMOS processing allows the sensing transducer and electronic circuits to be fabricated on a single chip, whilst being just a few micrometres apart. Other inherent advantages that come with the CMOS process include:

- i. CMOS MEMS can be manufactured in extremely high volume and thus do not offer problems with scalability and provide lower manufacturing costs.
- ii. Having on-chip electronics alongside the sensing element and a connection between the two allows the miniaturisation of the entire sensing system.
- iii. The sensor performance can be improved due to repeatable and uniform material properties, reduced parasitic effects between sensors and electronics and very accurate production of the micro-structure geometries.

Despite these advantages, the CMOS process provides some difficulties that need to be overcome. The first limitation is that the choice of materials and their layout must adhere to much more stringent design rules, limiting the design workspace and adding difficulty to the design process. Another limitation is that, due to the design rules, the design software for CMOS devices is separate to conventional MEMS design and optimisation software. This results in multi-software complications that increase the difficulty of design optimisation, although COMSOL Multiphysics software has been tackling this problem.

For most, the benefits far outweigh the drawbacks for the CMOS process, mostly due to the possibility of high quality and low cost manufacturing, on-chip electronics and increased reliability, which are two incomparable advantages in the world of commercial electronics.

### 1.2.3 Silicon-on-Insulator (SOI) Technology

A more recent addition to micromachining technologies is Silicon On Insulator (SOI) devices, where an SOI wafer contains a thin single crystal silicon layer that is isolated from the bulk silicon substrate by a Buried Oxide (BOX) in the form of a silicon dioxide ( $\text{SiO}_2$ ) layer. The SOI process has received sufficient commercial interest that established foundries can now incorporate this technology, stemming from the two realisation processes of Separation by Implanted Oxygen (SIMOX) and Smart Cut™. The former approach uses a high dose of oxygen ions that are implanted in the silicon substrate. With a high temperature annealing process, an oxide layer is synthesised underneath a superficial silicon film. The second approach implants hydrogen ions to damage the silicon lattice and, alongside a wafer bonding process, obtain a superficial thin layer of silicon. SOI devices offer a number of advantages over traditional bulk micromachining:

- i. SOI is particularly attractive for suspended structures because the BOX layer can act as an etch stop for both front and back micromachining techniques.
- ii. This BOX layer is also an excellent electrical and thermal insulator, isolating the silicon layer from the silicon substrate.
- iii. The thin single crystal silicon layer has superior mechanical and electrical properties when compared to polysilicon.
- iv. Electronic components are isolated vertically from the substrate and horizontally from each other by using trenches filled with oxide or MESA etching regions, resulting in very small leakage currents, reduced parasitic components, radiation hardness and superior miniaturisation potential.

Despite the technological landscape of SOI devices changing, their commercial price remains relatively high and their applications are limited to

markets where their advantages are necessary in order to absorb the extra cost. If SOI does not provide significant improvement over bulk that justify the additional cost, it will not be adopted.

### 1.2.4 Smart Technology Platform

This section describes the single technology platform that is used to develop all of the sensors designed in this thesis. Firstly, the material selected for the metal layers was tungsten. It has been well established that tungsten is a more robust material when it comes to use in thermal sensors [3]. Compared with aluminium it has a higher melting point, higher yield strength, higher young's modulus and lower thermal conductivity.

Table 1.1 shows a comparison of the common materials aluminium (Al), tungsten (W), gold (Au) and platinum (Pt), that are most often used for the metal layer and their important characteristics. The advantages of tungsten are then specifically discussed with regards to their relevant property.

The advantages of tungsten can be seen here where special attention should be taken of the Temperature Coefficient of Resistance (TCR), which defines device sensitivity. The high melting point of tungsten equates to a better reliability alongside the possibility of running the device at higher temperatures, which often means higher sensitivity. The lower thermal conductivity offers benefits by reducing the thermal conduction lost through the tracks. Electrically, the conductivity of tungsten is half of aluminium, which allows the miniaturisation of sensors as well as better power consumption due the higher electrical resistance yielding the more efficient heating up of the resistor.

The sensors reported throughout this thesis were all fabricated using a 1  $\mu\text{m}$  CMOS process through a commercial CMOS foundry. The process was used on two different wafers (SOI and bulk silicon), allowing the investigation

**Table 1.1:** Comparison between the materials that are commonly used for the metal layer within CMOS MEMS sensors.

Property (Units)	Al	W	Au	Pt
Electrical Conductivity ( $\Omega$ )	377	183	488	94
Melting Point ( $^{\circ}\text{C}$ )	660	3410	1064	1772
Density ( $\text{kg}/\text{m}^3$ )	2720	19350	19320	21450
TCR ( $10^{-4}\text{C}$ )	39	45	34	30
Thermal Conductivity ( $\text{W}/\text{m}/\text{K}$ )	236	177	319	72
Specific Heat Capacity ( $\text{J}/\text{K}/\text{kg}$ )	904	134	129	133
Linear Expansivity ( $\text{K}^{-1}$ )	23.1	4.5	14.2	8.8
Young's Modulus (GPa)	70	411	78	168
Yield Strength (MPa)	50	750	200	<14
Poisson's Ratio	0.35	0.28	0.44	0.38

into the benefits of the SOI technology. All of the layers are separated by a buried oxide (silicon oxide) layer that acts as a dielectric.

A schematic representation of the cross-section, illustrating the available layers is presented in Figure 1.1, showing a potential of three metal layers as well as the single crystal silicon and polysilicon layers. A silicon oxide and silicon nitride layer are added to the top to act as passivation layers for the CMOS electronics.

To create a membrane underneath the sensing element, a post-CMOS Deep Reactive Ion Etch (DRIE) step is performed at the backside of the CMOS 6" wafer that is approximately 375  $\mu\text{m}$  thick after thinning. This step was used to create membranes of different shape and resulted in the multi-layer membrane, illustrated in Figure 1.1, being approximately 4.5  $\mu\text{m}$  thick. The reason for the membrane is to reduce conductive heat loss and thus increase the efficiency of the device. The thickness of the membrane is limited by the

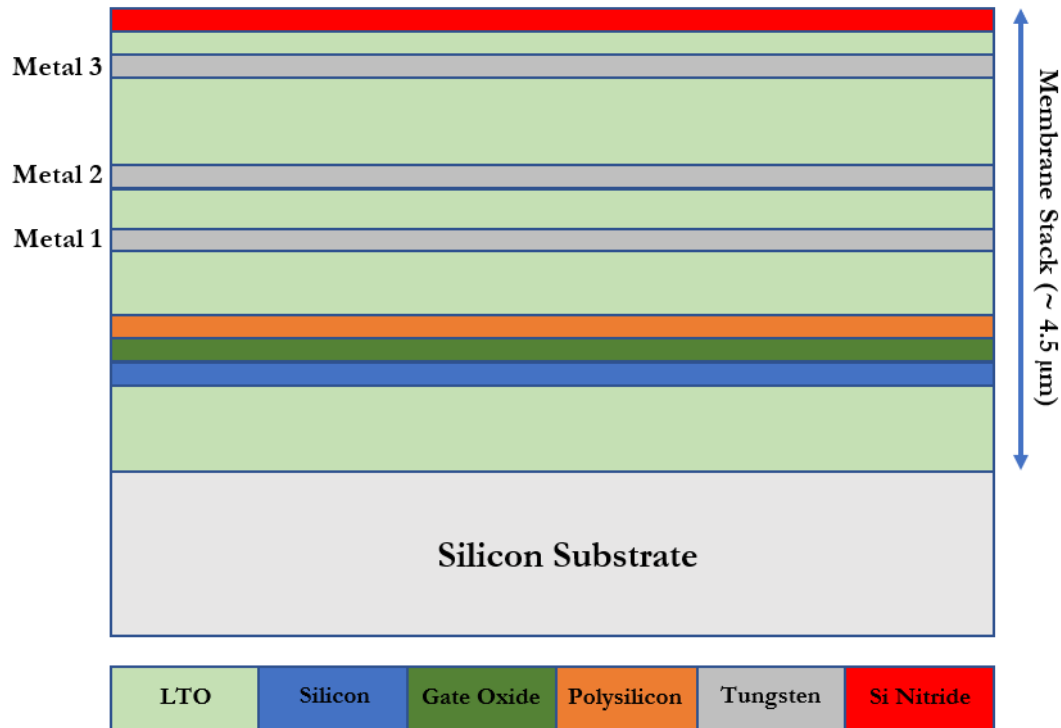


**Figure 1.1:** Schematic cross-section of the available layers in the membrane stack fabrication process. LTO is low temperature oxide.

CMOS process because the oxide layers must be above a minimum thickness, highlighting one of the disadvantages of the CMOS process.

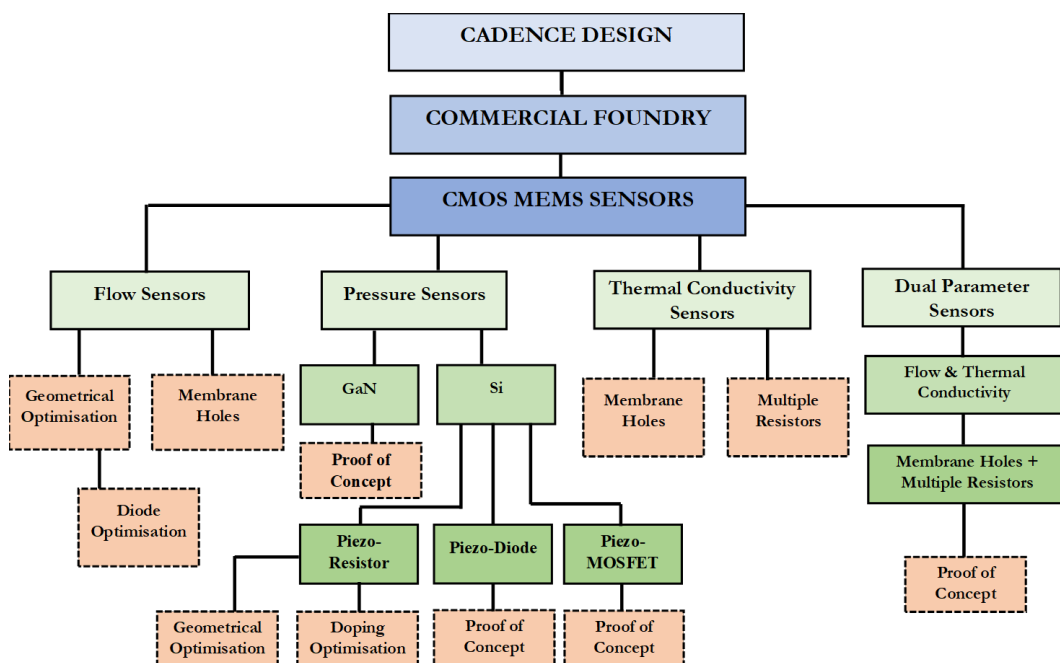
A further fabrication step has been developed where, before the final back side DRIE that creates the membrane, there is a front etching process that uses the silicon substrate as an etch stop in order to etch all the way through the membrane stack. This front etch, in conjunction with the back DRIE, results in holes through the membrane. The holes can be used to help control the heat conduction through the structure. The inclusion of these holes for sensing purposes alongside a discussion on their advantages and disadvantages is presented in chapter 4.

Figure 1.2 shows a block diagram process flow of the different types of sensors that were fabricated using the technology platform outlined in this section. The three main investigated sensor technologies are pressure sensors,



flow sensors and thermal conductivity sensors, which are discussed in more detail in the following chapter.

For the sensor designs that aim for a proof-of-concept, it is a first design and experimentation of these sensor types using the available technology platform. For the previously investigated sensor types, further optimisation has been carried out in order to advance the technology and make it more commercially attractive.



**Figure 1.2:** Flow chart representing sensor design through to the various investigated sensors, that are all created from the same smart technology platform.

## 1.3 MEMS Sensing Applications

### 1.3.1 Overview

A sensor is a device that measures information from the surrounding environment and transforms this information into an electrical signal. The information

that is being measured can be categorised into many classes, dependant on the energy domain. The classifications of MEMS sensor energy domains are shown in Figure 1.3 with examples of what they can sense.

The first commercially available MEMS sensor belonged to the mechanical classification and was a silicon strain gauge in 1958, almost 20 years after its discovery by Edward Simmons [4]. Following this, a silicon pressure sensor was demonstrated in 1961 [5] before the invention of surface micromachining in 1967 [6]. It is in the 1980s that the micromachining interest gained momentum, fuelled by the instrumental paper on silicon as a mechanical material [7]. The late 1980s spawned widespread commercial and academic experimentation with micromachining and led to the first MEMS conference in 1988. Currently, MEMS are used in high volume production across a huge array of applications in many different markets [8]. According to a recent report published by Allied Market Research, entitled "Microelectromechanical (MEMS) Market by Product Type and Application: Global Opportunity Analysis and Industry Forecast, 2018-2026," the global microelectromechanical system market size was valued at \$48.74 billion in 2018, and is projected to reach \$122.83 billion by 2026. The huge market value alongside the predicted continued growth highlights the importance of continued research in the field of MEMS.

In this thesis, sensors are developed that belong to the mechanical and thermal energy domains. The next two sections will give a brief introduction to the most commonly available technologies in these two domains. A more detailed description of the specific technology used for the sensor development in this work can be found in the introduction of each chapter.

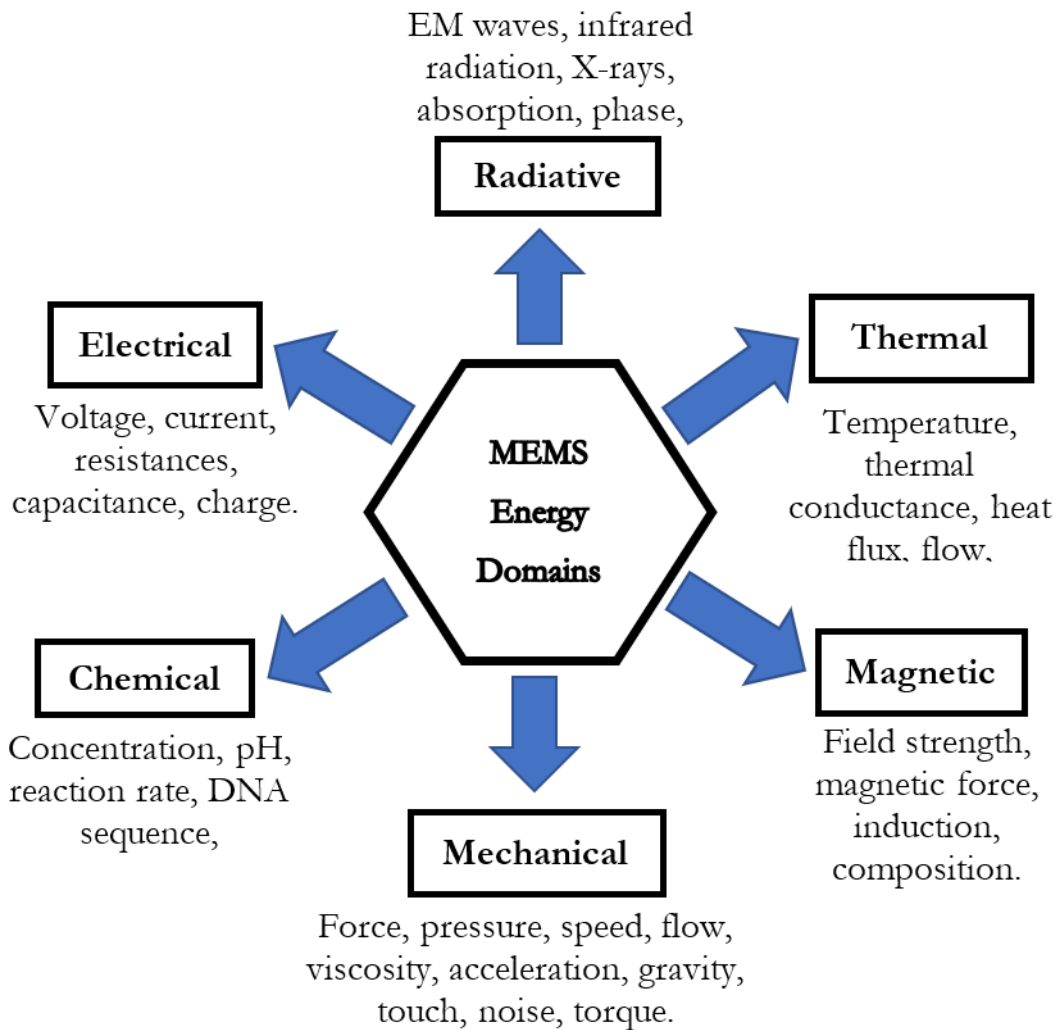


**Figure 1.3:** Classification of MEMS sensors by the energy domain that the sensor measurand principally works in.

### 1.3.2 Mechanical Sensors

Within the market demand for sensors, mechanical sensors have been the most sought after and will continue to be so for the foreseeable future. The most common mechanical sensors include pressure, force, acceleration, torque, inertia and flow and all convert a mechanical property to an electrical read-out. Figure 1.4 shows the most commercially available MEMS-based mechanical sensors alongside some examples of the fields and applications that they can be used for.

The most common sensing mechanisms are piezo-resistive, piezo-electric, piezo-capacitive and resonant. The piezo-resistive effect is when there is a change in the resistance of a material when there is strain applied and was first discovered by Lord Kelvin in 1856. When a piezoresistor changes dimensions, the change in resistance is measured and equated to the applied strain. Doped silicon makes an excellent piezo-resistive material and can be two orders of magnitude higher than that of the metal strain gauge effect [9]. It should also be mentioned, however, that piezo-resistance is generally anisotropic unlike metal strain gauges, which are isotropic. The first application of the piezo-resistive effect did not appear until the 1930s where thin-metal foils were glued onto a surface.

Piezo-electric sensors use the piezo-electric effect where an applied force on a crystal creates a potential difference across the crystal. This is a very unique and interesting effect that was first discovered in quartz by Jacques and Pierre Curie in 1880. The physical origin of the piezo-electricity is created because of an asymmetry within the crystal structure and can be separated into the two groups of crystals and ceramics, with some common piezoelectric materials being Lead Zirconate Titanate (PZT), barium titanate and lithium niobate. The effect can be exploited to measure a displacement or mechanical stress and devices that use this phenomenon include microphones [10], pressure sensors [11] and hydrophones [12]. It should be noted that silicon is not inherently piezo-electric and an extra layer must be incorporated in order to use it as such.

Capacitive sensing is one of the most widely used precision sensing methods for measuring the movement of an object. A device comprises of two parallel conducting plates separated by a small gap. The capacitance between the two plates changes when the distance between the plates varies, where the distance is altered with a change in pressure. Thus, a change in capacitance accurately correlates to change in pressure.

Finally, resonant sensors use a micro-structure (usually a beam or bridge) that is driven at its resonant frequency. These can be attached to a membrane or made to adhere to a particular substance. With the displacement of the membrane or build-up of particles, the resonant frequency of the beam changes proportionally to the desired measurand. A detailed description on all the transduction methods within the mechanical MEMS domain is given by Beeby et al. [13].

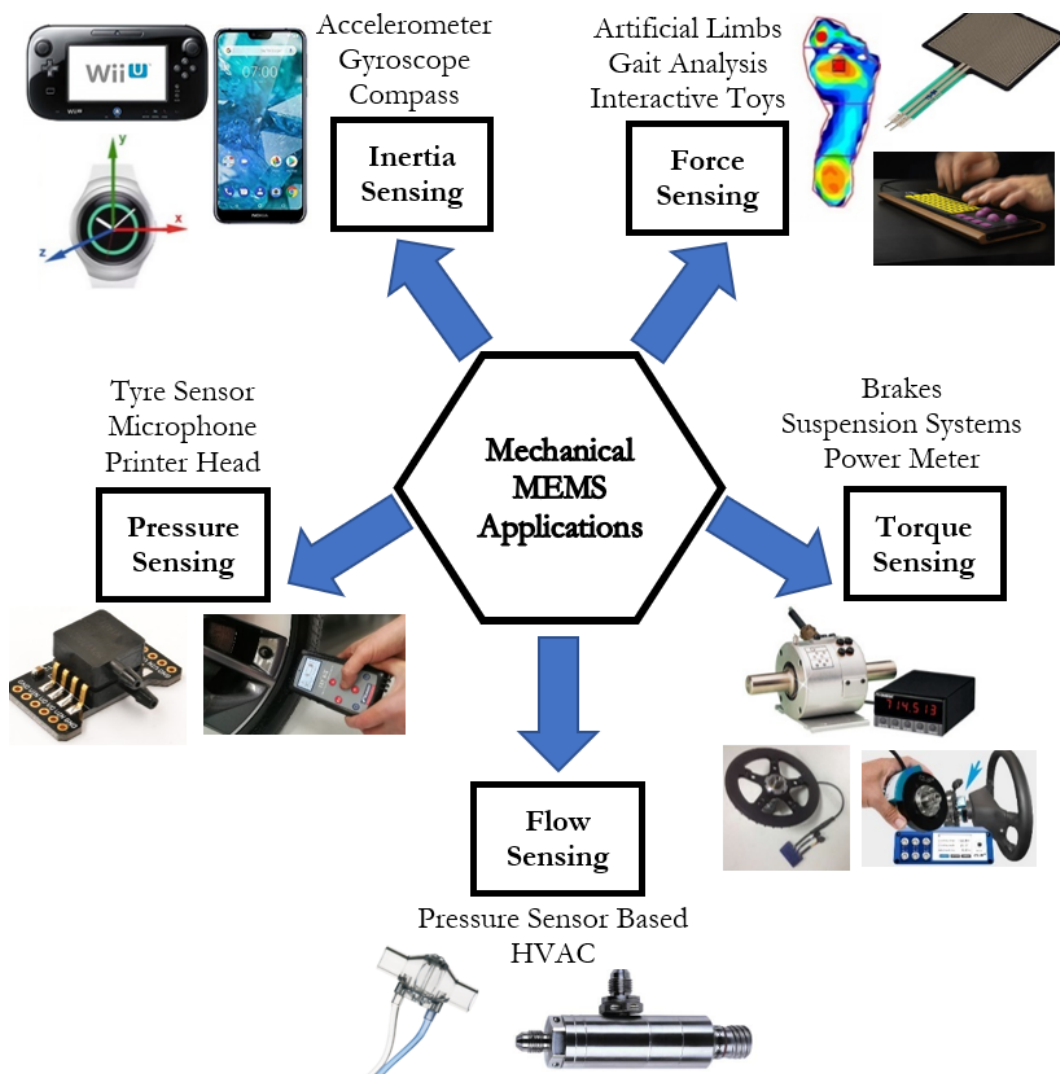


**Figure 1.4:** Different MEMS-based mechanical sensors and some of the various applications they can be used for.

In this thesis, the piezo-resistive effect is exploited for the design and fabrication of the pressure sensors. Effects of different piezoresistor designs

alongside sensor geometry alterations are explored. With the addition of SOI technology, electronic components such as diodes and transistors are fabricated and tested as piezo-electronic transducers.

### 1.3.3 Thermal Sensors

Thermal sensors all use the physical phenomena of heat and heat transfer to their advantage. This has benefits over mechanical sensors because there are no moving parts in the system, which can often cause a problem in reliability. The most common thermal sensors include temperature and flow sensors, with the main sensing mechanisms being thermo-mechanical, thermo-resistive and thermo-coupling. Figure 1.5 shows many of the available sensors that can be made with thermally based technologies as well as an indication of some of the industries that they are applied to.

Thermo-mechanical sensors exploit the coefficient of thermal expansion shown in materials. Generally, if two materials with a different coefficient of thermal expansion are attached to one another and a temperature change is applied, they will expand differently and cause movement in the system.

Thermo-resistive sensors exploit that the resistivity of materials changes with temperature, thus a simple measurement of the change in resistance can be used for attaining the require information. The rate of change of resistivity with temperature is known as the Temperature Coefficient of Resistance (TCR) and is paramount in defining the sensitivity of thermally based sensors.

A thermo-couple is a junction formed between two different electrical conductors where the voltage across the junction is dependent on the temperature. The thermoelectric effect (the voltage created via the temperature difference) is greater in semiconductors than metals, again highlighting the benefits of semiconductor materials.

The most common and widespread thermally based sensors are used for measuring temperature, which also forms the basis of many of the other thermal sensing principles such as for flow sensors and gas sensors. The three most common types of temperature sensor are thermocouple, Resistance Temperature Detector (RTD) and thermistor. A table summarising their relative advantages and disadvantages is given in Table 1.2.

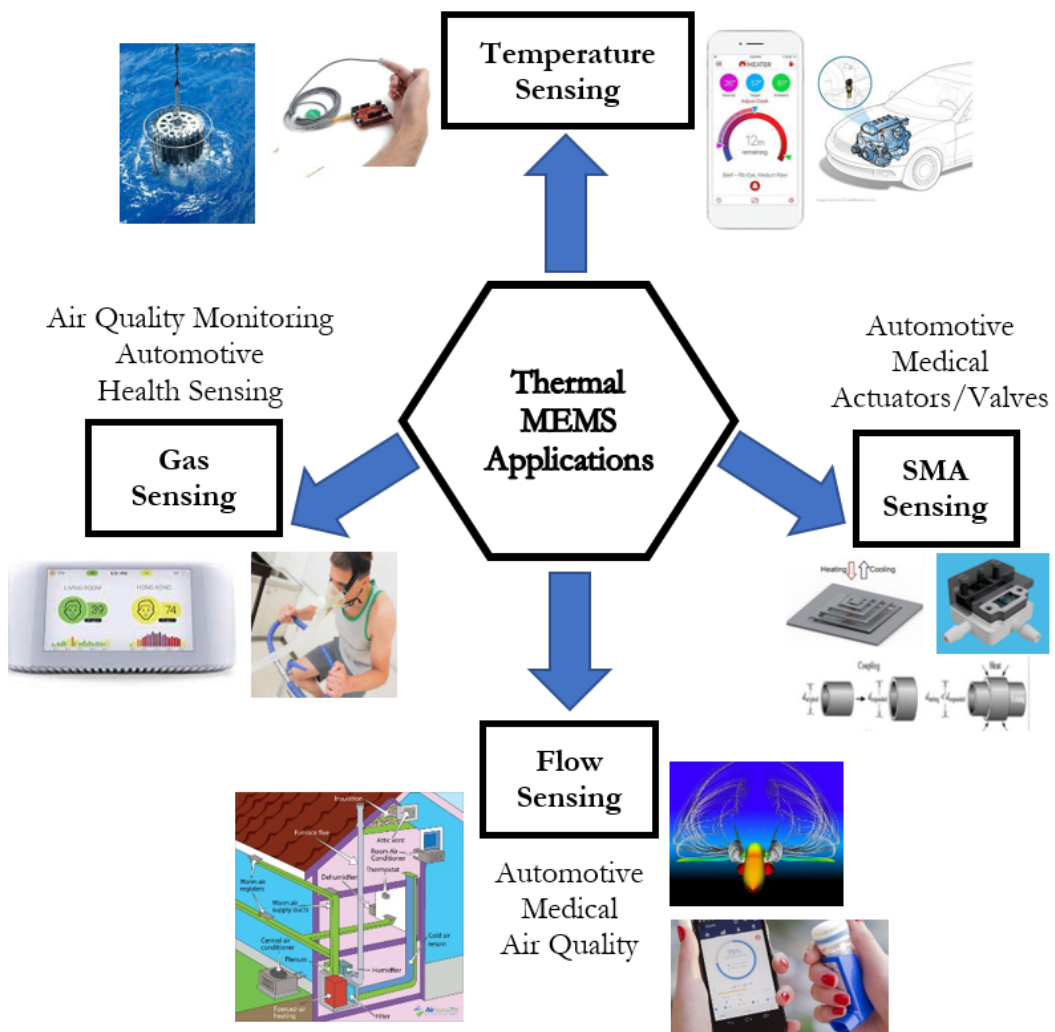


**Figure 1.5:** Different MEMS-based thermal sensors and some of the various applications they can be used for (SMA is Shape Memory Alloy).

Thermopiles are created by connected multiple thermocouples in series and thermocouples are based on the thermoelectrical effect generated in the junction of two dissimilar metals (or metal/silicon junctions). RTDs are based on the thermo-resistive principle and change values of electrical resistances

to indicate the change in temperature. Thermistors also detect temperature variability using their change in resistance but differ from RTDs because the material used is a ceramic or a polymer, as opposed to RTDs that use metals.

**Table 1.2:** A summary of the benefits and drawbacks of the most common temperature detectors.

Sensor Type	Thermopile	RTD	Thermistor
<b>Advantages</b>	Self-powered	High stability	Fast
	Wide temp range	Accurate	Cheap
	Cheap	Medium linearity	High Output
	Simple	Good temp range	
<b>Disadvantages</b>	Non-linear	Current sourced	Non-linear
	Low voltage	Self-heating	Low temp range
	Low stability	Expensive	Self-heating
	Low sensitivity		Low accuracy

In this thesis, thermal based MEMS technology is used as the foundation for developing flow sensors and thermal conductivity sensors, mainly relying on resistant temperature detectors. This form of temperature sensing is chosen because of its inherent advantages, including:

- i. High stability rendering a product with a long lifetime.
- ii. Medium linearity yielding read-out electronics that are not complicated.
- iii. Working temperature range (-40 °C to 125 °C) allowing operation in a variety of applications.
- iv. Ability to be bulk micro-machined.
- v. Requiring a small amount of space on the membrane, allowing integration with other membrane features such as the membrane holes.



## 1.4 Thesis Outline

Due to the market demand of sensors, there is a large amount of research surrounding any potential improvement on current devices, with the aim of displacing currently used commercial solutions. This thesis is another step towards designing, optimising and improving sensing technologies and doing so whilst using a single technology platform (which is common to all the sensors in this thesis). The thesis focuses on the development of CMOS-compatible sensors for commercial application, using both bulk silicon and SOI wafer technology. The thesis focuses specifically on flow sensors, pressure sensors and thermal conductivity sensors and is organised as follows, with each chapter containing an introduction on the technology:

*Chapter 1* provides background on the advent of micro-machining techniques and how this technology has helped to revolutionise the sensing world. Following this, there is a description of the technology platform that is used as a basis for all of the devices fabricated throughout this thesis. A brief discussion on mechanical and thermal MEMS sensors is also presented followed by an overview of how this thesis is organised.

*Chapter 2* outlines the progress made with developing MEMS pressure sensors using the technology platform. The design, fabrication and experiments are discussed with particular regards to sensitivity and linearity. Several different piezo-resistive designs were investigated as well as looking at several geometric alterations. In addition to this, SOI wafers were used to investigate using electronic components as the pressure transducing element, namely diodes and transistors. The results are compared with current technology and with one another to be used as a benchmark for designing future pressure sensors using this technology platform.

*Chapter 3* discusses the performance and optimisation of thermal flow sensors. Multiple designs are fabricated and tested for optimising the geometry of this commercially popular solution. The experimental data are substantiated by numerical models and the models are then used to further optimise aspects of flow sensing without the costly iterative process of design and fabrication. Sensitivity, accuracy and device behaviour are investigated in depth for both anemometric and calorimetric driving principles.

*Chapter 4* investigates using the technology platform for thermal conductivity gas sensors. In this chapter, a new fabrication step is utilised that can create holes through the membrane, thus thermally isolating transduction components. Anemometric thermal conductivity gas sensing is investigated as well as the proof-of-concept of a new differential method for measuring thermal conductivity. A theoretical and analytical optimisation of the differential method is also presented and provides pertinent knowledge for the next design and fabrication round of this new method.

*Chapter 5* combines the knowledge from chapter 3 and chapter 4 to measure both flow rate and thermal conductivity on a single device. The inclusion of membrane holes is used to increase the gas discrimination factor of the sensors in the presence of flow. With this, post-processing techniques including linear statistical methods and artificial neural networks are employed to decouple these two closely related parameters. This chapter is the first step towards using membrane holes with smart data processing to allow multi parameter sensing on a single chip.

*Chapter 6* gives some final concluding remarks as well as an insight into future research and development that could be carried out.

# Chapter 2

## Pressure Sensing

### 2.1 Introduction

THE most mature industrial use of micromachined sensors revolves around pressure transducers, of which various technologies have been developed. The inherent nature of micromachining allows these pressure sensors to become smaller, temporally faster, very accurate and require less power consumption. Mordor Intelligence valued the global pressure sensor market at 4481 million US dollars in 2017, with it predicted to grow to 6790 million US dollars by 2023, which equates to a Compound Annual Growth Rate (CAGR) of 7.3% over this period [14].

The pressure sensors market is dominated by piezoresistive and capacitive sensors which are heavily used in automotive, medical, petrochemical and the oil & gas industries [15–17]. However, consumer electronics has been marked as the segment with the fastest growth in this market, where MEMS pressure sensors become very attractive due to their low power consumption, small size and low cost. Table 2.1 outlines several commercial fields that require the use of pressure sensors. In addition to this, some examples of the important

applications they are used in are given, highlighting the extensive market requirement for pressure sensors and the driving force behind their continued research and development.

**Table 2.1:** A summation of fields where pressure sensors need to be used alongside some applications they are used within.

Field	Applications
Consumer	Tablets, smart phones, household appliances, coffee machines
Automotive	Tyre pressure, airbags, seat occupancy, particle filters HVAC systems.
Medical	Drug delivery, differential pressure flow measurement blood pressure monitoring, sleep apnoea machine
Industrial	Gas analysers, HVAC in buildings, hydraulic systems, monitoring pressurised gas tanks, equipment leak
High-end	Aeronautic, defence, electronic engine control
Other	Weather forecast, altitude, depth, drones, robotics

There are three types of pressure sensing that depend on the point of reference. Absolute pressure is zero-referenced against a perfect vacuum and is equal to gauge pressure plus atmospheric pressure, gauge pressure zero-references against ambient air pressure and is absolute pressure minus atmospheric pressure, and differential pressure is the difference in pressure between two points.

One of the first pressure sensors fabricated with silicon was in 1962 [18]. Since then, several designs and technologies have emerged which mostly rely on mechanical deformation in a membrane and converting the resulting strain

or displacement into electrical signals. The main principles used for sensing strain are piezoelectricity, a change in electrical resistance due to geometric changes or *piezoresistivity*, change in capacitance, change in resonant frequency of vibrating structure and changes in optical resonance. A brief introduction on the pressure sensing concepts is given below, however a detailed review can be found here [19].

There have been many membrane based optical pressure sensors reported, which mostly measure pressure induced deflections through interferometry [20–25]. A diagram illustrating the working principle of a simple optical pressure sensor is shown in Figure 2.1, where the cavity width varies with pressure and the most common method of measuring the change in this width is Fabry-Perot interferometry. The deflection measured from these devices varies linearly with pressure and can be accurate. The difficulties of this technology come with effectively aligning the optics, calibrating the sensors and post-processing the data. This creates a highly complex system meaning optical based pressure sensors have not found their way into the low-cost mass market.

A resonant pressure sensor operates by monitoring the resonant frequency of a micromachined structure. The resonant frequency of this micromachined structure is dependent on the extent it is deformed, i.e. by an applied pressure. Figure 2.2 shows an illustration of the working principle behind a resonant beam MEMS pressure sensor. Here, the resonant frequency is measured in a beam structure which is fabricated on top of the membrane diaphragm. The output signal is a frequency, which can be easily converted into a digital signal and interfaced with a computer. Many works have looked to change the structure for improving sensitivity and the important resonator performance parameter of the Q-factor [26–33]. Advantages of these resonant pressure sensors are that they exhibit high stability and high resolution. The large disadvantage, and reason they are not the most popular pressure sensing technique, is due to their fabrication difficulty and hence large fabrication costs.

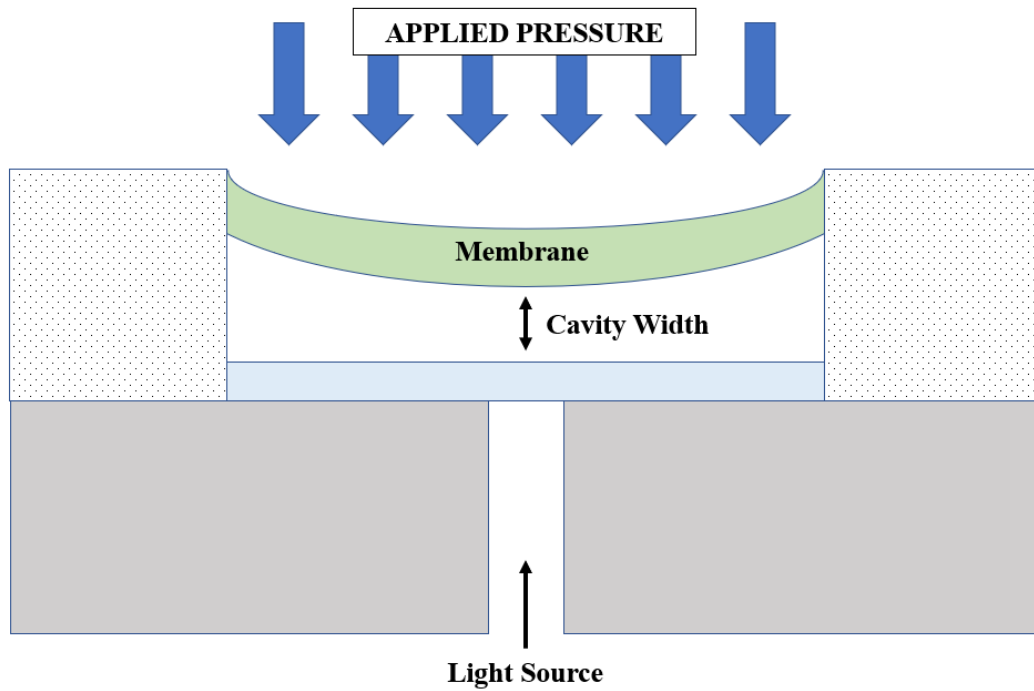


**Figure 2.1:** A diagram illustrating the working principle of an optical MEMS pressure sensor.

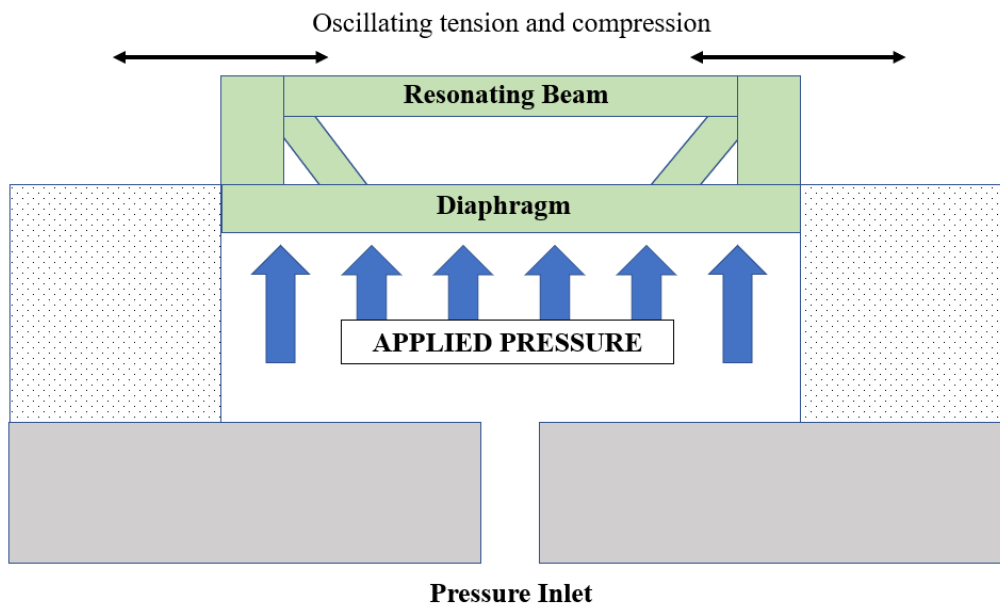


**Figure 2.2:** A diagram illustrating the working principle of a resonating beam MEMS pressure sensor.

The capacitive pressure sensor detects the deflection of the membrane by calculating the change in capacitance between two plates [34–38]. Figure 2.3 shows the working principle of a capacitive pressure sensor where the pressure deforms the membrane, resulting in a different capacitance between the two plates. Capacitive pressure sensors have a high sensitivity and are not affected by ambient temperature. However, the output capacitance must be converted into an electrical signal with the addition of electronic circuits, and this output is not linear with pressure. It is for this reason that capacitive pressure sensors have benefited more from advances in circuit design as opposed to micromachining techniques.

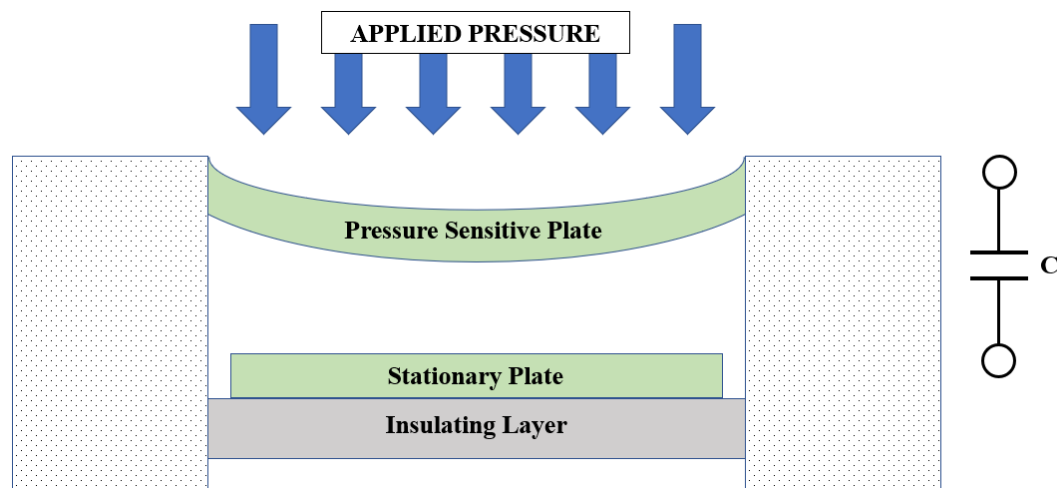


**Figure 2.3:** A diagram illustrating the working principle of a MEMS capacitive pressure sensor.

Among all the available pressure sensors technologies, the piezoresistive pressure sensor is the most industrially widespread and researched, which is due to it being the simplest to fabricate and directly providing an electrical output. This yields easy integration with microelectronics circuitry and a simple manufacturing process, ending in a cheap product to take to market. Table 2.2 summarises the main advantages and disadvantages of the discussed technologies for sensing pressure.

Piezoresistivity in semiconductors is caused by the deformation of energy bands with the application of stress. When the bands have deformed, the

**Table 2.2:** Advantages and disadvantages of the main transduction methods used in pressure sensors.

Pressure Sensor	Advantages	Disadvantages
<b>Optical</b>	Good reliability	Difficult to align Difficult to calibrate Large footprint
	Wide range	
	High repeatability	
	High spatial resolution	
<b>Resonant</b>	High stability	Expensive
	High resolution	Difficult to fabricate
<b>Capacitive</b>	High sensitivity	Cross-talk
	High spatial resolution	Noisy
	Temperature independent	Non-linear response
<b>Piezoresistive</b>	Simple	Hysteresis Low reproducibility
	Cheap	
	Good spatial resolution	

mobility of electrons and holes changes and thus the resistivity is changed. A detailed discussion on the stress-dependency of piezo-resistors in silicon can be found here [39].

Silicon happens to be an appropriate material for mechanical sensors due to its excellent mechanical properties, thus having the ability for reproducible linear elastic deformations under mechanical load, i.e. pressure. Silicon is also ideal for pressure sensing applications due to it not suffering from hysteresis and creep, which is due to it being a brittle material and hence not plastically deforming, but catastrophically breaking when subjected to its ultimate yield strength, which is larger than stainless steel.

The simplest form of a piezo-resistive silicon sensor uses a diffused resistor, where an n- or p- doped well sits within an p- or n- substrate. Normally,



n+ or p+ diffusions are added to create ohmic contacts. A schematic cross-section of a piezo-resistor is shown in Figure 2.4.

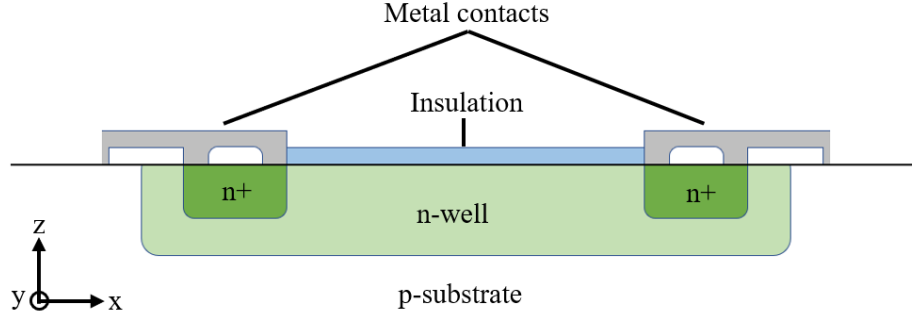


**Figure 2.4:** Schematic cross-section of a simple diffused n-type piezo-resistor.

For stress in the typical region (MPa range), the voltage drop seen in the resistor depends linearly on the applied stress. The voltage drop  $V_r$  across a piezo-resistor that is aligned in the x-direction can be defined as

$$V_r = R_{S0}I[1 + \pi_L\sigma_{xx} + \pi_T(\sigma_{yy} + \sigma_{zz})] \quad (2.1)$$

where  $R_{S0}$  is the stress free resistance,  $I$  the applied current,  $\pi_L$  and  $\pi_T$  are the longitudinal and transverse piezo-resistive coefficients and  $\sigma_{ij}$  are the three stress components. The coefficients of piezo-resistivity vary with the crystallographic orientation and doping profile and have been extensively researched [40–43].

After the discovery of the piezoresistive effect in silicon [37], silicon strain gauges with metal diaphragms were first commercially introduced in 1958. These early designs suffered from low yield and poor stability and were quickly replaced by single crystal diaphragms with diffused piezoresistors, benefiting from the many advantages silicon can offer.

The first silicon devices showed a gauge factor (which is defined as the relative change in resistance to the mechanical strain) larger than an order of magnitude better than their metal counterparts [44]. Using key

technologies that were later developed, such as anisotropic chemical etching [45], ion implantation, anodic bonding and Silicon-On-Insulator (SOI) techniques [45, 46], the performance of piezoresistive pressure sensors dramatically increased.

Figures 2.5, 2.6 and 2.7 show the structure and working principle of a typical micromachined semiconductor piezo-resistive pressure sensor. With an applied pressure, the thin membrane deforms and causes the deformation of energy bands within the piezo-resistors, causing a change in resistance.

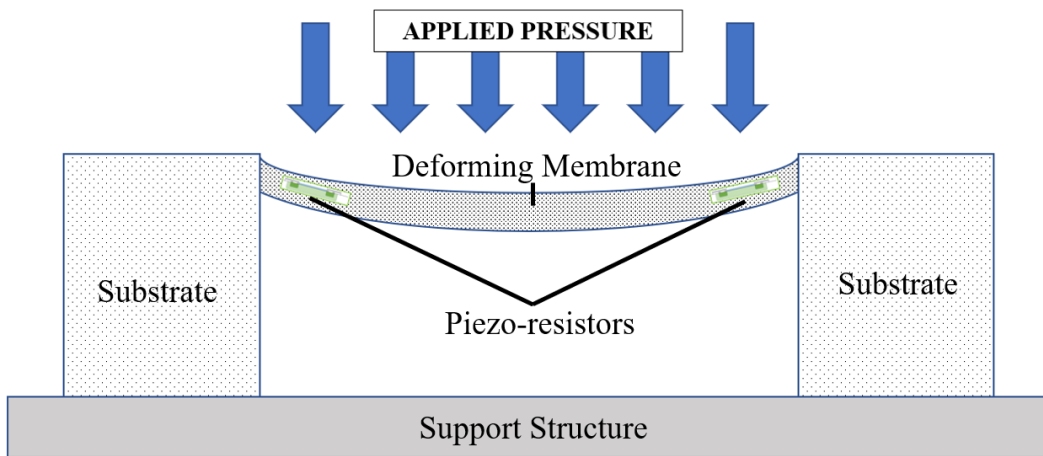


**Figure 2.5:** A cross-section showing structure and deformation of a typical piezo-resistor.

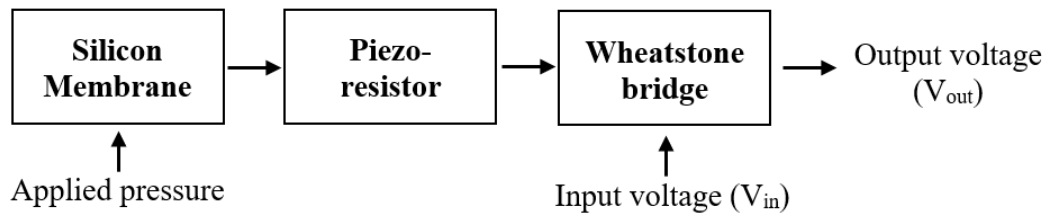


**Figure 2.6:** A flow chart defining the working principle of a typical piezo-resistor.

There are typically four piezo-resistors located in the membrane that are connected to a Wheatstone bridge for measuring resistance change. With the addition of a Wheatstone bridge and an applied pressure difference, the voltage output  $V_{out}$  changes due to the changing resistances of the Wheatstone bridge arms. This is because the piezo-resistors in different arms will change in the opposite direction due to the resistors being longitudinally or transversely

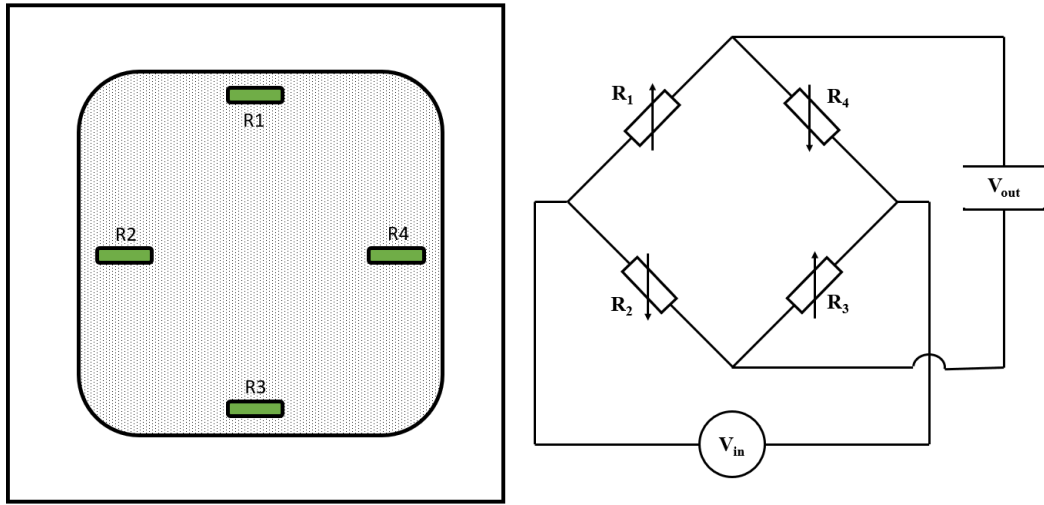


**Figure 2.7:** A top view showing the location of the piezo-resistors and the Wheatstone bridge circuit diagram.

stressed, thus greatly benefitting from a Wheatstone bridge configuration and its advantages, of which the main advantages are the high accuracy and easy implementation. The voltage output can be calculated through the following equation:

$$V_{out} = \left( \frac{R_3}{R_3 + R_2} + \frac{R_4}{R_4 + R_1} \right) V_{in} \quad (2.2)$$

where  $R$  is the resistance,  $V_{in}$  is the supplied constant bridge voltage and  $V_{out}$  is used to investigate and characterise the sensor response and performance with pressure.

The piezo-resistors are located close to the edge of each side of the square membrane because these are the areas of highest stress in a deformed membrane which has been thoroughly numerically and analytically researched for a number of standard membrane geometries [47]. Placing the piezo-resistors in the area of highest stress creates the largest change in resistance and thus maximises the sensitivity of the device.





Since the widespread commercial use of micromachining techniques, there have been many methods used for optimising the performance of piezoresistive pressure sensors. Many works look at using different materials (Polycrystalline Silicon [48], Silicon Carbide [17, 49, 50], Gallium Nitride [51, 52], Graphene [53, 54] and Carbon Nanotubes [55–57]).

Most work on optimising piezo-resistive pressure sensors is based on altering the geometric design of the membrane. Firstly, this includes analytically and numerically locating the area of highest stress on the membrane to position the piezoresistive element [40]. After this, methods include using thin, sculpted, bossed membranes or incorporating extra structures for engineering the stress on the membrane [58–63].

Table 2.3 displays some of the commercially available piezo-resistive pressure sensors. This highlights the low price that commercial pressure sensors have achieved using micromachining manufacturing techniques. It is therefore important to continue the development of the sensors for better accuracy, higher reproducibility and lower power consumption.

With the advent of SOI integrated sensors with electronics, piezjunction devices have been investigated. Piezjunction devices are similar to piezoresistive, except they use electronic devices as the pressure transducing elements. Their research maturity is far less than piezo-resistive devices, however there has been research into the fundamental effect of pressure on p-n junctions [64] and the effect of pressure on transistor channel resistance and carrier mobility [65]. Previous examples of utilizing active electronic devices in the fabrication of pressure sensors are a pressure sensor incorporating a stress-sensitive MOS operational amplifier [66]; MOSFETs combined with ring oscillators on dielectric membranes for a preliminary pressure sensing system [67], a pressure sensor using two embedded MOSFETs, and two embedded resistors in the Wheatstone bridge configuration [68]; the fabrication and modelling of a pressure sensitive

**Table 2.3:** Current commercial pressure sensors with their price and working range.

Commercial Product	Pressure Range	General Notes
<p>Infineon SP27</p> 	100-1300 kPa	£3, Bulk silicon and piezoresistive pick-up.
<p>Honeywell ABP</p> 	6-1000 kPa	£12, piezo-resistive silicon technology.
<p>Bosch BMP388</p> 	30-125 kPa	£3, 2.0 mm by 2.0 mm, low power consumption with temperature sensor.
<p>NXP MPX2202A</p> 	0-200 kPa	£9, silicon piezoresistive technology.

FET [69]; the use of a polyimide sacrificial layer and suspension gate MOSFET [70]; and a nc-Si/c-Si heterojunction MOSFET pressure sensor [71] showing a sensitivity of 2.15 mV/kPa and the design of a mirror sensing based MOSFET embedded pressure sensor [72]. Finally, [73] uses the piezo-MOS effect within a pressure sensitive differential amplifier.

In this section, we design, fabricate and test 13 CMOS MEMS piezoresistive pressure sensors for optimisation and comparison. Investigated parameters include the design of the piezo-resistive element (doping and shape), size of membrane and a variety of structures embedded in the metal layer for stress engineering. In addition to this, 4 designs of piezo-junction pressure sensor are designed and fabricated, including using MOSFETs and diodes as the electronic pressure transducing elements. The characterisation and performance of all the developed pressure sensors are shown. The performance of the devices is investigated using two known evaluation parameters. The first parameter is the sensitivity  $S$ :

$$S = \frac{V_0(P_m) - V_0(P_i)}{P_m - P_i} \quad (2.3)$$

where  $P_m$  and  $P_i$  denote the maximum and minimum applied pressure respectively and  $V_0(P_m)$  and  $V_0(P_i)$  denote their voltage outputs. The second parameter is non-linearity,  $NL$ :

$$NL = \left[ \frac{V_0(P_i) - \frac{V_0(P_m)}{P_m}(P_i)}{P_m} \right] \times 100\% \quad (2.4)$$

Using these two performance parameters, the various fabricated sensors can be quantitatively compared and then used as design guidelines.

## 2.2 Piezo-Resistive MEMS Pressure Sensors

### 2.2.1 Design and Fabrication Details

The piezo-resistive sensors investigated in this section were designed using the software Cadence TM Virtuoso Layout Editor (IC 5.1.4). A 1.0  $\mu\text{m}$  SOI CMOS fabrication process with tungsten metallization was used for fabrication through a commercial foundry. In order to create the thin membrane structure, Deep Reactive Ion Etching (DRIE) was used to etch the back-side silicon after wafer thinning, leaving a membrane of approximately 4.5  $\mu\text{m}$  remaining and wafer thickness of 375  $\mu\text{m}$ . The etching depth was accurately controlled by using the first  $\text{SiO}_2$  buried oxide layer as an etch-stop. DRIE was chosen as it can create almost vertical sidewalls, therefore reducing the sensor footprint. It also allows for the miniaturisation of diaphragm size, since it is not constrained by the silicon substrate lattice orientation. The 6" wafers were diced in an external commercial dicing house using the stealth dicing technique.

Thirteen different piezo-resistive designs were fabricated and tested, which are all listed with their relative varying parameters outlined in Table 2.4 and a micrograph of one of the fabricated sensors (Pr 01) shown in Figure 2.8 with its cross-section schematically displayed in Figure 2.9. In all sensors, the silicon dioxide membrane was designed to be square with rounded edges in order to obtain a uniform mechanical stress distribution around the edge and reduce the number of catastrophic membrane failures.

Four piezo-resistors were included in the membrane, allowing the implementation of a Wheatstone bridge whilst four off-membrane resistors are also included to allow for ambient temperature compensation [74]. The investigated sensors can be split into four six sections in which independent parameters can be constrained and analysed. Table 2.4 shows all investigated designs with their important parameters for reference.

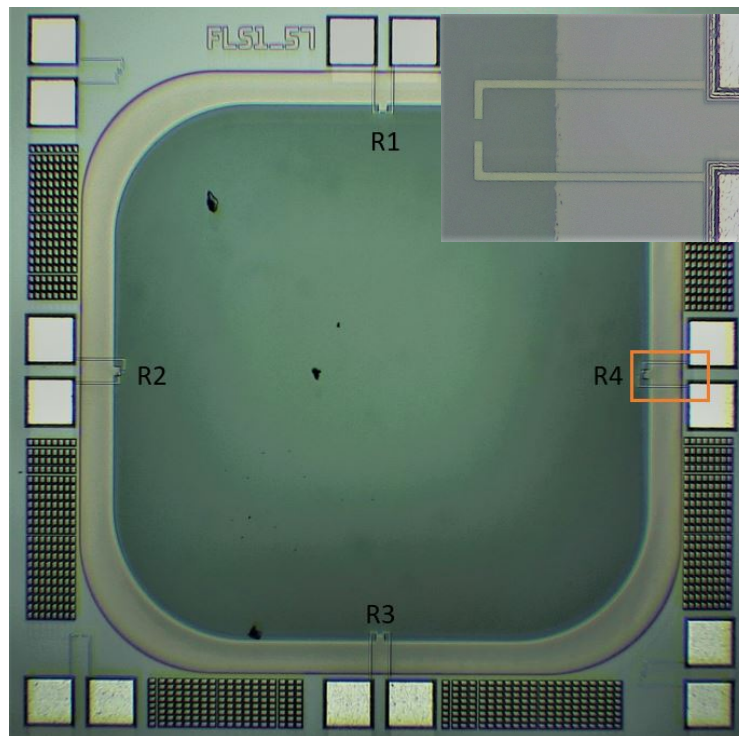


**Figure 2.8:** Optical micrograph of the fabricated sensor (Pr 09). Inset - detailed view of a fabricated diffused resistor (Pr 01).

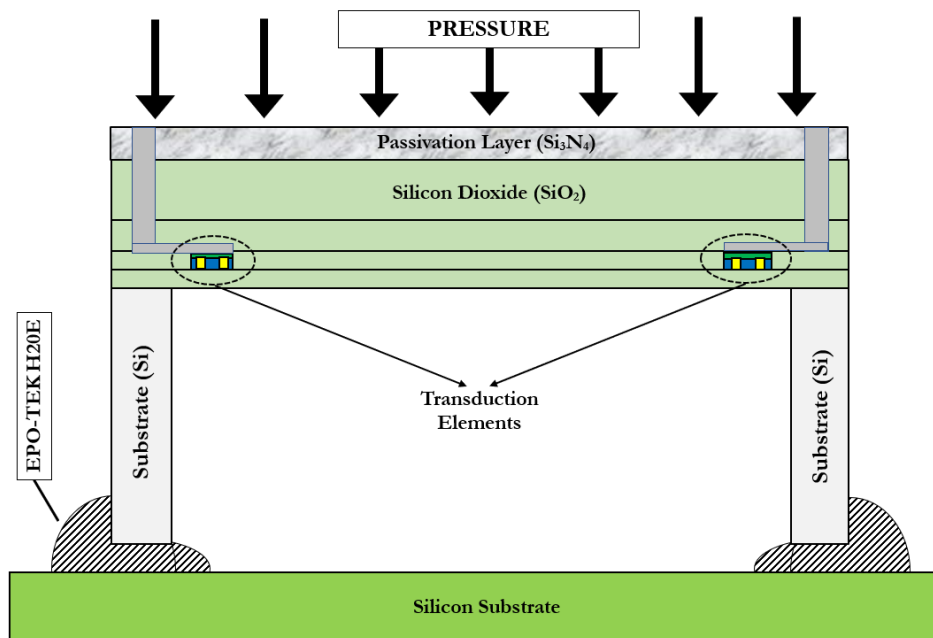


**Figure 2.9:** Cross-section of the pressure sensor illustrating the position of the piezo-resistors within the membrane.



**Silicon Layer Doping:** For devices Pr 01 to Pr 03 the piezo-resistive layer is altered. Pr 01 and Pr 02 contain p-doped designs with the two implantation concentrations of ‘well’ (low) and drift (higher). Pr 03 is a simple p+ design that does not incorporate a different doping concentration in the intrinsic layer. The shape, long intrinsic, is kept constant throughout these designs and is a rectangular area of  $15\ \mu\text{m}$  ( $PR_L$ )  $\times$   $5\ \mu\text{m}$ . A cross-section diagram of the piezo resistor fabricated in Pr 01 is shown in Figure 2.10.

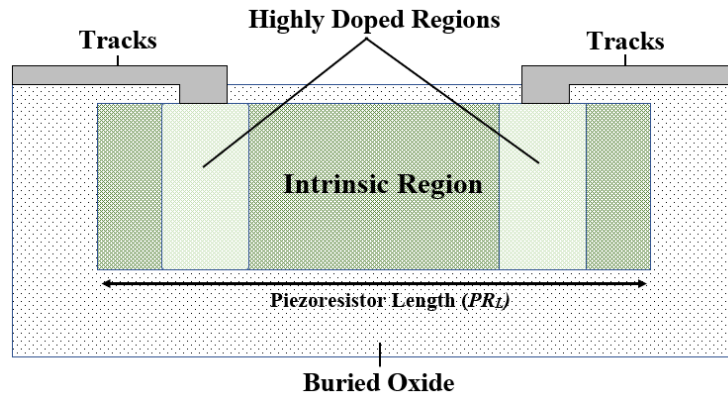


**Figure 2.10:** Cross-section diagram of the piezo resistor from device Pr 01.

**Membrane Size:** Designs Pr 04 to Pr 06 have three different membrane sizes of 1.2 mm, 0.8 mm and 0.4 mm, respectively. This allows for the investigation of membrane size and deflection with regards to sensor performance. For these designs the piezoresistor shape is changed into having three sections in series of  $8\ \mu\text{m} \times 4\ \mu\text{m}$ , called parallel.

**Metal Ring:** Designs Pr 04 and Pr 08 to Pr 11 are fabricated to investigate the new design idea where a metal ring is incorporated within two of the metal layers to create a new perimeter for the membrane (Figure 2.11). This increases the rigidity and is proposed to reduce the effect that over/under etching in the fabrication stage has on the reproducibility of the devices, due to the tight manufacturing tolerances within the metal layer. This also allows the resistor location to be closer to the region of highest stress. The metal ring, which can be seen in Figure 2.11, is fabricated in both available metal layers (1 and 2).

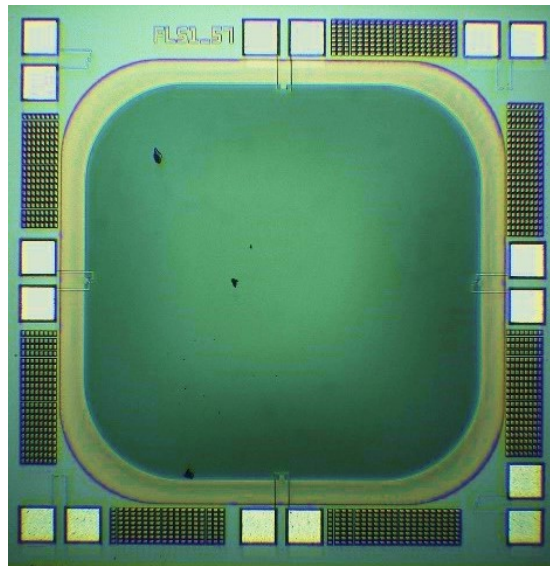


**Figure 2.11:** Optical micrograph of Pr 09, illustrating the implementation of the metal ring.

*No Membrane Silicon:* Etching is used to remove the silicon layer from the membrane area (except within the piezo-resistor), to investigate whether this will change the mechanical properties of the membrane. In addition to this, metal structures are added in the metal layer to alter the structural properties of the membrane. Figure 2.12 shows the design with cross track metal structures as well as containing no membrane silicon.

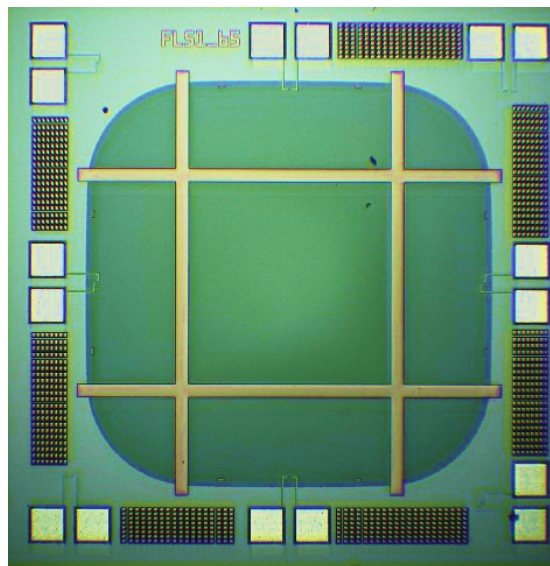


**Figure 2.12:** Optical micrograph of Pr 12, illustrating the implementation of the metal tracks without the addition of silicon.

**Table 2.4:** A summary of all the investigated pressure sensor designs and their pertinent design parameters.

Chip ID	Membrane Size (mm)		Silicon Layer		Piezo-Resistor		Metal Layer	
			Doping		Shape			
Pr 01	1.2		P-Well		Long Intrinsic		No	
Pr 02	1.2		P-Drift		Long Intrinsic		No	
Pr 03	1.2		P+		Long Intrinsic		No	
Pr 04	1.2		P-Well		Parallel		No	
Pr 05	0.8		P-Well		Parallel		No	
Pr 06	0.4		P-Well		Parallel		No	
Pr 07	1.2		P-Well		Rotated 90°		No	
Pr 08	1.24		P-Well		Parallel		No	
Pr 09	1.24		P-Well		Parallel		1.2 mm Ring (MET2 + MET3)	
Pr 10	1.28		P-Well		Parallel		1.2 mm Ring (MET2 + MET3)	
Pr 11	1.32		P-Well		Parallel		1.2 mm Ring (MET2 + MET3)	
Pr 12	1.32		P-Well		Long Intrinsic		0.04 mm Tracks (MET2 + MET3)	
Pr 13	1.2 (No Silicon)		P-Well		Long Intrinsic		No	

## 2.2.2 Experimental

For a deflection to occur, the sensors require a pressure difference between the two sides of the membrane, thus requiring hermetic sealing that ensures no leakage over time equalises this pressure difference. Using a cleaned glass substrate, a thin-walled square of thermal epoxy glue (EPO-TEK H20E) was applied using a high precision dispensing machine (Tresky 3000). The sensors were pressed onto the epoxy glue and more glue was dispensed circumnavigating the sensor to create a surrounding high wall to ensure no air gaps were present. The substrate and sensors were then cured in an oven for 45 minutes at 120 °C, allowing the glue to set and become hard.

A picture of the finalised substrate with attached and cured sensors is shown in Figure 2.13. An experiment was performed over a period of 24 hours at a pressure difference of 500 mbar in order to investigate the hermetic sealing. During this time, the pressure sensitive output of the resistors was constant, leading to the conclusion that there was no significant leakage during this time period and this simple sealing process could be used for all the experiments.

A SUSS MicroTec PMC200 Cryogenic Probe Station was used to create a negative pressure difference (i.e. reducing the pressure of the test chamber to below atmospheric pressure). Two internal direct current probes were connected from the sensor pads to an external Keithley 2450 which was used to bias a current through the resistors and simultaneously measure the output voltage, all of which were controlled by an in-house developed Labview program. At the three chosen bias currents of 1  $\mu\text{A}$ , 10  $\mu\text{A}$  and 100  $\mu\text{A}$ , 40 voltage measurements were recorded at 0.5 seconds apart and averaged for the output voltage value. This procedure was repeated for all four resistors located on the membrane. This electrical characterisation was subsequently carried out at seven pressure differences from 0 to minus 700 mbar (where 0 mbar is atmospheric pressure) in steps of 100 mbar, whilst maintaining a constant temperature of 25 °C.

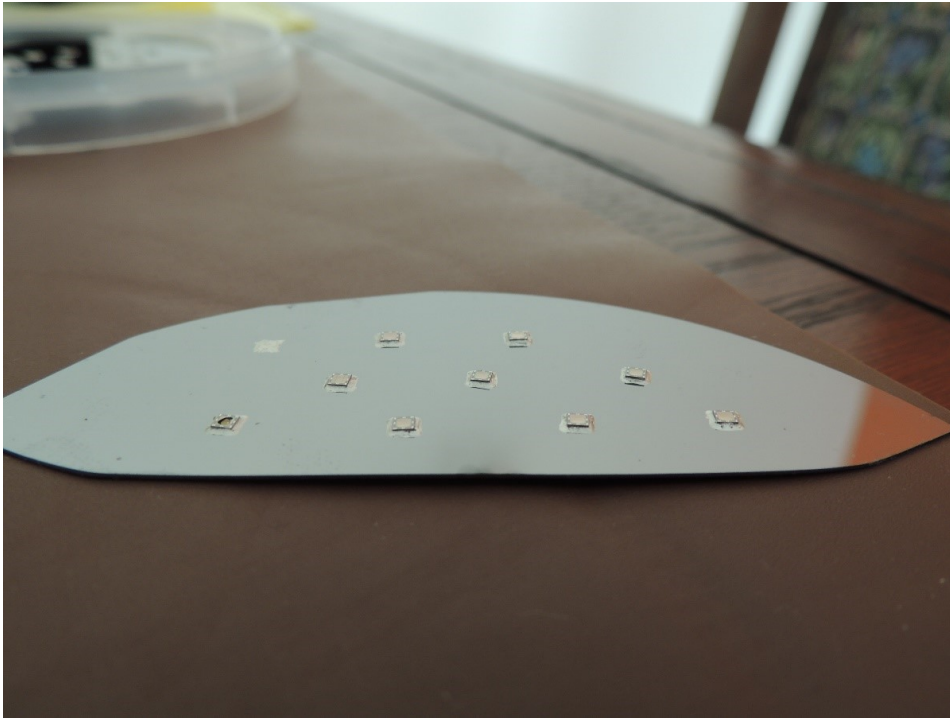


**Figure 2.13:** Picture of silicon substrate with sensors hermetically attached and cured.

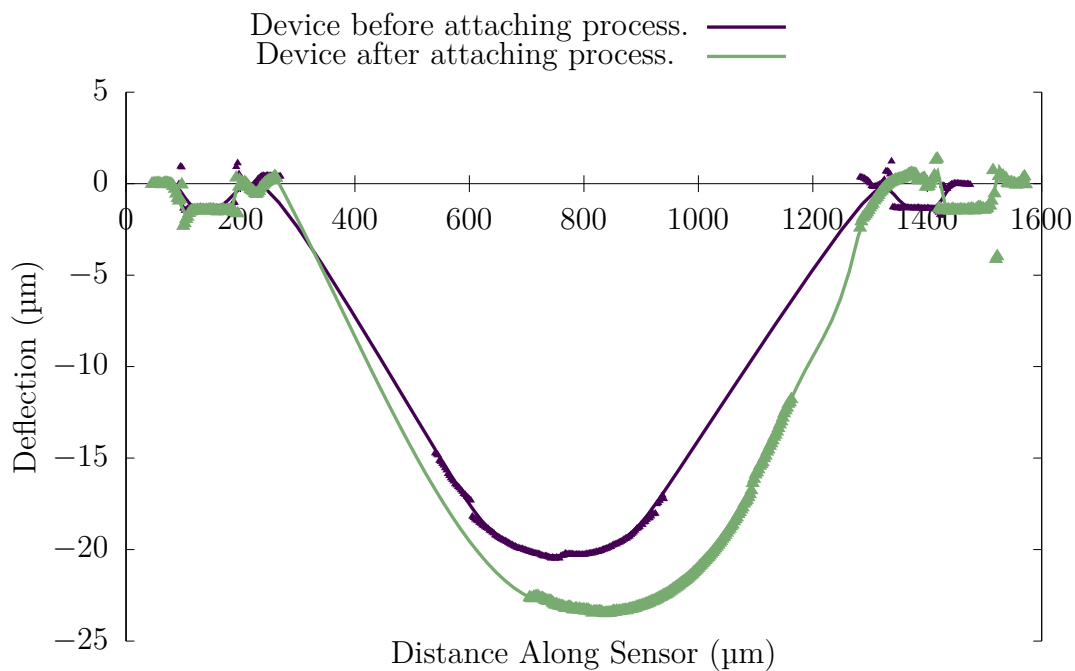
In addition to the electrical characteristics of the sensors, the mechanical deformations were also investigated due to membrane deformation being one of the axioms of functionality for all these sensors. The topology of the membrane was measured using a Fogale Nanotec Zoomsurf 3D Profilometer. This was carried out before the assembly stage (on the bare die) and after the assembly stage. In this way it was possible to see if the process of creating a hermetic seal had an effect on the deformation of the membrane, which would then affect the sensor response.

Figure 2.14 shows the deflection across the membrane at atmospheric pressure for the bare die and for the sensor after it was attached and cured. The gaps in the experimental profile data are due to the membrane material and thickness resulting in a partially transparent material, yielding no measured data from the experiment. An interpolated line is added to each measurement set using a piecewise polynomial to predict the overall membrane shape, represented by dashed lines. It should be noted that after the attaching process, the die

was not perfectly horizontally aligned, increasing the difficulty in the measuring the profile and thus explaining the skewed data points.

It is clearly visible that after the attaching process the membrane has larger deformations, with maximum deformation being over  $3\ \mu\text{m}$  larger. This leads to the conclusion that during the attaching process a slight pressure is created within the cavity below the membrane, the surrounding epoxy is then cured resulting in a small initial pressure difference. However, all the devices are attached and cured using the same process, resulting in a consistent attaching pressure change across all the experiments.

Due to the MicroTec probe station only being able to achieve a negative pressure difference, the membrane flips from a concave to a convex shape. The pressure where this event happened was noted for every sensor and varied by  $\pm 15\ \text{mbar}$ . Figure 2.15 shows an experiment where the pressure was varied by  $10\ \text{mbar}$  up and down and the output voltage of one of the piezo-resistors was measured.



**Figure 2.14:** The membrane deflection measured before and after the attaching process.

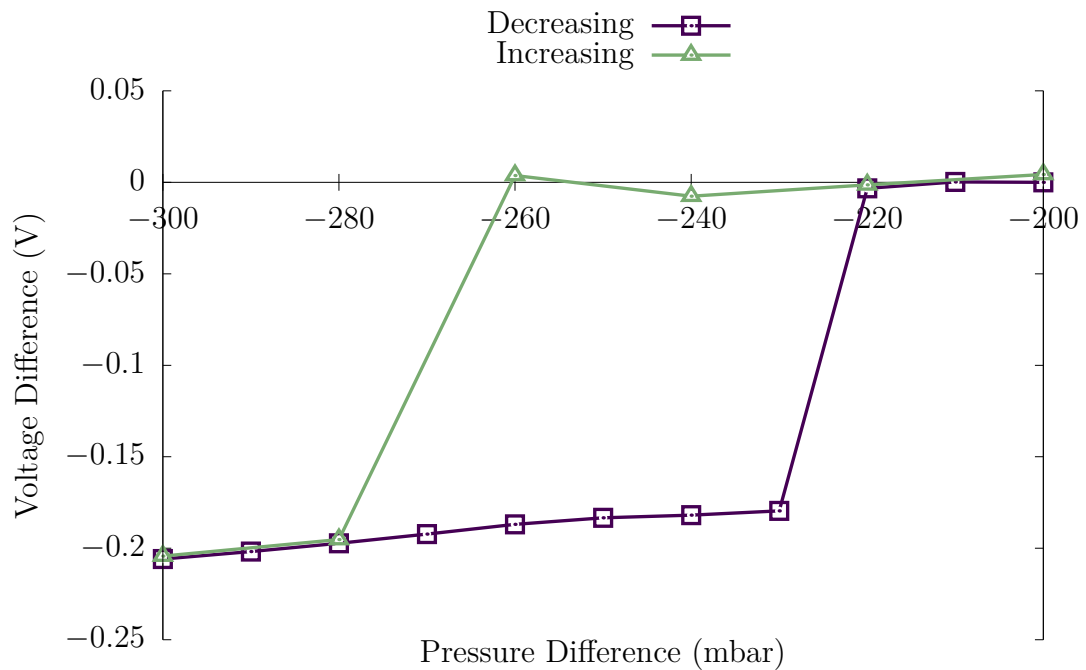


**Figure 2.15:** The voltage difference between -200 mBar and -300 mBar for both increasing and decreasing pressure to illustrate the membrane snapping.

When increasing the pressure difference, the membrane flip can be seen by the drastic change in voltage output, which happens at -270 mbar. This value differs when the pressure difference is being decreased and lies around 220 mbar. The values of voltage output after the membrane flip are linear, with the highly non-linear response only being displayed in the region near to the ‘membrane-flip’. It is for this reason that post processing data analysis will be performed in the range from -300 mbar to -700 mbar, because this has more data points than 0 – 200 mbar. This is a large region to give an accurate representation of the sensor characteristics.

It should be considered that if the sensor were to be used with positive pressure differences, there would be no problem of membrane flipping. More recent technology by our group also reduces the residual stress in the membrane, causing much less initial deflection and therefore also minimising this problem.

### 2.2.3 Discussion

#### Silicon Layer Doping

Figure 2.16 shows the voltage response of the three designs where the silicon doping regime is changed as well as the calculated linearity error. Pr 01, Pr 02 and Pr 03 showed sensitivities of 0.598 mV/mbar, 0.637 mV/mbar and 0.346 mV/mbar, respectively.

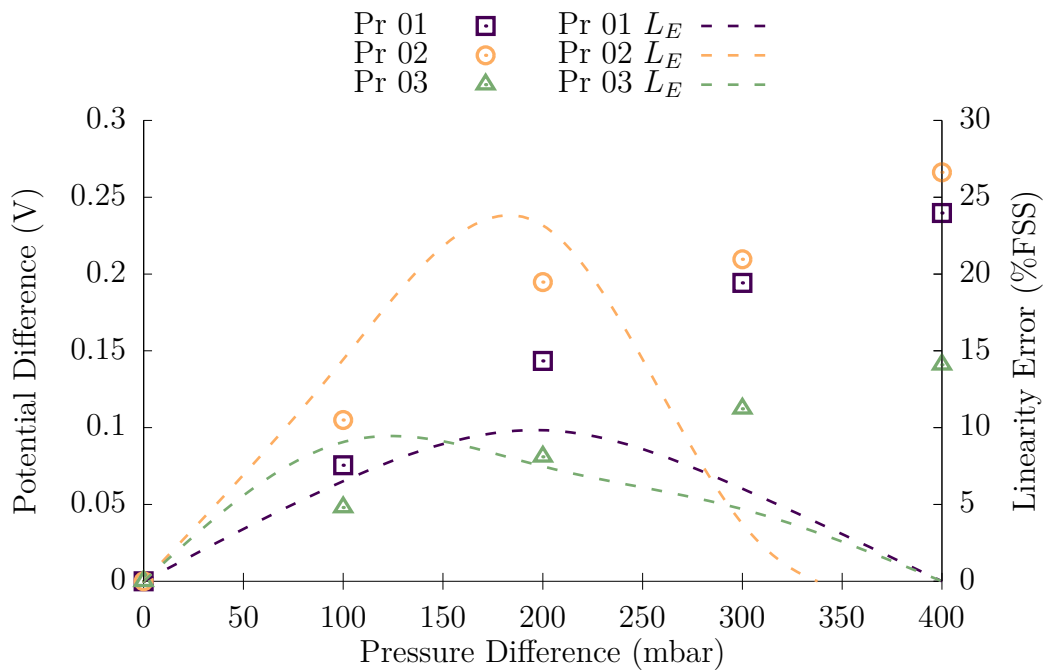


**Figure 2.16:** Voltage difference output for the designs with different doping layers.

It should be noted that it was not possible to bias Pr 02 with the two higher currents of 10  $\mu\text{A}$  and 100  $\mu\text{A}$  and the sensitivity is based off the lowest bias current of 1  $\mu\text{A}$ , which is due to the higher level of initial doping. Conversely, Pr 03 recorded no significant response at the lowest bias current of 1  $\mu\text{A}$  and required a bias current of 100  $\mu\text{A}$  or 1 mA to yield a significant response, which is because of the omission of the highly doped regions (Figure 2.10). Out of the three designs, the design with the higher doped intrinsic region (Pr 02) was more sensitive than the less doped design (Pr 01). However, this



extra sensitivity is not useful due to the large nonlinearity of this design, which originates from the large standard deviation in the voltage output. This large noise will increase the difficulty of producing a high accuracy with calibration.

### Membrane Size

Pr 04, Pr 05 and Pr 06 have membrane sizes of 1.2 mm, 0.8 mm and 0.4 mm, respectively. Every other parameter is kept constant in order to investigate the effect of membrane size on deformation and sensitivity to pressure. Figure 2.17 shows the deflection measured for each device by the profilometer where the dotted lines represent an interpolation of missing data with a piecewise polynomial.

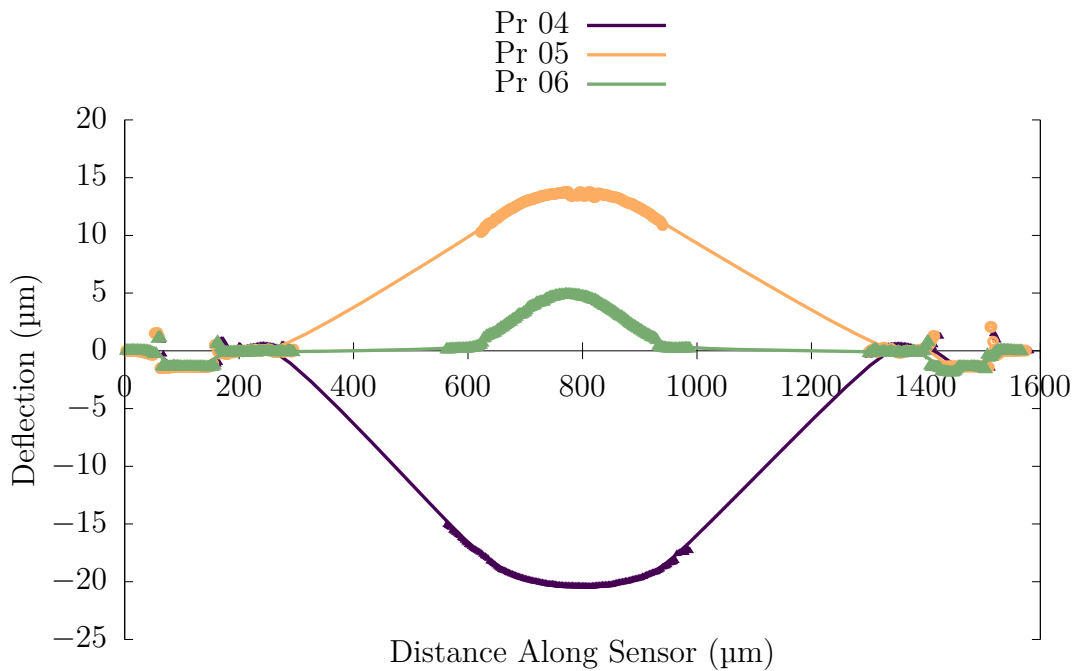


**Figure 2.17:** Deflection measured from the profilometer for the three designs with different membrane size at zero pressure difference. The dots represent the experimental data points and the line is an interpolation.

A maximum initial deflection of  $-20.4 \mu\text{m}$ ,  $+13.7 \mu\text{m}$  and  $+4.9 \mu\text{m}$  was measured for Pr 04, Pr 05 and Pr 06, respectively. Interestingly, for the designs with reduced membrane size the initial resting position of the membrane was

the opposite side of the large membrane. It should be noted that the membrane did not flip sides with the added small pressure from the attaching process. Figure 2.18 shows the voltage difference measured for the pressure sensors with change in pressure, which can be used to extract their sensitivity. The sensitivities of Pr 04, Pr 05 and Pr 06 are 0.889 mV/mbar, 0.839 mV/mbar and 0.623 mV/mbar respectively. The first finding is that the sensitivity increases if the membrane size is increased.

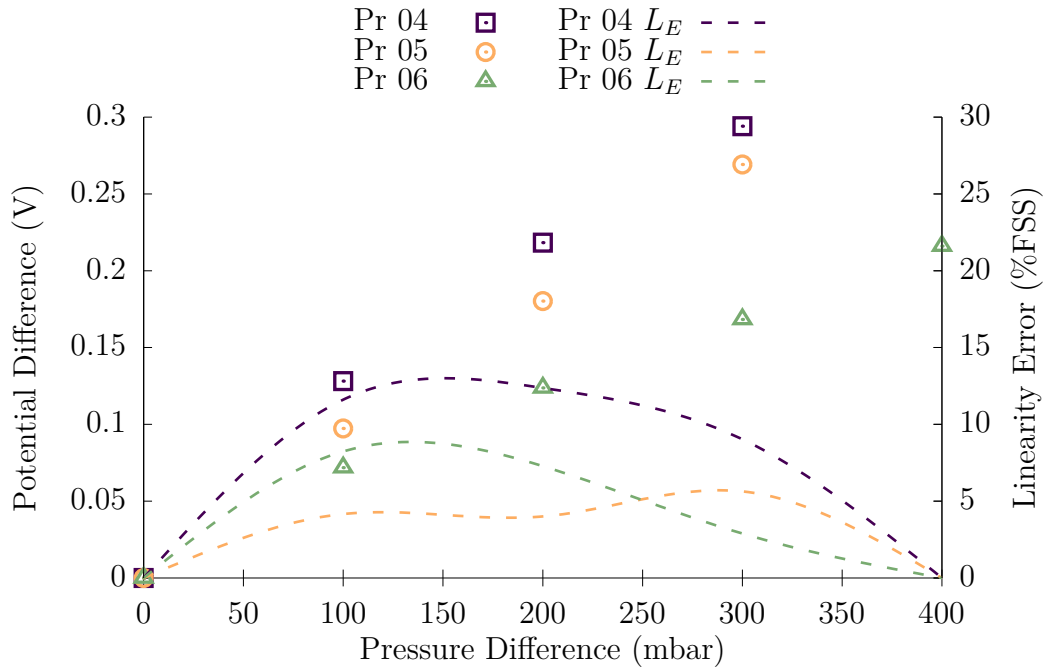


**Figure 2.18:** Voltage difference output for the change in pressure difference for the three designs with varying membrane size.

This agrees with thin-film deflection theory, whereby a larger membrane will deform more under the same pressure, thus inducing a larger signal difference in the transducing elements. This can be more aptly described by the maximum membrane deflection  $w_0$  under uniform applied pressure  $P$ .

$$P = E \frac{t^4}{W_M^4} \left( g_1 \frac{w_0}{t} + g_2 \frac{w_0}{t} \right) \quad (2.5)$$

where  $t$  is membrane thickness,  $W_M$  is membrane width,  $g_1$  and  $g_2$  are constant

material parameters relating to Poisson ratio and  $E$  is the material Young's modulus. The largest membrane also displayed a linearity error higher than the other two devices, which is due to  $w_0$  becoming larger than  $t$ , resulting in non-linear bending with applied pressure. Another factor is that if the deflection of the membrane is not small compared to the membrane thickness, the central plane of the membrane stretches in what's known as the balloon effect. Due to this, there is an induced in-plane stress component in addition to the stress caused by the membrane bending. The total stress on the membrane becomes a combination of bending stress and stretching stress, therefore the amount of bending stress is reduced as the membrane stretching increases, introducing nonlinearities by deviating from linear bending theory.

The membrane thickness on the investigated designs is 4.5  $\mu\text{m}$ , whilst the membrane deflection under atmospheric pressure is over 20  $\mu\text{m}$  for Pr 04. This ratio becomes smaller for Pr 05 and Pr 06. The nonlinearity is further worsened due to the negative pressure. This is due to the stretching stress always being positive whereas bending stress can be positive or negative (tension or compression), thus when a negative pressure is applied the bending stress is negative and the stretching stress is positive resulting in total stress being further from linear theory and pure bending. However, Pr 05 and Pr 06 show similar linearity errors. This can be ascribed to other parameters playing a more significant part in the variance of the signal output, including the residual stress of the multi-layered membrane resulting in a non-uniform deflection.

It is shown that very large and thin membranes can be used to produce a highly sensitive device but suffer from larger non-linearity errors. Future work needs to be carried out to reduce the non-uniformity across the membrane and reduce the residual stress for a more reproducible device.

## Metal Ring

The fabrication technology platform used gives the opportunity for three metal layers within the membrane. The deposition of metal structures can be used for engineering the stress across the membrane due to the higher rigidity of tungsten and is taken advantage of for its high manufacturing tolerances. A well-known problem on the reproducibility of MEMS sensors is due to the inherently low tolerances of etching. This is especially pertinent to pressure sensors due to the membrane size directly relating to the sensitivity of the device. The optical micrograph shown in Figure 2.11 shows a ring in the metal layer of diameter 1.2 mm. This design uses the high rigidity and fabrication tolerances to create a new perimeter to try and negate the variance caused by over and under etching. Figure 2.19 shows the sensitivity and linearity error of designs that vary membrane size to simulate over and under etching, with and without the addition of the metal ring.

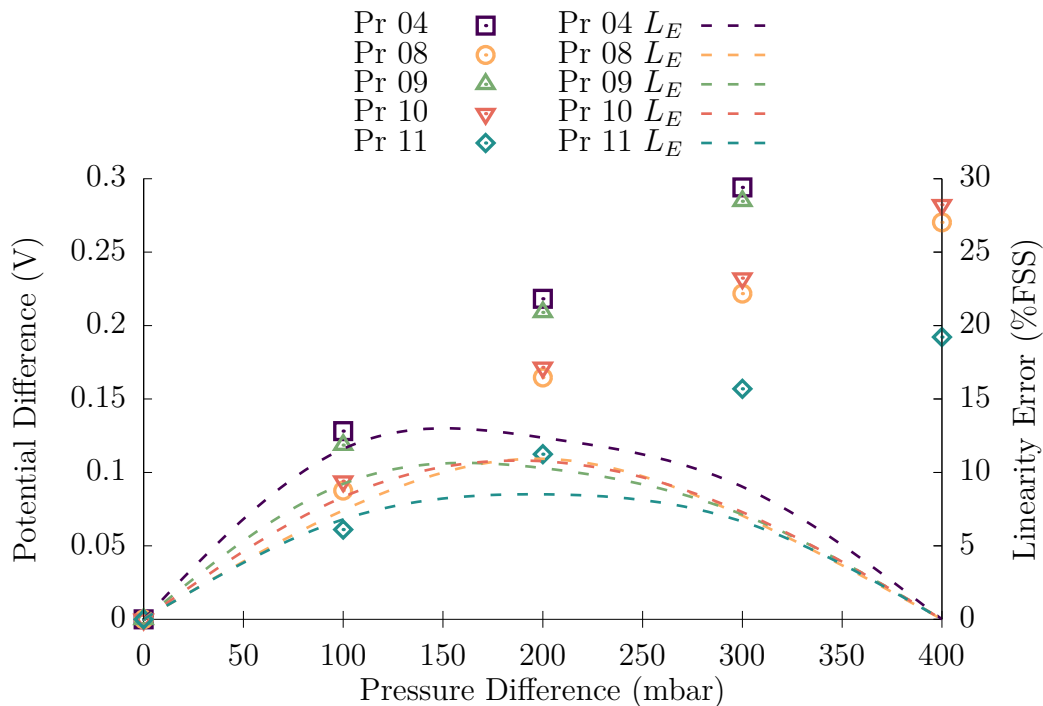


**Figure 2.19:** Voltage difference output for the designs investigating the effect of the metal ring.

Pr 08 shows a lower sensitivity than Pr 04, which is due to the different membrane size and hence the placement of the piezoresistor is not in the region of highest stress. However, when the metal ring is incorporated to mimic the membrane size in Pr 04, Pr 09 shows a very similar response. Pr 10 and Pr 11 show the results of a simulated 80  $\mu\text{m}$  and 120  $\mu\text{m}$  over etching with the metal ring to investigate the limit of functionality for this design. Here it can be seen that at 80  $\mu\text{m}$  or above of over etch, the metal ring does not provide enough rigidity to completely counteract the change in membrane size.

### **Metal Tracks and No Membrane Silicon**

In order to tackle the problem of high linearity error, two designs were fabricated that try to alter the mechanical properties of the membrane. The first of these incorporated metal tracks to try and support the membrane and increase homogeneity and can be seen in Figure 2.12. The second design uses etching to remove the silicon from the membrane except for the necessary locations within the piezo resistors. In Figure 2.20 it can be seen that the no silicon design offers a sensitivity 0.80 mV/mbar, whilst also increasing the non-linearity of the response. The increase in non-linearity and sensitivity is due to the membrane being thinner and thus experiencing more deflection whilst simultaneously increasing the balloon effect.

Figure 2.20 also shows that the metal track structures increase the sensitivity of the device (to 1.02 mV/mbar) and improve the linearity. The metal tracks act as structural supports that help the deformation across the membrane be more uniform. Alongside centre-embossed membranes and cross-beam designs, the metal tracks are able to engineer the stress across the membrane in order to reduce the central deflection (increase linearity) whilst simultaneously concentrating the stress on the piezoresistive elements and increasing sensitivity. There is a 41% sensitivity increase from the reference

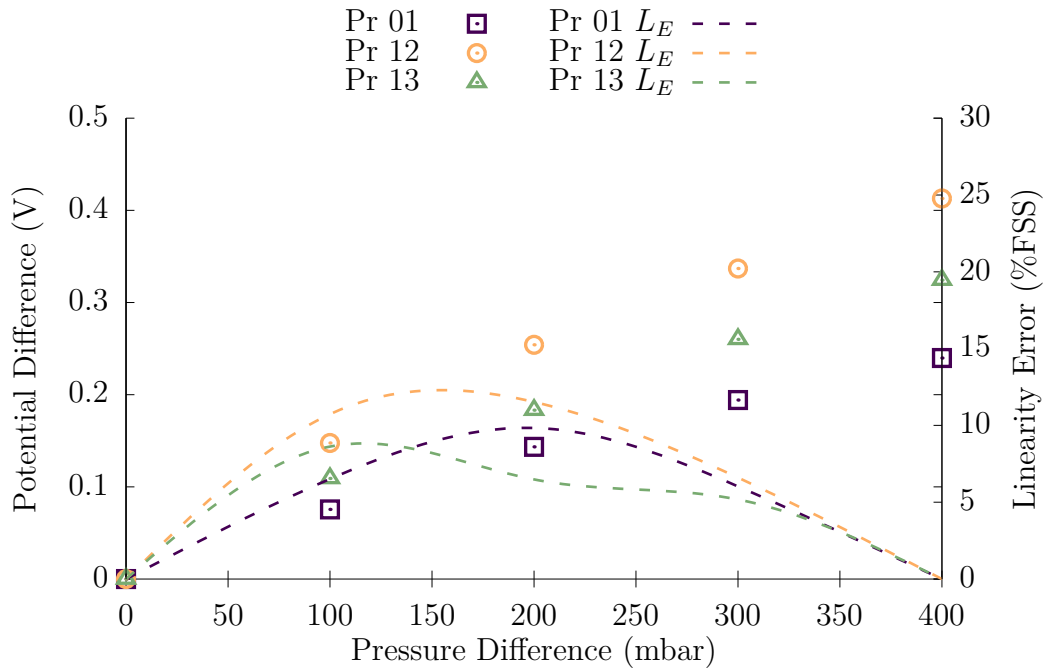


**Figure 2.20:** Voltage difference output for the two structural designs of metal tracks and no membrane silicon.

design, rendering it the design with the highest sensitivity out of all the investigated designs whilst simultaneously reducing the linearity error.

### Temperature Compensation

A major and ongoing problem associated with piezo-resistive pressure sensors is their sensitivity to temperature, which lowers the output voltage with the increase of operating temperature. This severely reduces the accuracy of the sensors which must be able to work in a multitude of environments without affecting the performance.

There have been many different methods for attempting to improve the temperature independence or to compensate for it. Some methods include using artificial neural networks and on-board memory to compensate [75], using extra polysilicon resistors with negative TCRs [76], half-bridge technique [77, 78] and

using circuitry or software in order to condition out the temperature effects or create calibration algorithms [79].

A very popular and effective method of temperature compensation is called the double-bridge method. Here, one bridge is from the resistors on the membrane and can be defined as active, whilst a second bridge is away from the membrane and independent of pressure, defined as inert. This technique is very promising due to its simplicity [80–82].

In all the fabricated devices there are four resistors located in the silicon outside of the membrane. This enables the technology to be temperature compensated using the double-bridge technique when it is further developed and used for applications, improving the versatility and implementation of the device.

#### 2.2.4 Summary

In this section, 13 designs of MEMS piezo resistive pressure sensor have been designed, fabricated, tested and evaluated with their performance in sensitivity and linearity. Different doping designs of the piezo resistor are shown alongside several geometric variations that can be used to optimise thin film pressure sensor design. The key findings are summarised below:

- Decreasing the membrane size helps to reduce non-linearity and also increases sensitivity.
- Having the intrinsic region in the piezo-resistor improved sensitivity, but when its doping concentration was too high the noise became so large that the extra sensitivity was useless.
- A structural metal ring was used to create a new perimeter that can nullify the problem of over and under etching.

- Incorporating metal cross track structures in the membrane was used to improve sensitivity whilst also improving linearity , proving to be the best device out of all the tested pressure sensors.

This study has taken the smart technology platform and developed the first iteration of pressure sensors using micromachining techniques with some novel geometric designs and studies. Recommendations on further work that should be carried out with pressure sensors is discussed in chapter 6.

## 2.3 Piezo-Junction MEMS Pressure Sensors

### 2.3.1 Design and Fabrication Details

The piezo-resistive sensors investigated in this section were designed using the software Cadence TM Virtuoso Layout Editor (IC 5.1.4). A 1.0  $\mu\text{m}$  SOI CMOS fabrication process with tungsten metallization was used for fabrication through a commercial foundry.

In order to create the thin membrane structure, Deep Reactive Ion Etching (DRIE) was used to etch the back-side silicon, leaving a membrane of approximately 4.5  $\mu\text{m}$  remaining. The etching depth was accurately controlled by using the  $\text{SiO}_2$  buried oxide layer as an etch-stop. DRIE was chosen as it can create vertical sidewalls, therefore reducing the sensor footprint. It also allows for the miniaturisation of diaphragm size, since it is not constrained by the silicon substrate lattice orientation. The 6" wafers were diced in an external commercial dicing house.

Four designs of piezo-junction were designed, fabricated and investigated that are discussed in this section. A summary of the four investigated designs



is tabulated in Table 2.5 and can be split into the two different electronic components utilised: the MOSFET and the diode.

In all sensors, the silicon dioxide membrane was designed to be square with rounded edges in order to obtain a uniform mechanical stress distribution around the edge and maintained a diameter of 1.2 mm. Four pressure transducing elements are embedded within the membrane as shown in the optical micrograph in Figure 2.21. The designs are split into two sections for investigation and comparison.

**Table 2.5:** Summary of all the investigated piezo-junction pressure sensor designs and their pertinent design parameters.

Chip ID	Electronic Transduction Component	Doping Regime
Pr A	MOSFET	pMOSFET
Pr B	MOSFET	nMOSFET
Pr C	Diode	p+/p-well/n+
Pr D	Diode	p+/p-drift/n+

### Piezo-MOSFET

Located within the single crystal silicon layer are the four piezo-MOSFETs connected to pads via 4  $\mu\text{m}$  tracks for source and drain and a 9  $\mu\text{m}$  track for the gate. Two types of MOSFET were designed and tested, pMOSFET and nMOSFET, with identical sizes for all the incorporated regions. The wafers are standard [110] orientation and the MOSFET crystallographic orientation is as described in Figure 2.21 with a detailed view of the MOSFET shown in Figure 2.22 as these have been shown to be the optimum orientation [36]. The

pMOSFET (Pr A) uses enhancement mode whilst the nMOSFET (Pr B) uses depletion mode by incorporating an n-channel.

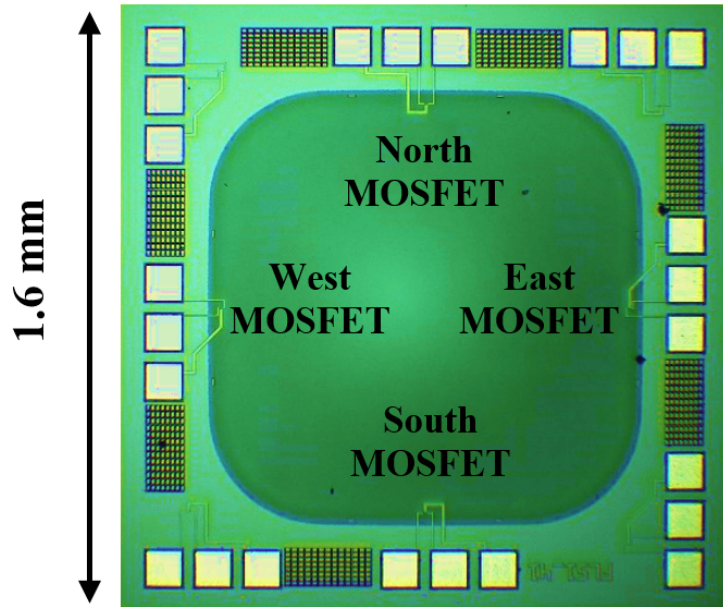


**Figure 2.21:** Micrograph of device Pr A. The crystallographic orientation of pMOSFET is [110] and follows the x-axis, whereas the nMOSFET is [100] and follows the y-axis.

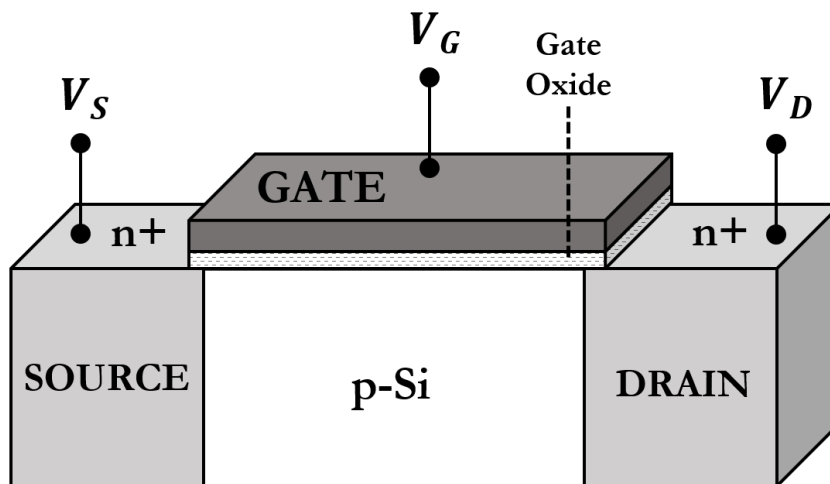


**Figure 2.22:** Schematic of n-channel piezo-MOSFET where p-Si denotes p-doped silicon.

### Piezo-Diode

The 4 piezo-diodes are situated in the single crystal layer at the four sides of the membrane connected to pads via 4  $\mu\text{m}$  wide tracks. Two piezo-diodes were designed and tested including p+/p-well/n+ (Pr C) and p+/p-drift/n+ (Pr D) where all the sizes of the doping regions were geometrically identical. A detailed schematic of the pn junction diodes is shown in Figure 2.23. Both designs used a crystallographic orientation in the  $[110]$  direction.

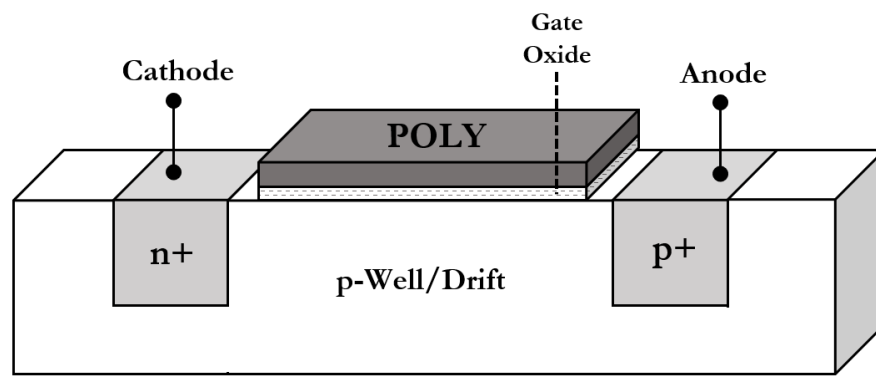


**Figure 2.23:** Schematic of a piezo-diode.

### 2.3.2 Experimental

The sensor requires a pressure difference between the top and bottom (within the cavity) of the membrane, thus requiring hermetic sealing that ensures no leakage over time for absolute pressure measurements. Using a cleaned glass substrate, a square of thermal epoxy glue (EPO-TEK H20E) was applied using a high precision dispensing machine (Tresky 3000). The sensors were pressed onto the epoxy glue, followed by dispensing the gel along every edge of the sensor to fill in any gaps. The substrate and sensors were then cured in an oven for 45 minutes at 120 °C, allowing the gel to become hard. All measured devices were packaged at the same time to be consistent across back-side cavity pressures and atmospheric pressure changes.

A SUSS MicroTec PMC200 Cryogenic Probe Station was used to create a pressure difference. Three internal DC probes were connected from the sensor pads to two external Keithley 2450's in order to bias and measure the MOSFETs (only two probes were needed for the diode measurements), all which were controlled by an in-house developed Labview program.

For the piezo-MOSFETs, the source-drain voltage was swept from 0 to  $\pm 5$  V in increments of 0.25 V for each gate voltage from 0 to  $\pm 5$  V in steps of 1 V. For the diode, the two bias currents of 1  $\mu$ A and 10  $\mu$ A were chosen and 40 voltage measurements were recorded at 0.5 seconds apart and averaged for the output voltage value. These measurements were carried out for all 4 MOSFETs and all 4 diodes located on the membrane.

This electrical characterization was subsequently repeated in steps of 100 mbar pressure difference from 0 to -700 mbar (where 0 mbar is atmospheric pressure), whilst maintaining a temperature of 25 °C. In addition to these, measurements were taken over a period of 24 hours at -500 mbar and showed that the hermetic sealing worked as the stress-sensitive readouts did not change during this time, thus no significant leakage was occurring.

### 2.3.3 Discussion

The experimental stage provided the voltage response for all four electronic transduction elements in the membrane at every pressure difference. For each pressure, the four voltages were put through the Wheatstone bridge equation in order to see their response when being implemented in the conventional configuration.

### Piezo-MOSFET

The MOSFETs exploit the piezoresistive effect induced by the sensitivity of carrier mobility under applied stress. The drain-to-source current  $I_{DS}$  of a device operated in the saturation region is given by

$$I_{DS} = \mu C_{ox} \frac{W}{L} \left( \frac{(V_G - V_T)^2}{2} \right) \quad (2.6)$$

where  $\mu$  represents the carrier mobility through the channel,  $C_{ox}$  is the capacitance of the oxide per unit area,  $W$  (4  $\mu\text{m}$ ) and  $L$  (10  $\mu\text{m}$ ) are the width and length of the channel, respectively,  $V_G$  is the gate voltage and  $V_T$  is the threshold voltage. When the MOSFET is operated in the saturation region, the variation of the current is proportional to the change in channel mobility,  $\mu$ . Due to the geometric designs in this report remaining the same,  $W$ ,  $L$  and  $C_{ox}$  can be assumed constant. The normalised change in current can then be written as

$$\frac{\Delta I_{DS}}{I_{DS}} = \frac{\Delta \mu}{\mu} - 2 \frac{\Delta V_T}{V_T} \left( \frac{V_T}{V_G - V_T} \right) \quad (2.7)$$

It is shown by [58] that the variation in drain current from applied mechanical stress is solely due to the change in carrier mobility ( $\Delta\mu/\mu$ ) and therefore the second term can be neglected and the change in drain current becomes

$$\frac{\Delta I_{DS}}{I_{DS}} \approx \frac{\Delta \mu}{\mu} \approx \pi_l \cdot \sigma_l + \pi_t \cdot \sigma_t \quad (2.8)$$

where  $\pi_l$  and  $\pi_t$  are the parallel and vertical channel piezoresistive coefficients and  $\sigma_l$  and  $\sigma_t$  are the longitudinal and transverse stress in the channel, respectively.

The change in piezo-resistance is also proportional to the mobility change, which can be expressed similarly using:

$$\frac{\Delta R}{R_0} \approx -\frac{\Delta\mu}{\mu} \approx \pi_l \cdot \sigma_l + \pi_t \cdot \sigma_t \quad (2.9)$$

With the addition of a Wheatstone bridge and an applied pressure difference, the voltage output  $V_{out}$  changes due to the changing channel resistances of the Wheatstone bridge arms  $V_{out} = \frac{\Delta R}{R_0} V_{DD}$ . This is because the MOSFETs in different arms will change in the opposite direction due to the resistors being longitudinally or transversely stressed, thus greatly benefitting from a Wheatstone bridge configuration. Expressing the output through a traditional Wheatstone bridge circuit shows how the change in voltage output depends on the majority carrier mobility. This can be further simplified assuming the MOSFETs display identical behaviour and that the two arms of the Wheatstone bridge will behave equally and opposite leading to a sensor output of

$$\frac{V_{out}}{V_{in}} = 2 \left( \frac{\Delta\mu}{\mu} \right) = 2(\pi_l \cdot \sigma_l + \pi_t \cdot \sigma_t) \quad (2.10)$$

The circuit schematic of the pressure sensor is shown in Figures 2.24 and 2.25 where Figure 2.24 shows the Wheatstone bridge configuration comprising of the four pressure sensitive MOSFETs, and Figure 2.25 shows the equivalent circuit when their channel resistances are taken as the piezo resistances.

Initially, it is important to look at the behaviour of the MOSFET when the pressure remains constant. Figures 2.26 and 2.27 show the characteristic curves for the on-membrane pMOSFET and nMOSFET at atmospheric pressure, which is the current from drain to source  $I_{DS}$  plotted against the voltage from drain to source MOSFETs with clear linear and saturation regions for both designs. This proves the designs function properly and were not corrupted during the design or fabrication phases. This also provides the information in order to bias the devices in the saturation region. As expected, the drain

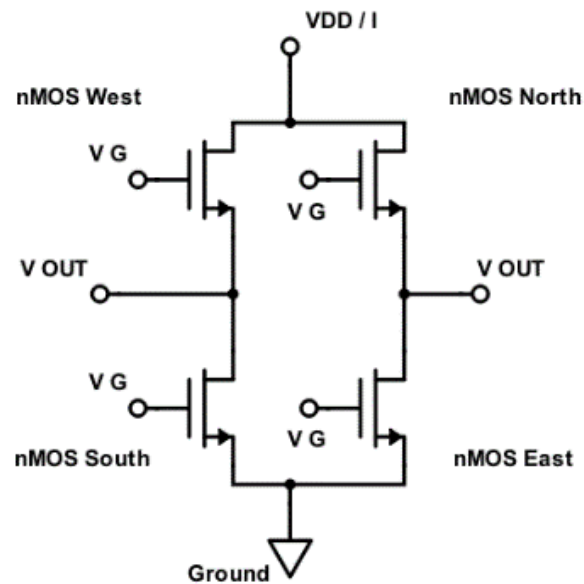


**Figure 2.24:** Schematic showing the operation of the MOSFET pressure sensor for Wheatstone bridge operation.

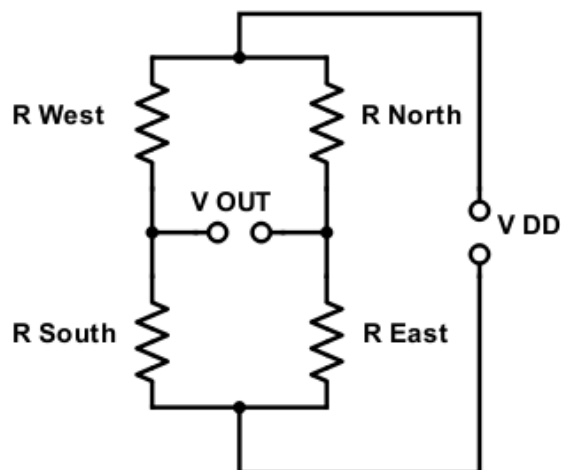


**Figure 2.25:** Schematic showing the operation of the MOSFET pressure sensor for the equivalent circuit as piezo resistances. N.B.  $V_G$  was held constant for all 4 MOSFETs.

current of the nMOSFET is approximately twice as large as the pMOSFET, which is due to carrier mobility being 2.5 times higher for electron mobility as opposed to hole mobility.

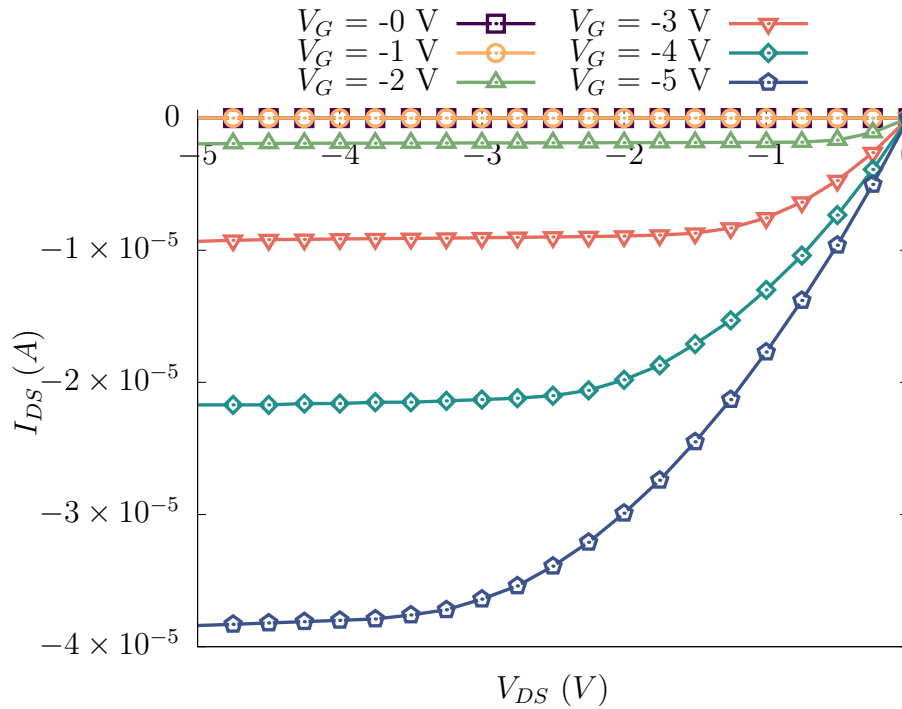


**Figure 2.26:** The characteristic curves of the pMOSFET.

Figure 2.28 shows the drain current plotted against the gate voltage, commonly known as the threshold curve. The threshold voltage  $V_T$  was calculated by plotting the square root of the drain current and taking the gate voltage intercept from the linear region of the curve. The pMOSFET design has a threshold voltage of -1.2 V whilst the nMOSFET displayed a threshold voltage of +1.5 V. The knowledge of these threshold voltages provides the point at which the devices turn on, and thus allowing the region of biasing to be used when measuring the response to pressure.

The experimental stage provided the characteristic curves of all 4 membrane MOSFETs at every pressure difference. These were converted into channel resistances and the Wheatstone bridge equation was used to attain a voltage output of the sensors with the increasing of pressure difference. Figure 2.29



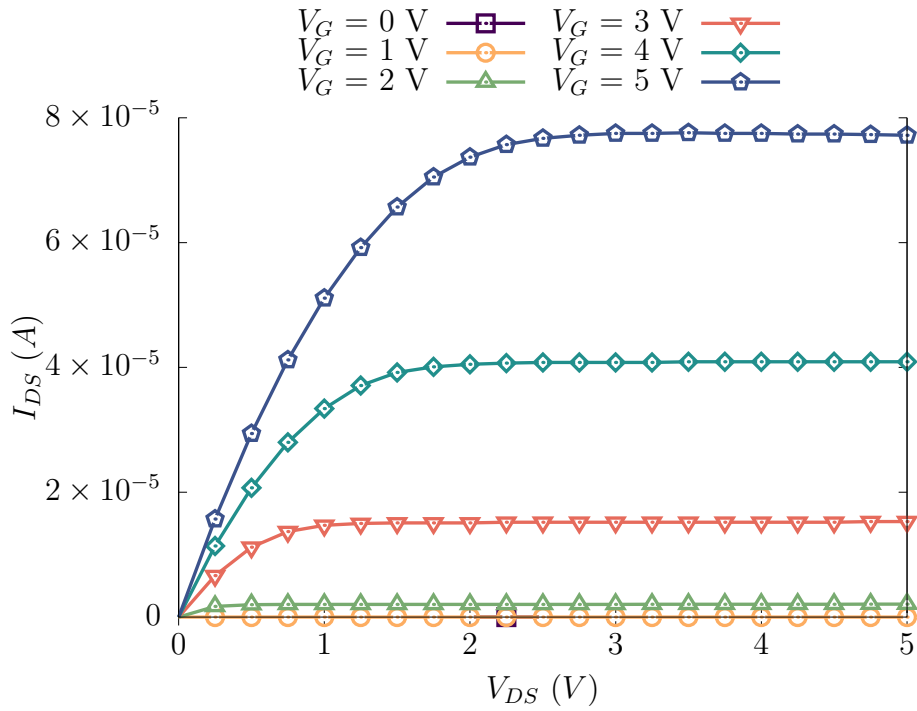


**Figure 2.27:** The characteristic curves of the nMOSFET.

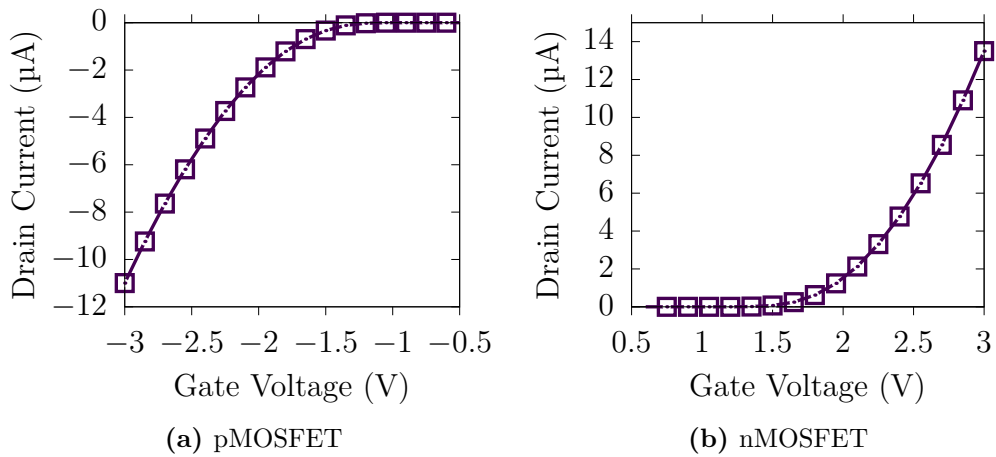


**Figure 2.28:** The drain current against gate voltage for calculating the threshold voltage.

and Figure 2.30 show the voltage response whilst varying the drain voltage and keeping the gate voltage at  $\pm 5$  V.

Figure 2.31 and Figure 2.32 show the voltage response for varying gate voltage and constant drain voltage. Varying the drain current has no effect on the voltage response, meaning that the lowest drain voltage possible should be used for the lowest power consumption. For all gate voltages above the threshold voltage, there is a strong increase in output voltage with increasing pressure. It can be seen that for the gate voltages of  $\pm 2$  V, the response is slightly higher, which can be ascribed to their functioning being within the ohmic region. Most importantly, the full-scale output voltage of the pMOSFET (0.21 V) is much larger than for the nMOSFET (0.096).

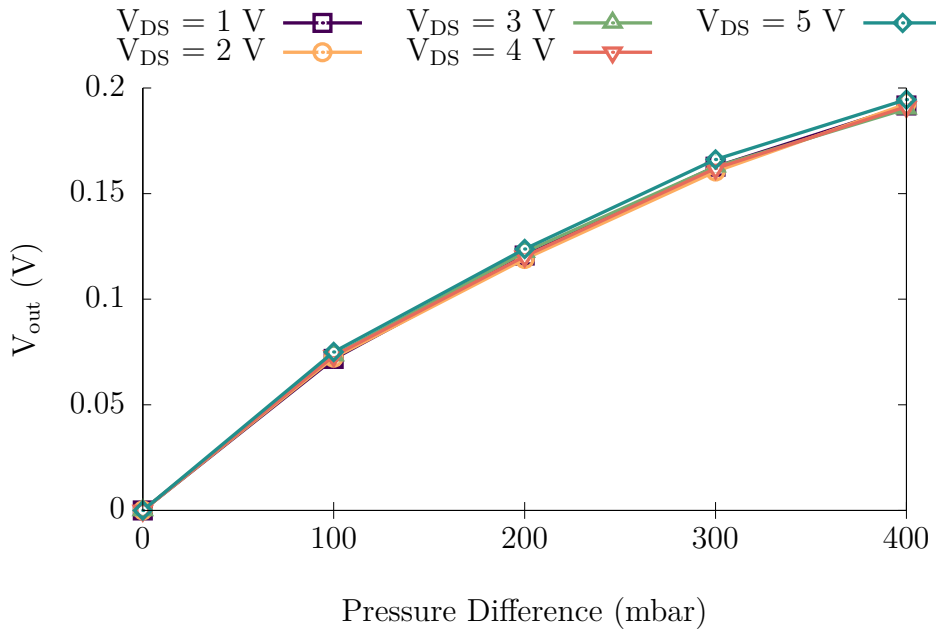


**Figure 2.29:** The change in voltage output with the evolution of pressure for the pMOSFET design with varying drain voltage.

Using the data displayed in Figure 2.27, the important performance parameters can be evaluated, including the voltage sensitivity. The sensitivity of the pMOSFET design is 5.21 mV/kPa whilst the nMOSFET design had a lower sensitivity of 2.40 mV/kPa. The total consumed power  $P$  was calculated using

$$P = V_{DS} \cdot I_{DS} \quad (2.11)$$

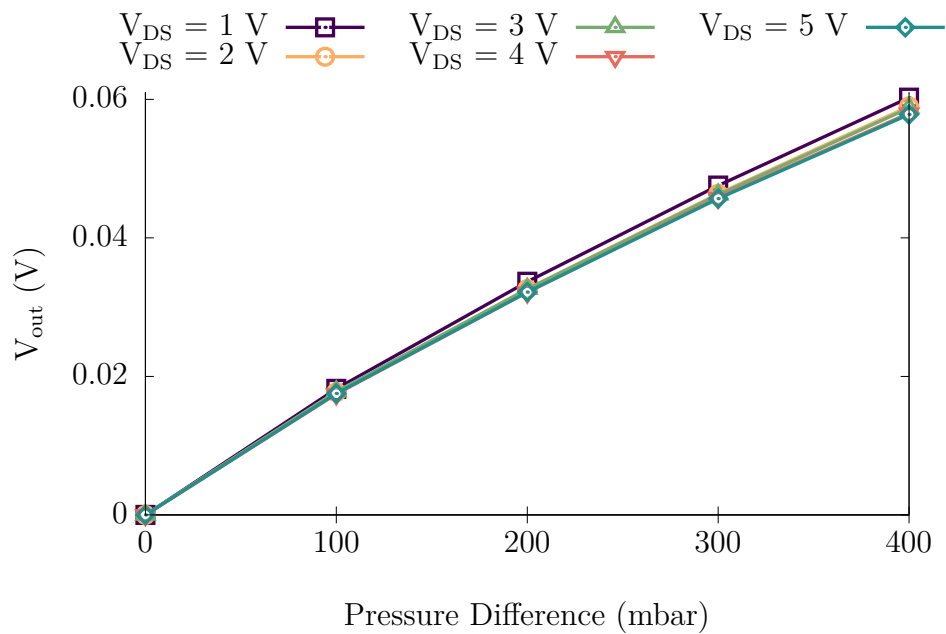


**Figure 2.30:** The change in voltage output with the evolution of pressure for the nMOSFET design with varying drain voltage.

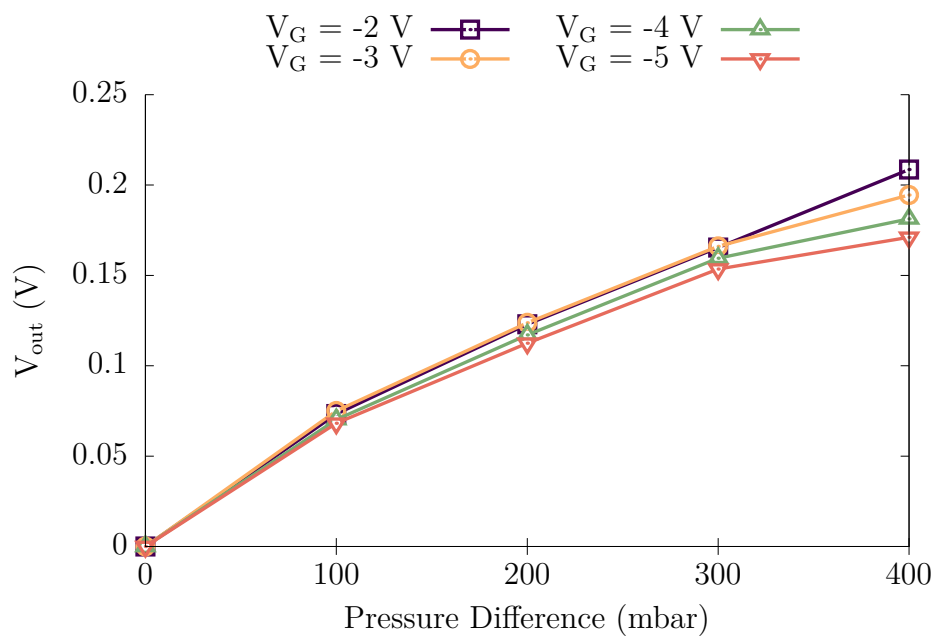


**Figure 2.31:** The change in voltage output with the evolution of pressure for the pMOSFET design with varying gate voltage.

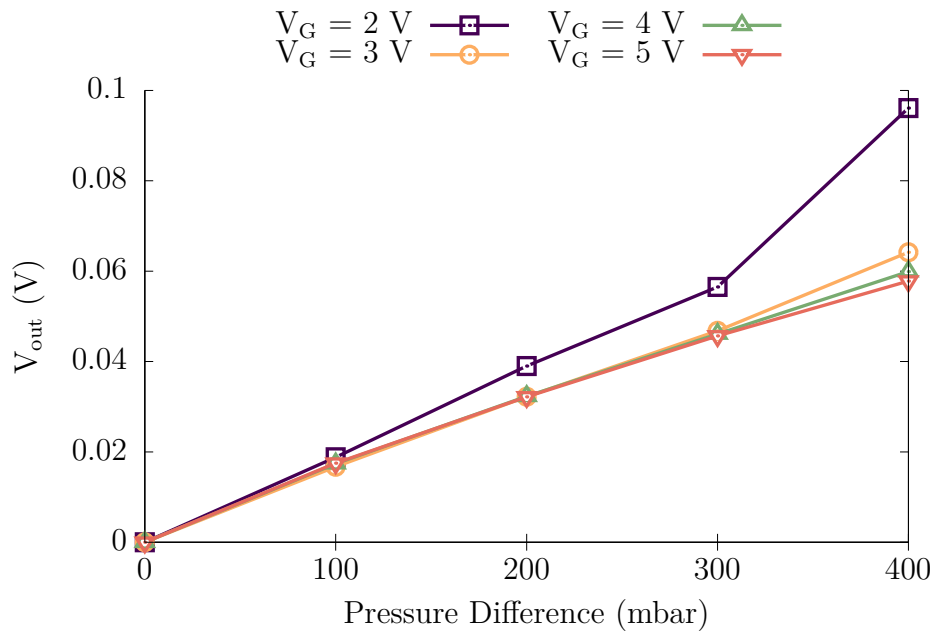


**Figure 2.32:** The change in voltage output with the evolution of pressure for the nMOSFET design with varying gate voltage.

resulting in a maximum power consumption of 0.19 mW for the pMOSFET and 0.39 mW for the nMOSFET. These performance parameters demonstrate a highly sensitive, low-power pressure transducer.

### Piezo-Diode

Initially, the I-V characteristics of the diodes were measured to ensure conventional silicon diode behaviour and show the functionality after the design and manufacturing stage. The voltage was swept from -1.5 V to +1.5 V using a Keithley 2410 with in-house developed Labview software.

Figure 2.33 shows the I-V curve from 0.5 to 1.5 V of all 4 diode-based designs with diodes located on the membrane being denoted with dashed lines whilst the diodes on the substrate use solid lines. The breakdown voltage was

below -1.5 V and no reverse leakage current was seen; therefore, the figure focuses on the interesting region around the threshold voltages.

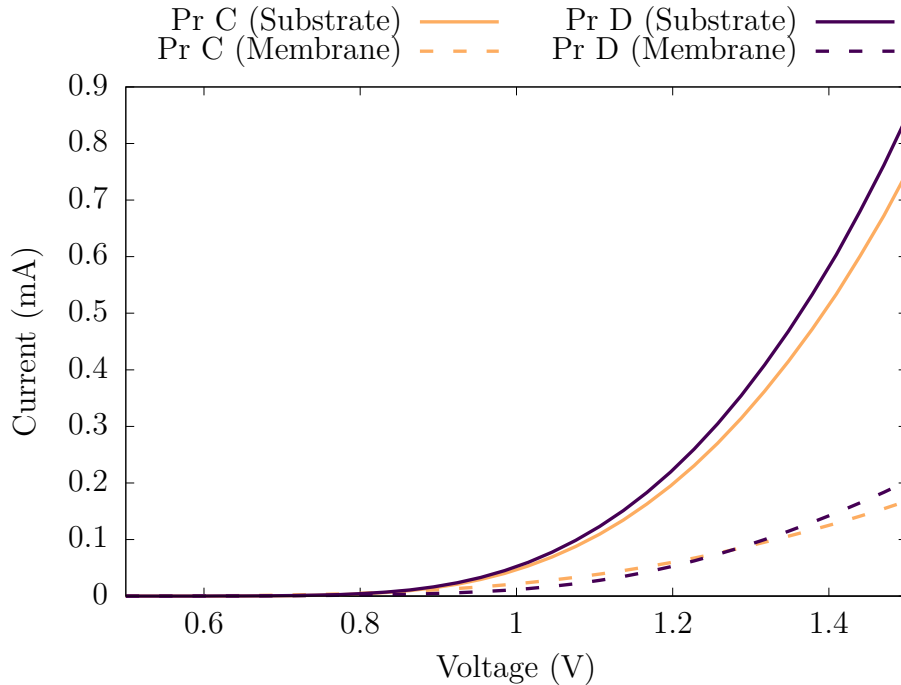


**Figure 2.33:** I-V curves for the 2 piezo-diodes where dashed lines are on-membrane diodes and solid lines are on-substrate diodes.

The first deduction is that all the designed diodes function as conventional silicon diodes, with threshold voltages at around 0.7 V. It can also be seen that the I-V curves for the diodes located on the substrate are sharper, thus closer to a theoretically ideal diode. This is likely due to the inherent residual stresses that are within the membrane after the DRIE process between all the incorporated layers with different atomic structures. This residual stress will increase the difficulty of charge carrier transport, hence yielding a lower current for the same applied voltage. It is with the knowledge that the diode designs on the membrane are proven to function conventionally and experiments can be carried out with varying pressure.

When pressure is applied to a body within its elastic limit, a proportional strain is produced. Under strain, the energy levels of silicon valence band split and become non-degenerate. This results in a modification of the carrier

concentration, i.e. changing the electrical response. In doped semiconductor materials, the band gap shift,  $\Delta E_g$ , produces a change in the minority carrier charge of

$$\frac{p_n}{p_0} = \exp\left(\frac{\Delta E_g}{k_B T}\right) \quad (2.12)$$

for n-type and

$$\frac{n_p}{n_0} = \exp\left(\frac{\Delta E_g}{k_B T}\right) \quad (2.13)$$

for p-type where  $k_B$  is the Boltzmann constant and  $T$  is temperature.

The band-gap shift is proportional to the applied pressure  $P$ , assuming  $P$  follows linear bending theory and provides a linear strain, by

$$\Delta E_g = k_p P \quad (2.14)$$

where  $k_p$  is a constant. This constant is usually extremely small, thus necessitating a very large pressure for significant changes to occur. From known semiconductor theory, the forward flowing current through an ideal n-p junction diode is

$$I \approx I_0 \left[ \exp\left(\frac{qV}{kT}\right) \right] \quad (2.15)$$

where  $I$  is the current flowing through the junction and saturation current  $I_0$  can be expressed by

$$I_0 = q \left( \frac{D_p p_n}{L_p} + \frac{D_n n_p}{L_n} \right) \quad (2.16)$$

Assuming that  $D_p$ ,  $D_n$ ,  $L_p$  and  $L_n$  are constant with stress and that the minority carrier concentrations  $p_n$  and  $n_p$  are proportional to the  $\exp(\Delta E_g/kT)$  term, they therefore correlate to the stress as the energy gap  $\Delta E_g$  is pressure sensitive. The forward current through the junction can now be written as

$$I_f \approx I_0 \left[ \exp\left(\frac{qV}{kT}\right) \left(V - \frac{1}{q}\Delta E_g\right) - 1 \right] \quad (2.17)$$

where  $I_0$  is the saturation current for zero stress. In a non-ideal junction, ideal current and currents from generation-recombination are present. Wortman and Hauser [83] have shown that including these effects, the forward current can be written as

$$I_f \approx I_{0t} \left[ \exp\left(\frac{-\Delta E_g}{kT}\right) \exp\left(\frac{qV}{kT}\right) \right] + I_{0r} \left[ \exp\left(\frac{-\Delta E_g}{2kT}\right) \exp\left(\frac{qV}{2kT}\right) \right] \quad (2.18)$$

where  $I_{0t}$  and  $I_{0r}$  are the ideal current and generation-recombination current, respectively. If these two currents are independent from the applied pressure, it can be seen that the change in voltage when biased with constant current will exactly represent the energy gap change  $\Delta E_g$ .

The experimentally observed band gap shift for the junction (where generation-recombination were also present) has been extracted from the values of raw voltage output with the change in pressure and were then used to calculate a pressure coefficient of energy gap of 15.2 eV/kBar. This value shows a dramatic increase when compared with Jayaraman et al. [84] of -1.5 eV/kBar for silicon p-n junctions. This high value can be explained by the thin membrane design, which deforms under pressure and further changes the characteristics of the valence band and carrier concentration. The main drawback of diode-based pressure sensors is the typically low value of  $k_p$  requiring high pressures. This higher value will mean a dramatic increase in sensitivity for the fabricated designs.

The raw resistor data were put through the equation of a Wheatstone bridge in order to calculate the voltage outputs of the designs. Figure 2.34 shows the voltage difference as the pressure is changed from -300 mbar to -700 mbar. From the results, all the output voltages change with applied pressure, showing

superior performance at 10  $\mu\text{A}$  bias current. The p+/p-drift/n+ provides the highest sensitivity, increasing by almost 3 times when biased at 10  $\mu\text{A}$  to 79  $\mu\text{V}/\text{mbar}$ . This value is higher than current piezo-junction designs [68, 72] as well as comparative to optimised piezo-resistive technology [85, 86] showing the potential competitiveness of this technology.

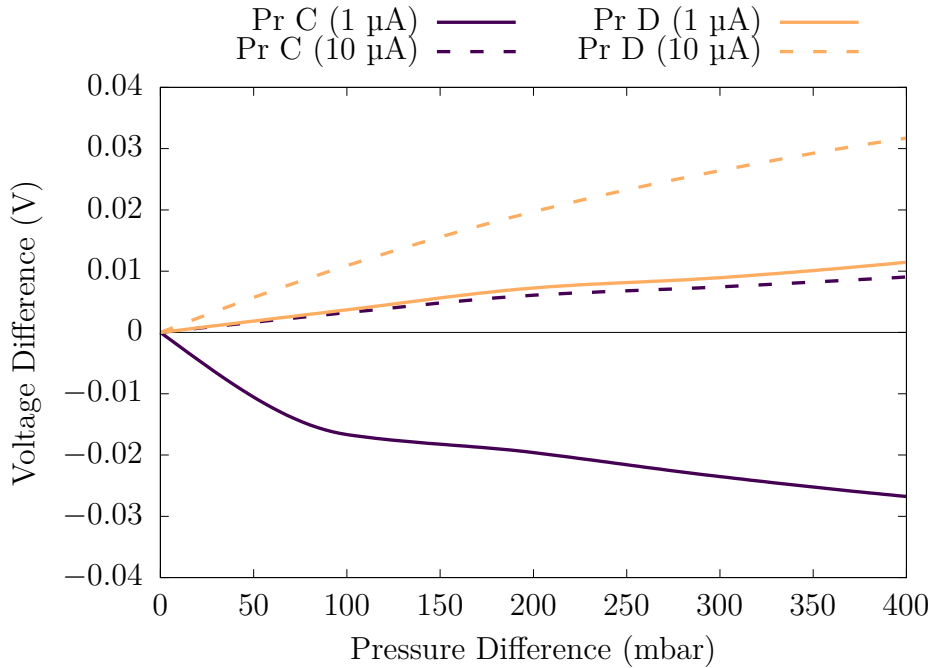


**Figure 2.34:** The voltage output of the Wheatstone bridge with the evolution of pressure for the piezo-diode designs.

These results can be compared with existing technologies that use pressure sensitive electronic components using Table 2.6. Here it can be seen that the pMOSFET presented in this chapter improves on the highest recorded sensitivity of a piezo-junction device documented by 2.4 times, even before any geometrical and electronic optimisation. The device shows a large increase on other MOSFET-based designs and is also more sensitive than many recent piezo-resistive sensors whilst also requiring a lower power consumption. It can also be seen that piezo-diodes are two orders of magnitude lower than the piezo-MOSFETs, despite improving sensitivity on current pressure sensing diode devices.



Overall, two piezo-MOSFETs and two piezo-diodes have been designed, fabricated, packaged and tested and have improved on existing similar technology with regards to pressure sensitivity. This is another step on the path towards the common place industrial utilisation of piezo-junction pressure sensors alongside the more well-known piezo-resistors.

**Table 2.6:** Table showing current technologies and their sensitivities.

Reference	Sensitivity (mV/V/10kPa)	Sensitivity (mV/kPa)	Sensing Element
[71]	2.3	1.14	Piezo-resistor.
[72]	N/A	0.051	Piezo-resistor.
[61]	N/A	0.30	Piezo-resistor and MOSFET.
[64]	7.18	2.15	nc-Si/c-Si MOSFET.
[65]	0.94	0.47	MOSFET Current Mirror.
[66]	7.82	1.29	MOSFET Differential Amplifier.
[Pr A]	13.03	5.21	pMOSFET.
[Pr B]	6.0	2.40	nMOSFET.
[Pr C]	-	0.022	Diode.
[Pr D]	-	0.079	Diode.



# Chapter 3

## Flow Sensing

### 3.1 Introduction

**F**LUID dynamic phenomena can be found ubiquitously and there is increasing demand to monitor and control the flow of both gases and liquids and thus there has been great interest in the development of flow sensors in the MEMS community since the first micromachined flow sensor in 1974 [87]. During the decades since, there have been numerous types of flow sensing devices developed with many becoming commercially available. In 2018, Global Industry Analysts, Inc. estimated the continued global growth of flow sensors with its market value reaching 6.5 billion US dollars by 2024 [88]. This is driven by strong expansion in key sectors that include automotive, oil & gas, medical, indoor climate control and home appliances. With the advent of modern technologies and smart flow sensors/systems, MEMS flow sensors will look to dominate this market with its major benefits strongly supporting the markets growing emphasis on energy efficiency, reduced cost, scalability and enhanced capabilities. Table 3.1 outlines several commercial fields that require the use of flow sensors. In addition to this, some examples of the important

physical parameters that they measure are also given, highlighting the extensive market requirement for flow sensors and the driving force behind their continued research and development.

**Table 3.1:** A summation of fields where flow sensors need to be used alongside some parameters that need to be specifically measured.

Field	Example Measurands
<b>Metrology</b>	Wind velocity, direction
<b>Automotive</b>	Fuel injection systems, combustion, vehicle performance, fuel cells
<b>Civil</b>	Wind forces on buildings, servers and data centres
<b>Environmental</b>	Dispersion of pollen
<b>Medical</b>	Respiration, blood flow, surgical tools, drug delivery, inhalers
<b>Indoor</b>	Ventilation, air conditioning
<b>Home</b>	Vacuum cleaners, hair dryers, fan heaters, air purifiers, robovacs
<b>Other</b>	Drones, AR/VR, E-cigarettes, gaming

The sensing of flow rate is a challenging prospect due to the complexity of the flow physics yet virtually any application can be addressed with the wide variety of technologies, materials, operation modes and transduction types available. MEMS-based sensors have been successfully used in the detection of flow rate and existing MEMS flow rate sensors fall into two categories: direct (e.g. floating element [89–91]) and indirect ones (e.g. micro fence [92, 93], micro optical [94, 95], micro pillar [96, 97] and thermal-based). Among these methods, the development of thermal flow sensors has seen significant advancement in recent years, due to

- i. The absence of moving parts.
- ii. Simple fabrication and packaging options
- iii. CMOS compatible fabrication with the result of thermal flow sensors being one of the most commonly commercially available sensors.

For thermal flow sensors, an electric current is sent through the wire, which causes the wire to heat up through Joule heating. When a fluid flows over the heated wire, it cools the wire by removing some of its energy. The amount of heat loss relates to an electrical change in system and this can be related to the flow rate.

In order to understand the relationship between the applied current and the velocity of the flow, heat balance equations can be solved. A brief analysis is now presented assuming steady-state conditions. In this lumped system analysis, the heat generated by Joule heating  $H_g$  can be assumed equal to the heat transferred into the fluid

$$H_g = I^2 R \quad (3.1)$$

where  $I$  is the heater current and  $R$  is the wire resistance. Here, thermal fluid sensors rely on this interaction between the heated element of the sensor itself and the flowing medium. The temperature of the heated element is calculated through its resistance using this equation:

$$R_T(T) = R_{T0}[1 + \alpha_T(T_s - T_0) + \beta_T(T_s - T_0)^2] \quad (3.2)$$

where  $R_T$  and  $R_{T0}$  are the resistances at the operation temperature ( $T_s$ ) and reference temperature ( $T_0$ ), respectively and  $\alpha_T$  (TCR1) and  $\beta_T$  (TCR2) are empirically measured and depend on the material properties of the heater.

If forced convection is considered the dominant form of heat transfer, conduction and radiation can be ignored and the generated heat is equal to the heat loss through convection

$$I^2 R_T = hA(R_T - R_{T0}) \quad (3.3)$$

where  $h$  is the coefficient of heat transfer and  $A$  is the heat transfer area. The dimensionless heat transfer coefficient Nusselt number and the Reynolds number can be used to substitute out the heat transfer coefficient in order to see the relationship to velocity:

$$I^2 R_T = (R_T - R_{T0})(A_1 + A_2 U^{0.5}) \quad (3.4)$$

where  $A_1$  and  $A_2$  are constants to be determined and  $U$  is the fluid velocity. If we define a ratio of resistances as  $R = R_s/R_0$  then current can be related to velocity through the following expression, which is referred to as King's Law:

$$I^2 = \left( \frac{R - 1}{R} \right) (A_1 + A_2 U^{0.5}) \quad (3.5)$$

This analysis has some simplifications that include neglecting axial heat conduction in the wire, heat loss through the structural support system, dynamic response of the heated wire and effects of the measurement circuitry.

Another common method of investigating the response of thermal flow sensors is through the measurement of wall shear stress  $\tau_w$ , which is related to velocity through Newton's law of viscosity:

$$\tau_w = \mu \left. \frac{du}{dy} \right|_{wall} \quad (3.6)$$

where  $\mu$  is the fluid dynamic viscosity and  $\left. \frac{du}{dy} \right|_{wall}$  is the velocity gradient

between the free stream and surface of the wall. It can be seen that wall shear stress is strongly proportional to the velocity, namely the velocity boundary layer.

This parameter is used in the optimisation carried out through simulation, because it provides a more accurate depiction of the sensor response in reality, which will depend on the velocity and thermal boundary layers at the wall.

Thermal flow sensors can be divided into three categories that pertain to the operation method in which they measure flow rate:

- i. Anemometric sensors directly measure the heat that is transferred from a heated element into the flowing fluid, in this case the heater serves as both the heating element and the temperature sensing element simultaneously and thus the resistance value measured depends on the flow rate.
- ii. Calorimetric sensors measure a thermal asymmetry produced by fluid flow over a centrally heated element coupled with two Resistive Temperature Detectors (RTD) that are located on either side of the heater, resulting in the mass flow rate being related to the temperature difference given between the two RTDs.
- iii. Time of Flight (ToF) sensors measure the transit time of a thermal pulse to extract the flow rate information, requiring a heater and at least one downstream thermal sensor.

A diagrammatic representation of all three methods is shown in Figure 3.1 with a table summarising their relative advantages and disadvantages given in Table 3.2.

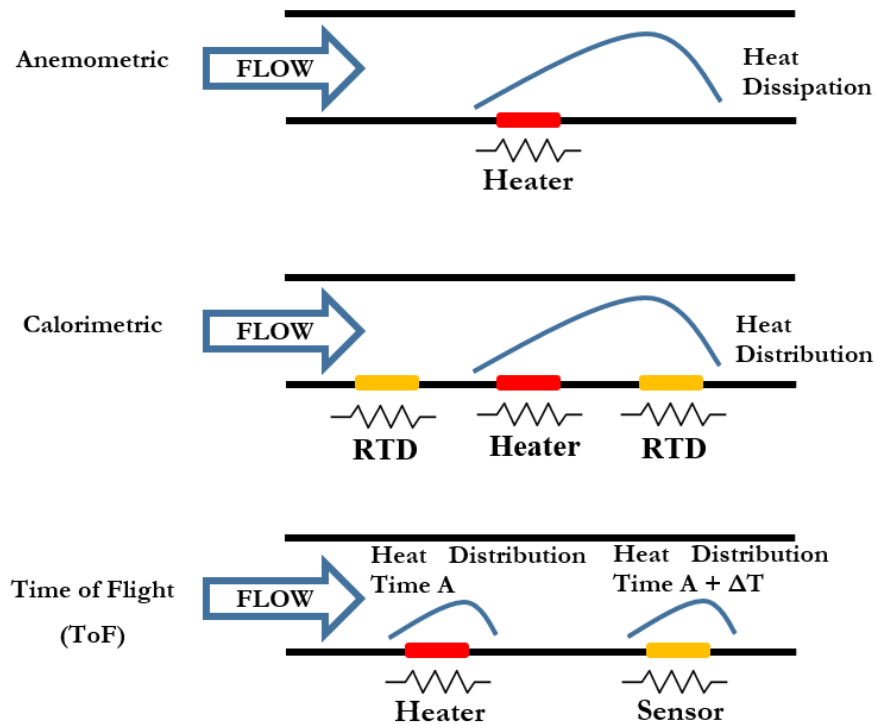


**Figure 3.1:** Diagrammatic representation of the three main operation modes for a thermal flow sensor.

**Table 3.2:** The main advantages and disadvantages of the three main operating modes used for thermal flow sensors.

Operation Mode	Advantages	Disadvantages
<b>Anemometric</b>	Simple technique. Wider flow range.	Non-linear response. Dependent on ambient temperature.
<b>Calorimetric</b>	Decouples heater and sensor. Bi-directional.	Restricted measuring range.
<b>Time of Flight</b>	Bi directional. Less dependent on ambient temperature.	Most complex. Low sensitivity for small flow rates.



The physical method of temperature measurement can also be split into three categories:

- i. Thermo-resistive sensors use resistive elements.
- ii. Thermo-electric transduction detects thermal changes using thermopiles.
- iii. Thermo-electronic transduction uses transistors or diode elements.

Detailed reviews of thermal fluid flow sensors can be found here [98–100]. A brief review of thermal flow sensors is hereafter presented.

One of the earliest patents outlining an anemometer was in 1918 [101] where a resistive element transduced electrical signal into temperature and vice-versa. With the advent of micromachining techniques in the 1970s, discrete anemometer elements were replaced with integrated MEMS solutions and the use of silicon also allowed the integration of embedded elements with on-chip circuitry [87, 102–104]. This also allowed the implementation of thermo-electronic transducing methods, which were proposed due to better temperature sensitivity and long term stability [105–107]. In the 1980s, a multitude of materials have been investigated for the heating and sensing elements that include polysilicon [108–114], aluminium [115][100], gold [116], platinum [117], tungsten [118], nickel [119], graphene [120] and carbon nanotubes [121]. Silicon is known to have a high thermal conductivity, resulting in high heat transfer into any silicon supporting structure and thus lower device sensitivity [122, 123]. This has been a major problem in thermal flow sensors leading to a multitude of methods being researched for the solution. A common approach is to replace the silicon with a thermally isolating material with low conductivity (e.g. polyimide [124, 125] & polysilicon [126]). Another method is to place the thin-film on a suspended membrane, thereby restricting the majority heat diffusion to the in-plane direction via the thin membrane [127, 128]. DRIE has also been used to create an air cavity [129, 130], taken further by implementing a wafer-bonded

vacuum cavity [117] and a surface micromachined vacuum cavity [109]. A thin film resistor has also been suspended on typically two or four micro bridges, restricting the heat conduction to the substrate with a nearly 1-dimensional structure (i.e. long and thin) [131–133]. A more recent publication shows that insulating trenches can also significantly increase the sensitivity of a thermal flow device [134]. It should be noted that in many of these cases CMOS compatible fabrication is not possible, leading to high manufacturing costs and low likelihood of commercial exploitation.

Most current literature considers powering devices with constant current or voltage, which lends itself to steady-state numerical modelling. Such methods are an essential tool for creating, developing and optimising any sensor. Flow sensing is a particularly challenging task due to the complex multi-physics phenomena and analytical solutions can rarely be attained. Numerically modelling MEMS flow sensors requires a fine mesh in order to measure accurately the relevant variables over the spatial domain. If the model requires more than one physical mechanism to be interlinked then the complexity of the solution greatly increases, explaining why most attempts in the literature are simplified. Approximations include only considering a 2-dimensional geometry [135], which has been shown to be too inaccurate for attaining quantitative data [136], or not including multi-physics [137]. A work by Sabate et al. [138] used 3D simulations as a design tool, however too many assumptions were made to match experimental data accurately and the simulations were used qualitatively rather than quantitatively.

All the conducted research has resulted in a thriving commercial scene for the design and application of flow sensors. Table 3.3 outlines several current commercial sensors that are specified for a flow rate range similar to the intended flow rate range for the device developed in this thesis. The two notable factors of all the devices is their large cost and bulky footprint. This highlights the downfall of current commercial sensors and leaves a space for improvement in

sensor size and cost, whilst maintaining the inherent advantages that MEMS thermal flow sensing provides.

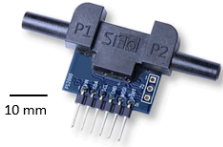
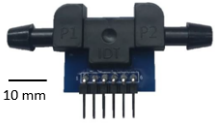
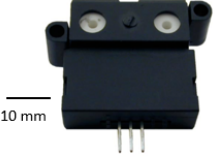




This chapter discusses the design, characterisation, numerical modelling and optimisation of various CMOS MEMS thermal flow sensors that have used a tungsten metallisation process for the metal layer and thus, have a tungsten heating element. In addition to this, single crystal thin silicon is used for thermo-electronic sensing methods. With these common features, novel designs have been investigated and compared with numerical simulations used to further understand their behaviour. This section can be used as a tool to help the design of thermally based MEMS sensors for measuring flow and will help to enable the next generation of low-cost, small, highly sensitive flow sensors.

## 3.2 Design and Fabrication Details

All the sensors were designed using the Cadence Virtuoso (IC 5.1.4) layout editor. Each sensor comprises of the same core CMOS MEMS layers. An optical micrograph of one of the chips is shown in Figure 3.2 with its cross-section, illustrating the layers, given in Figure 3.3.

The flow sensors were fabricated using a 1.0  $\mu\text{m}$  SOI CMOS process with tungsten metallization followed by a post-CMOS back-side deep reactive ion etch (DRIE), all of which were performed in a commercial foundry. All chips contain a tungsten heating resistor connected to wire bonding pads via 20  $\mu\text{m}$  tracks. Two extra tracks were incorporated off the central resistor to allow precise 4-wire resistance measurements.

**Table 3.3:** A summary of current commercial thermal gas flow sensors that operate in a similar flow rate range to the designed flow sensor in this thesis.

Product	Flow Range	General Notes
IDT FS2012 	0 - 2 SLPM	£60 Evaluation kit available
IDT FS1012 	0 - 2 SLPM	£28, differential amplifier recommended.
Honeywell AWM43600V 	0 - 6 SLPM	£101 Amplified output available, or external circuitry required.
Honeywell AWM3300V 	0 - 1 SLPM	£95 Amplified output available, or external circuitry required.
Aceinna MFC2030 	0 - 30 SLPM	£97 Bi-directional flow, RH up to 95%.
Sensirion SFM4100 	0 - 20 SLPM	£129 evaluation kit available (£48).
Sensirion SDP36 	-50 to +500 Pa	£25 Evaluation kit available including SDP31 (£49).

Increased thermal isolation and mechanical support for the tungsten heating resistor is achieved by the thin dielectric membrane. Tungsten was used instead of aluminium due to its superior thermo-mechanical properties including lower thermal conductivity, lower heat capacity, higher melting point, higher density, lower Poisson's ratio, lower thermal expansion and higher yield strength. These factors lead to a higher mechanical strength and lower electromigration susceptibility.

DRIE was chosen due to its ability to minimise the diaphragm size, which is due to it being an isotropic etch, i.e. the etch rate is independent of the orientation of silicon crystal structure. Below the heating resistor, situated in the single crystal silicon layer, a p+/p-well/n+ thermodiode is embedded and connected to pads through 1.5  $\mu\text{m}$  wide tracks. These devices can therefore be used both thermo-electronically and thermo-resistively, allowing an accurate comparison between the two transduction methods.

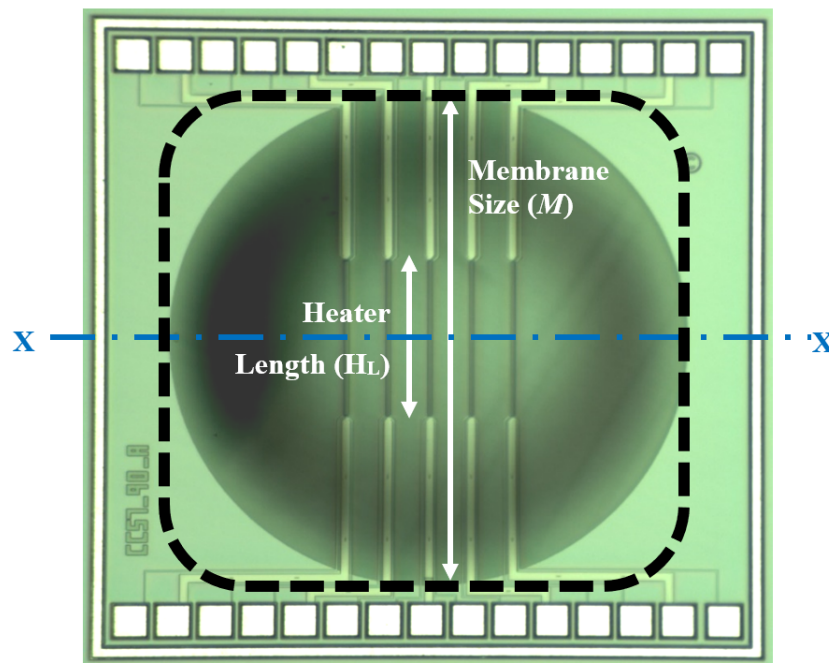


**Figure 3.2:** Optical micrograph of MEMS flow sensor with multiple heaters (FL 01) – die dimensions of 1.6 mm by 1.6 mm. The dotted black line represents the square with rounded corners membrane shape.

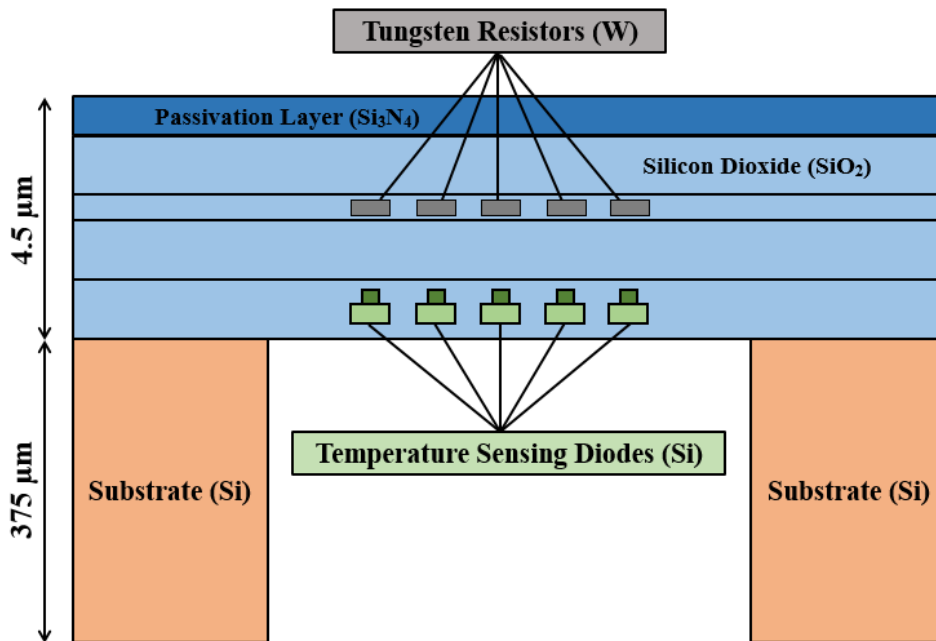


**Figure 3.3:** Cross-section of sensor along cut point X-X that is depicted in Figure 3.2 (not to scale) The tungsten heater connects to tracks within the same metal layer in the membrane which are connected to the surrounding pads.

Several different sensor designs were fabricated and tested, which are all listed with their relative varying parameters outlined in Table 3.4. The investigated sensors are split into four sections for carrying out analysis.

The first analysis uses Fl 01 to investigate the accuracy of 2-Dimensional and 3-dimensional numerical modelling. Fl 01 is also then used alongside numerical analysis to investigate optimisation of the device in calorimetric mode. Devices Fl 02 to Fl 09 are used to optimise the anemometric optimisation of the flow sensor, with particular regard to the geometry of the sensor parameters. Finally, devices Fl 02, Fl 10 and Fl 11 are used to analyse the use of thermodiodes as the temperature transduction component.

**Table 3.4:** A summary of all the investigated flow sensor designs and their pertinent design parameters where Sq. w/ RC stands for square with rounded corners.

Chip ID	Membrane Shape	Membrane Size ( $\mu\text{m}$ )	Heater Size ( $\mu\text{m}$ )	No. of Resistors	Diode Size ( $\mu\text{m}$ )	No. of Diodes
F1 01	Circular	1200	2 $\times$ 400	5	5	5
F1 02	Sq. w/ RC	1200	2 $\times$ 400	1	5	5
F1 03	Sq. w/ RC	800	2 $\times$ 270	1	5	5
F1 04	Sq. w/ RC	400	2 $\times$ 130	1	5	5
F1 05	Sq. w/ RC	1200	2 $\times$ 200	1	5	5
F1 06	Sq. w/ RC	1200	2 $\times$ 800	1	5	5
F1 07	Sq. w/ RC	1200	4 $\times$ 400	1	5	5
F1 08	Sq. w/ RC	1200	8 $\times$ 400	1	5	5
F1 09	Sq. w/ RC	1200	2 $\times$ 400	1	5	5
F1 10	Sq. w/ RC	1200	2 $\times$ 400	1	5	1
F1 11	Sq. w/ RC	1200	2 $\times$ 400	1	400	1

### 3.3 Numerical Model

COMSOL Multiphysics (v5.3) was used to define and implement the numerical simulation. The model consisted of three separate yet interlacing physics modules that are:

- i. **Electric Current** – a biasing current is defined for the central resistor and locally heats up the membrane via Joule heating.
- ii. **Heat Transfer** – heat transfer was defined into the membrane through conduction whereas conduction and convection were included for the fluid above and below the membrane.
- iii. **Fluid Dynamics** – laminar flow is introduced through the fluid above the membrane, affecting the amount of forced convection into the fluid. This results in an asymmetric thermal profile and changes the operating temperature of the heating resistor.

Interpolative tables were included for material properties such as thermal conductivity, density, viscosity and thermal expansion due to their dependence on temperature. Firstly, the biasing current must be related to the thermal power that is generated in the resistor. It is known that tungsten is non-linearly dependent on temperature and its resistance was approximated by equation (3.2) where parameters  $\alpha_T$  and  $\beta_T$  were empirically measured at  $2.05 \times 10^{-03} K^{-1}$  and  $5.0 \times 10^{-07} K^{-2}$ , respectively. A current source boundary condition was applied at one end on the heater tracks with the opposite edge being defined as ground. The heat transfer can be split into the heat transfer through solids (conduction) and the heat transfer through fluids (conduction and convection). The former is modelled by (3.3) whilst the latter is modelled by (3.4). A pressure-work term was added to heat transfer through fluids to account for phenomena such as heat from compressing air ( $\alpha_T T \mathbf{u} \cdot \Delta p_A$ ).



$$q = -k \cdot \nabla T \quad (3.7)$$

$$Q = \rho c_p \mathbf{u} \cdot \nabla T + \alpha_T T \mathbf{u} \cdot \nabla p_A + \nabla \cdot q \quad (3.8)$$

where  $q$  and  $Q$  are heat flux through solids and fluids respectively,  $\rho$  is density,  $c_p$  is the heat capacity at constant pressure,  $k$  is the thermal conductivity,  $\mathbf{u}$  is the velocity field,  $\alpha_T$  is the linear thermal expansion coefficient and  $p_A$  is the absolute pressure. The Navier-Stokes equations govern the motion of fluids and utilise (3.5) and (3.6) for our case of steady, compressible flow, where  $p$  is pressure,  $\mu$  is the viscosity and  $\mathbf{I}$  is the identity matrix.

$$\rho(\mathbf{u} \cdot \nabla)\mathbf{u} = \nabla \cdot [-p\mathbf{I} + \mu(\nabla\mathbf{u} + (\nabla\mathbf{u})^T - 2/3\mu(\nabla \cdot \mathbf{u})\mathbf{I})] + \rho g \quad (3.9)$$

$$\nabla \cdot (\rho\mathbf{u}) = 0 \quad (3.10)$$

Several dimensionless parameters can be used to understand the heat mechanisms and ensure the model will incorporate the necessary elements. The Grashof number  $Gr$  gives the ratio of buoyant forces to viscous forces

$$Gr = \frac{g\alpha_T\Delta TL^3}{\nu^2} \quad (3.11)$$

Due to the high temperature generated by the heater there is significant natural convection that plays a dominant role in stagnant flow conditions, meaning the gravity term  $[\rho g]$  cannot be omitted. The Richardson number

$$Ri = \frac{Gr}{Re^2} \quad (3.12)$$

parameterises the relative strength of free and forced convection. Due to the model considering laminar flow, the Richardson number warrants that natural convection cannot be omitted even with the addition of flow and it is therefore

considered for all flow rates. Finally, the Boltzmann number

$$Bo = \frac{\rho C_p u_\infty}{k_B T_\infty^3} \quad (3.13)$$

where  $k_B$  is the Boltzmann constant, is used to show the contribution of radiation to the overall heat transfer. For all values of flow, this dimensionless value shows a relatively high number, therefore showing radiation has an extremely weak effect and can be neglected in the simulations. This weak effect can be explained by operating temperature of the heater being low, radiation may need to be considered if this temperature is considerably increased.

The numerical model can be used to investigate the effect of changing design parameters in the sensors without the long, costly process of redesigning, fabricating and testing every time. This multiphysics numerical model allows the prediction of the temperature distribution across the entire surface of the device, which will be altered with the inclusion of fluid flow over the top. Figure 3.4 shows the temperature distribution across the surface of chip Fl 01 where temperatures are illustrated through a colour palette as well as the z-axis.

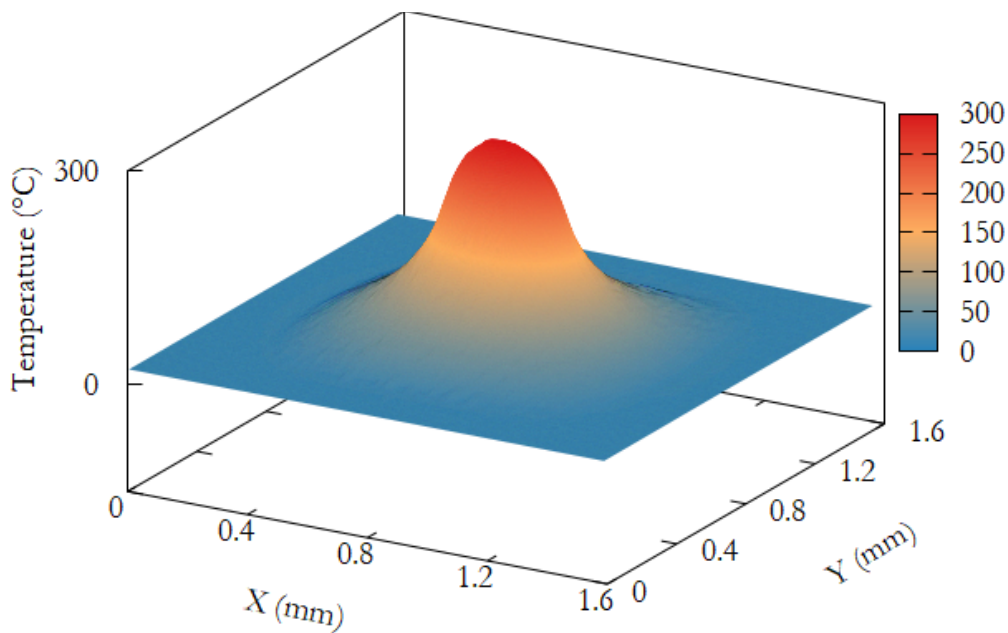


**Figure 3.4:** Temperature distribution across the membrane.

In order to display more clarity, Figures 3.5 and 3.6 display the temperature profiles seen from both sides, where the former shows a sharper peak due to the thin width of the heater as opposed to the latter which shows the temperature profile along the length of the heater.

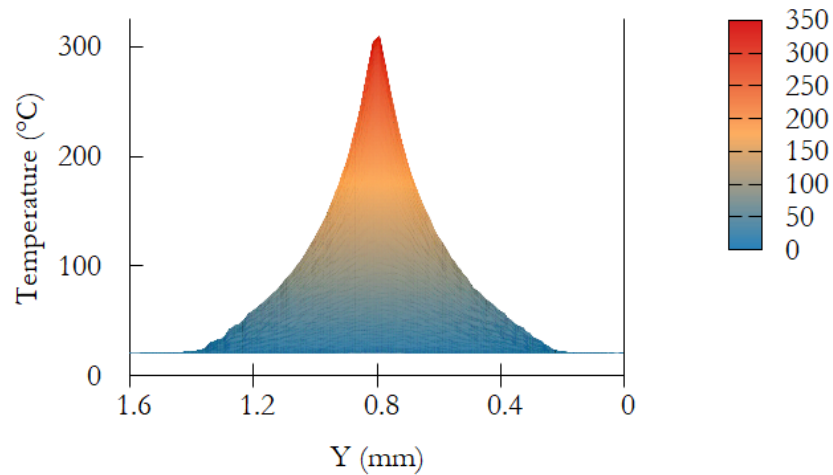


**Figure 3.5:** Temperature distribution across the membrane and heater, parallel to the direction of flow. This temperature distribution is for no flow and is therefore symmetric.

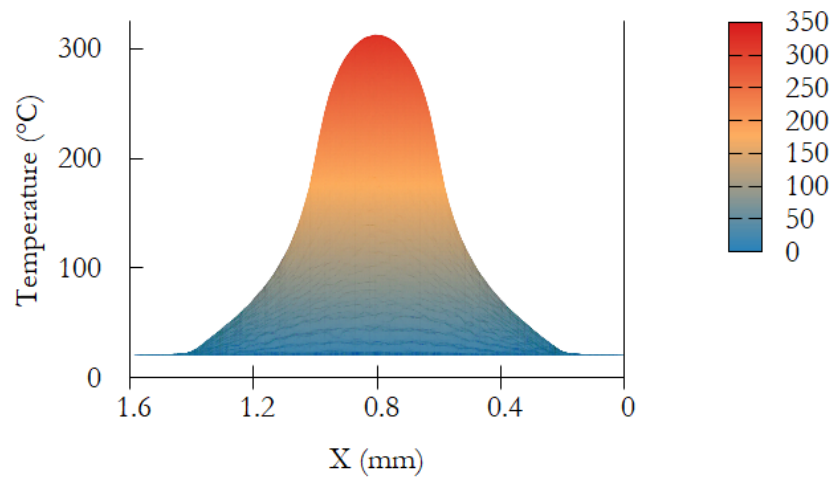


**Figure 3.6:** Temperature distribution along the heater, perpendicular to the direction of flow.

This numerical model allows in depth investigation into several parameters that affect the performance of the devices. The model is validated against experimental results in the discussion session of this chapter.

## 3.4 Experimental

In order to characterise the fabricated sensors between a temperature range of 25 °C and 300 °C, measurements were divided into two separate experiments. The first consisted of all the electro-thermal characterisation whilst the second pertained to all the flow measurements.

### 3.4.1 Electro-Thermal Characterisation

Initially, the two TCRs for the tungsten microheaters were determined between 25 °C and 300 °C. This was performed using a Cascade Microtech Summit 12000 probe station equipped with a hot chuck. A source meter (Keithley 2410) was used to bias simultaneously the heater with a constant current whilst measuring the resistance  $R_0$  at reference temperature  $T_0$ , in 2-wire and 4-wire configurations and the resistance at other higher temperatures  $T_S$ ,  $R_T$ . Knowing the heater current and resistance allows the temperature coefficients  $\alpha_T$  and  $\beta_T$  to be found, and in turn this allows resistance measurements to be converted into operating temperature measurements through  $R_H = R_0(1 + \alpha_T \times \Delta T + \beta_T \times \Delta T^2)$ , where  $\Delta T$  is the temperature difference between operating temperature  $T_S$  and reference temperature  $T_0$ . It should be noted that for reproducibility assessment purposes, chips were taken from different positions on the wafer (Central, North, South, West and East relative to wafer flat). In addition to this, the SMUs were used alongside the developed Labview software to measure the forward bias voltage output of the diodes in order to find their sensitivity to change in temperature. This was performed at the three different driving currents of 1  $\mu\text{A}$ , 10  $\mu\text{A}$  and 100  $\mu\text{A}$ .

### 3.4.2 Flow Characterisation

The dies were subsequently gold-wire bonded using a Kulicke and Soffa wedge bonder in-house onto commercially available dual in line (DIL8) packages. Figure 3.7 shows a picture of a packaged sensor. Using Si substrate and die attach, the sensor was raised to be flush with the surface of the DIL8 package. The surrounding cavities were then filled with a transparent liquid photopolymer and UV-cured. This resulted in a smooth, planar surface with the embedded chip, minimising flow disturbances that would alter the heat transfer.

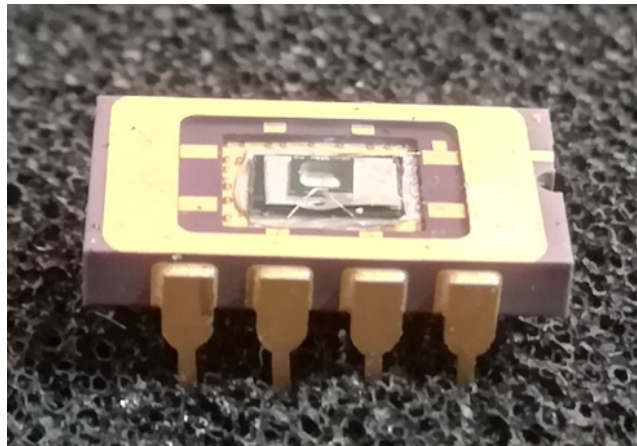
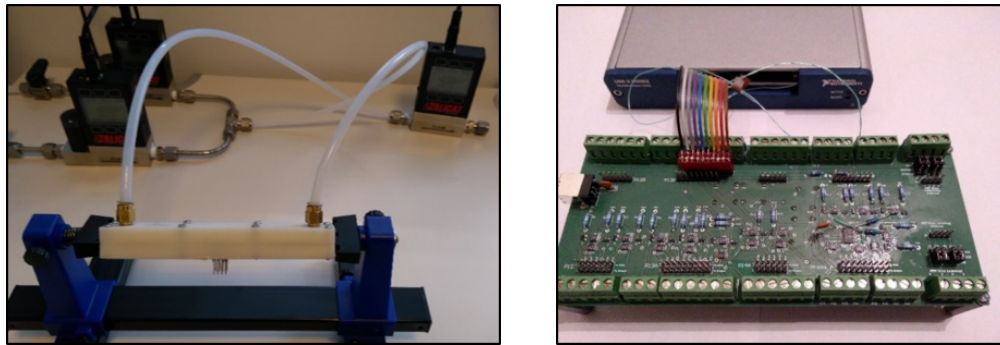


**Figure 3.7:** Photograph of a thermal flow sensor wedge bonded on a DIL8 package with the cavities full of a cured transparent photopolymer.

A picture of the experimental setup is shown in Figure 3.8 (a) where an Alicat mass flow controller (MFC [MC-5SLPM-D/5M]) with range 0-5 Standard Litres Per Minute (SLPM) was connected to a compressed gas cylinder containing synthetic clean air. Labview 2017 software (v17.0) was used to control the amount of gas flowing through the system and into the chamber. The custom designed chamber was 3D-printed via a formlabs Form 2 printer and comprises of two halves, which can be screwed together with an O-ring seal to ensure no leakages were present. The internal dimensions of the flow channel were  $2 \text{ mm} \times 2 \text{ mm} \times 120 \text{ mm}$ . This design also allowed the chips to be quickly and easily interchanged. A mass flow meter (MFM

[MC-5SLPM-D/5M]) was connected after the flow chamber and measured the received mass flow rate to ensure there were no leakages in the system. Figure 3.8 (b) shows the developed driving/readout PCB interfaced with a National Instruments DAQ [NI-USB-6343] and the Labview software for data logging. The flow and overall schematic for the flow characterisation system can be found in Figure 3.9.



(a) The MFC feeding the 3D printed “wind tunnel” followed by the MFM. (b) The read-out electronics and NI DAQ.

**Figure 3.8:** Pictures of the experimental setup.

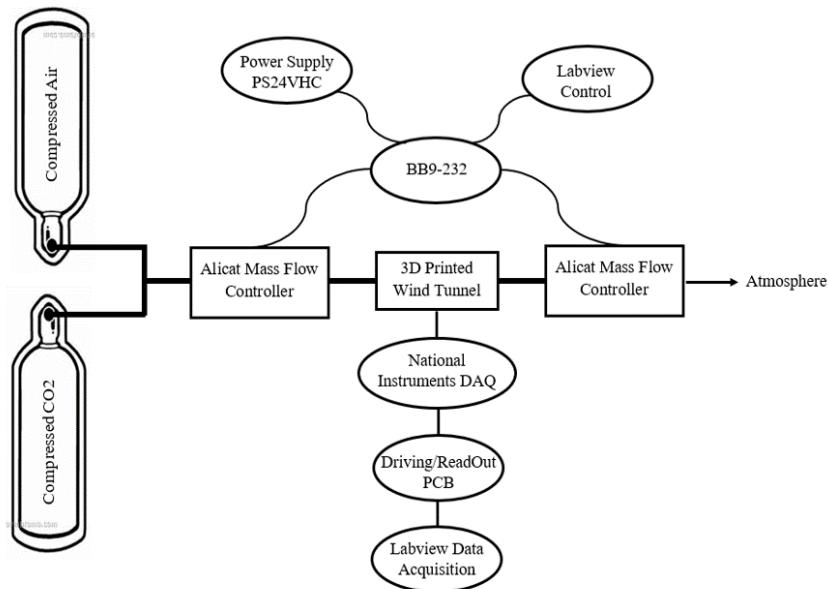


**Figure 3.9:** A block diagram representation of the experimental setup, for flow sensor measurements only the compressed air was used.

Both the 2-wire voltage across the resistor ( $V_{2w}$ ) and the 4-wire voltage across the resistor ( $V_{4w}$ ) were measured. Using the power – temperature curves

extracted from the electro thermal characterisation stage, the sensors were driven with a current corresponding to a heater temperature of 300 °C in stagnant air. Mass flow rate was measured from zero flow to 4 SLPM in steps of 0.5 SLPM. Each mass flow rate was run for 30 seconds before stepping to the next one whilst sampling the readout data at 100 Hz throughout. A 15 second period was allowed for the flow to stabilise in the channel. A 10 second sampling period was taken to calculate the mean and standard deviation for each flow rate. Whilst the heating element was biased with a current matching the operating temperature of 300 °C, a second SMU was used to bias the thermodiodes with 1  $\mu$ A, 10  $\mu$ A and  $\mu$ A and measure their change in voltage with the evolution of flow.

## **3.5 Optimisation of CMOS MEMS Flow Sensors**

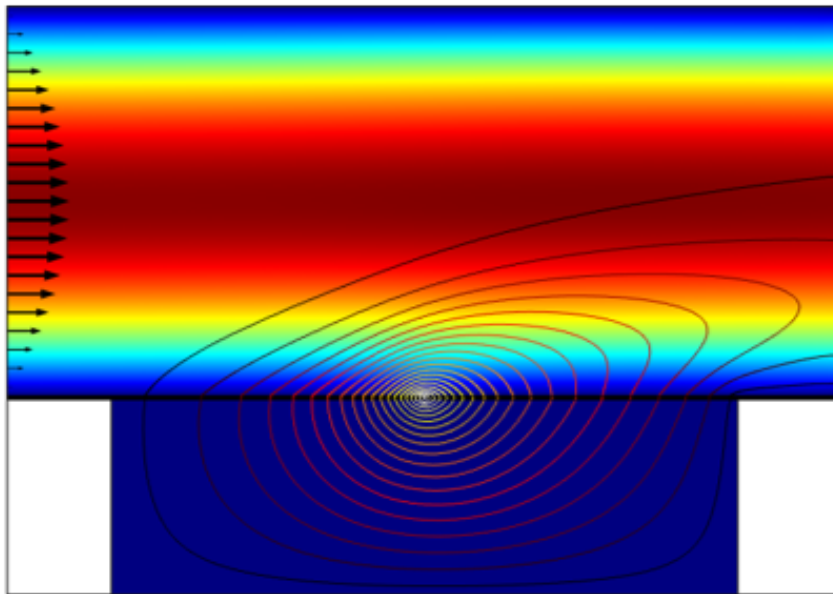
In this section, various methods will be used to optimise the performance of the CMOS thermal flow sensor. Several designs have been commercially fabricated to investigate the effect of geometric tolerances including heating element shape, location, membrane shape and diode design. The common SOI-CMOS process also allows a direct comparison between thermo-resistive and thermo-electronic transduction methods. In addition to this, numerical modelling is used to deepen the physical understanding and to optimise the location of measurement when the sensor is being run in a calorimetric method.

### **3.5.1 2-D vs 3-D Numerical Modelling**

A numerical model must be validated against experimental data before it can be trusted and used for further analysis. In this section, the numerical model

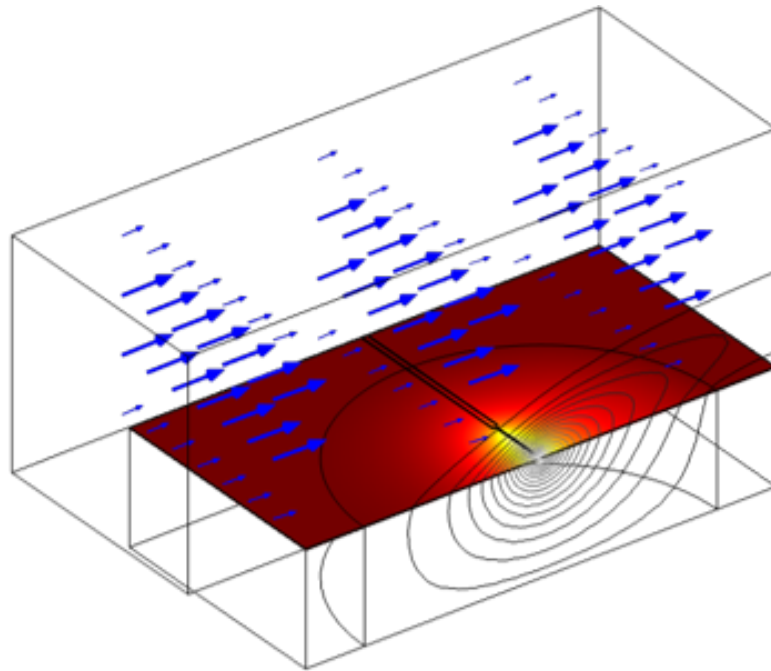
is compared with experimental data using chip F1 01 in order to ensure the physical phenomena are being accurately portrayed. In addition to this, both 2-D and 3-D numerical models are used and compared with regards to accuracy and computational requirements.

Figure 3.10 shows the 2D model created, located at the X-X slice shown in Figure 3.2. The model contains a section underneath the membrane with stagnant air where conduction and natural convection equations are solved. Over the sensor is another region of air that represents the channel. In this region conduction, natural and forced convection equations are solved. All this is coupled with the Joule heating generated within the membrane heater, where conduction equations are also solved. Figure 3.11 shows the full 3D model of the sensor. Similarly to the 2D model, underneath the circular membrane is a volume of stagnant air and above it an air channel. The two lateral channel walls were defined as outflow and so do not exhibit the no-slip condition.



**Figure 3.10:** A snapshot 2D simulation result with air flowing above the sensor. A thermal contour plot as well as velocity colour mapping are presented along with arrows indicating the flow velocity profile. The colour map goes from highest velocity at red to zero velocity at dark blue.





**Figure 3.11:** A snapshot 3D simulation result with air flowing above the sensor. A thermal contour plot as well as surface temperature distributions are presented along with arrows indicating the flow velocity profile.

Firstly, it is paramount that the biasing current and power dissipation correlate accurately to the temperature change of the heater. Figure 3.12 shows the temperature output of the heater with respect to the applied power. The 3D simulation accurately matches the experimental data ( $<1\%$ ), leading to the conclusion that this simulation is accurately depicting Joule Heating. Whilst showing the same trend, the 2D simulation is predicting temperatures greater than are seen experimentally, with a sensitivity error of  $16\%$  ( $3.4\text{ }^{\circ}\text{C}/\text{mW}$ ). This over-estimation of the heater temperature can be explained by some of the simplifications in the geometry. Most significantly, the 2D geometry does not incorporate the length of the tungsten heater and the tungsten tracks leading to the membrane edge. This cannot be neglected because there is a large amount of heat transfer via conduction transporting heat away from the heater through this metal track and hence reducing the temperature. In addition to this, the 2D simulation only considers the thermal resistances along x and y directions, meaning the heat dissipation in the z-direction through conduction

and convection is being neglected. In opposition to this, the 2D simulation is unable to model the membrane as circular, but instead assumes a square membrane which results in larger thermal resistance. However, this factor has less effect in comparison with the previous points.

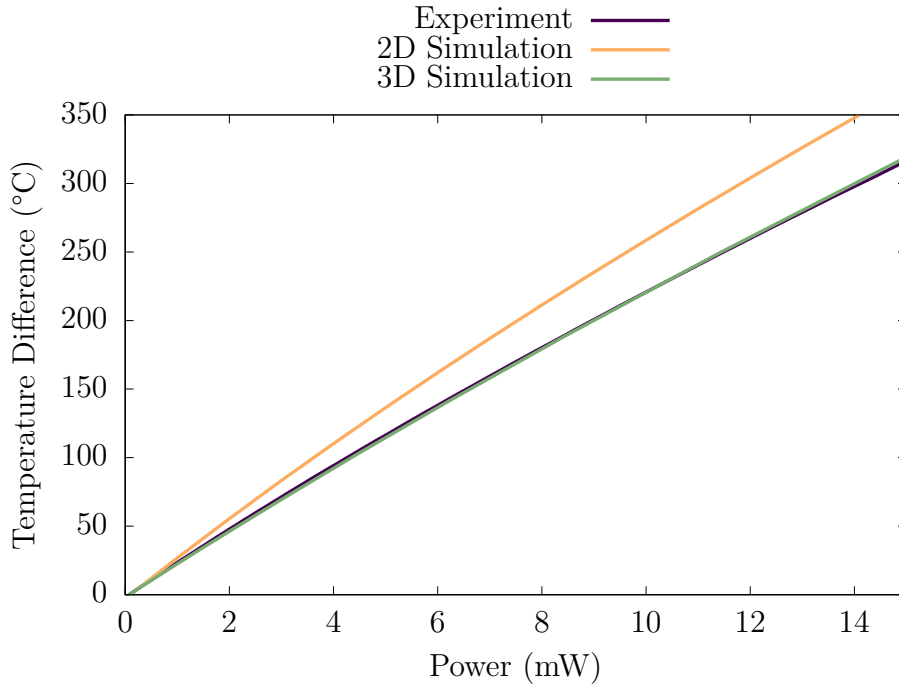


**Figure 3.12:** Temperature reached by the heater for specified power input.

Knowing that a 2D simulation over-estimates heater temperature, this temperature will henceforth be matched to the experimental value to compensate for the 2D inaccuracy and provide a valid comparison to the 3D model in terms of on-membrane temperature profile distribution. Figure 3.13 shows the temperature profile parallel to the direction of flow for stagnant conditions ( $\tau_w = 0$  Pa) and laminar flow ( $\tau_w = 1$  Pa). Again, the 3D simulation accurately matches the experimental data with all errors being under 5% which validates that the multi-physics coupling between the heating of the resistor and the heat transfer through the remaining structure is valid. The addition of forced convection via moving air was validated by measuring temperatures for a wall shear stress up to 1 Pa, again with errors all below 5%, proving that the 3D simulation accurately models and couples all three physics throughout the

geometric domain. After temperature compensation, the 2D simulation does not display the same temperature profile, with a general over-estimation of the temperature at any point. This behaviour can be explained by the incorrectly assumed thermal resistance in the  $z$ - direction. With increasing distance from the heater, the 2D simulation increases its over-estimation due to the omission of the extra dimension for heat dissipation to take place. This error reaches a maximum (30%) at the mid-point and then starts to reduce because here the effect of the substrate comes into significance. With the introduction of flow, the same temperature over-estimation can be seen but is less due to the relative importance of forced convective heat transfer reducing the membrane conduction error. Once the substrate is reached, the conduction through the bulk solid is large and the temperature is quickly reduced to ambient.

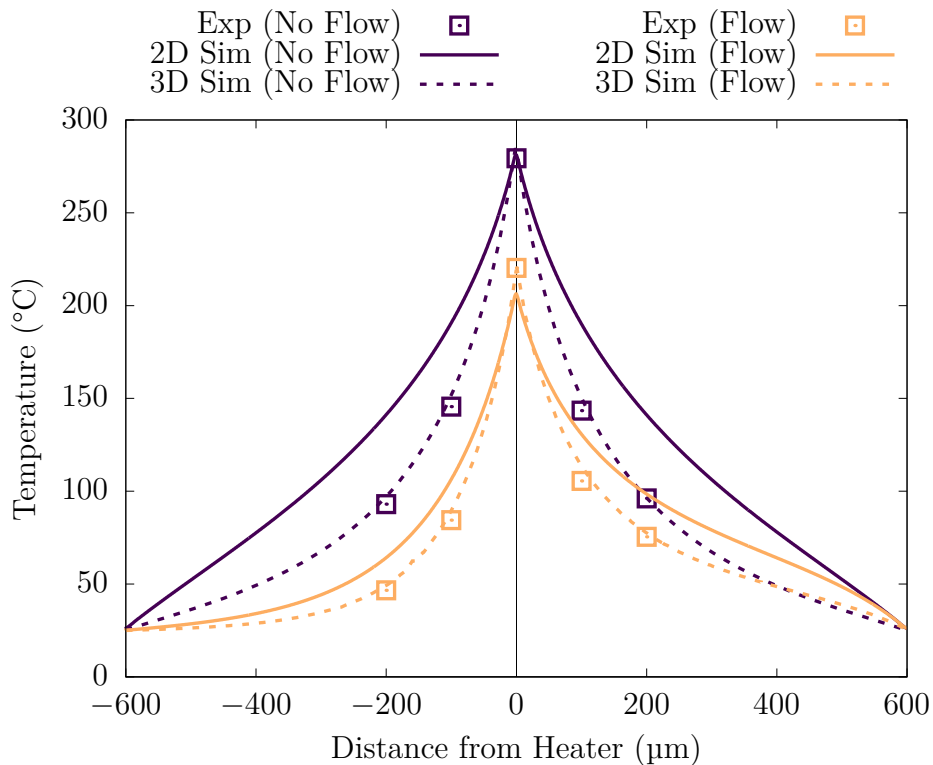


**Figure 3.13:** Temperature profile along the line X-X from Figure 3.2 for no flow ( $\tau_w = 0$  Pa) and flow ( $\tau_w = 1$  Pa). Heater location is set at zero with each direction extended to the edge of the membrane, temperature after this (through the substrate) is negligibly close to ambient.

There are two commonly used methods for thermally measuring the flow:

- i. **The Anemometric Approach** – which correlates the temperature difference of the central heater to the incoming flow with respect to the stagnant flow condition (Figure 3.13).
- ii. **The Calorimetric Approach** – which correlates the temperature difference between two symmetrically situated locations upstream and downstream of the central heater to the incoming flow with respect to the stagnant flow condition (Figure 3.15).

Despite the 3D simulation more closely mapping the on-membrane temperature profile, both 2D and 3D simulations are accurate to within 10% in predicting the anemometric temperature difference and interestingly, both simulations illustrate the trend produced when increasing wall shear stress. For the calorimetric approach, the over-estimation of temperature is again present in the 2D simulation. However, it again correctly portrays the trend of increasing wall shear stress, with an initial sharp rise in temperature followed by a gradual decrease in sensitivity. This leads to the conclusion that although 2D is not as numerically accurate as 3D, it provides sound qualitative results for the behaviour of devices. Finally, the 2D simulations took less than 2% of the time required by 3D leading to a trade-off between time and numerical accuracy. If detailed quantitative data is essential, 3D simulations must be used, however in order to attain general device behaviour, 2D simulations are adequate and extremely time efficient.

In conclusion, this section has provided the knowledge that the developed 3D numerical model can accurately portray temperature profile across the membrane with the addition of varying flow rates. This numerical model will be used throughout the remainder of the chapter in order to further investigate the designs and to help with the optimisation process.

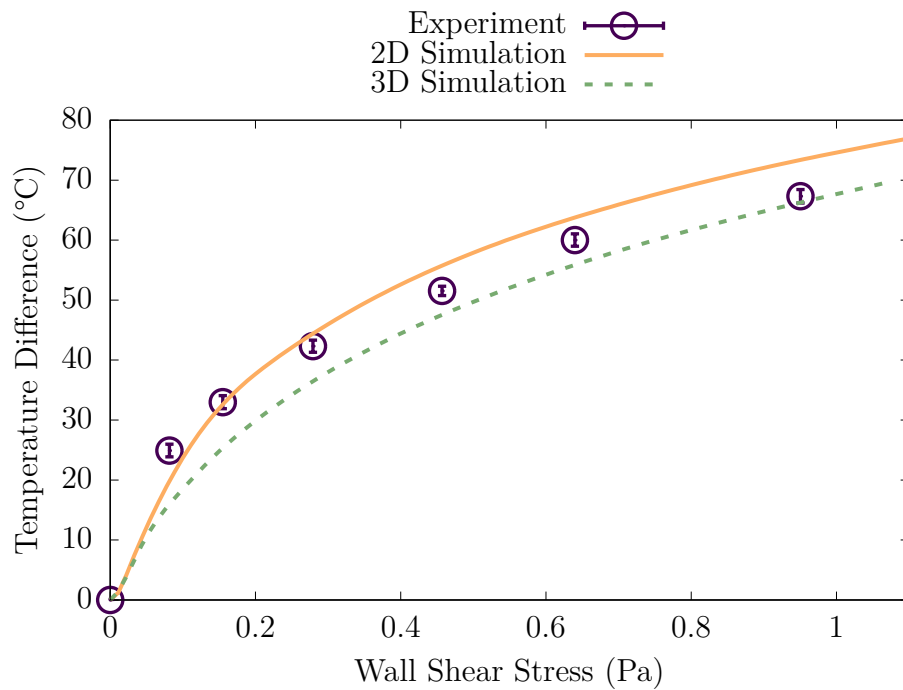


**Figure 3.14:** Temperature difference output as a function of wall shear stress for anemometric approach. Voltage standard deviation measurements are converted to temperature and added to the experimental plot.

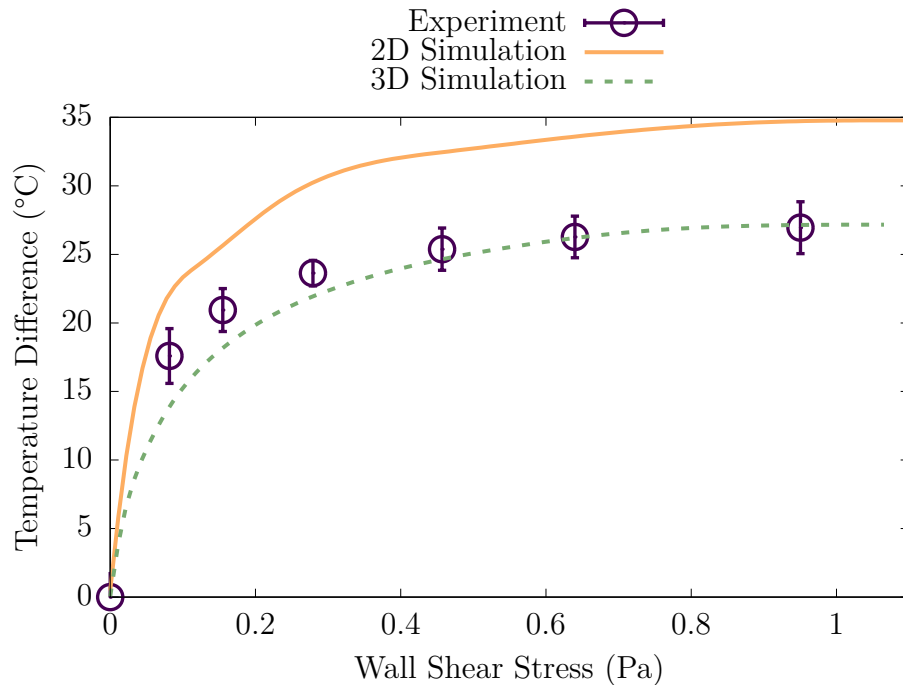


**Figure 3.15:** Temperature difference output as a function of wall shear stress for calorimetric approach at 400  $\mu\text{m}$  either side of the heater.

### 3.5.2 Calorimetric Flow Sensor Optimisation

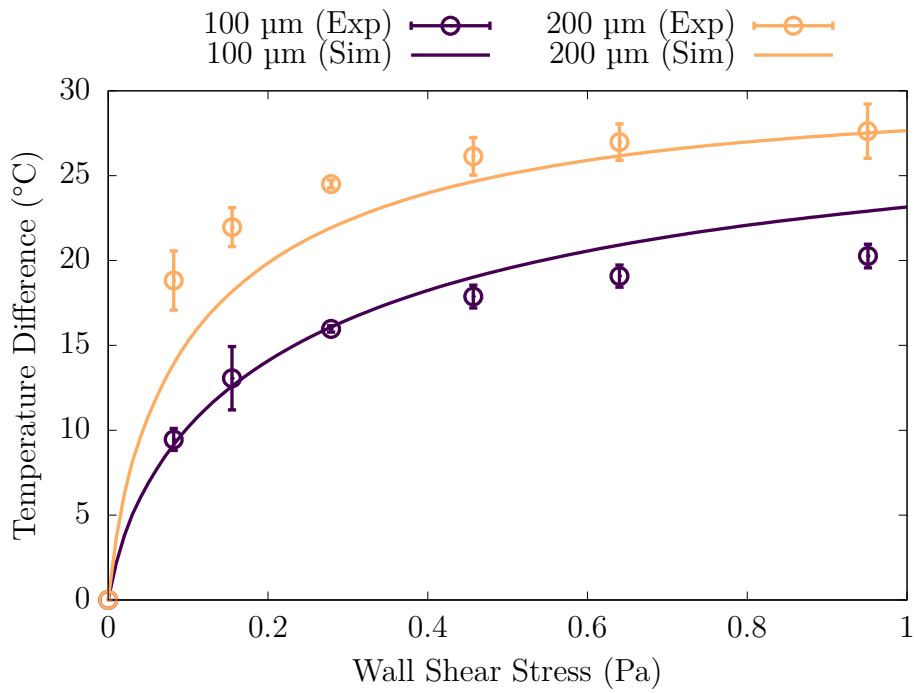
In the calorimetric method, the temperature difference between the upstream and downstream diodes is measured and correlated to the flow conditions. In calorimetric flow sensors the location of the diodes must be optimised for the highest possible sensitivity.

Figure 3.16 shows that leaving a larger gap between the sensing diode and the heater results in a sharper temperature increase for low flow rates (low shear stress), but the sensitivity saturates earlier. This leads to the conclusion that the optimum distance is dependent on the flow velocities being measured. Figure 3.17 shows how the temperature difference varies as the diode becomes further from the heater. For each flow rate there is an optimum distance where the temperature difference is the largest, hence leading to the highest sensitivity. However this distance becomes larger as the flow rate decreases. Therefore the optimised distance of sensing elements can be selected based on the desired range of flows. A constant heater length of 200  $\mu\text{m}$  and heater width of 2  $\mu\text{m}$  were used.

Another important geometrical parameter determining the performance of the sensor is the ratio between the membrane and heater size. Firstly, it is important to minimise the power dissipation into the substrate below. Assuming that the heated area around the hot-film and the membrane are circular and have radii of  $r_1$  and  $r_2$  respectively, the thermal resistance,  $R_{th}$ , can be defined as:

$$R_{th} = \int_{r_1}^{r_2} \frac{1}{k(2\pi r t)} dr = \frac{1}{k(2\pi t)} \ln \left[ \frac{r_2}{r_1} \right] \quad (3.14)$$

where  $t$  is the thickness of the membrane. If it is also assumed that the temperature at the edge of the membrane is ambient, i.e.  $T(r_2) = T_0$ , and



**Figure 3.16:** The evolution of temperature difference against wall shear stress for the calorimetric method at the two distances of 100  $\mu\text{m}$  and 200  $\mu\text{m}$  from the central heater.

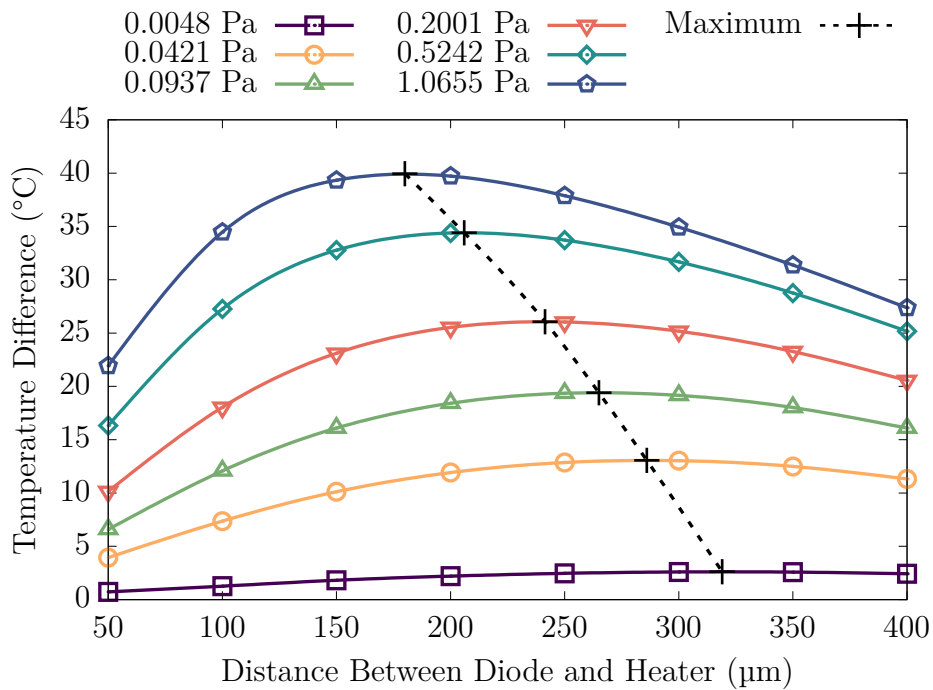


**Figure 3.17:** Temperature output as a function of diode distance from central heater for varying wall shear stress, the dotted line bisects each flow rate at its point of highest sensitivity.

that  $T(r_1)$  equals the temperature of the sensor,  $T_s$ , then the conduction power dissipation through the membrane can be expressed as:

$$P_c = \frac{2\pi kt}{\ln(r_2/r_1)}(T_s - T_0) \quad (3.15)$$

This shows that power loss from the membrane into the substrate depends on membrane thickness and the ratio of  $r_2/r_1$ . Membrane thickness cannot be altered because it is limited by the foundry fabrication process and must maintain mechanical robustness. Simultaneously to reducing power dissipation into the substrate, it is important to maximise the sensitivity. It is undesirable to increase the diameter of the membrane due to this causing increased fragility and cost. The effect of different ratios can be altered by changing the length of the heater. All simulations were run at a constant power of 11.7 mW and constant membrane diameter of 1.2 mm.

The first observation is that shorter heaters produce larger temperature differences; due to the fact the current density must increase in order to exhibit identical power. Figure 3.18 shows the optimum location for temperature measurement at each wall shear stress for the different heater lengths. At low wall shear stresses the heater length can be considered negligible. However, when the wall shear stresses are significantly high, using a longer heater provides an optimum temperature measurement location that varies less dramatically, leading to the conclusion that longer heater lengths would be more suitable in situations where a wide range of flow rates need to be measured. The selection of heater length then becomes a compromise and must be chosen specific to application.

Unlike heater length, heater width had negligible effect on the optimum temperature measurement location meaning it should be kept as thin as possible to allow the maximum achievable temperature without exceeding the current



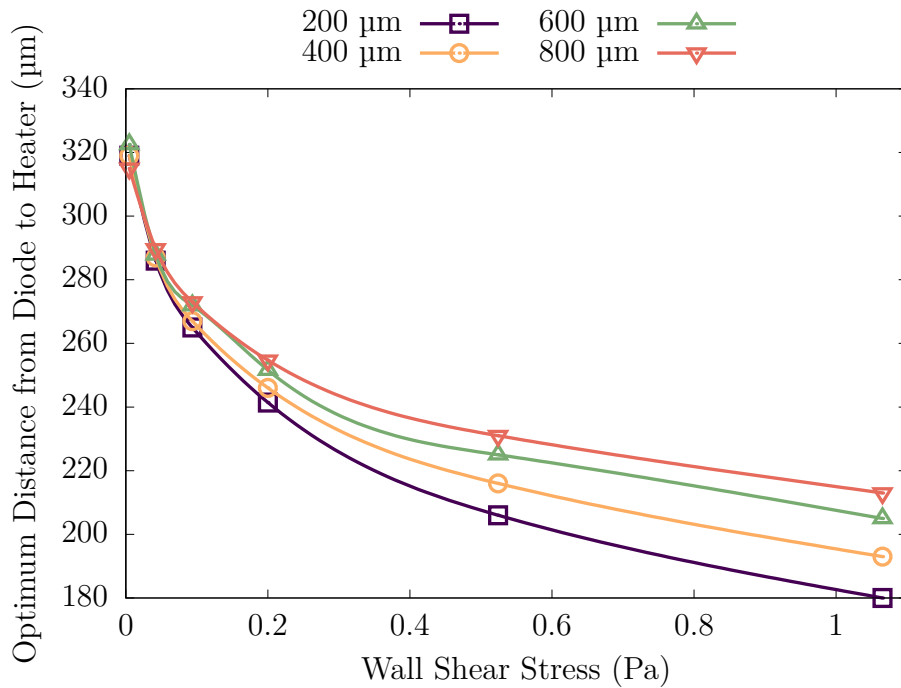


**Figure 3.18:** Optimum diode distance for varying wall shear stress at 4 different heater lengths where the legend refers to the heater length.

density limit. In fact, simulations in stagnant flow (Figure 3.19) showed a significant difference in the shape of heated zone within the membrane (more circular for shorter heaters). The important conclusion is that the most important factor in deciding the separation distance of the temperature measurement transduction to the heater is the shape of the membrane temperature profile produced by the heater.

### 3.5.3 Anemometric Flow Sensor Optimisation

Four geometric parameters have been isolated in order to investigate their individual effect. These include membrane length (where the membrane to heater ratio is held constant),  $M_L$ , heater length,  $H_L$ , heater width,  $H_W$ , and finally membrane shape where Sq. w/ RC stands for square with rounded corners.

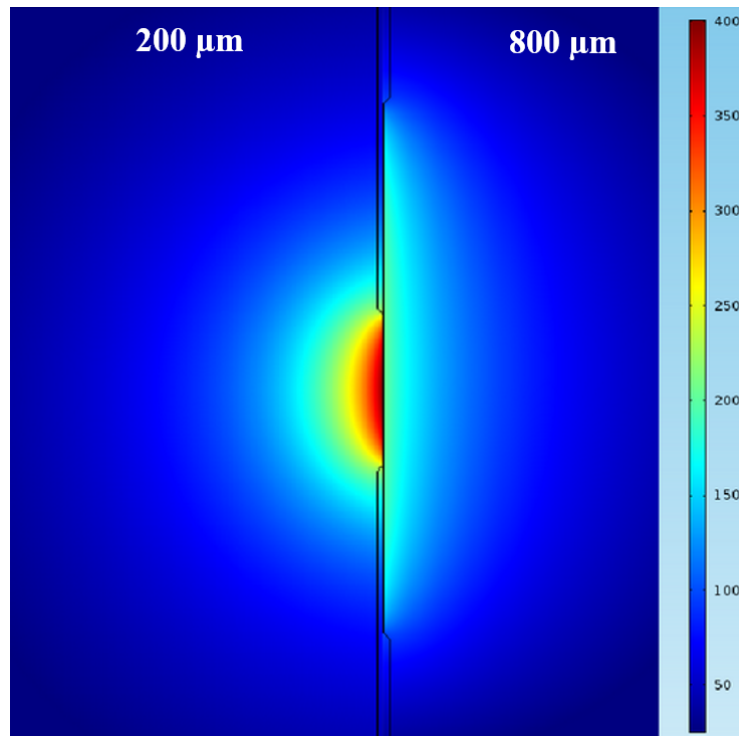


**Figure 3.19:** Thermal colour plot of numerical simulation showing the difference in heated region shape for heater lengths 200  $\mu\text{m}$  (left) and 800  $\mu\text{m}$  (right). The temperature legend is in degrees Celsius and applies to both sides of the figure.

Firstly, as stated in §3.4.1, the electro-thermal characterisation was used to calculate TCRs  $\alpha_T$  and  $\beta_T$  for each of the sensors. Using this and the results from the current sweep, the relationship between power input and temperature can be established for each device. Table 3.5 displays the slope of the power-temperature plot (which pertains to electrothermal efficiency) for every device and the standard deviation of this slope for the 5 devices measured for each geometry. The first conclusion to be made is that the largest effect comes from changing the length of the resistor, with the shortest resistor (Fl 05) having the best efficiency and the longest resistor (Fl 06) having the worst. Relating to this, it is better to keep the heater length to membrane ratio smaller due to the fact there is a larger relative electro-thermal efficiency when the membrane is kept at its maximum size. This correlates with the theory that having a large cavity beneath the membrane reduces the conduction through the substrate. However, there is a significant advantage to minimising the

membrane area, which reduces the overall size of the sensor whilst still attaining increased electro-thermal efficiency. Interestingly, varying the width of the resistor has a very small effect on the electro-thermal efficiency whilst using a square membrane with rounded edges increases this efficiency by approximately 3 %.

**Table 3.5:** Electrothermal efficiency of the different designs flow sensor designs driven in anemometric mode.

Chip ID	Average (°C/mW)	Standard Deviation (%)
<b>F1 02</b>	23.77	0.63
<b>F1 03</b>	28.83	0.25
<b>F1 04</b>	33.37	0.59
<b>F1 05</b>	37.50	1.58
<b>F1 06</b>	13.90	2.48
<b>F1 07</b>	24.06	0.96
<b>F1 08</b>	24.47	4.42
<b>F1 09</b>	23.14	0.74

Figure 3.20 shows the evolution of voltage drop with increasing flow rate for the 2-wire measurement configurations. These data provide the relative sensitivities of the different designs and allows a comparison between them. Next in the geometrical alterations is reducing the heater length whilst keeping its ratio with the membrane size the same. This clearly causes a reduction in the sensitivity that can be associated with the reduced size giving less resistor area exposed to the flow - so with the same flow rate less heat is being dissipated via forced convection. This theory agrees with the trend seen when altering the heater length (whilst keeping the membrane constant). The highest sensitivity can be seen from the geometry with the longest resistor (F1 06) where the voltage drop is almost double that of the reference sensor. This is seen in opposition with F1 05 where there is a much smaller voltage drop.

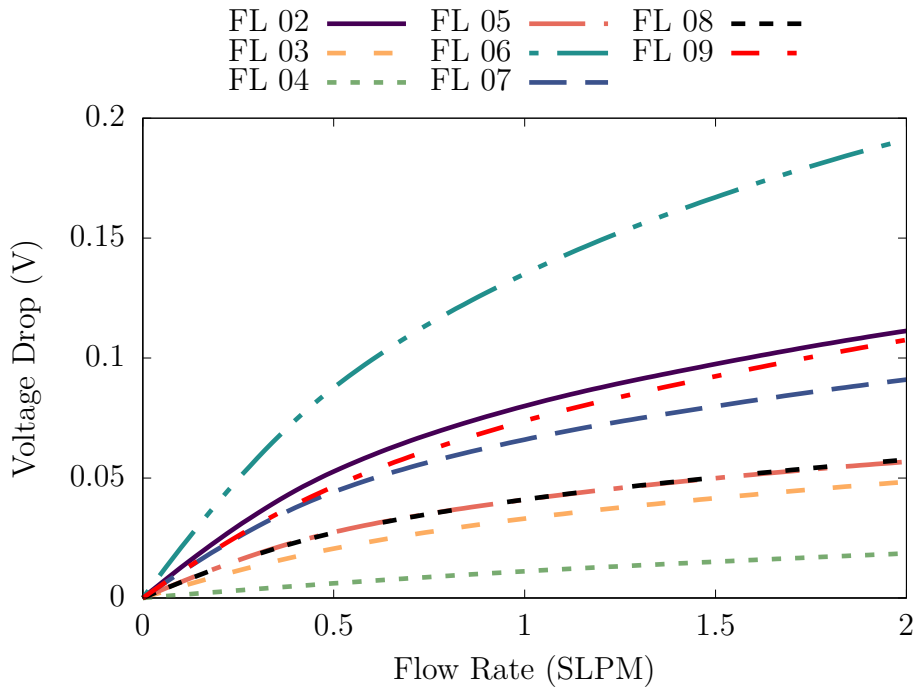


**Figure 3.20:** Experimental voltage drop change measured across the resistor in 2-wire configuration.

Interestingly, despite having a larger surface area exposed to the flow, increasing the width of the resistor reduces the change in voltage for increasing flow rate. A thermal boundary layer starts growing at the front edge of the sensor element. Thus, the rear end of the sensor is exposed to a higher flow temperature and stays at a more constant temperature for different flow rates. This was corroborated by the  $\Delta T$  measured across the resistor width in the numerical simulation. The  $\Delta T$  measured across FL 08 was 2 times larger than that of FL 02 (with the higher temperature being at the trailing edge). This proves that the resistor width is not negligibly small, and a thermal boundary layer exists.

Consequently, increasing length is the most effective method for increasing sensitivity, although this is coupled with the major drawback of lower electrothermal efficiency. In summary, decreasing the resistor length increases electrothermal efficiency because of less power is required to reach the same temperature. This decrease also yields lower sensitivity due to less area perpen-

dicularly exposed to the flow for heat transfer to occur. When the membrane is scaled with the resistor, the change in electrothermal efficiency is due to the resistor becoming less thermally isolated. Resistor width has minimal effect on electrothermal efficiency and should be kept thin for maximum sensitivity. Within this combination of parameters lies an optimum specific to the designer's choice.

However, of great importance is the accuracy (defined as the ratio between sensitivity and noise), meaning the low sensitivity designs should not yet be discarded. A standard deviation,  $\sigma$ , was calculated from the measured voltage data for both measurement configurations. This standard deviation was added to and subtracted from the mean measurement (i.e.  $2\sigma$  accuracy) and then converted into a flow rate using a 4th order polynomial for accurate interpolation. This results in an absolute error/accuracy in SLPM for each flow rate which was then converted into a % accuracy of each flow rate to indicate its performance compared with the exact flow regime it is measuring. This is known as % reading (% RD) and the values against flow rate for 2-wire measurement configuration can be seen in Figure 3.21.

Chips Fl 02, Fl 05, Fl 06 and Fl 07 have the same membrane diameter of 1200  $\mu\text{m}$  with only the heater geometry ( $H_L$  and  $H_W$ ) changing. It can be concluded from this that in our experimental setup, altering the resistor geometry does not significantly affect the accuracy of the sensor, most likely because the difference is negligible compared to the primary source of noise already seen in the experiment.

There are three different forms of noise that can be found in this system: thermal noise/Johnson-Nyquist noise from the resistor, noise produced by the read-out electronics and noise induced from the gas flow. Electronic and flow noise can be assumed constant across all the sensors because the same read-out electronics (i.e. gain-bandwidth) and flow chamber was used, therefore meaning

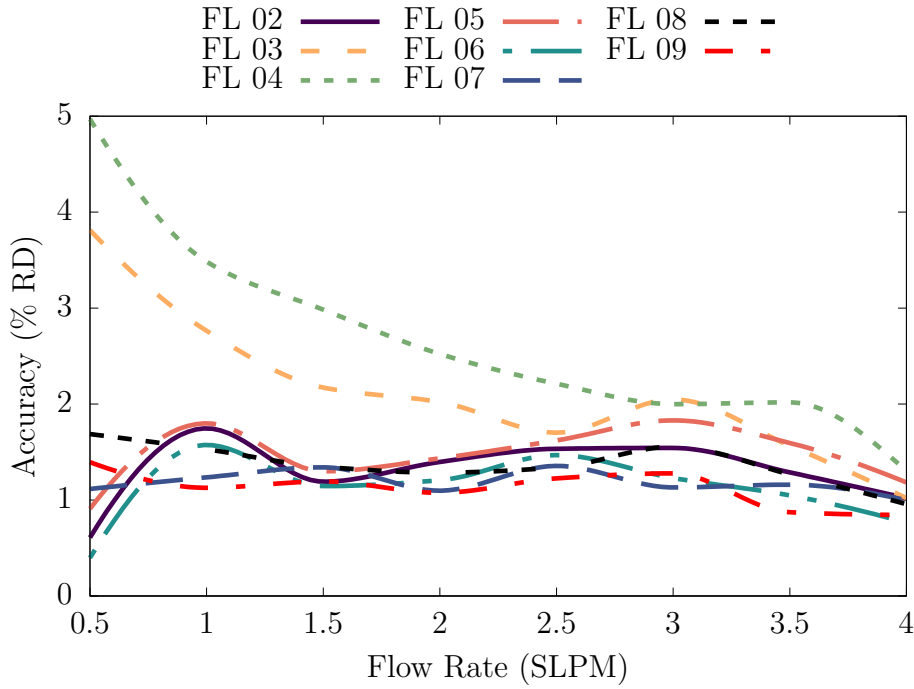


**Figure 3.21:** Percentage accuracy of the flow rate reading measured in 2-wire configuration for all the sensors with varying resistor geometries.

the varying accuracy seen in chips Fl 03 and Fl 04 must be related to the thermal Johnson voltage noise,  $E_V$  (V RMS), which is defined by:

$$E_v = \sqrt{4BR_t k_B T} \quad (3.16)$$

where  $k_B$  is the Boltzmann constant and  $B$  is the bandwidth in Hz. As is stated by Issa and Lang [139], minimum detectable flow is relative to the noise through the system and in the case of zero flow, the resistor noise comprises of the thermal Johnson voltage noise combined with the noise produced from natural convection. For Issa and Lang, the noise from natural convection was negligible due to the sensor being run at room temperature, however this is not the case in this study with the resistor being run at 300 °C where temperature fluctuations in the surrounding atmosphere will be much larger.

The ratio of the Grashof number against the Reynolds number squared ( $Gr/Re^2$ ) is known as the Richardson number ( $Ri$ ), which describes the relative

importance of buoyancy to convection in a flow:

$$Ri = \frac{gL_C\beta_v\Delta T}{V^2} \quad (3.17)$$

where  $\beta_V$  is the volumetric expansion coefficient and  $L_C$  is the characteristic length, further defined in the bidimensional case as the length of the heated area.

In Figure 3.21 it can be seen that chips Fl 03 and Fl 04 (which have small heaters and small membranes) have a worse accuracy at low flow rates. This result contradicts the Richardson equation that suggests that a larger heating area would increase natural convection and create more noise. However for Fl 05, with a small resistor and large membrane, the initial accuracy is not worse which leads to the conclusion that accuracy does not decrease with resistor size but with reduction in membrane size and therefore the Richardson number cannot be used to estimate the contribution of natural convection to the noise. This is because the Richardson number describes the global magnitude of natural convection in a system and does not describe the temperature gradients driving higher local velocity fluctuations. The on-membrane temperature reaches ambient at the edges of the membrane, i.e. when the substrate is reached. Therefore, reducing the size of the membrane increases the temperature gradient, resulting in stronger natural convection eddies in the vicinity of the resistor surface.

Using the COMSOL Multiphysics numerical model previously described, Figure 3.22 shows the natural convection present above Fl 02 (top), Fl 04 (middle) and Fl 05 (bottom). It is clear from these results that Fl 04 creates stronger local recirculation above the heated resistor, despite the system total natural convection being lower. This effect can be decoupled from resistor length by observing that the natural convection currents produced by Fl 05 are very similar to Fl 02, despite Fl 05 having a very small resistor length. This

result verifies numerically the previous hypothesis, which relates the accuracy seen at very low flow rates to the temperature gradient in the immediate vicinity of the measuring resistor.

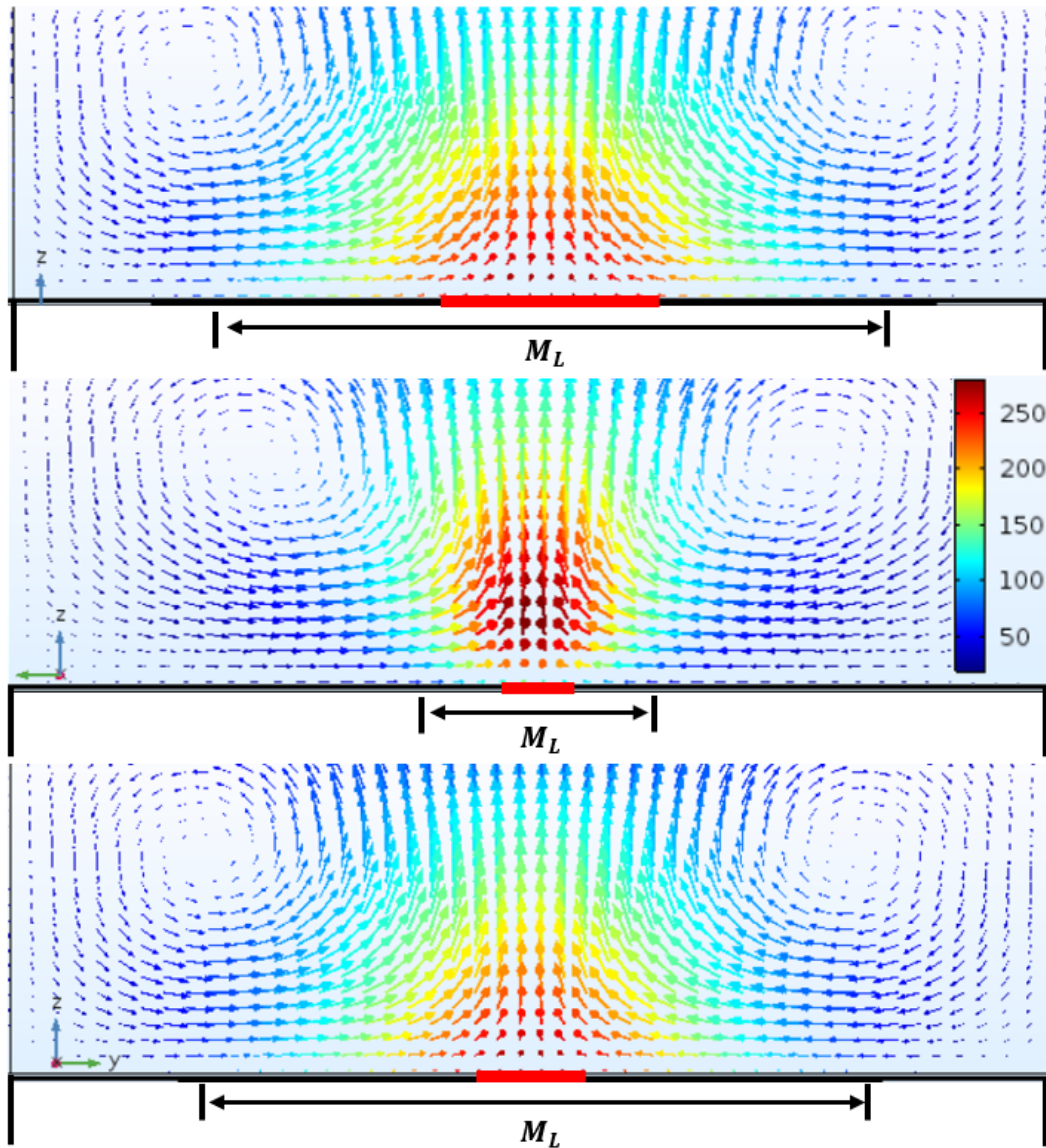


**Figure 3.22:** Direction and proportional magnitude of air velocity in stagnant flow for (top) F1 02, (middle) F1 04 and (bottom) F1 05. The red segment schematically represents position and length of the heating element. The scale bar legend is in degrees Celsius and applies to all three scenarios.



### 3.5.4 Thermo-Diode Temperature Sensing

This section reports the use of a thermo-diode for temperature transduction. The thermo-diode and resistor are both embedded in the membrane allowing, for the first time, a simultaneous comparison between thermo-resistive and thermo-electronic MEMS flow sensors. The resistor and membrane size are varied in three designs and diode length in another two designs. This should give an accurate comparison between the two methods and will eventually lead to the definition of technology curves considering not only trade-offs between the usual flow sensor metrics (power, accuracy, size, range, etc.) but also transducing methods. The accuracies seen in this technology are comparable and often superior to off-the-shelf products.

From the electro-thermal characterisation, the forward bias voltages as a function of temperature can be found in Figure 3.23 for three different biasing current (1  $\mu\text{A}$ , 10  $\mu\text{A}$  and 100  $\mu\text{A}$ ), showing that the longer diode possesses a greater sensitivity of  $-1.7 \text{ mV}/^\circ\text{C}$  as opposed to  $-1.5 \text{ mV}/^\circ\text{C}$  (for 100  $\mu\text{A}$ ) despite producing a lower absolute signal. It is also noted that the short diode suffers from a non-linearity when biased at 1  $\mu\text{A}$  and 10  $\mu\text{A}$ , which is not seen at the higher biasing current. This phenomenon can be ascribed to current leakage from the edge of the diode, which becomes negligible when compared to a large diode length or higher biasing current.

The forward bias voltage drop in Figure 3.24 shows a higher sensitivity with flow rate for the long diode. This opposes previous hypotheses that suggest the short diode would have a higher sensitivity due to it measuring a higher average temperature. It is well known that the diode forward voltage decreases linearly with temperature, where the voltage drop across an ideal p-n junction is:

$$V = \frac{k_B T}{q_e} \ln \left( \frac{I_d}{I_s(T)} + 1 \right) \quad (3.18)$$

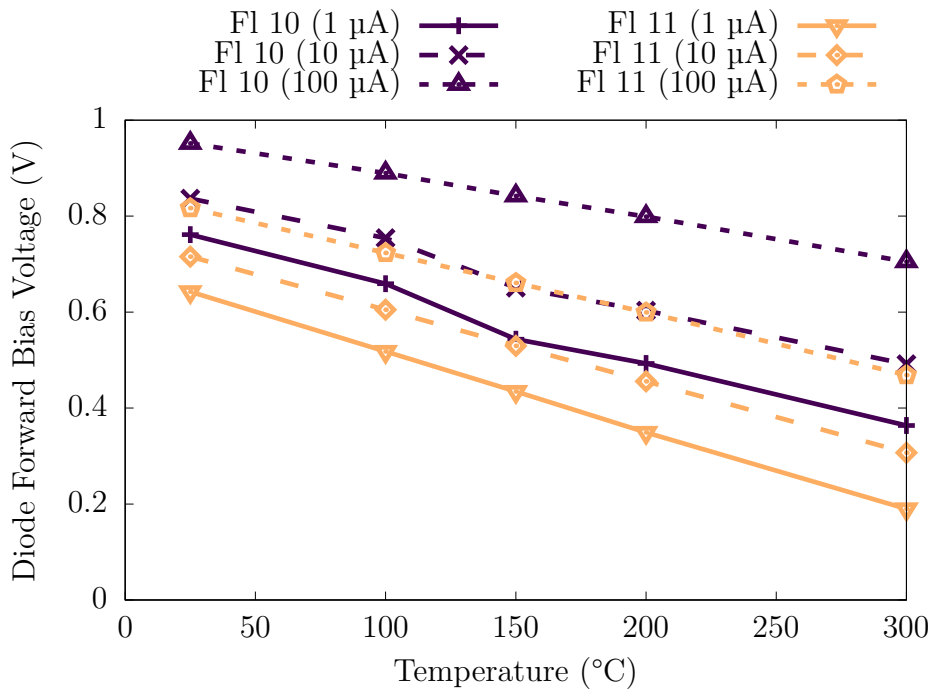


**Figure 3.23:** Experimental forward bias voltage against temperature for the long (Fl 11) and short (Fl 12) diode at three different driving currents (1  $\mu\text{A}$ , 10  $\mu\text{A}$  and 100  $\mu\text{A}$ ).

Here,  $k_B$  is the Boltzmann constant,  $T$  is temperature,  $q_e$  is electron charge,  $I_d$  is the diode biasing current and  $I_s$  is the saturation current. From Figure 3.23, it is clear that the average temperature measured by the diodes produces a higher absolute voltage, but the sensitivity of this voltage depends also on the length of the diode measuring the heated element. This then also transfers to a higher sensitivity with flow rate. However, when the sensitivity is taken as part of an overall sensor accuracy, the accuracy is approximately 30 % better for the short diode (1.1 % RD on average as opposed to 1.6 % for the long diode). This can be ascribed to the higher temperature being measured in the short diode, resulting in the produced noise being less significant in the overall reading.

Using device Fl 02, Fl 03 and Fl 04, the thermo-diode can be directly compared to the resistor whilst the membrane size is changing. Interestingly, as the membrane and resistor decrease in size, the diode has a higher relative

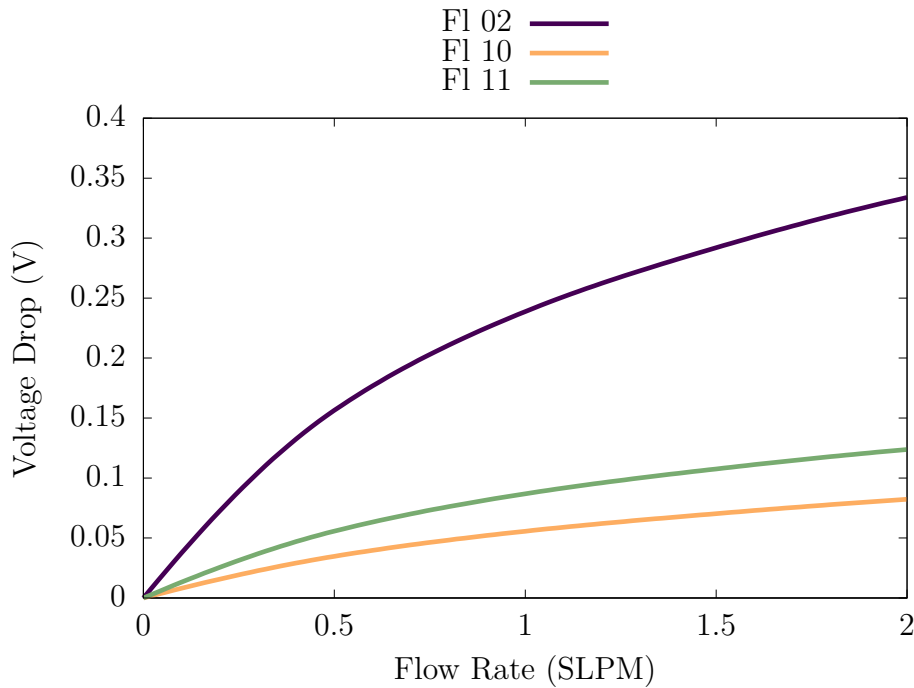


**Figure 3.24:** Experimental voltage drop change measured across the diode for small and large designs. The original design of 5 short diodes in series is also shown as a reference.

sensitivity. This can also be seen in the accuracy of the device where the accuracy becomes worse for decreasing membrane/resistor size only for the heating resistor (Figure 3.25). With this geometrical decrease the diode accuracy remains constant. This can be explained by the length of the sensing element. With the decreasing of heating element length, the length of resistor exposed to perpendicular flow is reduced. It was shown in the previous section that the amount of heater perpendicularly exposed to the flow plays a much more significant role than in the parallel plane (i.e. width). This is not the case for the diode which remains constant in length and does not sacrifice sensitivity when the membrane size is decreased, hence providing better relative sensitivity and consistent accuracy with the miniaturization of the sensor.

In this section, the sensitivity and accuracy of the thermo-resistive method reduced with decreasing membrane/resistor size, which differs to the thermo-electronic accuracy which remained constant throughout, leading to

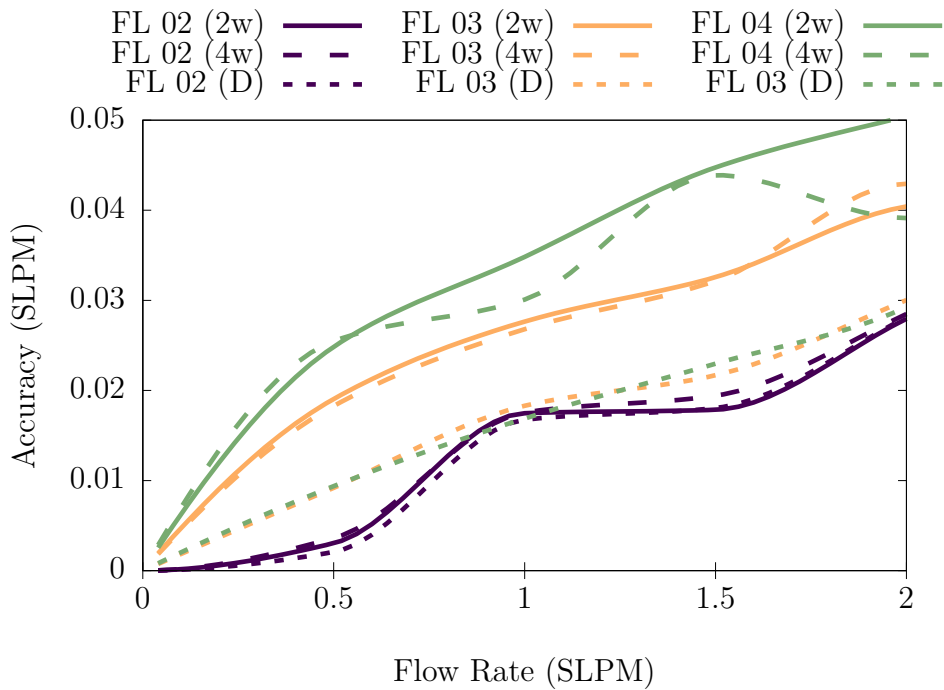


**Figure 3.25:** The accuracy calculated for each flow rate. The purple lines represent FL 02, orange FL 03 and green FL 04. Solid lines are for 2-wire (2w) resistance measurements, dashed for 4-wire (4w) resistance measurements and dotted for diode (D) measurements.

the conclusion this could be the superior transduction method when further miniaturizing sensors. In addition to this, two sensors were investigated that have different diode lengths. It was found that the short diode had approximately 30 % better accuracy due to it measuring a higher temperature on average. This can be used towards a reference for designers who want to decide which transduction principal to use.

### 3.6 Summary

Design, fabrication, packaging, experiment, numerical simulations, electro-thermal characterisation and flow rate calibration results of 11 CMOS MEMS thermal flow sensors based on a tungsten heating element were presented. The SOI CMOS fabrication process allows low-cost, high-volume production

of miniaturised flow sensors with the possibility of on-chip electronics whilst providing superior performance and reproducibility. DRIE was used to minimise conductive heat loss whilst maintaining its mechanical strength. Key findings are summarised below:

- i. A numerical model was validated against experimental data and used to show 3-dimensional modelling is needed for quantitative analysis.
- ii. The numerical model was used to find the optimum location for RTDs in calorimetric mode.
- iii. The effects of geometrically altering the sensor structure was investigated, showing sensitivity relies on heater length and not heater width.
- iv. Numerical modelling was used to highlight an area of recirculation above the heater that generates noise at low flow rates.
- v. Thermo-electronic devices were simultaneously compared to thermoresistive and showed to retain their accuracy with the miniaturisation of the membrane.
- vi. A diode that is too short will have non-linear electrothermal behaviour due to current leakage.

This study will lead to the design of a new generation of MEMS thermal flow sensors with improved performance for application in industry and domestic. Recommendations on further work that should be carried out with flow sensors is discussed in chapter 6.



# Chapter 4

## Thermal Conductivity Sensing

### 4.1 Introduction

RECENT decades have seen increased concern over environmental pollution and potentially harmful substances that could have an effect on life and industrial processes. This has led to a large increase of research in the area of gas sensors, which need to be able to identify or monitor the toxic and flammable chemicals of any particular environment, especially to ensure the safety of humans, plants and animals. The global market value for gas sensors was estimated at 2.05 billion US dollars in 2018, with a predicted growth rate of 7.8% Compound Annual Growth Rate (CAGR), highlighting an area driven by commercialisation with demand only set to increase over the coming years [140].

Another report stated that the major trend driving the gas sensors market is the development of wireless capabilities and miniaturisation, coupled with improved integration into various devices and machines [141]. Micromachined gas sensors are among the most suitable devices to continue this trend due to their small size, low cost, low power consumption and reliability, with easy

integration when fabricated using a standard CMOS process. A brief overview of micromachined gas sensing technologies is now outlined.

Gas detectors can be used to detect combustible, flammable and toxic gases where the level of concentration detection needed differs drastically. For the detection of combustible and flammable gases, the necessary detection limit is much higher and is defined by the Lower Explosive Limit (LEL), which is defined as the lowest concentration of a vapour in air that can produce a flash of fire in the presence of an ignition source. This level is 4% and 5% for the highly industrially important detection of Hydrogen (H<sub>2</sub>) and Methane (CH<sub>4</sub>) [142]. It is in the detection of toxic gases that low concentrations need to be detected and thus necessitate a highly sensitive system.

For toxic gases, OSHA regulations define the Permissible Exposure Limit (PEL), which is the legal limit of for exposure of an employee to a chemical substance. With even lower concentrations than this, the Recommended Exposure Limit (REL) is the recommended upper limit for exposure to hazardous substances and is based on the acceptable level of exposure for a worker to be safe over a working lifetime. Working to these limits, it is essential to monitor the level of toxic substances in any environment.

Alongside the well-known harmful environmental gases (e.g. carbon monoxide, carbon dioxide, ammonia) [143], particular interest has risen around the detection of Volatile Organic Compounds (VOC), which refer to organic chemicals that are gaseous at room temperature. Exposure to VOCs has been linked with acute effects such as headaches, dizziness, eyes and nose irritation [144] as well as more serious associations with asthma and lung function [145–147].

For a meaningful detection of VOCs, sensors must be able to detect gases at small concentrations, such as tens of ppm (e.g. acetone) to as little as a few ppb (e.g. formaldehyde). In such small concentrations, the thermal



conductivity of the gas is very minimally changed and thus it is very hard to detect this concentration with thermally based technology.

Many gas sensing technologies have been developed that are based on different physical or chemical effects. The market trend set by the commercial industry has seen recent focus on the development of low-cost, low-power gas sensors with a small footprint and fast response. The most common techniques are catalytic, electrochemical, infrared, acoustic, Metal Oxide (MOx) and thermal conductivity. Table 4.3 gives a comparison between the gas sensing technologies.

Catalytic are the oldest of all the gas sensor technologies with their discovery in 1923 [148]. Combustible gases and gas mixtures do not burn until they attain a certain temperature, known as the ignition temperature. This temperature can be lowered in the presence of particular chemicals that ‘catalyse’ the reaction. The two sub-divisions of catalytic gas sensors are pellistor and thermoelectric. Pellistor-type gas sensors consist of two coils, one of which is activated with a catalyst. Voltage is used to raise the temperature of the coil, causing the gas to ignite and thus raising the temperature of the detector coil. Recent works have combined this technique with the inherent advantages of micromachining technology [149–155]. In 1985 the first thermoelectric gas sensor was shown [156]. Thermoelectric sensors generates an electrical signal based on the temperature difference (Seebeck effect) caused by a catalysed exothermal oxidation reaction. They are able to work at much lower temperatures than pellistor-type, but still suffer from the inherent disadvantages of high-power consumption and long response times. Ongoing research is trying to improve these problems and take advantage of micromachining techniques [157–164].

Electrochemical sensors detect change in electrical properties caused by electrochemical reactions at a sensing electrode and are split into amperometric and potentiometric classes based on operating principle. Amperometric

**Table 4.1:** A comparison between the gas sensing technologies with their relative advantages and disadvantages.

Gas Sensor	Advantages	Drawbacks
<b>Catalytic</b>	<ul style="list-style-type: none"> <li>Detects combustible gases</li> <li>Long lifetime</li> <li>Good selectivity</li> <li>Low sensitivity to temperature</li> </ul>	<ul style="list-style-type: none"> <li>High power consumption</li> <li>Long response time</li> <li>Only flammable gases</li> <li>Cannot measure below LEL</li> </ul>
<b>Electro-chemical</b>	<ul style="list-style-type: none"> <li>Short response time</li> <li>High accuracy</li> <li>Wide detection range</li> <li>Low cost</li> </ul>	<ul style="list-style-type: none"> <li>Short lifespan</li> <li>Large footprint</li> <li>Hard to miniaturise</li> <li>Susceptible to poisoning</li> <li>Not for VOCs</li> </ul>
<b>Infrared</b>	<ul style="list-style-type: none"> <li>High sensitivity</li> <li>Fast response time</li> <li>Good selectivity</li> <li>Low drift</li> </ul>	<ul style="list-style-type: none"> <li>High-cost</li> <li>Sensitive to humidity</li> <li>Hard to miniaturise</li> <li>High power consumption</li> </ul>
<b>Acoustic</b>	<ul style="list-style-type: none"> <li>Long lifetime</li> <li>High sensitivity</li> <li>Low power consumption</li> <li>Fast response time</li> </ul>	<ul style="list-style-type: none"> <li>Low selectivity</li> <li>Sensitive to temperature</li> <li>Sensitive to pressure</li> <li>Noisy</li> <li>Expensive</li> </ul>
<b>Metal Oxide</b>	<ul style="list-style-type: none"> <li>Low cost</li> <li>Wide range of gases</li> <li>High sensitivity</li> <li>Small footprint</li> </ul>	<ul style="list-style-type: none"> <li>High power consumption</li> <li>Cross-sensitivity</li> <li>Sensitive to humidity</li> <li>Baseline drift</li> </ul>
<b>Thermal Conductivity</b>	<ul style="list-style-type: none"> <li>Low cost</li> <li>Low power consumption</li> <li>High sensitivity</li> <li>No adsorption/catalyst</li> <li>Fast response time</li> <li>Long lifetime</li> <li>Small footprint</li> </ul>	<ul style="list-style-type: none"> <li>Low sensitivity</li> <li>Low selectivity</li> <li>Sensitive to humidity</li> </ul>

uses a constant voltage bias and the signal is a diffusion dependent current, potentiometric differs by ideally working at zero current and measuring the electromotive force between sensing and reference electrodes. Amperometric are more sensitive and produce linear response, but measured signal from potentiometric devices is independent of size, providing a huge advantage with the miniaturisation of sensors. Several works have looked to improve both amperometric [165–169] and potentiometric [170–175] technology and a recent market survey has shown it is the most commercially employed hydrogen sensor [176].

Infrared gas sensing is based upon the varying vibrations of the atoms in a molecule. By passing infrared radiation through a gas mixture and measuring the infrared spectrum the gas composition can be determined by the fraction of infrared radiation absorbed at a particular wavelength. The most commonplace infrared technique for gas sensing is called Non-Dispersive InfraRed (NDIR) where a typical system consists of an emitter, a gas chamber and a detector. Interference occurs when there is cross-over between the adsorption bands of different gases, resulting in a non-selective gas sensor. Several works have looked at improving interference and limiting cross-sensitivity [177–183]. The detection limit has been improved through many methods including pre-treatment of the inlet-gas [184, 185], improving the source [186–189], enhancing the optical pathway [190], using an optical filter [191, 192] and improving the detector [193–195].

Acoustic waves change in velocity and amplitude when propagated through or along a medium. The frequency and phase characteristics can then be correlated to the physical composition of the medium. Acoustic sensors started with the Quartz Crystal Microbalance (QCM) with its first application in organic vapour sensing done in 1964 [196]. This idea was extended to the more recently researched and used Surface Acoustic Wave (SAW) devices where the sensor is chemically coated with selective layer. Due to attractive results

showing high sensitivity, selectivity and response times, extensive research has been carried out to optimise this technology, [197–201]. Their limiting factor is the difficulty in fabrication due to their small size, which results in a costly sensor.

Metal Oxide gas sensors are the most investigated gas sensor due to their high sensitivity, low cost and small size making them very commercially attractive, especially for portable gas detection devices. This chemi-resistive technique consists of a heating element, a sensing element and a deposited MOx on the surface where reactions involving the targeted gas take place and alter the electrical resistance of the heater. Extensive research has been carried out into the deposited oxide surface material in order to optimise sensitivity and selectivity to the targeted gas with a detailed review recently given [202].

Thermal conductivity gas sensors use the difference in gases' thermal conductivities to extract varying amounts of heat from a heated element, thus changing the electrical response. It is for this reason that they are commonly used for detecting gases with high thermal conductivities such as hydrogen and methane, meaning there is a larger difference in the heat extracted. These devices are commonly referred to as Thermal Conductivity Detectors (TCD). Figure 4.1 illustrates the working principle of a thermal conductivity detector where  $q$  is the heat transfer through conduction and convection. It has been shown previously that at an operating temperature of 300 °C, the effects of radiation are negligible and can be ignored.

In steady state analysis, the energy balance implies that the ratio of heat transfer from the lumped solid object is equal to the rate of heat generation within the object, in this case the heater. Therefore the rate of heat generation in a simplified 2-dimensional model can be written as

$$\dot{Q} = h_T A_S \left. \frac{dT_f}{dy} \right|_{wall} \quad (4.1)$$

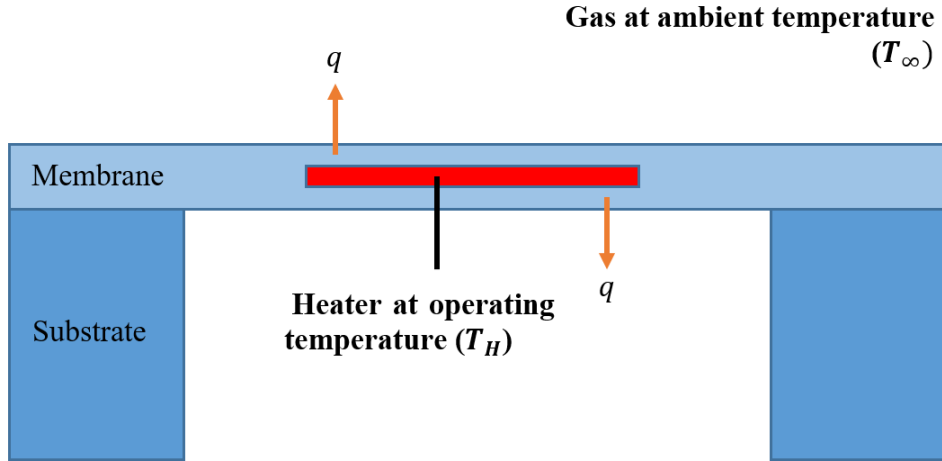


**Figure 4.1:** An illustration of the working principle behind the thermal conductivity detector.

where  $\dot{Q}$  is the rate of heat generation in the heating resistor,  $h_T$  is the heat transfer coefficient (combined for conduction and convection),  $A_S$  is the surface area,  $\left. \frac{dT_f}{dy} \right|_{wall}$  is the temperature gradient between gas and the surface of the heating resistor. This can be replaced with the temperature of the heater  $T_H$  and the ambient temperature of the gas  $T_\infty$  to give the more relatable

$$\dot{Q} = h_T A_S (T_H - T_\infty) \quad (4.2)$$

The rate of heat generation is representative of the dissipated electrical power,  $I^2 R$ . Combining this with the known dependence of on resistance given by the TCRs results in the following equation:

$$I^2 R_{T0} (1 + \alpha_T (T_H - T_\infty) + \beta_T (T_H - T_\infty)^2) = h_T A_S (T_H - T_\infty) \quad (4.3)$$

From this equation, it can be seen that the temperature (and therefore resistance) is related to the heat transfer from the heated resistor to the gas, which will change when a different gas is present in the atmosphere, thus displaying the working principle of the TCD devices. Whilst both conduction and convection are taking place for heat transfer into the gas, there is a considerable amount of conduction from the heater into the solid structures that surround

the heater. This heat transfer is wasted because it is not interacting with the gaseous medium, but being lost through solid conduction. Therefore, the heater temperature depends on the proportion of heat interacting with the gas, highlighting the need to minimise conduction losses through the surrounding solid structures.

The heat transfer coefficient is dependent on the thermal conductivity of the gas. This makes the detection of gases with thermal conductivity similar to air very difficult, such as ammonia, carbon monoxide, butane and carbon dioxide. Table 4.2 shows the thermal conductivity of several common gases at 300 K.

**Table 4.2:** The thermal conductivity values of common gases.

<b>Gas</b>	<b>Thermal Conductivity (W/mK)</b>
<b>Air</b>	0.026
<b>Ar</b>	0.018
<b>CO</b>	0.025
<b>CO<sub>2</sub></b>	0.017
<b>H</b>	0.182
<b>He</b>	0.151
<b>N<sub>2</sub></b>	0.026
<b>Ne</b>	0.049
<b>NH<sub>3</sub></b>	0.024
<b>O<sub>2</sub></b>	0.027
<b>CH<sub>4</sub></b>	0.033

This electro-thermal sensing does not rely on gas adsorption and/or a reaction with a catalyst, resulting in sensors with high response times that can be used continuously and do not suffer from as much degradation with time. With micromachining technology, TCD devices are becoming miniaturised and

have found themselves developed for gas chromatography systems [203–207]. Research has concentrated on improving the sensitivity of TCD devices to enable measurement of gases with similar thermal conductivities and to become comparable with other technologies, whilst providing all the other benefits outlined, thus making it a commercially attractive technology.

Many works have looked at the transient response of TCDs in order to measure thermal conductivity and thermal diffusivity [208–213], however this requires sophisticated data acquisition systems alongside complicated post-processing techniques that make it commercially undesirable.

Comparatively to the other gas sensing techniques, steady-state TCD technology has been minimally investigated. Attempts have been made at improving the read-out electronics [214], whilst many other examples look at measuring hydrogen levels [215, 216]. Some groups have investigated using nano scale devices through using carbon nanotubes [217], nanowires [218], or nanobelts [219], and although it helps improve sensitivity, is not using standard CMOS compatible technology.

In this chapter the design, fabrication and investigation of micro-TCD gas sensors for measuring CO<sub>2</sub> in air is presented. A novel fabrication step that uses front-etching is outlined that creates holes through the membrane and thermally isolates the heating resistor. The characterisation and performance of two designs is outlined and compared to a reference design, highlighting the dramatic sensitivity improvement. An asymmetric design is also fabricated and tested with a method of measuring thermal conductivity in a calorimetric readout. Here, one side of the sensor is forced to have more interaction with the gas medium through membrane holes, creating an offset with the other side. This new approach is coupled with an illustration of designs that could improve the sensitivity of this novel technique coupled with theoretical proof and numerical simulations.

## 4.2 Design and Fabrication Details

The sensors were initially designed in software package Cadence Virtuoso (IC 5.1.4) and were then commercially fabricated using a 1.0  $\mu\text{m}$  SOI CMOS process with tungsten metallization. After this, Deep Reactive Ion Etching (DRIE) was used on the backside to create four separate membranes on each sensor. An example of one of the chips is shown in Figure 4.2 with its cross-section schematic displayed in Figure 4.3. Each sensor consists of 4 separate membranes that can be heated independently, allowing multiple designs to be simultaneously measured on a single device, yielding accurate and fair comparisons. All designs include 3 parallel tungsten heating resistors connected to wire bonding pads with 20  $\mu\text{m}$  tracks. All 4 central resistors share a common ground whilst the 8 non-central resistors also share a common ground.

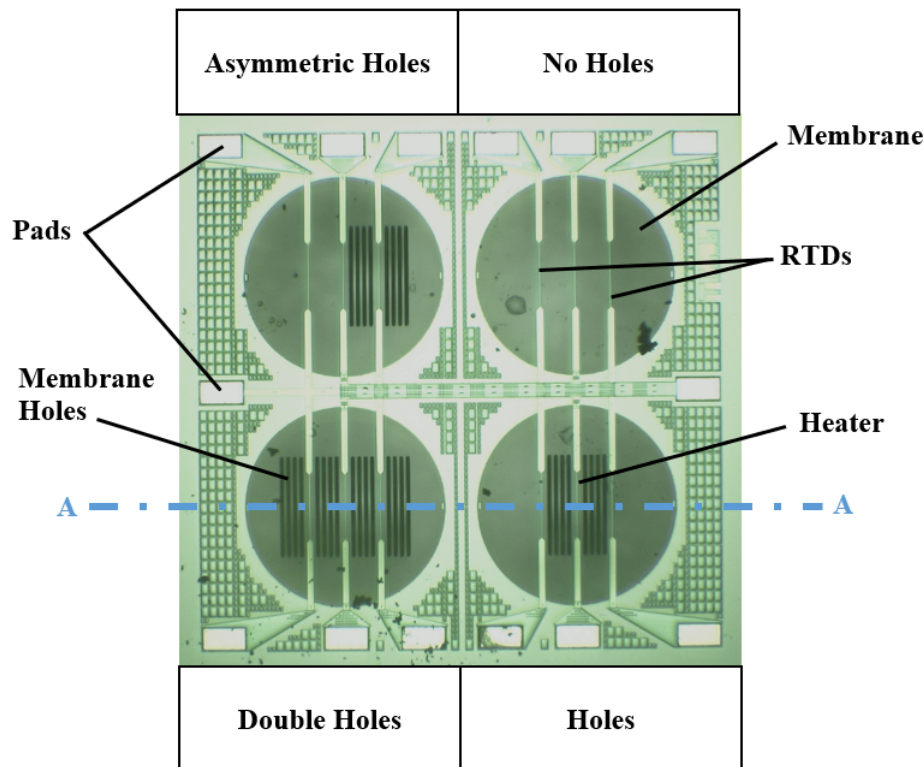


**Figure 4.2:** Optical micrograph of one of the sensor chips – die dimensions of 2.0 mm  $\times$  2.0 mm.



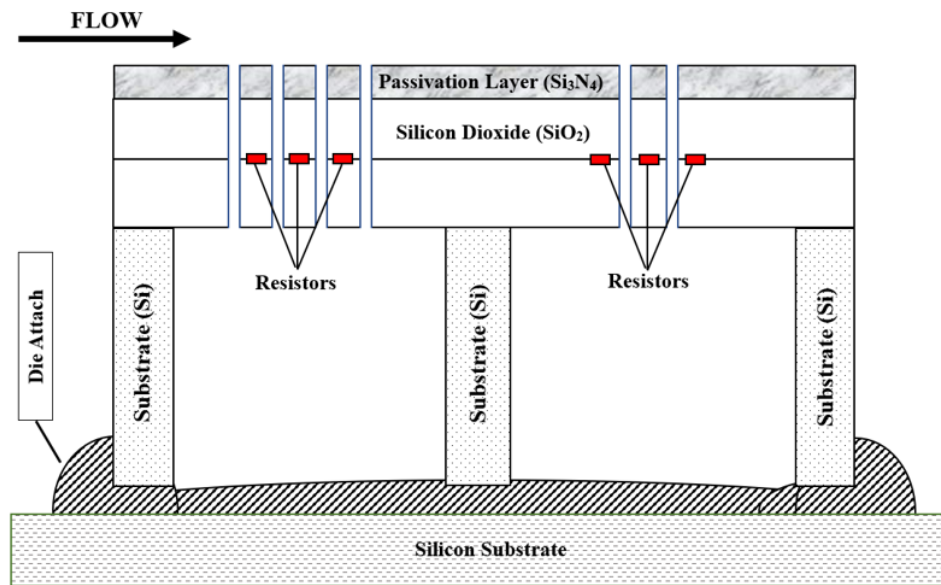


**Figure 4.3:** Cross-section of sensor along cut point A-A that is depicted in Figure 4.2 (not to scale).

The combination of tungsten heating elements and the thin-film membrane structure lead to superior thermo-mechanical properties. An extra processing level was incorporated in order to add holes through the thin-film membrane through front-etching, using the silicon as an etch stop before the DRIE back-etching process. These holes are incorporated for three reasons:

- i. to reduce the chance of catastrophic breakage due to pressure difference below and above the membrane.
- ii. to isolate the heating resistor and reduce losses through conduction.
- iii. to force more interaction with the passing medium, i.e. increased levels of convection with the flowing gas.

The four designs within a single sensor are named as ‘no holes’ (reference design), ‘holes’ and ‘double holes’ (heating resistor isolation and isolation of heater and both RTDs, respectively) and ‘asymmetric holes’ (isolating holes for one RTD). All membrane holes have the same geometry of  $10\ \mu\text{m} \times 200\ \mu\text{m}$  with rounded edges to avoid stress concentration factors. These geometric

differences give the ability to test and de-couple the relative importance and improvement seen from the different designs, leading to a better understanding on how isolating membrane holes can be used to optimise this technology.

The four designs use membrane holes in order to manipulate the thermal profile through the membrane to their advantage.

- i. **Holes and Double Holes** were incorporated in a symmetric design on both sides of the heating resistor. This helps to reduce the heat loss through conduction into the membrane and also encourages more interaction with the gas. This design should improve electro-thermal efficiency as well as increase the sensitivity to changing gas concentration.
- ii. **Asymmetric Holes** were incorporated into one side of the structure, inducing an asymmetric thermal profile across the membrane. This results in the two RTDs having a different relationship with thermal conductivity, and thus the difference between these two RTDs will change with gas concentration.

### 4.3 Experimental

Measurements were performed in two separate experimental protocols. Firstly, the electro-thermal characterisation of the device heaters was performed between 25 °C and 300 °C. Using the information from this characterisation, measurements were performed using different concentrations of CO<sub>2</sub> in air.

*Electro-thermal Characterisation* - The electro-thermal characterisation of the devices was performed at wafer level using a Cascade Microtech Summit 12000 probe station equipped with a hot chuck and an external Keysight B1505 power device characterisation system. Firstly, the resistance was measured from 25 °C and 300 °C allowing the calculation of the Temperature

Coefficients of Resistance (TCR). A current sweep was then biased through the central heater from 0.5 mA to 13 mA in steps of 0.5 mA whilst measuring the voltage.

***Thermal Conductivity Characterisation*** - Using a Kulicke and Soffa wedge bonder, the sensors were bonded onto standard issue Dual in Line (DIL8) packages. A lid was custom designed and 3D printed via a Formlabs Form 2 printer in order to create a flow channel over the sensors. The vertical inlet and outlet, of inner diameter 0.6 mm, feed the flow into a 1.5 mm  $\times$  2.5 mm rectangular channel where the flow is passed over the sensor. The lid is glued onto the DIL8 package to make a sealed system where silicone tubes can be used to connect the inlet and outlet. The packaged sensor and attached lid are shown in Figure 4.4.

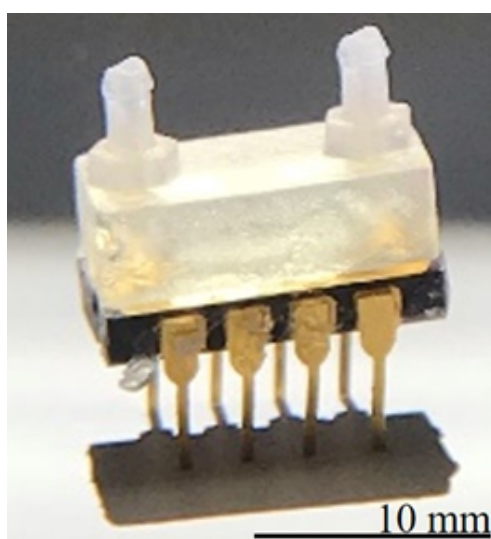


**Figure 4.4:** A photograph of the sensor packaged in a DIL8 base and attached to the 3D printed lid, containing barbs for connected to the inlet and outlet of the gas testing system.

An array of Alicat Mass Flow Controllers (MFC [MC-5SLPM-D/5M]) with range from 0 to 5 Standard Litres Per Minute (SLPM) were used to control the gas flow. Two MFCs were implemented before the package to control CO<sub>2</sub> and dry air flow. An MFM is also connected at the exhaust of the system to monitor flow rate and ensure there are no leaks present in the system.

All the MFCs are controlled by in-house developed software. Five different concentrations of CO<sub>2</sub> (0%, 5%, 10%, 15% and 20%) were exhausted through the system before ensuring stagnant flow by closing the control valves each side of the chamber. A ten second measurement period followed a 15 second stabilisation period.

Finally, three Source Meter Units (SMU [Keithley 2410s]) were used to power and measure the sensors. The first provides a current bias to the heater, equating to an operating temperature of 300 °C (using the electro-thermal characterisation data) whilst measuring the voltage. The second two SMUs provide a low bias current of 1 mA (to avoid self-heating) and measure the voltage of the upstream and downstream RTDs. With this setup, anemometric and calorimetric measuring techniques can be investigated simultaneously. LabVIEW 2017 software (v17.0) was used to control the current biasing whilst also logging the data.

## 4.4 Discussion

### 4.4.1 Symmetric Membrane Holes

The symmetric membrane hole designs include the ‘holes’ and ‘double holes designs.’ With these designs, the anemometric principle is used for measuring the thermal conductivity and compared to the reference design. Firstly, using the calculated TCR values for each of the sensors, the relationship between input power and temperature reached by the heater was established for each device and is shown in Figure 4.5.

The first conclusion to be made is that with the implementation of holes, there is a clear increase in the electro-thermal efficiency of the device. This means that the heating resistor can reach operating temperature using less

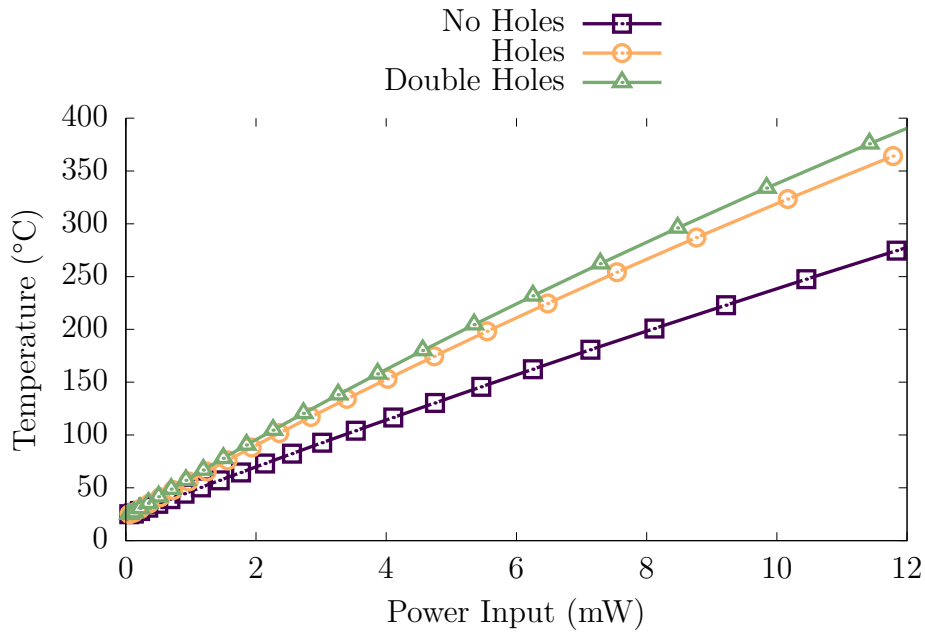


**Figure 4.5:** Electrothermal efficiency for the three investigated symmetric designs.

power and is because there is increased thermal isolation of the heater, i.e. less heat is wasted by conduction through the membrane. A summary of the increase in electrothermal efficiency is extracted from the power-temperature plots and presented in Table 4.3 as an average over the measured devices.

The largest increase in electrothermal efficiency is seen by the double hole design at 69%. It is shown that the largest improvement in electrothermal efficiency is caused by adding isolating holes on both sides of the resistor, with a minor additional advantage when using double isolation. Noticeably, the increase when using the double hole design is not significantly better than single hole isolation, thus leading to the conclusion that as long as the isolating holes are over the length of the heating resistor (i.e. fully isolated), increasing the number of holes in the perpendicular direction plays a less significant role in optimisation. This leads to the advantage that thin holes can be fabricated, leaving space to place optimised RTDs for calorimetric approaches or numerous RTDs for multi-parameter sensing.

The packaged devices were exposed to CO<sub>2</sub> at five concentrations (0%, 5%, 10%, 15%, 20%) in stagnant flow with a power input of 8 mW, to measure the sensor response to change in thermal conductivity. This was carried out for the reference design and the designs with symmetric membrane holes and the responses of the central heaters are displayed in Figure 4.6.

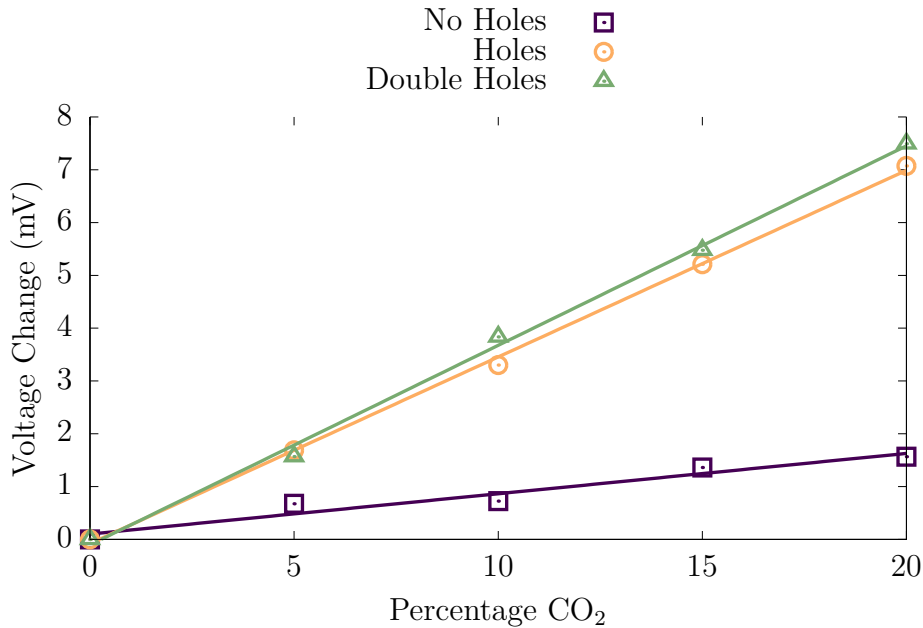


**Figure 4.6:** The voltage response of the central resistor with the evolution of CO<sub>2</sub> concentration.

It is clearly shown that with the addition of isolating holes, the response to CO<sub>2</sub> is significantly increased, hence increasing the sensitivity. The addition of isolating membrane holes improves the sensitivity by 273% for the best design of double holes. The double hole design only exhibits a marginal increase on the single hole design, further validating that the extra perpendicular isolation has a less important effect on increasing the interaction between the heating element and the surrounding medium and does not largely increase the thermal resistance. The average measured standard deviation across the double hole design was 10  $\mu$ V. However, it is not only the standard deviation that limits the detection in a full system and sensing 10  $\mu$ V in a commercial system would be extremely difficult because of electronics noise. For this reason, a more reasonable value of 100  $\mu$ V is chosen to extrapolate a detection resolution of

0.3% for the presented double holes device. 100  $\mu\text{V}$  is chosen due to its value being common in temperature sensors using the same technology principles.

**Table 4.3:** Electrothermal efficiency and relative percentage increase with the addition of isolating membrane holes.

Design	No Holes	Holes	Double Holes
<b>Electrothermal Efficiency</b> ( $^{\circ}\text{C}/\text{mW}$ )	14.85	24.76	25.08
<b>Percentage Increase</b>	Reference	66.7	68.9
<b>CO<sub>2</sub> Sensitivity</b> ( $\text{mV}/\%\text{CO}_2$ )	0.101	0.353	0.377
<b>Percentage Increase</b>	Reference	249.5	273.2

#### 4.4.2 Asymmetric Membrane Holes

The ‘asymmetric holes’ design that contains membrane holes on only one side is an investigation into new method of measuring thermal conductivity where the middle resistor is heated and the difference between the two RTDs is measured. Only one of these RTDs is surrounded and isolated with membrane holes, which forces more interaction between the sensor and the surrounding gas. Due to the isolating resistor having more interaction with the gas, when the percentage of gas is altered, the difference between the two RTDs also changes and can be correlated to the amount of gas. This is the first investigation into a new method for thermal conductivity gas measurements.

Figure 4.7 shows the difference in voltage readout between the two RTDs with the evolution of CO<sub>2</sub> percentage (in air). It can be clearly seen that as the percentage CO<sub>2</sub> increases, so does the voltage difference, providing a proof-of-concept for this technique. A linear curve of interpolation is used to estimate the sensitivity, which was calculated as 0.0050  $\text{mV}/\%\text{CO}_2$ . This is less

sensitive than the device run anemometrically, however it should be noted that when the read-out resistor is also used as the heater, the noise is far greater. Throughout the experiment, the standard deviation of the heater signal is over an order of magnitude larger than the standard deviation of the RTD signal. Using the standard deviation, an extracted detection resolution of 0.2% CO<sub>2</sub> is calculated, rendering this initial design less than an order of magnitude off the anemometric principle. This result is obtained from a first, unoptimized proof-of-concept and needs to be improved if it is to be seriously considered as a commercially viable sensing solution.

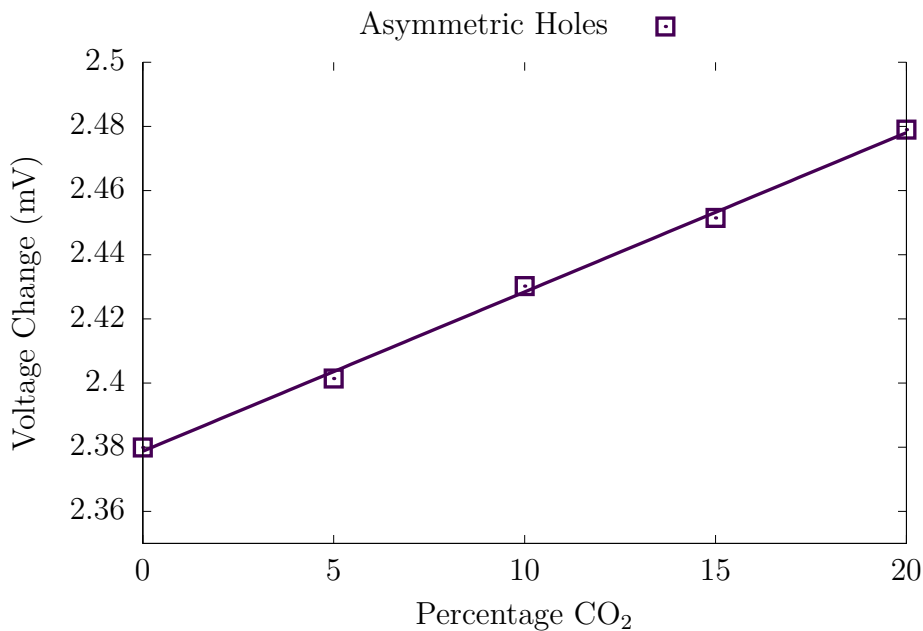


**Figure 4.7:** The difference in voltage between the two RTDs plotted against percentage CO<sub>2</sub> in air.

When doing calculations using thermal resistance, it is often beneficial to model the heat flow as an electric circuit where heat flow is current, temperatures are voltages, heat sources are current sources and thermal resistances are electrical resistances. Figure 4.8 shows the top schematic of the sensor with two designs that have different membrane hole layout. Design 1 is the same as the ‘asymmetric holes’ design with one RTD isolated whereas design 2 incorporates an extra hole isolating the other RTD from the substrate. The



thermal resistances (TR) between the heating resistor and RTDs, and between the RTDs and the substrate are labelled.

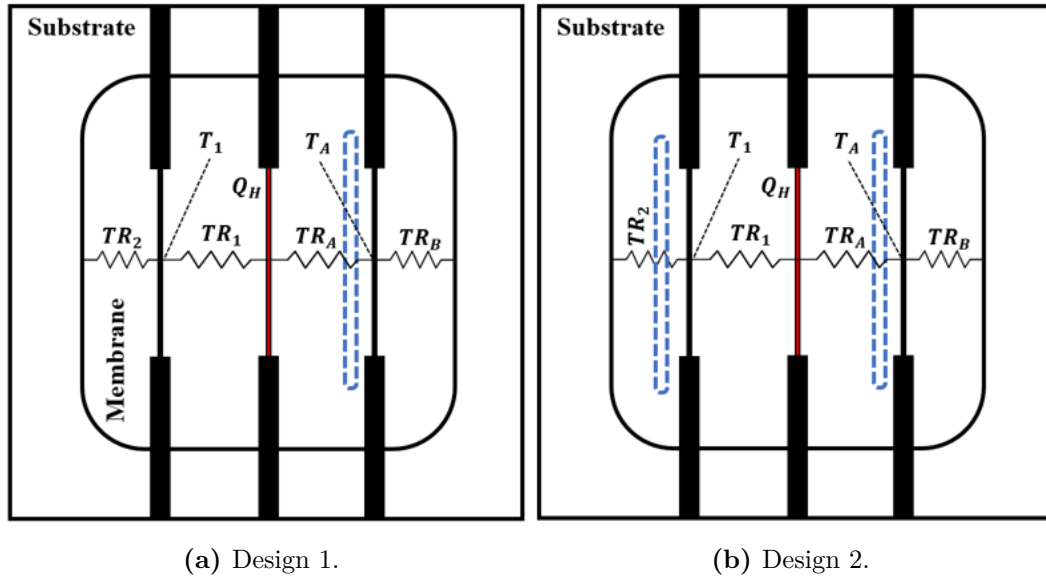


**Figure 4.8:** Top schematic of ‘asymmetric holes’ sensor with two different designs for membrane hole location. Blue dotted lines represent the location of the membrane holes. Electrical resistor symbols have been added to represent the Thermal Resistance (TR) between the heater and the RTDs.

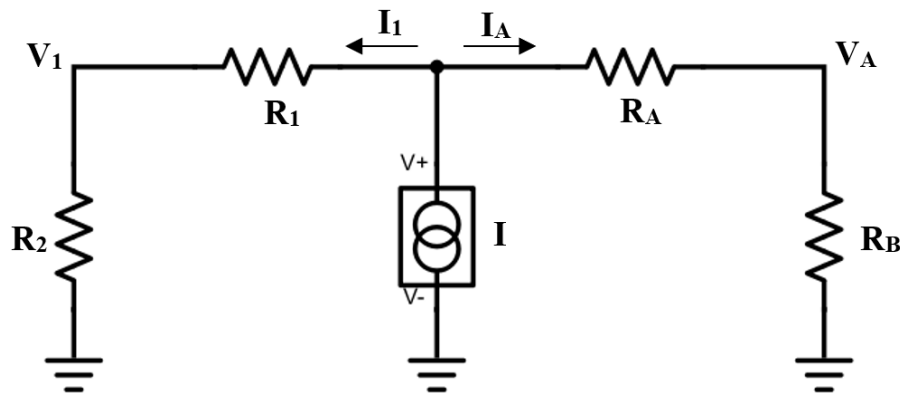


**Figure 4.9:** Electrically equivalent circuit of the heat transfer through the membrane.

Figure 4.9 shows the equivalent electrical circuit and allows us to theoretically compare the two designs with circuit analysis. Firstly, the currents going through each arm of the circuit can be written as:

$$I_1 = I \cdot \left( \frac{R_A + R_B}{(R_A + R_B) + (R_1 + R_2)} \right) \quad (4.4)$$

$$I_A = I \cdot \left( \frac{R_1 + R_2}{(R_A + R_B) + (R_1 + R_2)} \right) \quad (4.5)$$

The voltage at  $V_1$  and  $V_A$  (i.e. the temperatures at the two RTDs) is then the sum of the resistance and current:

$$V_1 = R_2 I_1 = \frac{R_2 (R_A + R_B) I}{R_A + R_B + R_1 + R_2} \quad (4.6)$$

$$V_A = R_B I_A = \frac{R_B (R_1 + R_2) I}{R_A + R_B + R_1 + R_2} \quad (4.7)$$

From these two voltages, we can calculate the voltage difference, which relates to the temperature difference between the RTDs. This temperature difference is the output in question and can give us important information of the performance of the designs.

$$V_A - V_1 = I \left( \frac{R_B R_1 - R_A R_2}{R_A + R_B + R_1 + R_2} \right) \quad (4.8)$$

If  $TR_A$  includes a hole through the membrane, the thermal resistance will be far greater than if the hole wasn't there as the thermal resistance through air is over two orders of magnitude larger than through the membrane. Therefore  $R_A \gg R_B, R_1, R_2$  for design 1 and  $R_A$  and  $R_2 \gg R_B, R_1$  for design 2. Thus, simplifying the previous equation results in:

$$\textbf{Design 1: } V_A - V_1 \approx -R_2 I \quad (4.9)$$

$$\textbf{Design 2: } V_A - V_1 \approx -\frac{R_A R_2}{R_A + R_2} I \quad (4.10)$$

From design 1, the system temperature difference depends on the small resistance of  $R_2$ , yielding low dependence on the high resistance provided by the membrane holes. The conclusion can be visualised by the fact the thermal resistance without any holes is so low, it is extracting the lots of heat from the heater and acting against positive benefits produced by the holes. For design 2, with identical holes we can assume that  $R_A \approx R_2$ , which results in  $V_A - V_1 \approx -0.5 R_A I$ . Here, the performance of the sensor relates to the much

higher resistance when membrane holes are present, thus theoretically yielding a device that should be orders of magnitude more sensitive. It should be noted that if  $R_A$ ,  $R_B$  and  $R_2$  all had membrane holes,  $V_A - V_1 \approx 1/3[R_A - 1]I$ . This extra membrane hole does not provide further advantage. With the next round of fabrication, new designs will be investigated considering the theoretical knowledge now gained. A new method of sensing through thermal conductivity with a way to increase sensitivity is an exciting start for new technology to emerge from.

## 4.5 Numerical Modelling

In order to substantiate the theoretical advantages of the proposed designs, numerical models can be used to predict the behaviour of the designs in the presence of CO<sub>2</sub> and air. Using the numerical model described in Chapter 3, geometrical alterations are made to add the membrane holes, as is shown in Figure 4.10. The inset shows a detailed view of the circled section of the design. All the layers present in the design correlate to a layer in the technology platform. For the designs with holes, all the hole layers are either set to air or CO<sub>2</sub> and treated as a fluid. This allows comparison of both the fabricated designs; holes and no holes.

In order to adequately model the conduction and convection across the holes, which have width of 10  $\mu\text{m}$ , a finer mesh was defined across these points specifically. A representation showing the mesh density is shown in Figure 4.11 where the colour legend defines the mesh size in meters. A quarter slice is taken out of the picture in order to show the higher density of mesh nodes closer to the heating resistor and surrounding the membrane holes. A maximum element growth is set as 1.6, reducing the overall number of mesh nodes whilst maintaining accuracy throughout the boundary between finer geometries and larger geometries.

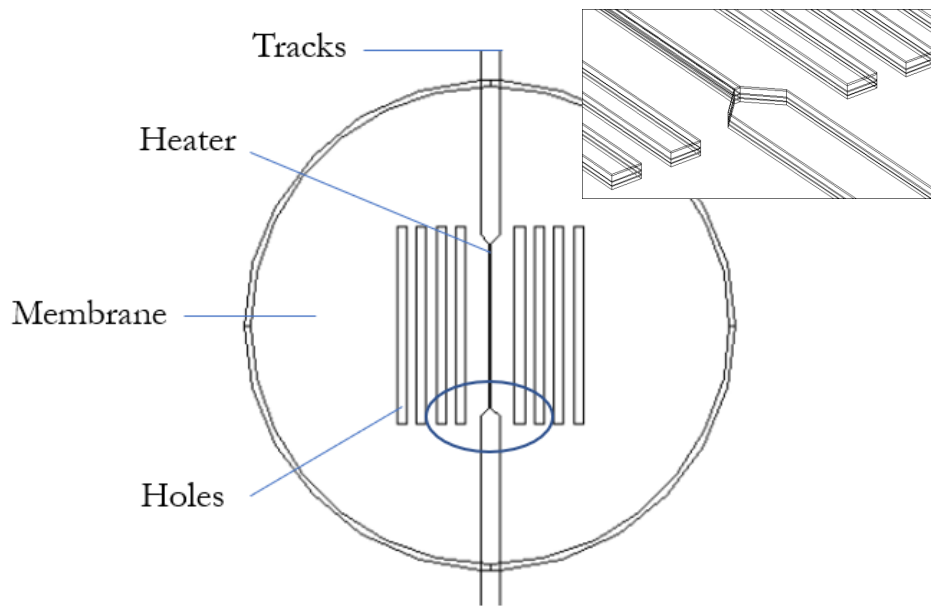


**Figure 4.10:** Geometry created for the numerical model with the inclusion of holes. Inset - 3D isometric detailed view of circled section showing fabrication layers.

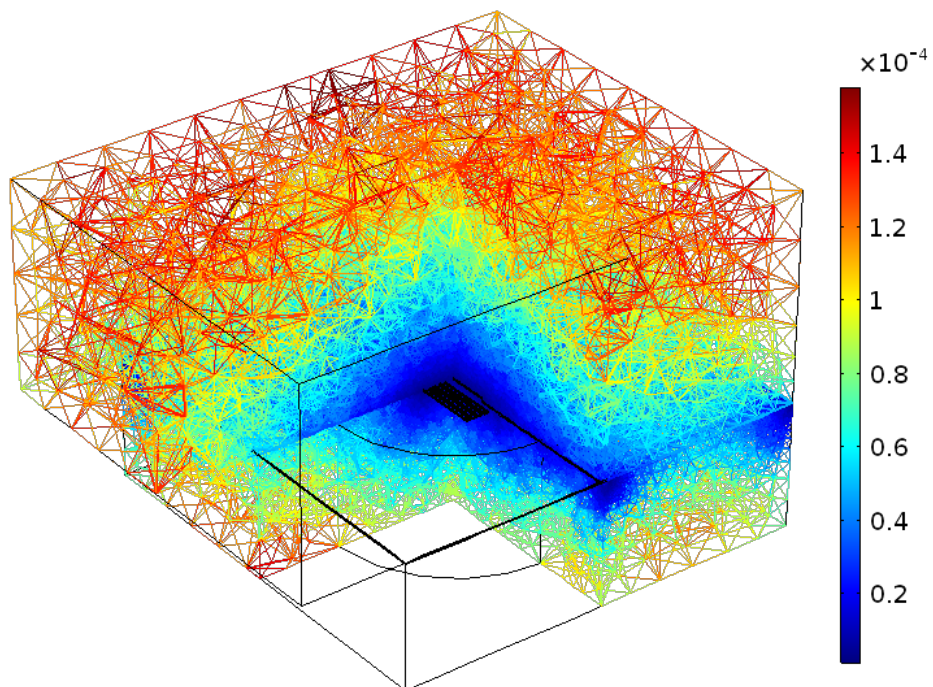


**Figure 4.11:** The mesh used in the numerical model for the design with holes where the colour legend illustrates mesh size in metres.

In order to create the medium of CO<sub>2</sub>, four more interpolative lookup tables were included for the material parameters thermal conductivity, specific heat capacity, thermal expansion coefficient, density and dynamic viscosity. The fluid initial conditions and laminar flow used these tables in order to model the device behaviour in this different gas and to accurately capture its non-linear behaviour with temperature.

Figure 4.12 shows simulation results for the temperature profiles across the membrane. This is the temperature profile cutting through the resistor and holes perpendicularly. The geometry is based on the fabricated design where there are four holes of 10  $\mu\text{m}$  by 200  $\mu\text{m}$  next to each other. In the case of design 1 these are located on one side of the resistor. For design 2, the four holes are included on the second side as well, with a gap of 120  $\mu\text{m}$ . Two vertical lines have been added to the figure at 200  $\mu\text{m}$  and 400  $\mu\text{m}$  which denote the location of the calorimetric (upstream and downstream) resistors.

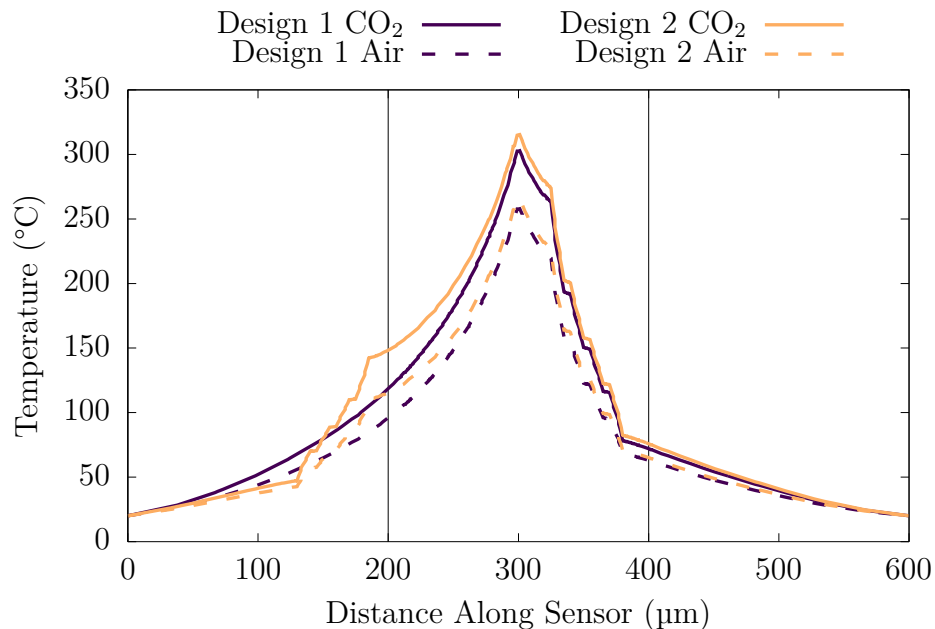


**Figure 4.12:** Simulation results of the temperature profile across the sensor for the original design (design 1) and the improved design (design 2) in both air and CO<sub>2</sub>.

The benefit of adding the second set of membrane holes can be seen through this figure. The calorimetric temperature difference calculated between the two side resistors are 14 °C for design 1 and 24 °C for design 2, yielding a %70 increase in the sensitivity to CO<sub>2</sub>. This is a large and worthwhile improvement and can still be further optimised with regards to hole location and size as well as resistor location and size.

The sensitivity increase shown in the simulation is not as large as predicted by the analytical model. This is for two reasons:

- i. As is shown in the numerical modelling section in Chapter 3, the simulation underpredicts the effect of convection in the system when compared with the effect of conduction. This means that when convection plays a more important role (thermal conductivity sensors with holes), the magnitude of this role is underpredicted in the simulation and the result is less than the effect in real life.
- ii. The analytical model assumes that the thermal resistance seen by both sides is that of air. In fact, due to the holes being 120 µm away from the resistor there is a large amount of thermal loss through conduction before the membrane holes are reached.

In addition to this, the numerical model was used to investigate if there is a sensitivity increase to thermal conductivity with increasing hole size, which would also substantiate the previous findings that adding extra holes does not provide a large amount of extra benefit. The model was run with a biasing power of 10 mW in air and CO<sub>2</sub>. A graphical depiction of the three hole sizes chosen is shown in Figure 4.13 and the sensitivities and their percentage improvement can be seen in Table 4.4, which is taken from the slope shown in Figure 4.14.

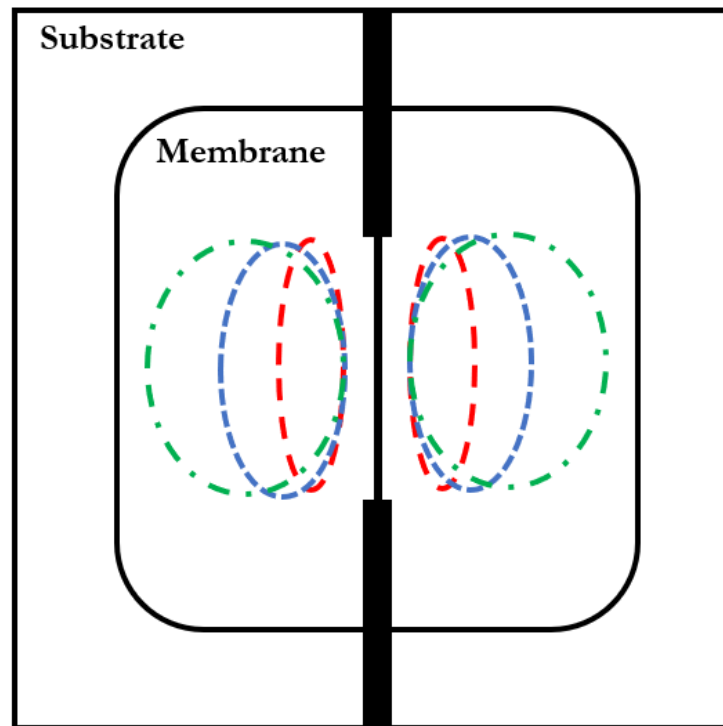


**Figure 4.13:** A graphical depiction of the three membrane holes investigated where small, medium and large holes are denoted by red, blue and green respectively.

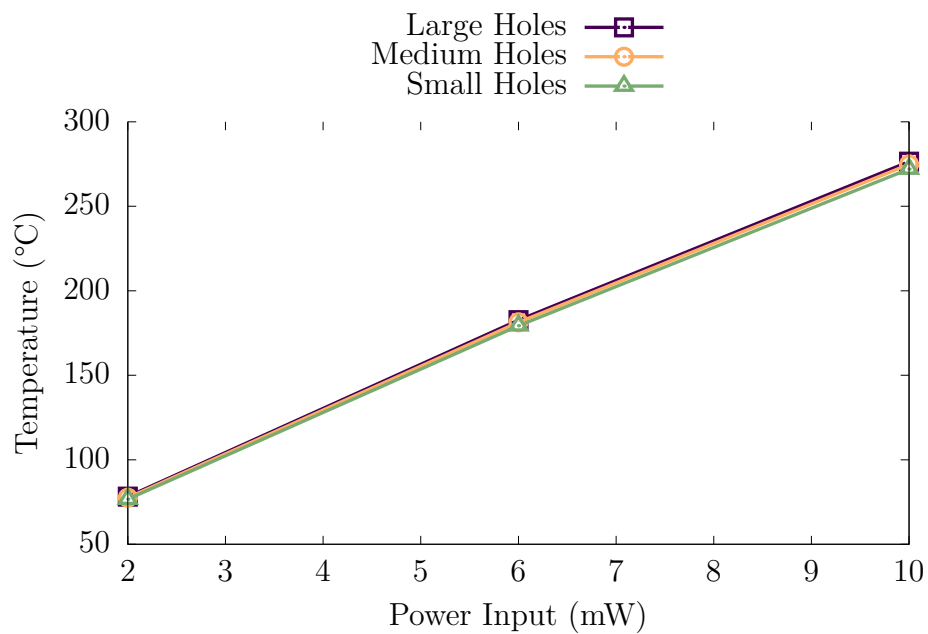


**Figure 4.14:** Temperature reached by the heater for the experiment and simulation.

**Table 4.4:** The sensitivity and improvement of the designs extracted from the power-temperature relationship.

Hole Type	Sensitivity (°C/%CO <sub>2</sub> )	Percentage Increase
Small Holes	0.416	-
Medium Holes	0.421	1.7
Large Holes	0.426	1.6

The addition of membrane holes shows that there is only a small increase in sensitivity to measuring the percentage CO<sub>2</sub> when widening the membrane holes, with the highest sensitivity increase being displayed by the large hole variation. This correlates with the earlier findings that two layers of holes in the fabricated designs did not add much improvement which is due to all three designs fully isolating the heating resistor by being longer, and thus varying their width does not have a large effect from more isolation.

The increase in efficiency is due to the much larger thermal resistance. Thermal conductivity  $k$  [W/mK] can be expressed by  $k = Q \cdot L / \Delta T$  where  $L$  is specimen thickness [m] and  $\Delta T$  is the temperature difference. Thermal resistance  $R$  expresses the difficulty of heat transfer and is given by  $R = L/k$  [K · m<sup>2</sup>/W]. Considering the ratio of thermal resistance through the membrane  $R_M$  against air  $R_A$  (with worst-case scenario of enclosed system through air),  $R_M/R_A = 50,000$ , thus the heat transfer from the heater is drastically reduced. The increase of the width of the holes doesn't significantly increase this ration, revealing why larger holes have a similar effect.

Finally, it should be noted that the simulation validation showed a slight underprediction of the change in heater temperature with percentage CO<sub>2</sub>, telling us that the increased sensitivity will be even larger when the devices are fabricated and tested. The small difference in sensitivity for hole size variation



is advantageous because in fabrication, small holes can be used allowing more resistors upstream and downstream of the heater. This will allow the sensor to be used with calorimetric and anemometric techniques, whilst also providing more parameters to increase the sensitivity to CO<sub>2</sub>.

## 4.6 Summary

Design, fabrication, packing and experiments were performed on thermal element gas thermal conductivity sensors. An extra manufacturing step was including to incorporate holes through the membrane, presenting a multitude of ways to improve the sensitivity to gases. In this section, the differentiation between air and CO<sub>2</sub> was investigated due to their large market need and difficulty of measurement thanks to their close thermal conductivity values. Key findings from this chapter are summarised below:

- i. It is shown that with the implementation of holes there is a large increase in the electro-thermal efficiency of the devices, with the largest increase seen for the double hole design at 69%.
- ii. It is then concluded that as long as the membrane hole covers the length of the heating resistor, there is not much further benefit in the addition of extra holes, which is due to the conductive path from the heater already being mostly blocked.
- iii. With the inclusion of isolating holes on both sides of the membrane, there is a 273 % increase in the sensitivity of measuring CO<sub>2</sub>.
- iv. A new method using asymmetric membrane holes is shown to be able to detect thermal conductivity by creating a difference with the amount of interaction with the gas upstream and downstream of the heater.

- v. Analytical and numerical methods are used to show designs that improve the sensitivity of this new method.

This study will aid with a new generation of low-cost MEMS thermal gas thermal conductivity sensors for application in industry and domotics. Recommendations of further work to be carried out with this sensing application is discussed in Chapter 6.

# Chapter 5

## Dual Flow and Thermal Conductivity Sensing

### 5.1 Introduction

**W**ITH the discovery and wide-spread use of micromachining techniques, thermal based sensors for the measurement of physical phenomena have found themselves in high demand across a multitude of industrial applications. This is thanks to their ability of implementation in a wide range of applications such as flow, thermal conductivity, diffusivity, heat capacity and pressure, among others. With their commonplace and continued research, these devices are becoming smaller, cheaper, more power efficient, more sensitive, more accurate and smarter.

In fact, the global MEMS market size was valued by Allied Market Research at 48.74 billion US dollars in 2018 and is projected to reach 122.83 billion by 2026, registering a CAGR of 11.30% in this time frame [1][206]. The largest contributing factors to this growth are predicted to come from smartphones, developments in the portable electronic market, increase in

popularity of the Internet of Things (IOT) and demand in the automation industry. This can be classified as a large increase in smart consumer electronics, which is shown to be of increasing prevalence in the future of the market by Figure 5.1.

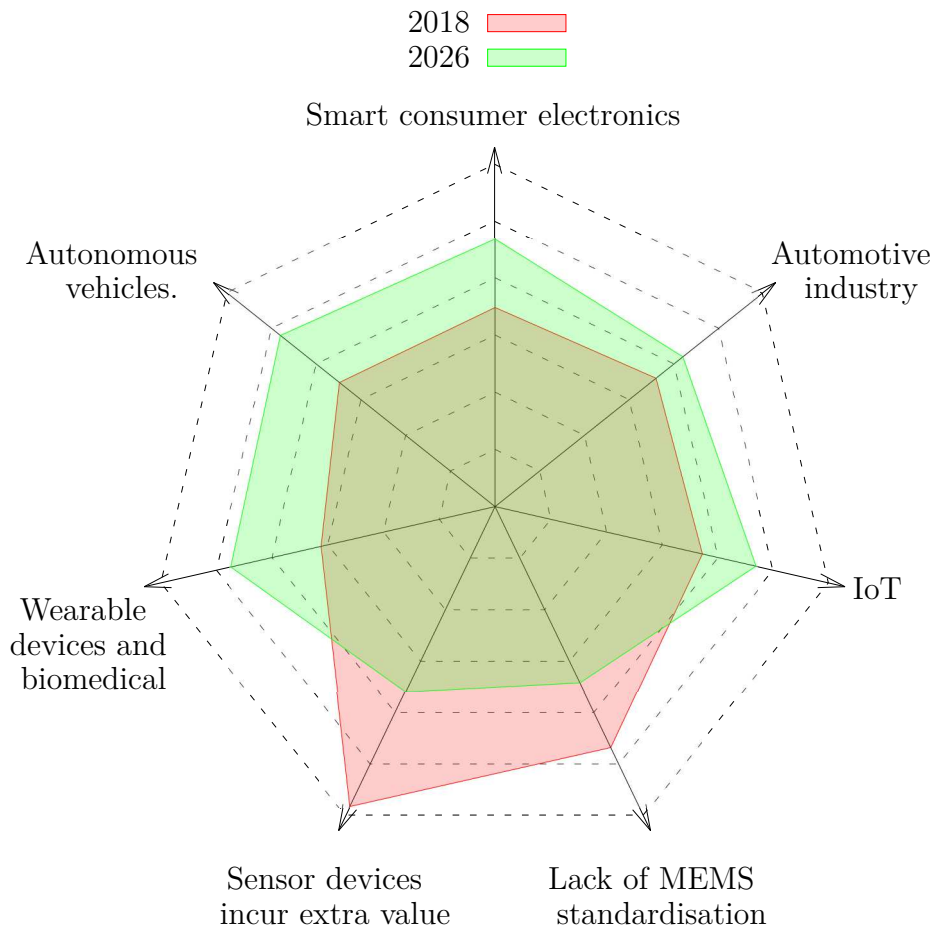


**Figure 5.1:** A chart showing the development of the top impacting factors on the global MEMS market from 2019 to 2026, trends are taken from [1].

It is with the knowledge that the future landscape of MEMS is trending towards smart consumer electronics and wearable devices that sensors must become smaller, more power efficient and most importantly, smarter.

Using micromachined thermal sensors for the measurement of thermal conductivity has attracted recent attention over their more researched counterparts of calorimetric or metal oxide gas sensors. This is due to their ability

to take measurements more quickly and that they do not rely on a reaction with a catalyst. In addition to this, micromachined flow sensors can be used to detect thermal properties of fluids such as thermal conductivity and thermal diffusivity using transient excitation such as the  $3\omega$  method [209, 210][194], [195].

Simultaneous thermal conductivity and thermal diffusivity sensing has also been shown [208][193]. There has been work looking to exploit the benefits of these sensors for gas chromatography [203][188], and for gas discrimination through DC and transient excitation [205, 213][190], [198]. Despite these recent advancements, there is still little research into solving the problem of dual flow and thermal conductivity sensing, due to the high interdependence of both parameters on sensor response. This has been investigated by combing results from several sensors in conjunction with complicated data acquisition [220][207]. [221][208] used a calorimetric flow sensor to measure thermal gas properties in non-stagnant flow. However, this method only works in previously calculated regions of flow independence.

The fabricated devices in this report incorporate holes through the membrane on either side of the resistor that isolate the resistor. This new design provides multiple benefits that include:

- i. The ability to negate front and back-side pressure differences, resulting in a large reduction in the number of catastrophic membrane breakages during fabrication and, especially, packaging, hence increasing through yield of the final device.
- ii. Minimising conductive heat losses through the membrane, thus improving the electro-thermal efficiency and power consumption of the device.
- iii. Minimising conduction through the membrane which also forces more interaction between the measuring resistors and the fluid flowing.

- iv. Creating an opening to the cavity below the membrane, resulting in twice the exposure to the gas and thermal heat losses from both sides of the resistor.

Smart sensors and sensor systems involve so many variables that it isn't practical to seek a hard, analytical model explicitly relating all the parameters. Many such methods for providing solutions have been proposed, with particular interest and success coming from linear statistical methods, such as Principal Component Regression (PCR) and Partial Least Squares Regression (PLSR). Some examples of such techniques in order to discriminate substances from a variety of inputs include [222, 223], with an overview of the technique and its diversity in applications here [224].

Artificial Neural Networks (ANNs) are another desirable tool used for powerful pattern recognition and data discrimination. This has led to the widespread use of ANNs for solving multi-variable functions, and more specifically for use with arrays of sensors. Some examples include electronic noses [225, 226], where a combination of metal oxide sensors are used in conjunction with one another, an optical sensor array for identifying multiple analytes [227], the use of impedance spectroscopy for the classification of wine [228], decoupling carbon monoxide and methane using platinum and tin dioxide sensors [229] and more recently, gas discrimination using a metal oxide-modified graphene-based sensor array [230].

In this work, linear statistical method Partial Least Squares Regression (PLSR) and Principal Component Regression Analysis (PCR) as well as an ANN approach for processing signals that arise from three resistors located in the membrane of a CMOS MEMS thermal flow sensor. The thermal flow sensor incorporates isolating holes through the membrane in order to enhance the gas discrimination, as shown in the previous chapter. These post-processing

techniques are used to de-couple the closely related parameters of thermal conductivity and flow rate.

A sensor that can successfully discriminate between these parameters will be in high demand throughout industrial applications and this paper serves to pave the way for the combination of a single-membrane, low-cost, low-power sensor and smart post-processing techniques for a new generation of multi-parameter sensing solutions.

## 5.2 Experimental

### 5.2.1 Sensor Design & Fabrication

The sensors were designed using Cadence Virtuoso (IC 5.1.4) and commercially fabricated with a 1.0  $\mu\text{m}$  standard CMOS process. The backside of the chip was etched using DRIE to create multiple thin-film membranes on one sensor, benefiting from multiple independent sensors on one device. An example of one of the chips is shown in Figure 5.2 with its cross-section depicted in Figure 5.3.

For this work, two membranes on the same chip that can be run independently were investigated. Both designs include 3 parallel tungsten heating resistors of identical dimensions and separation connected to wire bonding pads with 20  $\mu\text{m}$  tracks. An extra processing level was incorporated in order to add holes through the thin-film membrane in one of these designs. The two designs used are ‘no holes’ (reference design), and ‘holes’ (heating resistor isolation through holes on both sides of central resistor). The ‘holes’ design contains 4 holes in parallel on both sides of the central heater, ensuring full isolation. All membrane holes have the same geometry of 10  $\mu\text{m}$   $\times$  200  $\mu\text{m}$  with rounded edges to avoid stress concentration factors. Using a Kulicke and Soffa wedge bonder, the sensors were bonded onto Dual in Line (DIL8) packages, raised

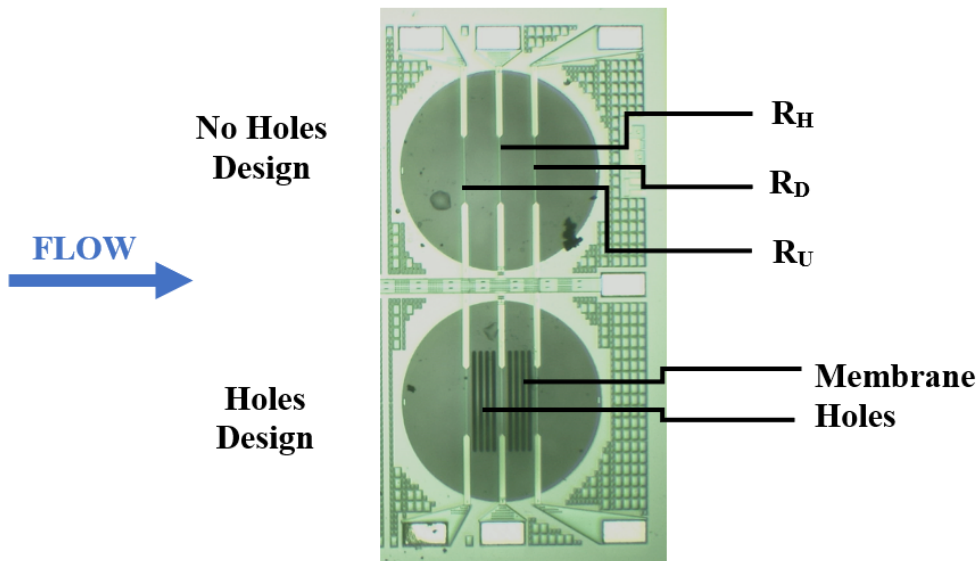


**Figure 5.2:** Optical micrograph of the investigated sensor chips – die dimensions of 2.0 mm  $\times$  2.0 mm.

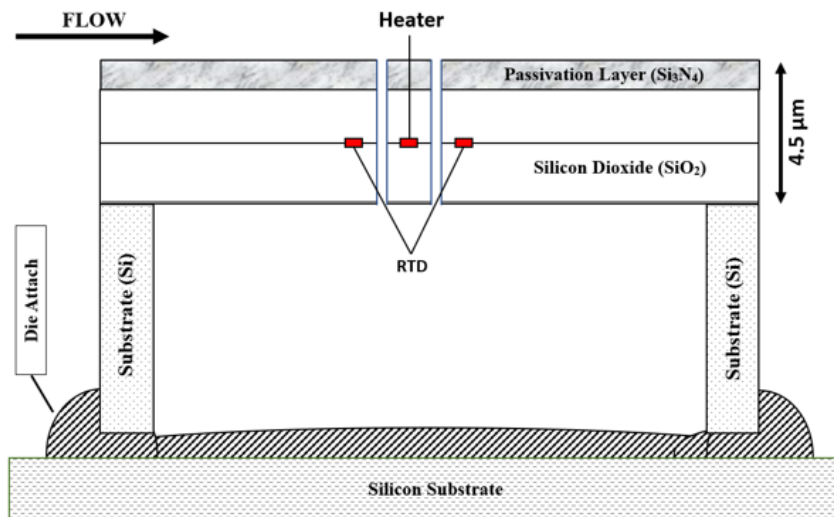


**Figure 5.3:** A cross-section of the layer technology used in fabrication for the design with membrane holes.



and filled to ensure a planar surface and integrated into an in-house 3D-printed channel of cross-sectional area  $1.5 \text{ mm} \times 2.5 \text{ mm}$ .

### 5.2.2 Measuring Setup & Testing Protocol

Measurements were performed in two separate experimental protocols. Firstly, the electro-thermal characterisation of the device heaters was performed between  $25 \text{ }^\circ\text{C}$  and  $300 \text{ }^\circ\text{C}$  using a Cascade probe station and hot chuck with Keithley source meters for data acquisition. This enabled the collection of important material properties such as the TCRs and electrothermal efficiency. For more detail on the details of electrothermal characterisation please refer to §4.3.

Using the information from this characterisation, the measurements with flow and  $\text{CO}_2$  were carried out using an array of Alicat Mass Flow Controllers (MFC), alongside an array of Keithley 2410 Source Meter Units (SMU) for data acquisition of the three resistors. An MFC was located after each gas cylinder to control the amount of both  $\text{CO}_2$  and air, which was subsequently fed into a mixing valve before the flow tunnel or order to vary the  $\text{CO}_2$  concentration. The packaged devices were subsequently exposed to a flow rate from 0 to 240 SCCM in steps of 40 SCCM in five different concentrations of  $\text{CO}_2$  in air (0%, 5%, 10%, 15%, 20%).

Such a flow range was chosen to ensure laminar behaviour was maintained in the channel. A bias current of 8 mA was applied to the central resistor for all experiments. The three resistors  $R_H$ ,  $R_U$  and  $R_D$ , where subscripts  $H$ ,  $U$  and  $D$  represent the heater, upstream resistor and the downstream resistor, respectively, are measured and the change in voltage of each  $V_H$ ,  $V_U$  and  $V_D$  are considered as the input variables for the post-processing techniques.

### 5.2.3 Linear Statistical Methods

Linear statistical methods were employed in order to test whether they can establish a predictive model from a set of independent variables (inputs) onto another set of continuous variables (targets). Partial Least Squares Regression (PLSR) and Principal Components Regression (PCR) are both methods that are used to model a response variable with many input variables, when the input variables are highly correlated or collinear. Both techniques construct new predictive components which are linear combinations of the original input variables, however the formation of these components is different and both methods are employed in order to see which is the most effective at mapping the behaviour correctly.

The main difference between the two techniques is that PCR does not consider the target variable to explain observed variability in the inputs, whereas PLSR does, thus often leading to an adequate fit in fewer components. PLSR assumes that the predictive components account for most of the variation measured by the original variables  $X(n, p)$ , that are linked to the response  $Y(n, 1)$  through the linear relationship of

$$\mathbf{Y} = \alpha + \mathbf{X}\beta + \Theta \quad (5.1)$$

where the unknown regression parameters are  $\alpha$  and  $\beta$  and  $\Theta$  is the error term. PLSR combines the properties of multiple linear regression and principal component regression analysis, producing a technique that separates sample noise and makes linear combinations in a dependent concentration matrix. It is widely used as the most effective linear statistical method for chemometrics and so is considered the best technique to use [231].

### 5.2.4 Network Architecture

Artificial Neural Networks (ANNs) consist of an interconnected web of parallel, adaptive elements, of which the architecture is based upon the physical biological system, namely on neurons and their interconnections, i.e. synaptic links. In our case, ANNs have been employed in order to de-couple the closely related parameters of flow and thermal conductivity. A network of three layers is chosen, due to its previous success in multi-parameter gas sensing and that adopting this format has enough degrees of freedom to solve any problem [232].

This three-layer network was implemented in order to model our 3-element system, where the input layer contains 3 nodes that correspond to each of the on-membrane resistor outputs  $V_H$ ,  $V_U$  and  $V_D$ . Each input node is connected to 10 nodes in the hidden layer, in which the elements are to be experimentally determined during the training phase. The outer layer consists of 2 nodes that correlate to the 2 parameters which we want to identify, namely the flow rate (SCCM) and thermal conductivity ( $\%CO_2$ ). The network consists of 3 input nodes that are fully connected to 10 neurons in the hidden layer, which are fully connected to the two output nodes. A diagram of the network architecture is illustrated in Figure 5.4.

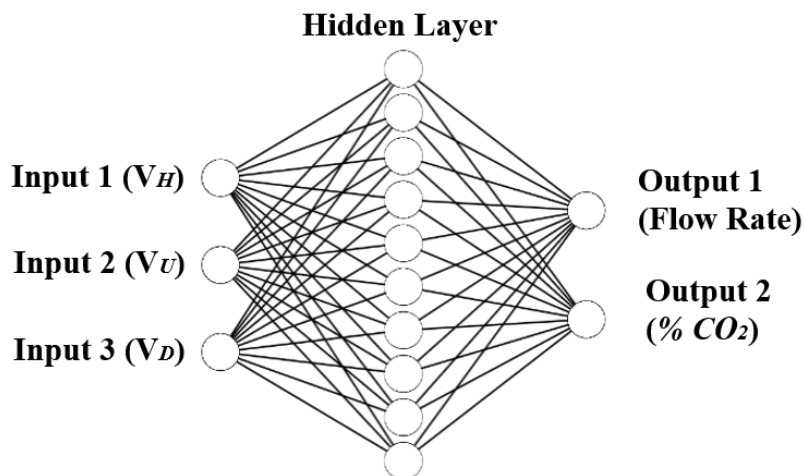


**Figure 5.4:** A diagram of the 3-layer network incorporated for 3 inputs and 2 outputs fully connected with 10 neurons in the hidden layer.

It is known that the learning algorithms of the nodes determine the performance of any implemented network. There are a multitude of different algorithms, and we have chosen the widely used back-propagation method.

## 5.3 Discussion

### 5.3.1 Response to Flow & Thermal Conductivity

The packaged devices were exposed to a flow rate from 0 to 240 SCCM in steps of 40 SCCM. This flow rate range was chosen due to turbulent flow being produced above this value, resulting in more heat extracted from the heater yielding an unpredictable response. The range is used to evaluate the advantages of the designs in the laminar region, which could easily be expanded, for example by enlarging the flow tunnel dimensions.

Figures 5.5, 5.6 and 5.7 show the enhanced gas discrimination shown between air and 20% CO<sub>2</sub> for the designs with and without holes for all three resistors. All values of voltage change were normalised by the base resistance by taking the voltage change with respect to no flow. It should be noted that the plots also show the absolute values of voltage change. Figure 5.5 shows the voltage change of the heater  $V_H$ , which shows a higher sensitivity with flow as well as clear differentiation between the line of air and 20% CO<sub>2</sub>, yielding strong discrimination between gases even with the presence of flow. Figure 5.6 is the voltage change in the downstream resistor  $V_D$ . As the peak of the thermal profile is shifted through forced convection, the voltage change is initially negative. This effect is significantly increased with the addition of membrane holes, resulting in the increased calorimetric benefit as well as providing more identifiable and detectable features for multi parameter data analysis, specifically with regards to flow rate as this feature is solely due

to fluid flow and not its thermal conductivity. Finally, Figure 5.7 shows the upstream resistor  $V_U$ , providing another parameter with higher sensitivity to flow and better gas discrimination.

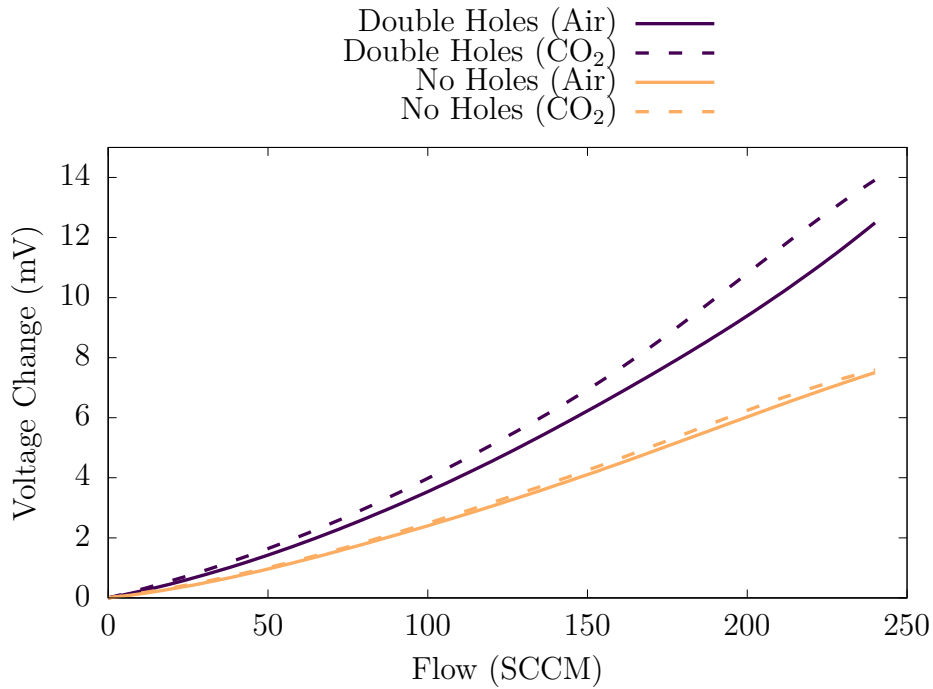


**Figure 5.5:** The discrimination between air and 20% CO<sub>2</sub> after being normalised by base resistance for the designs with double holes and without holes for the central resistor.

Using membrane holes has vastly increased the selectivity to thermal conductivity with the presence of flow. Using this design and all the improved gas selectivity responses, linear statistical methods and ANNs will be used to try and successfully identify and discriminate these two parameters.

### 5.3.2 Data Pre-Processing

It is important to examine the data that is generated by the array of three resistors in order to make the most informed choice of pre-processing method. Informed decisions can be designed to help analyse the data for our specific

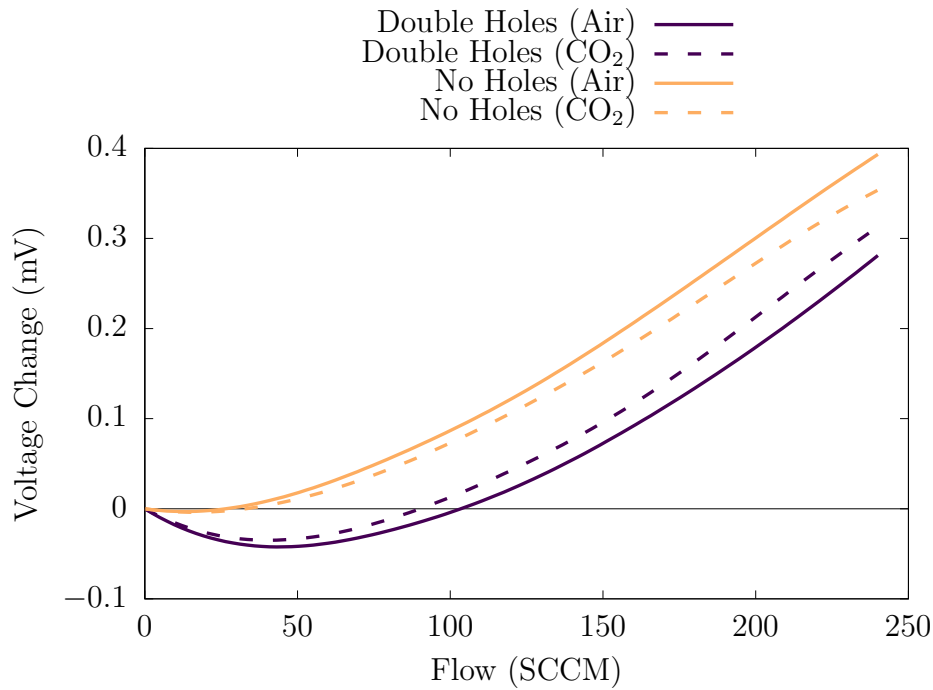


**Figure 5.6:** The discrimination between air and 20% CO<sub>2</sub> after being normalised by base resistance for the designs with double holes and without holes for the downstream resistor.

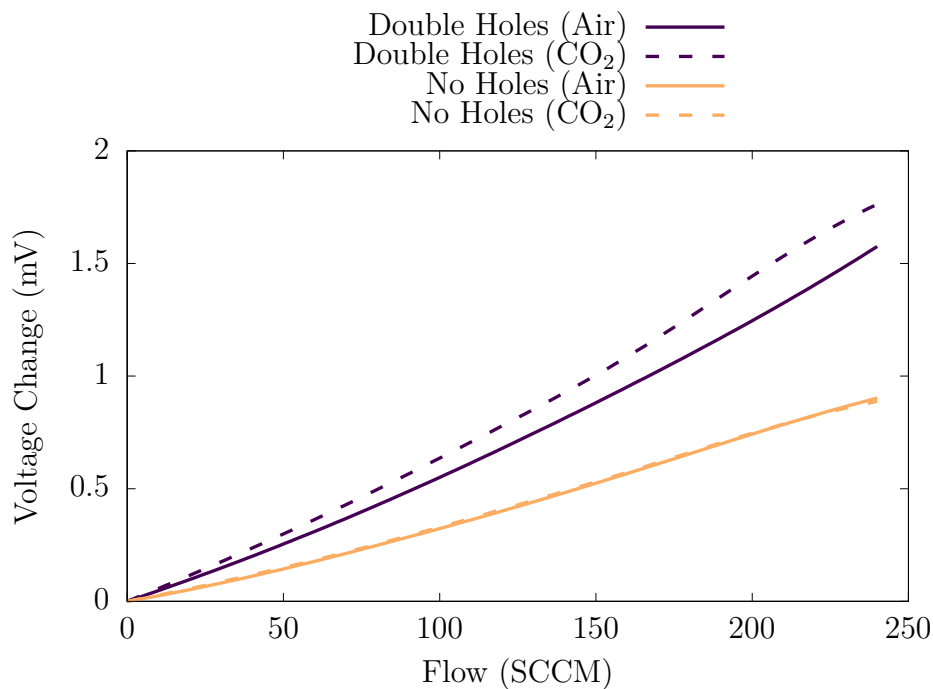


**Figure 5.7:** The discrimination between air and 20% CO<sub>2</sub> after being normalised by base resistance for the designs with double holes and without holes for the upstream resistor.

problem, such as compensating for fluctuations in the vectors. There were two pre-processing protocols implemented in this work:

- i. The input values  $V_H$ ,  $V_U$  and  $V_D$  were auto ranged in order to make their range from -1 to +1 by using the equation  $[2(V - V_{MIN}) / (V_{MAX} - V_{MIN}) - 1]$ .
- ii. The output values were normalized to  $U/U_{Max}$  and  $\%CO_2/\%CO_{2,Max}$ , where  $U$  refers to the flow rate in Standard Cubic Centimetres per Minute (SCCM),  $U_{Max}$  is the highest value of flow rate,  $\%CO_2$  is the percentage  $CO_2$  in air and  $\%CO_{2,Max}$  is the max percentage of  $CO_2$  in air.

These pre-processing techniques will help the performance of the multi-variable analysis. Auto-ranging the data means that all three sensors are made to be equal magnitude, and therefore have equal influence on the network. Auto-ranging the inputs whilst also normalizing the targets is performed to help set the weights in the neural network that will start in this range, yielding quicker and better convergence.

### 5.3.3 Linear Statistical Methods

Two linear statistical methods were investigated to see whether they could adequately map the system in order to predict the outputs for flow and  $CO_2$ . Initially, three PLS components were calculated and it is shown that using 2 or 3 components accounts for 99% of the variance shown in the inputs whereas 1 component shows 85% variance explanation. Therefore, it is known that there is no benefit of using 3 components and 2 components are used for the rest of the analysis. Using two components for both PLSR and PCR, the data of the actual response is plotted against the data of the fitted response for the output of flow rate (Figure 5.8 (a)) and  $\%CO_2$  (Figure 5.8 (b)). Both

methods show a close relationship between the experimental outputs and those estimated by the linear methods for flow rate, meaning a good prediction of flow rate can be achieved by implementing these methods. The R-Squared value for PLSR is 0.9938 and is 0.9934 for PCR, resulting in neither method being superior. Interestingly, Figure 5.8 (b) shows that neither method can accurately predict the response of CO<sub>2</sub> with R-squared values of 0.6436 and 0.6179 for PLSR and PCR, respectively. This suggests that the mapping is nonlinear, i.e. the principle of linear superposition does not apply, which is likely due to the strong effect from flow that is highly different for all three resistors. It is for this reason that the following investigation of using artificial neural networks is carried out.

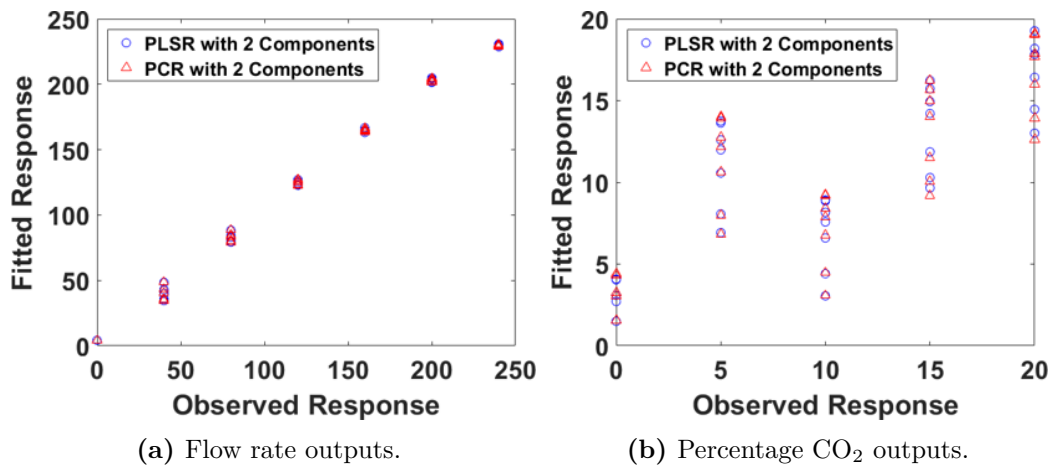


**Figure 5.8:** The observed responses of the experiment against the fitted responses from PLSR and PCR linear correlation methods.

### 5.3.4 Implementation of Artificial Neural Networks

An artificial neural network has been employed to de-couple the closely related parameters of flow rate and thermal conductivity, which could not be achieved through linear statistical methods. The splitting of data method known as ‘Training-and-test’ was used due to its extensive use for classification and discrimination problems. This method divides the available data into two groups. The first group is used to train the data using the back-propagation



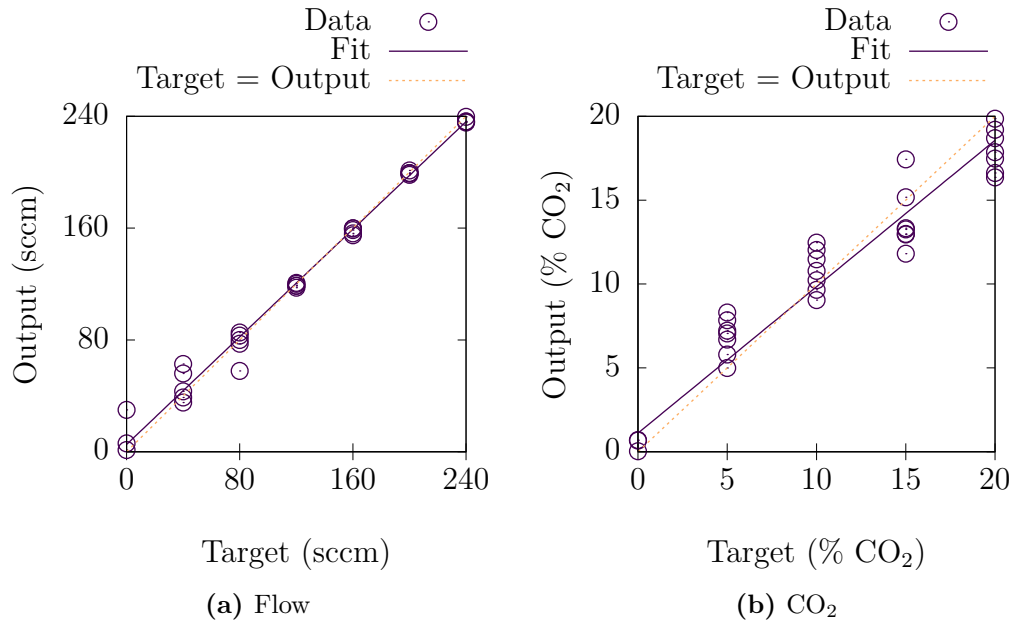
learning algorithm whilst the second group is used to test the trained data. In our case, 30 samples of the data were used as the training set whilst the remaining 6 were used to test the network. The Bayesian Regularization training algorithm was used due to its ability at good generalization for small noisy datasets, with the training stopping according to the adaptive weight minimization.

After training the network, the sensor with holes showed a quicker convergence using 541 iterations as opposed to 1021 for the no holes design. The 6 extra samples were run through the trained network as testing data. The Mean Squared Error (MSE) is the average squared difference between the outputs from the tested data through the network and the targets.

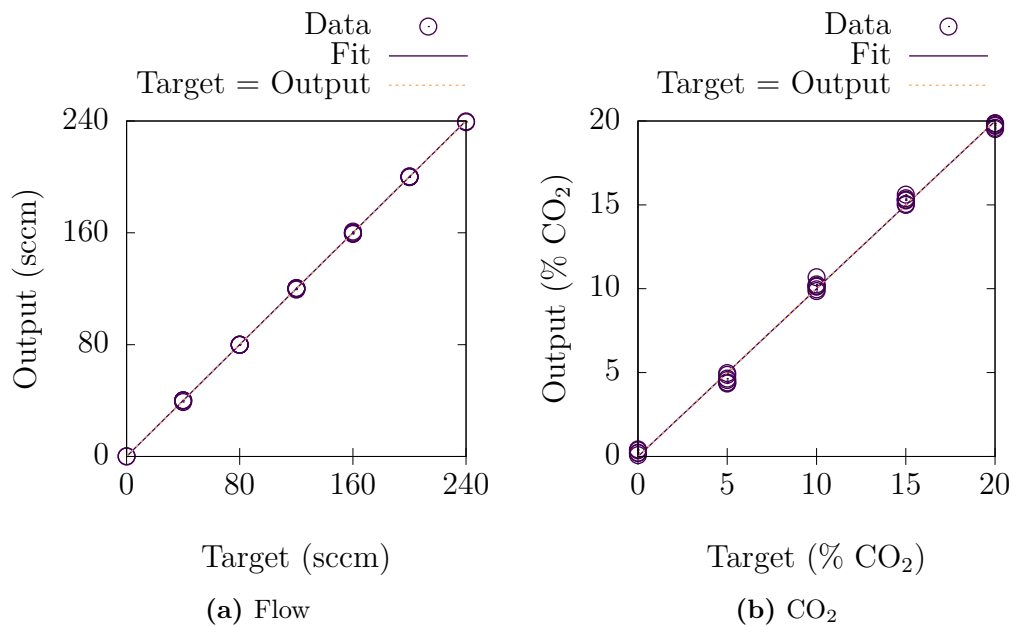
The device with membrane holes showed an average MSE of  $7.28 \times 10^{-5}$ , whereas the device without membrane holes had an average MSE of  $1.13 \times 10^{-2}$ . This shows an increase of over 150 times, providing strong evidence that the membrane holes provide a superior response for enhanced gas discrimination. In addition to this, Figure 5.9 and Figure 5.10 show the output value from the neural network compared to the target value taken from the measured data. The outputs are split into response to flow and % CO<sub>2</sub> for both designs of holes and no holes. A line of best fit is added that encompasses all of the data points and a dotted line is also added that represents the exact mapping of targets onto outputs, which can be considered a perfect response.

Figure 5.9 (a) shows that the network has a larger variance of outputs in the lower flow rates, but can better predict the flow rate in the higher regions. This is due to forced convection having a much stronger effect at these higher flow rates, allowing distinguishable features to be captured. Figure 5.9 (b) shows a large error when trying to predict the CO<sub>2</sub> concentration as well as the best fit line being noticeably different to the exact mapping line. This poor result is because the design with no holes shows very similar response with

changing gas concentration, thus not providing any different features to be recognised by the neural network.



**Figure 5.9:** The output values from the neural network compared against the target values from experimental data for the design with no holes.



**Figure 5.10:** The output values from the neural network compared against the target values from experimental data for the design with holes.

With the addition of holes in the membrane, Figure 5.10 shows that there is large improvement for both the prediction of flow rate and gas concentration. This can be ascribed to the membrane holes inducing different responses with changing gas concentration, allowing it to be more easily differentiated to both flow rate and gas concentration simultaneously.

The regression value,  $R$ , quantitatively shows the correlation between these outputs and their targets. For the design with no holes, the  $r$ -values are 0.995 and 0.962 for flow and  $\text{CO}_2$ , respectively. These values increase to 0.9999 and 0.9997 for flow and  $\text{CO}_2$ , respectively. This numerically shows that the addition of membrane holes dramatically improves the ability to separate and predict both parameters.

Table 5.1 & Table 5.2 show the results of 6 samples used for testing the trained network for the designs with no holes and holes respectively. Here the network provided a flow rate and percentage  $\text{CO}_2$  for previously unseen  $\text{CO}_2$  concentration and/or flow rates.

A Full Scale (FS) percentage error has been calculated via the difference between the target and network output as a percentage of the full reading range (i.e. 240 SCCM). Firstly, it is shown that the neural network successfully de-couples the two parameters. In addition to this, the addition of isolating holes in the membrane has multiplied the accuracy of flow measurement by approximately 10 times and the percentage  $\text{CO}_2$  by over 2 times.

Although discrimination has been displayed, there are many aspects that need to be investigated that can further optimize this sensing solution. The network is trained on relatively few data samples, using more could increase the accuracy and an optimum training set size should be investigated, i.e. decreasing the step size for percentage  $\text{CO}_2$  or flow rate measurements. In addition to this, optimum network architecture needs to be investigated, such as the number of hidden layers, neurons in these layers and back-propagation

**Table 5.1:** Table showing the results of testing the trained network 1 for the design with no holes.

Target		Output		% FS Error	
Flow (SCCM)	% CO <sub>2</sub>	Flow (SCCM)	% CO <sub>2</sub>	Flow (SCCM)	% CO <sub>2</sub>
40	10	41.95	9.55	0.81	0.45
40	20	57.44	19.37	7.27	0.63
160	0	160.22	1.46	0.10	1.46
160	10	161.03	10.79	0.43	0.79
120	15	114.92	10.39	2.12	4.61
80	5	84.35	9.33	1.81	4.33
<b>Average</b>				<b>2.09</b>	<b>2.05</b>

**Table 5.2:** Table showing the results of testing the trained network 1 for the design with holes.

Target		Output		% FS Error	
Flow (SCCM)	% CO <sub>2</sub>	Flow (SCCM)	% CO <sub>2</sub>	Flow (SCCM)	% CO <sub>2</sub>
40	10	39.94	8.66	0.025	1.34
40	20	39.69	20.03	0.13	0.03
160	0	158.28	1.75	0.72	1.75
160	10	159.89	9.15	0.046	0.85
120	15	119.64	13.65	0.15	1.35
80	5	79.12	4.37	0.37	0.63
<b>Average</b>				<b>0.24</b>	<b>0.98</b>

techniques. Heater temperature measurements would be a highly interesting parameter that could be incorporated into this post-processing in order to compensate for these variables. In future work, the system should be designed for real-time updating of the network training. This will allow an adaptive network that can be used for many different sensors.

## 5.4 Summary

An experimental method for applying artificial neural networks and two linear statistical methods in order to discriminate between flow rate and thermal conductivity has been described. The method uses a single CMOS MEMS thermal flow sensor that has three resistors embedded in the membrane. In addition to the resistors, there are two designs tested where one incorporates holes through the membrane that isolate the central resistor, forced enhanced interaction with the flowing fluid.

It is shown that there is an increase in the ability to discriminate between different thermal conductivities even with the addition of flow. Using a three-layer network architecture, it was found that the two closely related parameters of thermal conductivity could be de-coupled. In addition to this, the addition of the membrane holes increases the sensitivity towards flow rate by 10 times and the sensitivity towards thermal conductivity by 2 times. This sensor design coupled with well-known post-processing techniques will enable a new generation of multi-parameter sensing solutions.



# Chapter 6

## Conclusions & Further Work

### 6.1 Preface

THE main objective of the work in this thesis was to develop low-cost, low-power, small devices capable of high-volume production and monolithic integration using the same smart technology platform for fabrication. The driving factors for this work stem from industry and the commercial need for cheaper, smaller sensors with the continuing growth of portable consumer products.

Chapter 1 provided the motivation behind research and development of sensors with specific focus on MEMS-based sensors. An overview of CMOS-MEMS and SOI technologies are discussed with a summary of their benefits and drawbacks. The technology platform used to fabricate all of the sensors in this thesis is described and the chapter is concluded with a discussion on mechanical and thermal based MEMS sensors, with a focus on their prevalent technologies and commercial applications.

Chapters 2 - 4 are self-containing chapters that each discuss a different sensing technology. Each chapter has an introduction to the relevant technology and goes on to describe the work carried out from design through to experiment and discussion.

Chapter 5 gave an example of multi-parameter sensing from a single sensor device, using smart post-processing methods. This is an example of how both the sensor design and data analysis can be used together to successfully create more intelligent sensors.

Finally, this chapter describes the conclusions and suggested further work specific to each chapter.

## 6.2 General Conclusions

Some general conclusions that can be made about all the chapters contained within this thesis and are summarised below:

- i. A 1.0  $\mu\text{m}$  CMOS MEMS commercial fabrication process was used to create a variety of miniaturised silicon sensors. Several proof-of-concepts and technology optimisations were presented in order to advance the understanding and help application integration of MEMS sensors.
- ii. A multi-physics numerical model was developed and substantiated by experimental data. This model was used to provide quick and accurate optimisation without the need of an iterative fabrication procedure.
- iii. Silicon-On-Insulator (SOI) wafers were used to investigate the advantages of integrating electronic components within the thin single crystal silicon layer. SOI devices were then compared with their bulk silicon counterparts to analyse their relative price/performance ratios.



## 6.3 General Further Work

A few ideas are hereafter presented for general further work that could be carried out, spanning across the sensing technologies presented in this thesis.

- i. Although considerable work has been carried out for optimisation and proof-of-concepts for many sensing designs, these have not been bespoke for application. Further work could look at sensor requirements in terms of cost, power consumption and performance for industrial and commercial applications. Sensors could then be optimised specifically for such applications to provide a new solution that could displace currently used technologies.
- ii. All the sensors designed in this process are CMOS compatible. Further work could be carried out that takes advantages of integrated CMOS electronics in order to have integrated micromachined electronics that help increase accuracy and simplicity of the sensor data acquisition system.

The future of MEMS is linked to market trends and is thus driven by the increasing demand to monitor and control our environment, equipment and instruments that we use in our daily lives. This demand undoubtedly leads to the need for more sensors. In order to avoid complex systems that contain hundreds of sensors and wires, many sensors will need to be wireless and self-sustaining. As a result, sensors will need to require very low power consumption so they may be couple with energy harvesting systems. The miniaturisation of MEMS using micromachining technology will drive size reduction, which will result in lower power consumption and in turn enable higher levels of integration. Ultimately developing alongside the market.

## 6.4 Pressure Sensors

### 6.4.1 Conclusions

Chapter 2 discussed the design, fabrication and characterisations of MEMS pressure sensors. The chapter was split into two sections where the former discussed the characterisation of the piezo-resistive designs and the latter discussed the piezo-junction designs. These devices are particularly attractive for consumer electronics due to their small size, low power consumption and very low price when produced in high volume.

The piezo-resistive pressure sensors were created by using a Deep Reactive Ion Etch (DRIE) to remove the backside silicon and create a thin membrane that deforms under pressure. Doped regions were used to create four piezo-resistors in the membrane where a Wheatstone bridge can be used to read out the asymmetry produced when a pressure is applied. Key findings from this section are condensed into the following points:

- i. With the reduction of membrane size, the linearity of the response is improved, which agrees with known thin-film deflection theory. However, in the case of the fabricated sensors, the sensitivity also increases, which can be attributed to the large membrane size/thickness ratio meaning there is a ballooning effect which may not be in the location of the piezo-resistors. With the reduction in membrane size, this effect is reduced and a more uniform deformation is achieved and thus increases the device sensitivity.
- ii. Having the intrinsic region in the piezo-diode improved sensitivity, but when its doping concentration was too high the noise became so large that the extra sensitivity was useless.
- iii. A structural metal ring was used to create a new perimeter. This perimeter has a higher rigidity than the silicon dioxide membrane and creates a

new edge to the deflection under pressure. When there is over or under etching of the membrane, the reproducibility of the sensor response is not affected as much due to the high tolerances that are achieved with the placement of the metal layer.

- iv. Incorporating metal cross track structures in the membrane was used to improve sensitivity whilst also improving linearity, proving to be the best device out of all the tested pressure sensors.

Using SOI technology, electronic devices were embedded within the membrane to act as the pressure transducing elements. MOSFETs and diodes were investigated to see their benefits when compared to the more traditional piezoresistive transduction method. Key findings from this section are condensed into the following points:

- i. The design, fabrication, experiment, and results of a MOSFET based pressure sensor are reported. The design embeds four MOSFETs within a silicon dioxide membrane via CMOS microelectromechanical system technology and incorporates a Wheatstone bridge in order to relate the change in carrier mobility in the MOSFET channel to the change in pressure.
- ii. The pMOSFET showed the highest sensitivity of 5.21 mV/kPa, showing significant improvement on other MOSFET-based technologies in addition to piezoresistive designs while retaining a low power consumption.
- iii. Piezo-resistors are resistive based devices and therefore have a large power consumption. The piezo-MOSFET is shown to have lower power consumption and therefore gives a better sensitivity when normalised by input voltage.
- iv. Design, fabrication and characterisation of piezo-diodes has been shown, proving these components can be used within a pressure sensor.

- v. The pressure coefficient of energy band-gap has been dramatically increased when comparing to a traditional p-n junction, resulting in a higher sensitivity.
- vi. The sensitivity is found to be highest for the p+/p-drift/n+ diode with bias current of 10  $\mu\text{A}$ , where the sensitivity is 79  $\mu\text{V}/\text{mbar}$ .
- vii. The sensitivity of the piezo-diode device is much lower than the other piezo transduction technologies and needs to be improved further in order to commercially competitive.

These results pave the way for future commercial implementation of pressure sensors using this technology platform as well as giving deeper understanding into some geometrical properties and the possibility of implementing electronic components for a more power efficient transduction element.

## 6.4.2 Further Work

This chapter provides a first step in the process towards generating a pressure sensor that can outperform current pressure sensors in the market, thus giving them reason to be replaced. The work carried out could be extended in several directions. A few suggestions of further steps are summarised below:

- i. The main drawback of all the fabricated sensors is the high non-linearity of the sensor response. This non-linearity is caused by the geometry of the membrane, in particular the very high ratio between membrane diameter and membrane thickness, causing the balloon effect. It is essential to minimise this non-linearity into the region displayed by other commercial pressure sensors. This can be done by altering the membrane size, thickness and/or adding supporting structures throughout

the membrane to create a consistent and predictable deflection throughout the membrane.

- ii. Using previous literature and TCAD numerical modelling, the doping regime of the piezo-resistive element can be optimised for doping concentration for the different regions as well as the shape of these regions.
- iii. During the proof-of-concept showing the piezo-MOSFET, only one design of pMOSFET (better performance than nMOSFET) was investigated. If this technology is to become commercially viable, the design of the pressure sensing MOSFET itself must be optimised now that it has been proved to function.

## 6.5 Flow Sensors

### 6.5.1 Conclusions

Chapter 3 discusses the design, fabrication, packaging, experiment, numerical simulations, electro-thermal characterisation and flow rate calibration results of CMOS MEMS thermal flow sensors based on a tungsten heating element. The CMOS fabrication process allows low-cost, high-volume production of miniaturised flow sensors with the possibility of on-chip electronics whilst providing superior performance and reproducibility. DRIE was used to minimise conductive heat loss whilst maintaining its mechanical strength. Key findings from this section are condensed into the following points:

- i. A numerical model was created using COMSOL Multiphysics and was validated against experimental data. 2-dimensional and 3-dimensional models were compared and contrasted and it is found that 3-dimensional

modelling is needed for quantitative analysis, however 2-dimensional can be used if a quick answer on qualitative device behaviour is wanted.

- ii. The numerical model was used to find the optimum location for RTDs in calorimetric mode. It is shown that the location of highest sensitivity depends in the targeted flow rate and provides the information for designers to take this into account when creating application specific devices.
- iii. The effects of geometrically altering the sensor structure was investigated, with particular regard to electro-thermal efficiency, sensitivity and accuracy. The device with highest electrothermal efficiency had the shortest resistor length whilst maintaining a large membrane size. It is also shown that the sensitivity relies on heater length and is minimally affected by heater width.
- iv. Numerical modelling was used to highlight an area of recirculation around the heater in stagnant to low flow rates that generates noise.
- v. Thermo-electronic devices were simultaneously compared to thermo-resistive and showed to retain their accuracy with the miniaturisation of the membrane.
- vi. A diode that is too short has non-linear electrothermal behaviour due to current leakage.

This study will lead to the design of a new generation of MEMS thermal flow sensors with improved performance for application in industry and domotics.

### **6.5.2 Further Work**

Some suggestions of future work that could be carried out with regards to flow sensors are summarised below:

- i. All the geometric analysis was performed using constant current driving. Comparing constant temperature driving with constant current with regards to how they can be optimised individually would be a worthwhile examination.
- ii. With the ability to fabricate multiple resistors across the membrane, Time of Flight measurements could be investigated, leading to a comparison between anemometric, calorimetric and ToF operation principles.
- iii. The flow sensing in this thesis used steady state analysis. It would be interesting to investigate the transient response of the sensor to try and obtain more information from the surrounding medium, such as thermal conductivity and thermal diffusivity. Methods such as the 3-omega technique could be explored to create a smarter device.

## 6.6 Thermal Conductivity Sensors

### 6.6.1 Conclusions

Chapter 4 discusses the design, fabrication and characterisation of four different designs of CMOS MEMS thermal conductivity sensor for use as gas sensors. The sensors are fabricated using a tungsten metallisation process and thus, have a tungsten heating element. A numerical model is also developed in order to further optimise the device performance. Key findings from this section are condensed into the following points:

- i. Four sensors have been fabricated that have holes through the membrane to isolate the heating resistor and/or RTDs. These holes are created by incorporating a front-etch that uses the silicon as an etch-stop before the backside DRIE.

- ii. The main purpose of incorporating membrane holes was the increase the yield of high-volume manufacturing. This is due to the self-equalising properties of a device with membrane holes, resulting in fewer catastrophic failures caused by pressure differences when packaging.
- iii. When fully isolating the heating resistor, there is an improvement in the electro-thermal efficiency by 69%, resulting in a more power efficient device.
- iv. Full isolation of the heater also increases the sensitivity to measuring CO<sub>2</sub> in air by 270%.
- v. A novel method of measuring percentage CO<sub>2</sub> is presented that uses asymmetric membrane holes to force more interaction with the gas from one of the RTDs, inducing an asymmetric read out that depends on the thermal conductivity of the surrounding gas.
- vi. Theoretical and numerical analysis are presented showing how to improve the sensitivity of the asymmetric method by an order of magnitude.

### 6.6.2 Further Work

This chapter is the first work carried out towards using this technology platform for thermal conductivity gas sensors. There are many directions in which this work could be further extended, a few suggestions are listed:

- i. The sensors were primarily intended to be used as flow sensors and thus have not been specially optimised for thermal conductivity. A detailed look at the geometry of the sensor and heater and how this can be optimised for thermal conductivity measurements should be carried out.
- ii. With the description of the new asymmetric measurement technique came a solution for increasing the sensitivity. Figure 6.1 and Figure 6.2 show



an optical micrograph of the suggested improvement with two designs. These devices must be tested to validate their sensitivity improvement and check whether they can compete with the traditional anemometric operating principle.

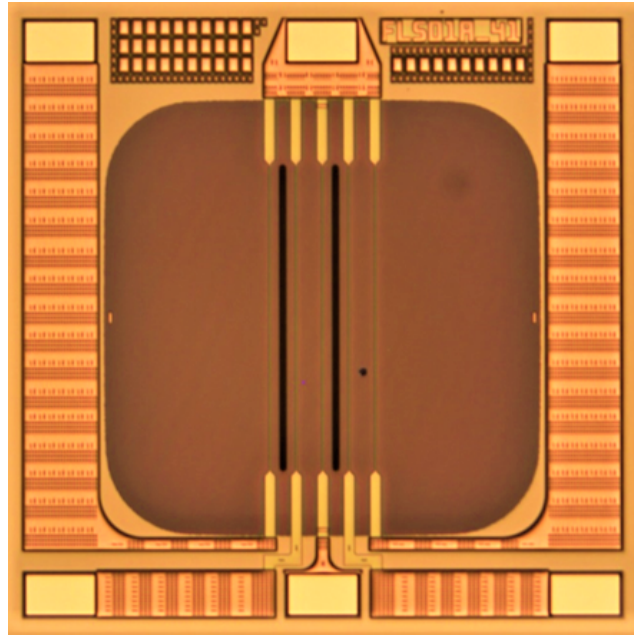


**Figure 6.1:** Optical micrograph showing an example of a fabricated design with asymmetric membrane holes for optimising sensitivity.

- iii. Using Differential Thermal Analysis (DTA) could be explored to counteract the inherent selectivity issue in thermal conductivity detectors. This technique consists of a sample and reference zone, which could be heaters at either end of the membrane for temperature control. The two elements are heated simultaneously with a heating and cooling profile that is identical, whilst one of the elements is in some way different to the other. The differential temperature is plotted against time or temperature and behaves differently for different gases, making the use of pattern recognition analytical methods for gas discrimination possible. This method has been used to discriminate gas mixtures with success [233] and similar techniques could be applied to increase the selectivity of the devices.

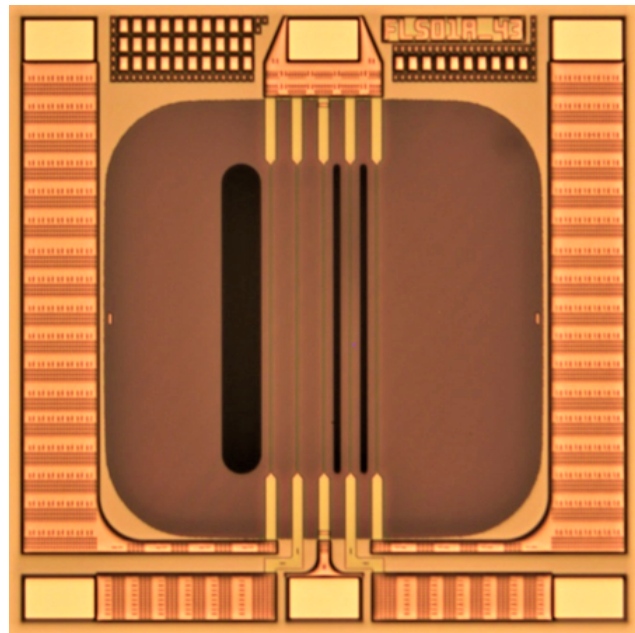


**Figure 6.2:** Optical micrograph showing an example of a second fabricated design with asymmetric membrane holes for optimising sensitivity.

## 6.7 Multi-Parameter Sensors

### 6.7.1 Conclusions

Chapter 5 discusses the design, characterisation, experiment and post-processing techniques used in order to measure both flow rate and thermal conductivity simultaneously. Namely, linear statistical methods and artificial neural networks are employed to separate the two closely related parameters.

- i. It is shown that with the addition of isolating membrane holes, the discrimination between gases is made more prevalent even in the presence of flow, providing features that help to distinguish gas as well as flow rate.
- ii. It is shown that linear statistical methods partial least squares regression and principle component analysis are capable of predicting the flow rate seen but can not accurately tell the CO<sub>2</sub> concentration.

- iii. An Artificial Neural Network (ANN) is trained using 70% of the data and then applied to data unseen to the network. The network predicts both flow rate and percentage CO<sub>2</sub> to within 1% full scale error with the design that contains isolating membrane holes.

### 6.7.2 Further Work

Chapter 5 discusses using post-processing techniques to measure more than one parameter using the same chip. Several directions can be taking to further this research with regards to multi-parameter sensing on a single chip, a few suggestions are summarised below:

- i. Although discrimination has been displayed, there are many aspects that need to be investigated that can further optimize this sensing solution. The network is trained on relatively few data samples, using more could increase the accuracy and an optimum training set size should be investigated, i.e. decreasing the step size for percentage CO<sub>2</sub> or flow rate measurements. In addition to this, optimum network architecture needs to be investigated, such as the number of hidden layers, neurons in these layers and back-propagation techniques.
- ii. Other work could look at implementing extra parameters as the input variables that will add information and contribute to the discrimination. One interesting parameter would be the heater temperature.
- iii. With the combination of multiple resistors and multiple holes of any size, many more designs can be investigated and created for helping to discriminate between flow and thermal conductivity. Figure 6.3 shows an example design where the heating resistors parallel to the flow are less affected by the flow and more by thermal conductivity, whilst the perpendicular heater can be used to measure the flow. This design could

help to further discriminate between the two parameters and there are a multitude of new designs to explore with this technology.

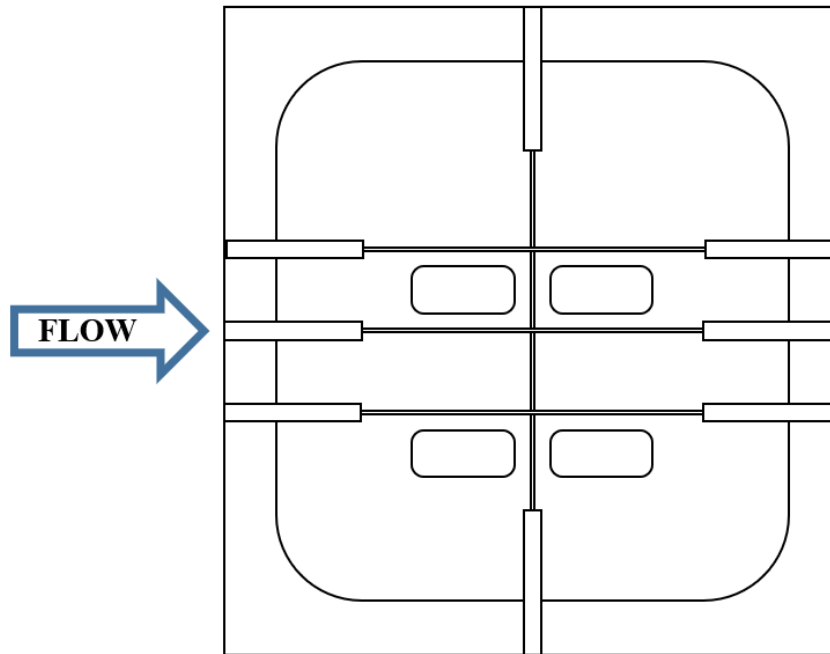


**Figure 6.3:** A design idea for both thermal conductivity and flow measurement using perpendicular wires.

- iv. With the technology platform providing a base for several sensing technologies, a large area for future investigation could be the combination of two sensor technologies on one membrane. An example is shown in Figure 6.4 where pressure sensitive piezo-resistors and a heater for flow rate measurement are incorporated onto a single membrane. Further investigation into this device and other combinations should be investigated to provide more multi sensing solutions on a single chip.

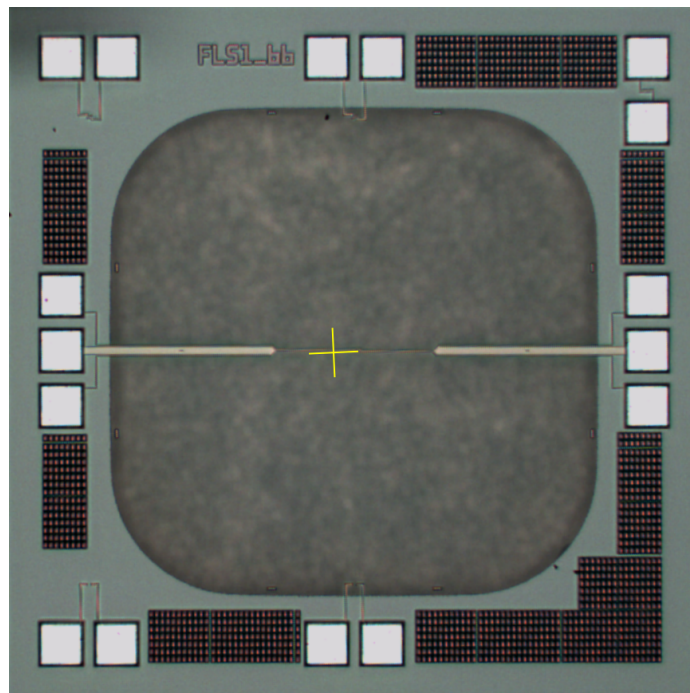


**Figure 6.4:** An optical micrograph of a sensor with a heater for flow measurements and piezo-resistive pressure sensitive elements.



# References

- [1] Supradip Baul Divyanshi Tewari. Microelectromechanical System (MEMS) Market by Type (Sensors, & Actuators), and Application (Consumer Electronics, Automotive, Industrial, Aerospace & Defense, Healthcare, and Telecommunication, and Others): Global Opportunity Analysis and Industry Forecast, 2019–2026. Technical report, Allied Market Research.
- [2] Rob Lineback. O-S-D Report—A Market Analysis and Forecast for Optoelectronics, Sensors/Actuators, and Discretes. Technical report, IC Insights, February 2019.
- [3] J.W. Gardner, T. Ahmed, P.T. Moseley, S.Z. Ali, M.F. Chowdhury, and F. Udrea. High Temperature Robust SOI Ethanol Sensor. *Procedia Engineering*, 25:1317–1320, 2011.
- [4] Jr Edward E. Simmons. Strain gauge and method for making same, May 1944.
- [5] Victor R. Palmeri. Pressure responsive resistor, June 1961.
- [6] I. W. Drummond and J. V. P. Long. Scanning ion microscopy and ion beam micro-machining. *Nature*, 215(5104):950, 1967.
- [7] Kurt E. Petersen. Silicon as a mechanical material. *Proceedings of the IEEE*, 70(5):420–457, 1982.
- [8] Prosenjit Rai-Choudhury. *MEMS and MOEMS Technology and Applications*, volume 85. Spie Press, 2000.
- [9] Min-Hang Bao. *Micro mechanical transducers: pressure sensors, accelerometers and gyroscopes*. Elsevier, 2000.
- [10] Robert P. Ried, Eun Sok Kim, David M. Hong, and Richard S. Muller. Piezoelectric microphone with on-chip CMOS circuits. *Journal of Microelectromechanical Systems*, 2(3):111–120, 1993. Publisher: IEEE.

- 
- [11] Wook Choi, Junwoo Lee, Yong Kyoung Yoo, Sungchul Kang, Jinseok Kim, and Jeong Hoon Lee. Enhanced sensitivity of piezoelectric pressure sensor with microstructured polydimethylsiloxane layer. *Applied Physics Letters*, 104(12):123701, 2014. Publisher: American Institute of Physics.
- [12] Sungjoon Choi, Haksue Lee, and Wonkyu Moon. A micro-machined piezoelectric hydrophone with hydrostatically balanced air backing. *Sensors and Actuators A: Physical*, 158(1):60–71, 2010. Publisher: Elsevier.
- [13] Steve P. Beeby. MEMS Mechanical Sensors. 2004.
- [14] Pressure Sensors Market Report, Market Analysis (2018-2023).
- [15] William J. Fleming. Overview of automotive sensors. *IEEE sensors journal*, 1(4):296–308, 2001.
- [16] S. Samaun, K. Wise, E. Nielsen, and J. Angell. An IC piezoresistive pressure sensor for biomedical instrumentation. In *1971 IEEE International Solid-State Circuits Conference. Digest of Technical Papers*, volume 14, pages 104–105. IEEE, 1971.
- [17] Robert S. Okojie, John C. DeLaat, and Joseph R. Saus. SiC pressure sensor for detection of combustor thermoacoustic instabilities [aircraft engine applications]. In *The 13th International Conference on Solid-State Sensors, Actuators and Microsystems, 2005. Digest of Technical Papers. TRANSDUCERS'05.*, volume 1, pages 470–473. IEEE, 2005.
- [18] O. N. Tufte, P. W. Chapman, and Donald Long. Silicon diffused-element piezoresistive diaphragms. *Journal of Applied Physics*, 33(11):3322–3327, 1962. Publisher: American Institute of Physics.
- [19] William P. Eaton and James H. Smith. Micromachined pressure sensors: review and recent developments. *Smart Materials and Structures*, 6(5):530, 1997.
- [20] Henri Porte, Veronique Gorel, Stefan Kiryenko, Jean-Pierre Goedgebuer, William Daniau, and Pascal Blind. Imbalanced Mach-Zehnder interferometer integrated in micromachined silicon substrate for pressure sensor. *Journal of lightwave technology*, 17(2):229, 1999.
- [21] D. Wagner, J. Frankenberger, and P. P. Deimel. Optical pressure sensor using two Mach-Zehnder interferometers for the TE and TM polarization. *Journal of Micromechanics and Microengineering*, 4(1):35, 1994.
- [22] Masashi Ohkawa, Masayuki Izutsu, and Tadasi Sueta. Integrated optic pressure sensor on silicon substrate. *Applied optics*, 28(23):5153–5157, 1989.



- 
- [23] J. A. Dziuban, A. Gorecka-Drzazga, and U. Lipowicz. Silicon optical pressure sensor. *Sensors and Actuators A: Physical*, 32(1-3):628–631, 1992.
- [24] Kentaro Totsu, Yoichi Haga, and Masayoshi Esashi. Ultra-miniature fiber-optic pressure sensor using white light interferometry. *Journal of Micromechanics and Microengineering*, 15(1):71, 2004.
- [25] Qingxu Yu and Xinlei Zhou. Pressure sensor based on the fiber-optic extrinsic Fabry-Perot interferometer. *Photonic Sensors*, 1(1):72–83, 2011.
- [26] Frans R. Blom, S. Bouwstra, J. H. J. Fluitman, and M. Elwenspoek. Resonating silicon beam force sensor. *Sensors and Actuators*, 17(3-4):513–519, 1989.
- [27] Goran Stemme. Resonant silicon sensors. *Journal of Micromechanics and Microengineering*, 1(2):113, 1991.
- [28] Erik Stemme and Göran Stemme. A balanced resonant pressure sensor. *Sensors and Actuators A: Physical*, 21(1-3):336–341, 1990.
- [29] J. C. Greenwood. Etched silicon vibrating sensor. *Journal of Physics E: Scientific Instruments*, 17(8):650, 1984.
- [30] Yang Chuan and Guo Can. Investigation based on MEMS double Si<sub>3</sub>N<sub>4</sub> resonant beams pressure sensor. In *2010 IEEE 5th International Conference on Nano/Micro Engineered and Molecular Systems*, pages 5–8. IEEE, 2010.
- [31] Deyong Chen, Dafu Cui, Li Wang, and Xiaotong Gao. SiN beam resonant pressure sensors with a novel structure. In *SENSORS, 2002 IEEE*, volume 2, pages 994–997. IEEE, 2002.
- [32] Rongjun Cheng, Yulong Zhao, Cun Li, Bian Tian, Zhongliang Yu, and Keyin Liu. Design and fabrication of a resonant pressure sensor by combination of DETF quartz resonator and silicon diaphragm. *Microsystem Technologies*, 21(3):631–640, 2015.
- [33] Xiaohui Du, Liying Wang, Anlin Li, Lingyun Wang, and Daoheng Sun. High accuracy resonant pressure sensor with balanced-mass DETF resonator and twinborn diaphragms. *Journal of Microelectromechanical Systems*, 26(1):235–245, 2016.
- [34] Craig S. Sander, James W. Knutti, and James D. Meindl. A monolithic capacitive pressure sensor with pulse-period output. *IEEE Transactions on Electron Devices*, 27(5):927–930, 1980.

- [35] Y. Hezarjaribi, M. N. Hamidon, Sayyed-Hossein Keshmiri, and A. R. Bahadorimehr. Capacitive pressure sensors based on MEMS, operating in harsh environments. In *2008 IEEE International Conference on Semiconductor Electronics*, pages 184–187. IEEE, 2008.
- [36] M. Shahiri-Tabarestani, B. A. Ganji, and R. Sabbaghi-Nadooshan. Design and simulation of high sensitive capacitive pressure sensor with slotted diaphragm. In *2012 International Conference on Biomedical Engineering (ICoBE)*, pages 484–489. IEEE, 2012.
- [37] Tamás Kárpáti, Csikósné Pap, Andrea Edit, and Sándor Kulinyi. Prototype MEMS Capacitive Pressure Sensor Design and Manufacturing. *Periodica Polytechnica Electrical Engineering*, 57(1):3–7, 2013.
- [38] Wen Cheng, Linwei Yu, Desheng Kong, Zhongwei Yu, Huiting Wang, Zhong Ma, Yunmu Wang, Junzhan Wang, Lijia Pan, and Yi Shi. Fast-Response and Low-Hysteresis Flexible Pressure Sensor Based on Silicon Nanowires. *IEEE Electron Device Letters*, 39(7):1069–1072, 2018.
- [39] P. Kleimann, B. Semmache, M. Le Berre, and D. Barbier. Stress-dependent hole effective masses and piezoresistive properties of p-type monocrystalline and polycrystalline silicon. *Physical review B*, 57(15):8966, 1998.
- [40] Robert E. Beaty, Richard C. Jaeger, Jeffrey C. Suhling, R. Wayne Johnson, and Ronald D. Butler. Evaluation of piezoresistive coefficient variation in silicon stress sensors using a four-point bending test fixture. *IEEE Transactions on components, hybrids, and manufacturing technology*, 15(5):904–914, 1992.
- [41] Chun-Hyung Cho, Richard C. Jaeger, and Jeffrey C. Suhling. Characterization of the Temperature Dependence of the Piezoresistive Coefficients of Silicon From  $150^{\circ}\text{C}$  to  $125^{\circ}\text{C}$ . *IEEE Sensors Journal*, 8(8):1455–1468, 2008.
- [42] Richard C. Jaeger, Jeffrey C. Suhling, Martin T. Carey, and R. Wayne Johnson. Off-axis sensor rosettes for measurement of the piezoresistive coefficients of silicon. *IEEE Transactions on components, hybrids, and manufacturing technology*, 16(8):925–931, 1993.
- [43] Yozo Kanda. A graphical representation of the piezoresistance coefficients in silicon. *IEEE Transactions on electron devices*, 29(1):64–70, 1982.
- [44] S. Charles. S., “Piezoresistive effect in germanium and Silicon”. *Physical Review*, 94(1):42–49, 1954.
- [45] Kenneth E. Bean. Anisotropic etching of silicon. *IEEE Transactions on electron devices*, 25(10):1185–1193, 1978.

- [46] W. P. Maszara, Goetz Goetz, A. Caviglia, and J. B. McKitterick. Bonding of silicon wafers for silicon-on-insulator. *Journal of Applied Physics*, 64(10):4943–4950, 1988.
- [47] S. Santosh Kumar and B. D. Pant. Design principles and considerations for the ‘ideal’ silicon piezoresistive pressure sensor: a focused review. *Microsystem technologies*, 20(7):1213–1247, 2014.
- [48] V. Mosser, J. Suski, J. Goss, and E. Obermeier. Piezoresistive pressure sensors based on polycrystalline silicon. *Sensors and Actuators A: Physical*, 28(2):113–132, 1991.
- [49] Shuwen Guo, Harald Eriksen, Kimiko Childress, Anita Fink, and Mary Hoffman. High temperature high accuracy piezoresistive pressure sensor based on smart-cut SOI. In *2008 IEEE 21st International Conference on Micro Electro Mechanical Systems*, pages 892–895. IEEE, 2008.
- [50] Alex A. Ned, Robert S. Okojie, and Anthony D. Kurtz. 6H-SiC pressure sensor operation at 600/spl deg/C. In *1998 Fourth International High Temperature Electronics Conference. HITEC (Cat. No. 98EX145)*, pages 257–260. IEEE, 1998.
- [51] R. Gaska, M. S. Shur, A. D. Bykhovski, J. W. Yang, M. A. Khan, V. V. Kaminski, and S. M. Soloviov. Piezoresistive effect in metal–semiconductor–metal structures on p-type GaN. *Applied Physics Letters*, 76(26):3956–3958, 2000.
- [52] V. Tilak, A. Vertiatchikh, J. Jiang, N. Reeves, and S. Dasgupta. Piezoresistive and piezoelectric effects in GaN. *physica status solidi c*, 3(6):2307–2311, 2006.
- [53] Shou-En Zhu, Murali Krishna Ghatkesar, Chao Zhang, and GCAM Janssen. Graphene based piezoresistive pressure sensor. *Applied Physics Letters*, 102(16):161904, 2013.
- [54] A. D. Smith, Frank Niklaus, A. Paussa, Sam Vaziri, Andreas C. Fischer, Mikael Sterner, Fredrik Forsberg, Anna Delin, D. Esseni, and P. Palestri. Electromechanical piezoresistive sensing in suspended graphene membranes. *Nano letters*, 13(7):3237–3242, 2013.
- [55] Jihun Hwang, Jaeyoung Jang, Kipyoo Hong, Kun Nyun Kim, Jong Hun Han, Kwonwoo Shin, and Chan Eon Park. Poly (3-hexylthiophene) wrapped carbon nanotube/poly (dimethylsiloxane) composites for use in finger-sensing piezoresistive pressure sensors. *Carbon*, 49(1):106–110, 2011.
- [56] C. Stampfer, T. Helbling, Dirk Obergfell, B. Schöberle, M. K. Tripp, A. Jungen, Siegmund Roth, V. M. Bright, and C. Hierold. Fabrication

- of single-walled carbon-nanotube-based pressure sensors. *Nano letters*, 6(2):233–237, 2006.
- [57] Muhammad Aniq Shazni Mohammad Haniff, Hing Wah Lee, Daniel Chia Sheng Bien, Aun Shih Teh, and Ishak Abdul Azid. Highly sensitive integrated pressure sensor with horizontally oriented carbon nanotube network. *Nanoscale research letters*, 9(1):49, 2014.
- [58] Joseph R. Mallon Jr, Farzad Pourahmadi, Kurt Petersen, Phillip Barth, Ted Vermeulen, and Janusz Bryzek. Low-pressure sensors employing bossed diaphragms and precision etch-stopping. *Sensors and Actuators A: Physical*, 21(1-3):89–95, 1990.
- [59] S. Marco, J. Samitier, O. Ruiz, J. R. Morante, and J. Esteve. High-performance piezoresistive pressure sensors for biomedical applications using very thin structured membranes. *Measurement science and technology*, 7(9):1195, 1996.
- [60] Zhongliang Yu, Yulong Zhao, Lu Sun, Bian Tian, and Zhuangde Jiang. Incorporation of beams into bossed diaphragm for a high sensitivity and overload micro pressure sensor. *Review of Scientific Instruments*, 84(1):015004, 2013.
- [61] S. Angel and R. Joseph Daniel. Sensitivity enhancement by striped arrow embossed diaphragms in low pressure MEMS piezoresistive pressure sensors. In *2017 Trends in Industrial Measurement and Automation (TIMA)*, pages 1–5. IEEE, 2017.
- [62] Chuang Li, Francisco Cordovilla, and José L. Ocaña. The design and analysis of a novel structural piezoresistive pressure sensor for low pressure measurement. *Microsystem Technologies*, 23(12):5677–5687, 2017.
- [63] Tingzhong Xu, Libo Zhao, Zhuangde Jiang, Xin Guo, Jianjun Ding, Wei Xiang, and Yulong Zhao. A high sensitive pressure sensor with the novel bossed diaphragm combined with peninsula-island structure. *Sensors and Actuators A: Physical*, 244:66–76, 2016.
- [64] H. Kressel and A. Elsea. Effect of generation-recombination centers on the stress-dependence of Si p-n junction characteristics. *Solid-State Electronics*, 10(3):213–224, March 1967.
- [65] Arthur T. Bradley, Richard C. Jaeger, Jeffrey C. Suhling, and Kevin J. O’Connor. Piezoresistive characteristics of short-channel MOSFETs on (100) silicon. *IEEE Transactions on Electron Devices*, 48(9):2009–2015, 2001.
- [66] Li Jingjing, Yue Ruifeng, and Liu Litian. MOSFET differential amplifier with input pair and active load pair being stress-sensitive both. In *2001 6th International Conference on Solid-State and Integrated Circuit*

- Technology. Proceedings (Cat. No. 01EX443)*, volume 2, pages 812–815. IEEE, 2001.
- [67] Nicolas André, T. P. Delhaye, Mohamad Al Kadi Jazairli, Benoit Olbrechts, Pierre Gérard, L. A. Francis, Jean-Pierre Raskin, and Denis Flandre. Ultra-low-power SOI CMOS pressure sensor based on orthogonal pMOS gauges. In *XXII IMEKO TC4 International Symposium and XX International Workshop on ADC Modelling and Testing*, 2017.
- [68] Zhao-Hua Zhang, Yan-Hong Zhang, Li-Tian Liu, and Tian-Ling Ren. A novel MEMS pressure sensor with MOSFET on chip. In *SENSORS, 2008 IEEE*, pages 1564–1567. IEEE, 2008.
- [69] Ryszard S. Jachowicz and Zbigniew M. Ażgin. FET pressure sensor and iterative method for modelling of the device. *Sensors and Actuators A: Physical*, 97:369–378, 2002.
- [70] M. Fernández-Bolaños, N. Abelé, V. Pott, D. Bouvet, G. A. Racine, J. M. Quero, and A. M. Ionescu. Polyimide sacrificial layer for SOI SG-MOSFET pressure sensor. *Microelectronic engineering*, 83(4-9):1185–1188, 2006.
- [71] Xiaofeng Zhao, Dianzhong Wen, and Gang Li. Fabrication and characteristics of an nc-Si/c-Si heterojunction MOSFETs pressure sensor. *Sensors*, 12(5):6369–6379, 2012.
- [72] P. K. Rathore and B. S. Panwar. Design and optimization of a CMOS-MEMS integrated current mirror sensing based MOSFET embedded pressure sensor. In *2013 IEEE International Conference on Control Applications (CCA)*, pages 443–448, August 2013.
- [73] Vitor Garcia and Fabiano Fruett. A mechanical-stress sensitive differential amplifier. *Sensors and Actuators A: Physical*, 132(1):8–13, 2006.
- [74] Young Tae Lee, Hee Don Seo, Akihisa Kawamura, Tetsuhiro Yamada, Yoshinori Matsumoto, Makoto Ishida, and Tetsuro Nakamura. Compensation method of offset and its temperature drift in silicon piezoresistive pressure sensor using double Wheatstone-bridge configuration. In *Proceedings of the 1995 8th International Conference on Solid-State Sensors and Actuators and Eurosensors IX. Part 1 (of 2)*, pages 570–573. IEEE, 1995.
- [75] C. Pramanik, T. Islam, and H. Saha. Temperature compensation of piezoresistive micro-machined porous silicon pressure sensor by ANN. *Microelectronics Reliability*, 46(2):343–351, February 2006.
- [76] M. Aryafar, M. Hamed, and M. M. Ganjeh. A novel temperature compensated piezoresistive pressure sensor. *Measurement*, 63:25–29, March 2015.

- [77] Kuo Huan Peng, C. M. Uang, and Yih Min Chang. The temperature compensation of the silicon piezo-resistive pressure sensor using the half-bridge technique. In *Reliability, Testing, and Characterization of MEMS/MOEMS III*, volume 5343, pages 292–301. International Society for Optics and Photonics, December 2003.
- [78] M. Akbar and M.A. Shanblatt. A fully integrated temperature compensation technique for piezoresistive pressure sensors. *IEEE Transactions on Instrumentation and Measurement*, 42(3):771–775, June 1993. Conference Name: IEEE Transactions on Instrumentation and Measurement.
- [79] Guanwu Zhou, Yulong Zhao, Fangfang Guo, and Wenju Xu. A Smart High Accuracy Silicon Piezoresistive Pressure Sensor Temperature Compensation System. *Sensors*, 14(7):12174–12190, July 2014. Number: 7 Publisher: Multidisciplinary Digital Publishing Institute.
- [80] Po-Tsung Hsieh, Y. M. Chang, J. M. Xu, and Chii-Maw Uang. Double bridge technique for temperature compensation of piezoresistive pressure sensor. In *Smart Structures and Materials 2002: Smart Structures and Integrated Systems*, volume 4701, pages 627–633. International Society for Optics and Photonics, July 2002.
- [81] Shyam Aravamudhan and Shekhar Bhansali. Reinforced piezoresistive pressure sensor for ocean depth measurements. *Sensors and Actuators A: Physical*, 142(1):111–117, March 2008.
- [82] J. Dziuban, A. Górecka-Drzazga, U. Lipowicz, W. Indyka, and J. Wasowski. Self-compensating piezoresistive pressure sensor. *Sensors and Actuators A: Physical*, 42(1):368–374, April 1994.
- [83] J. J. Wortman, J. R. Hauser, and R. M. Burger. Effect of Mechanical Stress on p-n Junction Device Characteristics. *Journal of Applied Physics*, 35(7):2122–2131, July 1964.
- [84] A. Jayaraman, M. E. Sikorski, J. C. Irvin, and G. H. Yates. Effect of Hydrostatic Pressure on *p-n* Junction Characteristics and the Pressure Variation of the Band Gap. *Journal of Applied Physics*, 38(11):4454–4459, October 1967.
- [85] Vijaykumar Sandrimani and Kirankumar B Balavalad. Design and Simulation of Silicon on Insulator Based Piezoresistive Pressure Sensor. page 7, 2018.
- [86] Shuang Chen, Ming-quan Zhu, Bing-he Ma, and Wei-zheng Yuan. Design and optimization of a micro piezoresistive pressure sensor. In *2008 3rd IEEE International Conference on Nano/Micro Engineered and Molecular Systems*, pages 351–356. IEEE, 2008.

- [87] A. F. P. Van Putten and S. Middelhoek. Integrated silicon anemometer. *Electronics Letters*, 10(21):425–426, 1974.
- [88] Flow Sensors (MCP-8137) - Global Industry Analysts, Inc.
- [89] Vijay Chandrasekharan, Jeremy Sells, Jessica Meloy, David P. Arnold, and Mark Sheplak. A microscale differential capacitive direct wall-shear-stress sensor. *Journal of microelectromechanical systems*, 20(3):622–635, 2011.
- [90] Nicolas André, Bertrand Rue, Gilles Scheen, Denis Flandre, Laurent A. Francis, and Jean-Pierre Raskin. Out-of-plane MEMS-based mechanical airflow sensor co-integrated in SOI CMOS technology. *Sensors and Actuators A: Physical*, 206:67–74, 2014.
- [91] Brett Freidkes, David A. Mills, Casey Keane, Lawrence S. Ukeiley, and Mark Sheplak. Development of a Two-Dimensional Wall Shear Stress Sensor for Wind Tunnel Applications. In *AIAA Scitech 2019 Forum*, page 2045, 2019.
- [92] Bing He Ma and Cheng Yu Ma. A MEMS surface fence for wall shear stress measurement with high sensitivity. *Microsystem Technologies*, 22(2):239–246, 2016.
- [93] Tilmann von Papen, Ulrich Buder, Ha Duong Ngo, and Ernst Obermeier. A second generation MEMS surface fence sensor for high resolution wall shear stress measurement. *Sensors and Actuators A: Physical*, 113(2):151–155, 2004.
- [94] Volkan Otugen and Valery Sheverev. Micro-optical wall shear stress sensor, April 2010.
- [95] U. K. Ayaz, T. Ioppolo, and M. V. Ötügen. Wall shear stress sensor based on the optical resonances of dielectric microspheres. *Measurement science and technology*, 22(7):075203, 2011.
- [96] S. Große and Wolfgang Schröder. Two-dimensional visualization of turbulent wall shear stress using micropillars. *AIAA journal*, 47(2):314–321, 2009.
- [97] Mohammad Ali Mohammadzadeh Kashan, Ainan Leong, Tridib Saha, Vineetha Kalavally, Varghese Swamy, and N. Ramakrishnan. QCM-Micropillar-Based Coupled Resonators in the Detection of Gas Mass Flow Rates. *IEEE Transactions on Instrumentation and Measurement*, 68(1):303–305, 2018.
- [98] Jonathan TW Kuo, Lawrence Yu, and Ellis Meng. Micromachined thermal flow sensors—A review. *Micromachines*, 3(3):550–573, 2012.

- [99] N. T. Nguyen. Micromachined flow sensors—a review. *Flow measurement and Instrumentation*, 8(1):7–16, 1997.
- [100] B. W. Van Oudheusden. Silicon thermal flow sensors. *Sensors and Actuators A: Physical*, 30(1-2):5–26, 1992.
- [101] William S. Hadaway Jr. Meter, May 1918.
- [102] A. F. P. Van Putten. An integrated silicon double bridge anemometer. *Sensors and Actuators*, 4:387–396, 1983.
- [103] Anton FP van Putten. An integrated silicon anemometer. In *IEE Colloquium on Solid State and Smart Sensors*, pages 4–1. IET, 1988.
- [104] M. A. Mullins, A. F. P. Van Putten, R. Bayford, and J. B. Butcher. Potential for a smart sensor based on an integrated silicon anemometer. *Sensors and Actuators A: Physical*, 47(1-3):342–348, 1995.
- [105] JOHAN H. Huijsing, JACOB P. Schuddemat, and WOUTER Verhoef. Monolithic integrated direction-sensitive flow sensor. *IEEE Transactions on Electron Devices*, 29(1):133–136, 1982.
- [106] Walter S. Kuklinski, Ganesan Sadasiv, and Dov Jaron. Integrated-circuit bipolar transistor array for fluid-velocity measurements. *Medical and Biological Engineering and Computing*, 19(5):662–664, 1981.
- [107] Tong Qin-Yi and Huang Jin-Biao. A novel CMOS flow sensor with constant chip temperature (CCT) operation. *Sensors and actuators*, 12(1):9–21, 1987.
- [108] Edvard Kálvesten. *Pressure and wall shear stress sensors for turbulence measurements*. PhD Thesis, Citeseer, 1996.
- [109] Chang Liu, Jin-Biao Huang, Zhenjun Zhu, Fukang Jiang, Steve Tung, Yu-Chong Tai, and Chih-Ming Ho. A micromachined flow shear-stress sensor based on thermal transfer principles. *Journal of Microelectromechanical Systems*, 8(1):90–99, 1999.
- [110] Motoaki Kimura, Steve Tung, James Lew, Chih-Ming Ho, Fukang Jiang, and Yu-Chong Tai. Measurements of wall shear stress of a turbulent boundary layer using a micro-shear-stress imaging chip. *Fluid dynamics research*, 24(6):329, 1999.
- [111] J. B. Huang, F. K. Jiang, Y. C. Tai, and C. M. Ho. A micro-electro-mechanical-system-based thermal shear-stress sensor with self-frequency compensation. *Measurement Science and Technology*, 10(8):687, 1999.
- [112] Xuan-Qi Wang, Zhigang Han, Fukang Jiang, Thomas Tsao, Qiao Lin, Yu-Chong Tai, Vincent Koosh, Rodney Goodman, James Lew, and Chih-Ming Ho. A fully integrated shear stress sensor. In *Proc. International*



- Conference on Solid-State Sensors and Actuators (Transducer)*, pages 7–10. Citeseer, 1999.
- [113] Yong Xu, Yu-Chong Tai, Adam Huang, and Chih-Ming Ho. IC-integrated flexible shear-stress sensor skin. *Journal of Microelectromechanical Systems*, 12(5):740–747, 2003.
- [114] Wei Xu, Bo Gao, Shenhui Ma, Anping Zhang, Yi Chiu, and Yi-Kuen Lee. Low-cost temperature-compensated thermoresistive micro calorimetric flow sensor by using 0.35  $\mu\text{m}$  CMOS MEMS technology. In *2016 IEEE 29th International Conference on Micro Electro Mechanical Systems (MEMS)*, pages 189–192. IEEE, 2016.
- [115] Ibraheem Haneef, Syed Zeeshan Ali, Florin Udrea, John D. Coull, and Howard P. Hodson. High performance SOI-CMOS wall shear stress sensors. In *SENSORS, 2007 IEEE*, pages 1060–1064. IEEE, 2007.
- [116] Takuya Sawada, Osamu Terashima, Yasuhiko Sakai, Kouji Nagata, Mitsuhiro Shikida, and Yasumasa Ito. Measurement of wall shear stress fluctuation with the micro-fabricated hot-film sensor in a boundary layer of a wall jet. *Journal of the Japanese Society for Experimental Mechanics*, 14(Special\_Issue):s13–s18, 2014.
- [117] Mark Sheplak, Venkataraman Chandrasekaran, and Anthony Cain. Characterization of a silicon-micromachined thermal shear-stress sensor. *AIAA journal*, 40(6):1099–1104, 2002.
- [118] Ethan LW Gardner, Timothy A. Vincent, Rhys G. Jones, Julian W. Gardner, John Coull, Andrea De Luca, and Florin Udrea. MEMS Thermal Flow Sensors—An Accuracy Investigation. *IEEE Sensors Journal*, 2019.
- [119] Xiaoying Li, Yanbing Li, Binghe Ma, and Leitao Wang. Modelling and calibration of microthermal sensor for underwater wall shear stress measurement. *Micro & Nano Letters*, 9(7):486–489, 2014.
- [120] Haider Al-Mumen, Fubo Rao, Lixin Dong, and Wen Li. Thermo-flow and temperature sensing behaviour of graphene based on surface heat convection. *Micro & Nano Letters*, 8(10):681–685, 2013.
- [121] Winnie WY Chow, Yanli Qu, Wen J. Li, and Steve CH Tung. Integrated SWCNT sensors in micro-wind tunnel for air-flow shear-stress measurement. *Microfluidics and Nanofluidics*, 8(5):631–640, 2010.
- [122] Lennart Löfdahl and Mohamed Gad-el Hak. MEMS applications in turbulence and flow control. *Progress in Aerospace Sciences*, 35(2):101–203, 1999.
- [123] Jonathan W. Naughton and Mark Sheplak. Modern developments in shear-stress measurement. *Progress in Aerospace Sciences*, 38(6-7):515–570, 2002.

- [124] Goeran N. Stemme. A monolithic gas flow sensor with polyimide as thermal insulator. *IEEE transactions on Electron Devices*, 33(10):1470–1474, 1986.
- [125] L. Löfdahl, G. Stemme, and B. Johansson. Silicon based flow sensors used for mean velocity and turbulence measurements. *Experiments in Fluids*, 12(4-5):270–276, 1992.
- [126] Edvard Kälvesten, Christian Vieider, Lennart Löfdahl, and Göran Stemme. An integrated pressure—flow sensor for correlation measurements in turbulent gas flows. *Sensors and Actuators A: Physical*, 52(1-3):51–58, 1996.
- [127] Fukang Jiang, Yu-Chong Tai, Bhusan Gupta, Rodney Goodman, Steve Tung, Jin-Biao Huang, and Chih-Ming Ho. A surface-micromachined shear stress imager. In *Micro Electro Mechanical Systems, 1996, MEMS'96, Proceedings. An Investigation of Micro Structures, Sensors, Actuators, Machines and Systems. IEEE, The Ninth Annual International Workshop on*, pages 110–115. IEEE, 1996.
- [128] M. Ashauer, H. Glosch, F. Hedrich, N. Hey, H. Sandmaier, and W. Lang. Thermal flow sensor for liquids and gases. In *Micro Electro Mechanical Systems, 1998. MEMS 98. Proceedings., The Eleventh Annual International Workshop on*, pages 351–355. IEEE, 1998.
- [129] Andrea De Luca, Ibraheem Haneef, John D. Coull, Syed Zeeshan Ali, Claudio Falco, and Florin Udrea. High-sensitivity single thermopile SOI CMOS MEMS thermal wall shear stress sensor. *IEEE Sensors Journal*, 15(10):5561–5568, 2015.
- [130] Ibraheem Haneef, John D. Coull, Syed Zeeshan Ali, Florin Udrea, and Howard P. Hodson. Laminar to turbulent flow transition measurements using an array of SOI-CMOS MEMS wall shear stress sensors. In *SENSORS, 2008 IEEE*, pages 57–61. IEEE, 2008.
- [131] Thorbjörn Ebefors, Edvard Kalvesten, and Goran Stemme. Three dimensional silicon triple-hot-wire anemometer based on polyimide joints. In *Micro Electro Mechanical Systems, 1998. MEMS 98. Proceedings., The Eleventh Annual International Workshop on*, pages 93–98. IEEE, 1998.
- [132] C. Lyons, A. Friedberger, W. Welsler, G. Muller, G. Krotz, and R. Kassing. A high-speed mass flow sensor with heated silicon carbide bridges. In *Micro Electro Mechanical Systems, 1998. MEMS 98. Proceedings., The Eleventh Annual International Workshop on*, pages 356–360. IEEE, 1998.
- [133] Alireza Mahdaviifar, Ricardo Aguilar, Zhengchun Peng, Peter J. Hesketh, Melvin Findlay, Joseph R. Stetter, and Gary W. Hunter. Simulation and

- fabrication of an ultra-low power miniature microbridge thermal conductivity gas sensor. *Journal of The Electrochemical Society*, 161(4):B55–B61, 2014.
- [134] Y. Ye, Z. Yi, S. Gao, M. Qin, and Q. A. Huang. Effect of Insulation Trenches on Micromachined Silicon Thermal Wind Sensors. *IEEE Sensors Journal*, 17(24):8324–8331, December 2017.
- [135] Qiao Lin, Fukang Jiang, Xuan-Qi Wang, Zhigang Han, Yu-Chong Tai, James Lew, and Chih-Ming Ho. MEMS thermal shear-stress sensors: Experiments, theory and modeling. In *Technical Digest of 2000 Solid-State Sensor and Actuator Workshop*, pages 304–307, 2000.
- [136] Ethan LW Gardner, Andrea De Luca, and Florin Udrea. 2D and 3D thermal flow sensor modelling—A comparative analysis. In *Semiconductor Conference (CAS), 2017 International*, pages 197–200. IEEE, 2017.
- [137] P. Fürjes, G. Légrádi, Cs Dűcs\Ho, A. Aszódi, and I. Bársony. Thermal characterisation of a direction dependent flow sensor. *Sensors and Actuators A: Physical*, 115(2-3):417–423, 2004.
- [138] N. Sabaté, J. Santander, L. Fonseca, I. Gràcia, and C. Cané. Multi-range silicon micromachined flow sensor. *Sensors and Actuators A: Physical*, 110(1-3):282–288, 2004.
- [139] Safir Issa and Walter Lang. Minimum Detectable Air Velocity by Thermal Flow Sensors. *Sensors (Basel, Switzerland)*, 13(8):10944–10953, August 2013.
- [140] Gas Sensor Market Size and Share | Global Industry Report, 2019-2025.
- [141] Gas Sensors Market Size | Growth, Trends, Forecast (2019-24).
- [142] Read "*Emergency and Continuous Exposure Guidance Levels for Selected Submarine Contaminants: Volume 2*" at [NAP.edu](http://NAP.edu).
- [143] John Nolt. How harmful are the average American's greenhouse gas emissions? *Ethics, Policy and Environment*, 14(1):3–10, 2011.
- [144] Krassi Rumchev, Helen Brown, and Jeffery Spickett. Volatile organic compounds: do they present a risk to our health? *Reviews on environmental health*, 22(1):39–56, 2007.
- [145] Ahmed A. Arif and Syed M. Shah. Association between personal exposure to volatile organic compounds and asthma among US adult population. *International archives of occupational and environmental health*, 80(8):711–719, 2007.

- [146] K. Rumchev, J. Spickett, Mahesh Bulsara, M. Phillips, and S. Stick. Association of domestic exposure to volatile organic compounds with asthma in young children. *Thorax*, 59(9):746–751, 2004.
- [147] Sabit Cakmak, Robert E. Dales, Ling Liu, Lisa Marie Kauri, Christine L. Lemieux, Christopher Hebborn, and Jiping Zhu. Residential exposure to volatile organic compounds and lung function: results from a population-based cross-sectional survey. *Environmental pollution*, 194:145–151, 2014.
- [148] J. G. Firth, Alan Jones, and T. A. Jones. The principles of the detection of flammable atmospheres by catalytic devices. *Combustion and Flame*, 20(3):303–311, 1973.
- [149] Eui-Bok Lee, In-Sung Hwang, Jung-Ho Cha, Ho-Jun Lee, Won-Bae Lee, James Jungho Pak, Jong-Heun Lee, and Byeong-Kwon Ju. Micromachined catalytic combustible hydrogen gas sensor. *Sensors and Actuators B: Chemical*, 153(2):392–397, 2011.
- [150] Anna Harley-Trochimczyk, Jiyoung Chang, Qin Zhou, Jeffrey Dong, Thang Pham, Marcus A. Worsley, Roya Maboudian, Alex Zettl, and William Mickelson. Catalytic hydrogen sensing using microheated platinum nanoparticle-loaded graphene aerogel. *Sensors and Actuators B: Chemical*, 206:399–406, January 2015.
- [151] Yael Nemirovsky, Sara Stolyarova, Tanya Blank, Sharon Bar-Lev, Alexander Svetlitza, Alex Zviagintsev, and Igor Brouk. A New Pellistor-Like Gas Sensor Based on Micromachined CMOS Transistor. *IEEE Transactions on Electron Devices*, 65(12):5494–5498, 2018.
- [152] Thomas Hübert, L. Boon-Brett, Gráinne Black, and Ulrich Banach. Hydrogen sensors—a review. *Sensors and Actuators B: Chemical*, 157(2):329–352, 2011.
- [153] Chi-Hwan Han, Dae-Woong Hong, Il-Jin Kim, Jihye Gwak, Sang-Do Han, and Krishan C. Singh. Synthesis of Pd or Pt/titanate nanotube and its application to catalytic type hydrogen gas sensor. *Sensors and Actuators B: Chemical*, 128(1):320–325, December 2007.
- [154] V. R. Katti, A. K. Debnath, S. C. Gadkari, S. K. Gupta, and V. C. Sahni. Passivated thick film catalytic type H<sub>2</sub> sensor operating at low temperature. *Sensors and Actuators B: Chemical*, 84(2):219–225, May 2002.
- [155] A. Katsuki and K. Fukui. H<sub>2</sub> selective gas sensor based on SnO<sub>2</sub>. *Sensors and Actuators B: Chemical*, 52(1):30–37, September 1998.
- [156] J. F. McAleer, P. t. Moseley, P. Bourke, J. O. W. Norris, and R. Stephan. Tin dioxide gas sensors: use of the seebeck effect. *Sensors and Actuators*, 8(3):251–257, November 1985.

- [157] Masahiko Matsumiya, Fabin Qiu, Woosuck Shin, Noriya Izu, Norimitsu Murayama, and Shuzo Kanzaki. Thin-film Li-doped NiO for thermoelectric hydrogen gas sensor. *Thin Solid Films*, 419(1):213–217, November 2002.
- [158] V. Casey, J. Cleary, G. D’Arcy, and J. B. McMonagle. Calorimetric combustible gas sensor based on a planar thermopile array: fabrication, characterisation, and gas response. *Sensors and Actuators B: Chemical*, 96(1):114–123, November 2003.
- [159] Fabin Qiu, Woosuck Shin, Masahiko Matsumiya, Noriya Izu, Ichiro Matsubara, and Norimitsu Murayama. Miniaturization of thermoelectric hydrogen sensor prepared on glass substrate with low-temperature crystallized SiGe film. *Sensors and Actuators B: Chemical*, 103(1):252–259, September 2004.
- [160] Kazuki Tajima, Fabin Qiu, Woosuck Shin, Noriya Izu, Ichiro Matsubara, and Norimitsu Murayama. Micromechanical fabrication of low-power thermoelectric hydrogen sensor. *Sensors and Actuators B: Chemical*, 108(1):973–978, July 2005.
- [161] M. Nishibori, W. Shin, N. Izu, T. Itoh, I. Matsubara, S. Yasuda, and S. Ohtani. Robust hydrogen detection system with a thermoelectric hydrogen sensor for hydrogen station application. *International Journal of Hydrogen Energy*, 34(6):2834–2841, March 2009.
- [162] Hu Huang, Weiling Luan, Jian-Song Zhang, Yun-Shi Qi, and Shan-Tung Tu. Thermoelectric hydrogen sensor working at room temperature prepared by bismuth–telluride P–N couples and Pt/Al<sub>2</sub>O<sub>3</sub>. *Sensors and Actuators B: Chemical*, 128(2):581–585, January 2008.
- [163] Seil Kim, Yoseb Song, Tae-Yeon Hwang, Jae-Hong Lim, and Yong-Ho Choa. Facial fabrication of an inorganic/organic thermoelectric nanocomposite based gas sensor for hydrogen detection with wide range and reliability. *International Journal of Hydrogen Energy*, 44(21):11266–11274, 2019.
- [164] Seil Kim, Yoseb Song, Young-In Lee, and Yong-Ho Choa. Thermochemical hydrogen sensor based on Pt-coated nanofiber catalyst deposited on pyramidally textured thermoelectric film. *Applied Surface Science*, 415:119–125, 2017.
- [165] C. Ramesh, N. Murugesan, M. V. Krishnaiah, V. Ganesan, and G. Periaswami. Improved Nafion-based amperometric sensor for hydrogen in argon. *Journal of Solid State Electrochemistry*, 12(9):1109–1116, September 2008.

- [166] Yente Chao, Sheng Yao, William J. Buttner, and Joseph R. Stetter. Amperometric sensor for selective and stable hydrogen measurement. *Sensors and Actuators B: Chemical*, 106(2):784–790, May 2005.
- [167] M. Sakthivel and W. Weppner. A portable limiting current solid-state electrochemical diffusion hole type hydrogen sensor device for biomass fuel reactors: Engineering aspect. *International Journal of Hydrogen Energy*, 33(2):905–911, January 2008.
- [168] Xianbo Lu, Shouguo Wu, Li Wang, and Zhenxi Su. Solid-state amperometric hydrogen sensor based on polymer electrolyte membrane fuel cell. *Sensors and Actuators B: Chemical*, 107(2):812–817, June 2005.
- [169] Sri Ayu Anggraini, Soichiro Yoshida, Hiroshi Ikeda, and Norio Miura. Selective NO<sub>2</sub> detection using YSZ-based amperometric sensor attached with NiFe<sub>2</sub>O<sub>4</sub> (+ Fe<sub>2</sub>O<sub>3</sub>) sensing electrode. *Sensors and Actuators B: Chemical*, 259:30–35, 2018.
- [170] L. P. Martin, A. Q. Pham, and R. S. Glass. Electrochemical hydrogen sensor for safety monitoring. *Solid State Ionics*, 175(1):527–530, November 2004.
- [171] T. Schober. Applications of oxidic high-temperature proton conductors. *Solid State Ionics*, 162-163:277–281, September 2003.
- [172] Young-Chang Yang, Jinsu Park, Junwoong Kim, Youngsun Kim, and Jong-Ook Park. Oxygen dependency of the hydrogen sensor based on high-temperature proton conductors. *Ionics*, 16(5):397–402, June 2010.
- [173] Yoshihiko Sadaoka and Masami Mori. Detection of VOC in air with a planar-type potentiometric gas sensor based on YSZ with a Pt electrode modified with TiO<sub>2</sub>. *Sensors and Actuators B: Chemical*, 248:878–885, 2017.
- [174] Fu-an Li, Han Jin, Jinxia Wang, Jie Zou, and Jiawen Jian. Selective sensing of gas mixture via a temperature modulation approach: New strategy for potentiometric gas sensor obtaining satisfactory discriminating features. *Sensors*, 17(3):573, 2017.
- [175] Bryan Blackburn and Eric D. Wachsman. Multifunctional potentiometric gas sensor array with an integrated temperature control and temperature sensors, August 2015.
- [176] L. Boon-Brett, J. Bousek, G. Black, P. Moretto, P. Castello, T. Hübner, and U. Banach. Identifying performance gaps in hydrogen safety sensor technology for automotive and stationary applications. *International Journal of Hydrogen Energy*, 35(1):373–384, January 2010.

- [177] H. Angus Macleod and H. Angus Macleod. *Thin-film optical filters*. CRC press, 2010.
- [178] J. Mayrwöger, W. Reichl, C. Krutzler, and B. Jakoby. Measuring CO<sub>2</sub> concentration with a Fabry–Perot based bolometer using a glass plate as simple infrared filter. *Sensors and Actuators B: Chemical*, 170:143–147, July 2012.
- [179] J. Mayrwöger, W. Reichl, P. Hauer, C. Krutzler, and B. Jakoby. CO<sub>2</sub> monitoring using a simple Fabry–Perot-based germanium bolometer. *Sensors and Actuators B: Chemical*, 154(2):245–250, June 2011.
- [180] J. Mayrwöger, W. Reichl, C. Krutzler, and B. Jakoby. Gas monitoring with a Fabry–Perot based bolometer: Cross-sensitivity to water vapor. *Procedia Engineering*, 5:1220–1223, January 2010.
- [181] Y. W. Sun, C. Liu, K. L. Chan, P. H. Xie, W. Q. Liu, Y. Zeng, S. M. Wang, S. H. Huang, J. Chen, Y. P. Wang, and F. Q. Si. Stack emission monitoring using non-dispersive infrared spectroscopy with an optimized nonlinear absorption cross interference correction algorithm. *Atmospheric Measurement Techniques*, 6(8):1993–2005, August 2013.
- [182] Qiulin Tan, Licheng Tang, Mingliang Yang, Chenyang Xue, Wendong Zhang, Jun Liu, and Jijun Xiong. Three-gas detection system with IR optical sensor based on NDIR technology. *Optics and Lasers in Engineering*, 74:103–108, 2015.
- [183] Lewis Fleming, Des Gibson, Shigeng Song, Cheng Li, and Stuart Reid. Reducing N<sub>2</sub>O induced cross-talk in a NDIR CO<sub>2</sub> gas sensor for breath analysis using multilayer thin film optical interference coatings. *Surface and Coatings Technology*, 336:9–16, 2018.
- [184] Xu Wang, Henrik Rödjegård, Bengt Oelmann, Hans Martin, and Bo Larsson. High performance CO<sub>2</sub> measurement based on pressure modulation. *Procedia Engineering*, 5:1208–1211, January 2010.
- [185] Adam Sklorz, Anika Schafer, and Walter Lang. Merging ethylene NDIR gas sensors with preconcentrator-devices for sensitivity enhancement. *Sensors and Actuators B: Chemical*, 170:21–27, July 2012.
- [186] Pierre Barritault, Mickael Brun, Serge Gidon, and Sergio Nicoletti. Mid-IR source based on a free-standing microhotplate for autonomous CO<sub>2</sub> sensing in indoor applications. *Sensors and Actuators A: Physical*, 172(2):379–385, December 2011.
- [187] Pierre Barritault, Mickael Brun, Olivier Lartigue, Jérôme Willemin, Jean-Louis Ouvrier-Buffet, Stéphane Pocas, and Sergio Nicoletti. Low power CO<sub>2</sub> NDIR sensing using a micro-bolometer detector and a micro-hotplate IR-source. *Sensors and Actuators B: Chemical*, 182:565–570, June 2013.

- [188] L. Scholz, A. Ortiz Perez, S. Knobelspies, J. Wöllenstein, and S. Palzer. MID-IR LED-based, Photoacoustic CO<sub>2</sub> Sensor. *Procedia Engineering*, 120:1233–1236, January 2015.
- [189] Antoine Godard. Infrared (2–12  $\mu\text{m}$ ) solid-state laser sources: a review. *Comptes Rendus Physique*, 8(10):1100–1128, December 2007.
- [190] Adam Sklorz, Steffen Janßen, and Walter Lang. Detection limit improvement for NDIR ethylene gas detectors using passive approaches. *Sensors and Actuators B: Chemical*, 175:246–254, December 2012.
- [191] Carlos Calaza, L. Fonseca, M. Moreno, S. Marco, C. Cané, and I. Gracia. A surface micromachining process for the development of a medium-infrared tuneable Fabry–Perot interferometer. *Sensors and Actuators A: Physical*, 113(1):39–47, June 2004.
- [192] S. Eliahou-Niv, R. Dahan, and G. Golan. Design and analysis of a novel tunable optical filter. *Microelectronics Journal*, 37(4):302–307, April 2006.
- [193] C. G. Wu, X. Y. Sun, J. Meng, W. B. Luo, P. Li, Q. X. Peng, Y. S. Luo, and Y. Shuai. Fast and wide-band response infrared detector using porous PZT pyroelectric thick film. *Infrared Physics & Technology*, 63:69–73, March 2014.
- [194] X. Y. Sun, W. B. Luo, J. Meng, X. Qing, W. Y. Fu, Y. Shuai, and C. G. Wu. Monolithic pyroelectric infrared detectors using SiO<sub>2</sub> aerogel thin films. *Sensors and Actuators A: Physical*, 228:69–74, June 2015.
- [195] Takashi Katsumata, Ryosuke Nishimura, Keisuke Yamaoka, Edson Gomes Camargo, Tomohiro Morishita, Koichiro Ueno, Seiichi Tokuo, Hiromasa Goto, and Naohiro Kuze. Uncooled InGaSb photovoltaic infrared detectors for gas sensing. *Journal of Crystal Growth*, 378:611–613, September 2013.
- [196] W. H. King. Analytical uses of the piezoelectric crystal. *Anal. Chem*, 36(1735):136, 1964.
- [197] Mohd Nizar Hamidon, V. Skarda, N. M. White, F. Krispel, P. Krempl, M. Binhack, and W. Buff. Fabrication of high temperature surface acoustic wave devices for sensor applications. *Sensors and Actuators A: Physical*, 123:403–407, 2005.
- [198] Adrian Venema, Evert Nieuwkoop, Michael J. Vellekoop, Walter J. Ghijsen, and Anton W. Barendsz. NO<sub>2</sub> gas-concentration measurement with a SAW-chemosensor. *IEEE Transactions on Ultrasonics Ferroelectrics and Frequency Control*, 34:148–155, 1987.



- [199] Liu Yang, Chenbo Yin, Zili Zhang, Junjing Zhou, and Haihan Xu. The investigation of hydrogen gas sensing properties of SAW gas sensor based on palladium surface modified SnO<sub>2</sub> thin film. *Materials science in semiconductor processing*, 60:16–28, 2017.
- [200] Md Nazibul Hasan, Santanu Maity, Argha Sarkar, Chandan Tilak Bhunia, Debabrata Acharjee, and Aneesh M. Joseph. Simulation and fabrication of SAW-based gas sensor with modified surface state of active layer and electrode orientation for enhanced H<sub>2</sub> gas sensing. *Journal of Electronic Materials*, 46(2):679–686, 2017.
- [201] Abhishek Ghosh, Chen Zhang, Sheldon Shi, and Haifeng Zhang. High temperature CO<sub>2</sub> sensing and its cross-sensitivity towards H<sub>2</sub> and CO gas using calcium doped ZnO thin film coated langasite SAW sensor. *Sensors and Actuators B: Chemical*, 301:126958, 2019.
- [202] Ananya Dey. Semiconductor metal oxide gas sensors: A review. *Materials Science and Engineering: B*, 229:206–217, 2018.
- [203] D. Cruz, J. P. Chang, S. K. Showalter, F. Gelbard, R. P. Manginell, and M. G. Blain. Microfabricated thermal conductivity detector for the micro-ChemLab™. *Sensors and Actuators B: Chemical*, 121(2):414–422, 2007.
- [204] Shree Narayanan, Bassam Alfeeli, and Masoud Agah. Two-Port Static Coated Micro Gas Chromatography Column With an Embedded Thermal Conductivity Detector. *IEEE Sensors Journal*, 12(6):1893–1900, June 2012.
- [205] David Puente, Fco Javier Gracia, and Isabel Ayerdi. Thermal conductivity microsensor for determining the Methane Number of natural gas. *Sensors and Actuators B: Chemical*, 110(2):181–189, 2005.
- [206] Apoorva Garg, Muhammad Akbar, Eric Vejerano, Shree Narayanan, Leyla Nazhandali, Linsey C. Marr, and Masoud Agah. Zebra GC: A mini gas chromatography system for trace-level determination of hazardous air pollutants. *Sensors and Actuators B: Chemical*, 212:145–154, 2015.
- [207] F. Haghghi, Z. Talebpour, and A. Sanati-Nezhad. Through the years with on-a-chip gas chromatography: a review. *Lab on a Chip*, 15(12):2559–2575, 2015.
- [208] J. Kuntner, F. Kohl, and B. Jakoby. Simultaneous thermal conductivity and diffusivity sensing in liquids using a micromachined device. *Sensors and Actuators A: Physical*, 130:62–67, 2006.
- [209] Sampath Kommandur, Alireza MahdaviFar, Peter J. Hesketh, and Shannon Yee. A microbridge heater for low power gas sensing based on the

- 3-Omega technique. *Sensors and Actuators A: Physical*, 233:231–238, 2015.
- [210] J. J. Van Baar, Remco J. Wiegerink, Theodorus SJ Lammerink, Gijbertus JM Krijnen, and M. Elwenspoek. Micromachined structures for thermal measurements of fluid and flow parameters. *Journal of micromechanics and microengineering*, 11(4):311, 2001.
- [211] Pascal Tardy, Jean-René Coulon, Claude Lucat, and Francis Menil. Dynamic thermal conductivity sensor for gas detection. *Sensors and Actuators B: Chemical*, 98(1):63–68, 2004.
- [212] Daniel Struk, Amol Shirke, Alireza MahdaviFar, Peter J. Hesketh, and Joseph R. Stetter. Investigating time-resolved response of micro thermal conductivity sensor under various modes of operation. *Sensors and Actuators B: Chemical*, 254:771–777, 2018.
- [213] Alireza MahdaviFar, Milad Navaei, Peter J. Hesketh, Melvin Findlay, Joseph R. Stetter, and Gary W. Hunter. Transient thermal response of micro-thermal conductivity detector ( $\mu$ TCD) for the identification of gas mixtures: An ultra-fast and low power method. *Microsystems & Nanoengineering*, 1(1):15025, December 2015.
- [214] Zeyu Cai, Robert HM van Veldhoven, Annelies Falepin, Hilco Suy, Eric Sterckx, Christian Bitterlich, Kofi AA Makinwa, and Michiel AP Pertijs. A ratiometric readout circuit for thermal-conductivity-based resistive CO<sub>2</sub> sensors. *IEEE Journal of Solid-State Circuits*, 51(10):2463–2474, 2016.
- [215] Isolde Simon and Michael Arndt. Thermal and gas-sensing properties of a micromachined thermal conductivity sensor for the detection of hydrogen in automotive applications. *Sensors and Actuators A: Physical*, 97:104–108, 2002.
- [216] G. De Graaf and R. F. Wolffenbuttel. Surface-micromachined thermal conductivity detectors for gas sensing. In *2012 IEEE International Instrumentation and Measurement Technology Conference Proceedings*, pages 1861–1864. IEEE, 2012.
- [217] Takeshi Kawano, Heather C. Chiamori, Marcel Suter, Qin Zhou, Brian D. Sosnowchik, and Liwei Lin. An Electrothermal Carbon Nanotube Gas Sensor. *Nano Letters*, 7(12):3686–3690, December 2007.
- [218] M. W. Ahn, K. S. Park, J. H. Heo, D. W. Kim, K. J. Choi, and J. G. Park. On-chip fabrication of ZnO-nanowire gas sensor with high gas sensitivity. *Sensors and Actuators B: Chemical*, 138(1):168–173, April 2009.

- [219] Choongho Yu, Qing Hao, Sanjoy Saha, Li Shi, Xiangyang Kong, and Z. L. Wang. Integration of metal oxide nanobelts with microsystems for nerve agent detection. *Applied Physics Letters*, 86(6):063101, January 2005.
- [220] Egbert van der Wouden, Jarno Groenesteijn, Remco Wiegerink, and Joost Lötters. Multi parameter flow meter for on-line measurement of gas mixture composition. *Micromachines*, 6(4):452–461, 2015.
- [221] Christoph J. Hepp, Florian T. Krogmann, and Gerald A. Urban. Flow rate independent sensing of thermal conductivity in a gas stream by a thermal MEMS-sensor—Simulation and experiments. *Sensors and Actuators A: Physical*, 253:136–145, 2017.
- [222] Konstantinos A. Aliferis, Petros A. Tarantilis, Paschalis C. Harizanis, and Eleftherios Alissandrakis. Botanical discrimination and classification of honey samples applying gas chromatography/mass spectrometry fingerprinting of headspace volatile compounds. *Food Chemistry*, 121(3):856–862, August 2010.
- [223] Christian Bur, Manuel Bastuck, Donatella Puglisi, Andreas Schütze, Anita Lloyd Spetz, and Mike Andersson. Discrimination and quantification of volatile organic compounds in the ppb-range with gas sensitive SiC-FETs using multivariate statistics. *Sensors and Actuators B: Chemical*, 214:225–233, July 2015.
- [224] Tahir Mehmood and Bilal Ahmed. The diversity in the applications of partial least squares: an overview, January 2016.
- [225] J. W. Gardner, E. L. Hines, and M. Wilkinson. Application of artificial neural networks to an electronic olfactory system. *Measurement Science and Technology*, 1(5):446, 1990.
- [226] SPCLHGMMS Balasubramanian, S. Panigrahi, C. M. Logue, H. Gu, and M. Marchello. Neural networks-integrated metal oxide-based artificial olfactory system for meat spoilage identification. *Journal of Food Engineering*, 91(1):91–98, 2009.
- [227] Stephen R. Johnson, Jon M. Sutter, Heidi L. Engelhardt, Peter C. Jurs, Joel White, John S. Kauer, Todd A. Dickinson, and David R. Walt. Identification of multiple analytes using an optical sensor array and pattern recognition neural networks. *Analytical Chemistry*, 69(22):4641–4648, 1997.
- [228] Antonio Riul, Humberto C. de Sousa, Roger R. Malmegrim, David S. dos Santos, André C. P. L. F. Carvalho, Fernando J. Fonseca, Osvaldo N. Oliveira, and Luiz H. C. Mattoso. Wine classification by taste sensors made from ultra-thin films and using neural networks. *Sensors and Actuators B: Chemical*, 98(1):77–82, March 2004.

- 
- [229] G. Huyberegts, P. Szecowka, J. Roggen, and B. W. Licznerski. Simultaneous quantification of carbon monoxide and methane in humid air using a sensor array and an artificial neural network. *Sensors and Actuators B: Chemical*, 45(2):123–130, 1997.
- [230] Dongzhi Zhang, Jingjing Liu, Chuanxing Jiang, Aiming Liu, and Bokai Xia. Quantitative detection of formaldehyde and ammonia gas via metal oxide-modified graphene-based sensor array combining with neural network model. *Sensors and Actuators B: Chemical*, 240:55–65, March 2017.
- [231] Teodoro Aguilera, Jesús Lozano, José A. Paredes, Fernando J. Álvarez, and José I. Suárez. Electronic Nose Based on Independent Component Analysis Combined with Partial Least Squares and Artificial Neural Networks for Wine Prediction. *Sensors (Basel, Switzerland)*, 12(6):8055–8072, June 2012.
- [232] R. Lippmann. An introduction to computing with neural nets. *IEEE ASSP Magazine*, 4(2):4–22, April 1987.
- [233] Ben Rogers, Steven Malekos, Lee Deal, Ralph Whitten, and Jesse Adams. Combined, solid-state molecular property and gamma spectrometers for CBRN E detection. In *2013 IEEE International Conference on Technologies for Homeland Security (HST)*, pages 607–612, November 2013. ISSN: null.

# Appendix A

## BreathFit

### A.1 Introduction

As highlighted throughout this thesis, the development of low-power sensors is essential in the global trend towards smart, autonomous electronics. Sensors will increasingly become part of sensor networks and systems where multiple measurands can be simultaneously measured and accounted for.

In recent decades, the concern over environmental pollution and potentially harmful substances has dramatically risen. This has equated to a large boom for research in the area of gas sensors, which need to be able to identify or monitor the chemical constituents of any particular environment to ensure the safety of humans, plants and animals. These requirements have led to a large range of technologies that have been developed and are commercially available, of which a majority involve the application of surface or bulk chemical and physical properties of materials and are defined as solid-state gas sensors.

Due to their high sensitivity and low power consumption, MOx sensors are often used in breath analysis applications. In these applications a human is

breathing into a system, resulting in an inability to control the flow rate. In these situations, it is important to know the flow rate in order to compensate for the change in MOx read-out that originates from the fluid flow and not the detection of gas, so that these two parameters can become fully independent.

This project was a collaborative effort to compensate for flow in breath analysis applications. A monolithically integrated combo-chip was presented that includes three MOx gas sensors and one flow sensor that are on separate membranes with separate micro-heater control. The metal oxide material is investigated and selected for the best selectivity towards acetone whilst minimizing cross-selectivity towards other gases that may interfere. Bespoke electronics incorporates the sensor into an ASIC system which is then assembled into an air-tight handheld packaging solution that includes a bypass to force the flow rate to be at an optimum speed for the gas sensors. The system response to acetone and other contaminating bio-markers is shown in the lab, alongside breath demonstrations that incorporate a flow compensation algorithm. Within diagnostic and consumer applications, there is an increasing demand for non-invasive sensors that monitor clinical markers in physiological media such as breath. One interesting clinical marker is acetone breath levels, which have been linked to weight reduction and conditions such as ketoacidosis.

This section provides a brief overview of the project with particular focus on the importance of flow sensing within the system.

## **A.2 Design and Fabrication Details**

### **A.2.1 Combo Sensor**

Software package Cadence Virtuoso (IC 5.1.4) was used to design the devices that have been fabricated in a commercial foundry using a 1  $\mu\text{m}$  CMOS process.

The platform technology which allows the integration of gas and flow sensors using microheaters (also referred to as micro-hotplates) made of tungsten alongside Deep Reactive Ion Etching (DRIE) at the back surface to create a thin membrane. A metal oxide is deposited over the surface of the microheaters to create the gas sensors. A wire and a spiral geometry were chosen for the flow and gas sensors, respectively. The chip and four embedded sensors are shown in Figure A.1 whilst the layer composition of the membrane is consistent with the technology platform used throughout this thesis. After the fabrication of the micro-hot plates, chemiresistors were produced by depositing different pastes by means of ink-jet printing. Pastes were prepared from metal-doped tin oxide (MOx1), metal-doped cerium oxide (MOx2) and vanadium-doped tin oxide (MOx3). An in-situ annealing step was performed on all the chemiresistors using the embedded microheater.

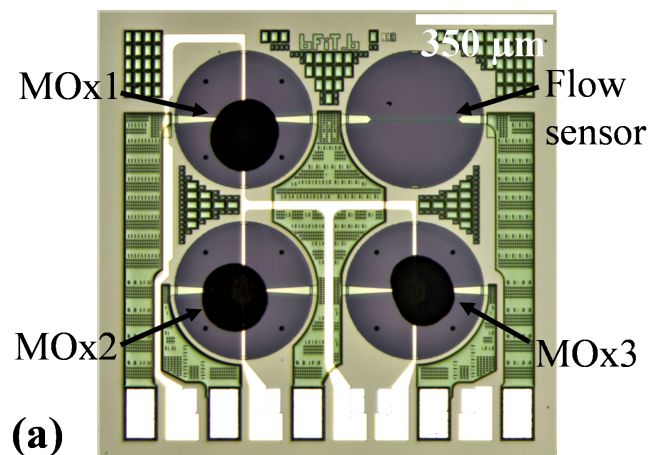


**Figure A.1:** Optical micrograph of the combo sensor that embeds three metal oxide sensors and one flow sensor.

First, it was essential to show that varying flow rates have an effect on the gas sensor responses. Figure A.2 (a) shows the resistance reading from one of the gas sensors (left axis) for increasing flow rate set by the MFC (right axis). It can be seen that the gas sensor response is strongly affected by flow. Figure A.2 (b) also shows the response of the gas sensor (left axis) and the response of the flow sensor (right axis) for three human exhailes, showing that

in order to accurately measure gas levels in human breath applications, flow must be compensated for.

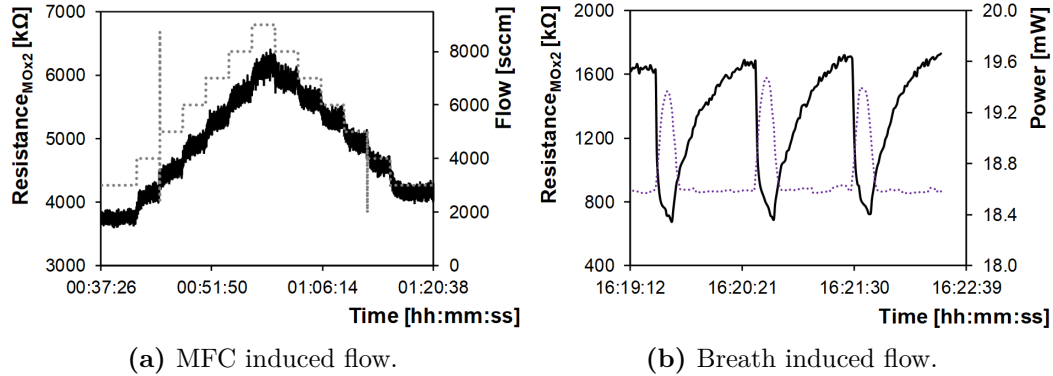


**Figure A.2:** The dependence of gas sensor response on the flow rate.

## A.2.2 Housing

In addition to the sensor, appropriate housing had to be developed to create a handheld module with all electronics embedded. A 3D model of the air-tight housing design is shown in Figure A.3 with each part of the assembly illustrated. A picture of the 3D printed and assembled version shown in Figure A.4. O-rings are used to ensure no leakage from the system whilst appropriately sized cavities are used to embed the electronics and sensor, with screws ensuring a tight fix.

Human breath has an output flow rate of between 2 SLPM and 6 SLPM, a value which is too high for the gas sensors to have a consistent interaction with the gas and provide an accurate read-out. To solve this problem, a bypass system was implemented within the housing, that creates a pressure drop across the main channel in order to redirect a portion of the flow into a bypass. The sensor will be measuring the gas flowing through this bypass, which needs to be at a flow rate between 100 SCCM and 500 SCCM for the gas sensors to function in their ideal range.

COMSOL Multiphysics was used to model a pressure drop flow restrictor and simulated the amount of flow being directed through the bypass. Figure



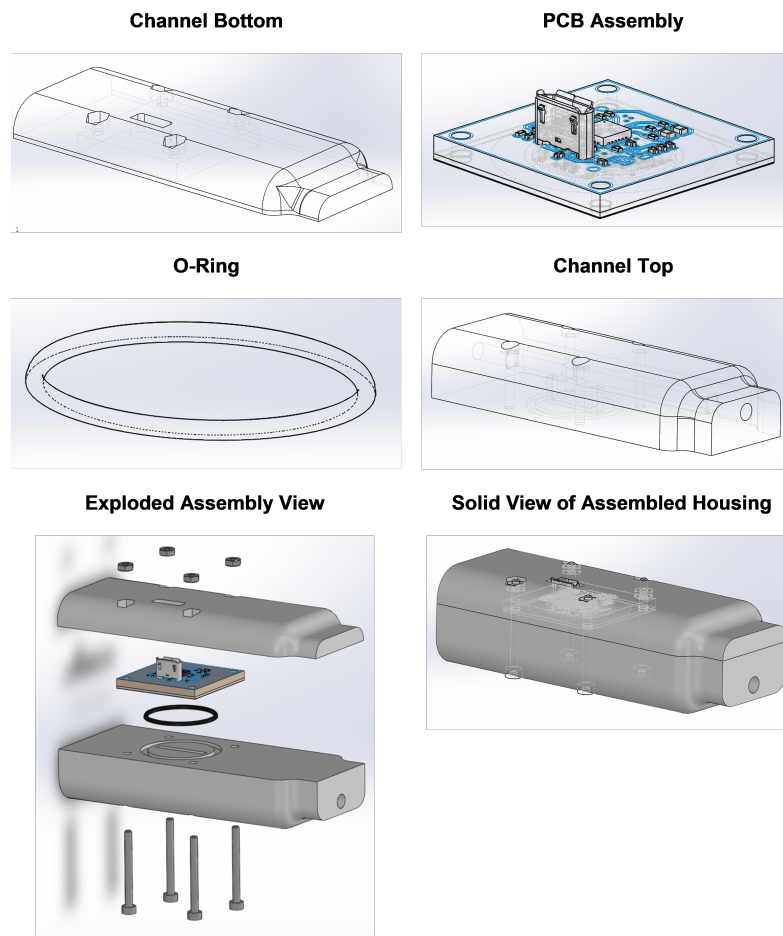


**Figure A.3:** 3D CAD models of each individual component and assembly of the housing that embeds the electronics and the sensor in an air-tight handheld system.

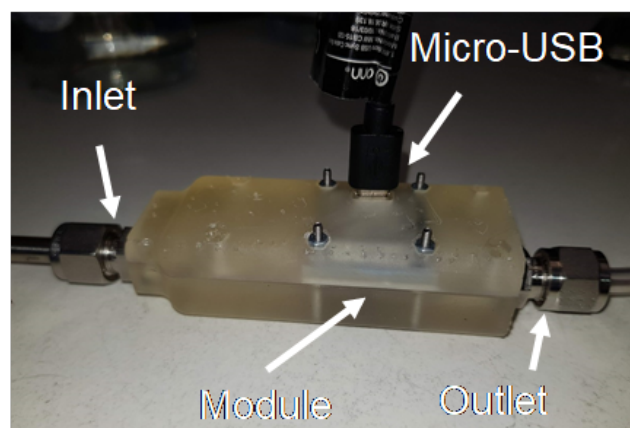


**Figure A.4:** A picture of the 3D printed housing assembly, also illustrating how it is connected to the gas rig for testing.

A.5 shows the velocity profile through a bypass design. The restrictor can be seen in the middle of the main channel, which directs a portion of the flow (at a slower velocity and smaller cross-sectional area) around the bypass and over the sensor.

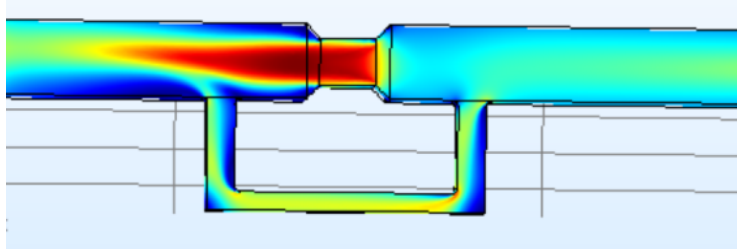


**Figure A.5:** Simulation results showing the velocity through the bypass system where flow is going from right to left.

In addition to numerical analysis, 3D chambers were printed with the bypass and used to experimentally verify the bypass. This was achieved by using two identical flow sensors to compare the flow through the main channel as well as the flow going through the bypass. Figure A.6 shows the experimental setup whilst Figure A.7 shows the results of this experiment.

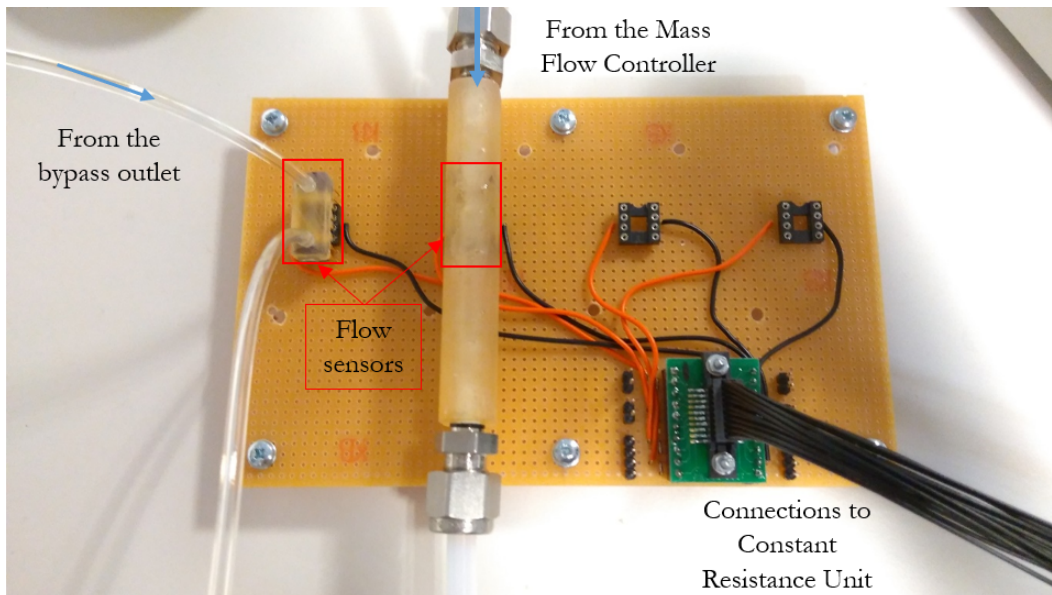


**Figure A.6:** Experimental set-up for bypass characterisation. The air first flows inside the big pipe, where it interacts with the first flow sensor, and then fed inside the bypass, collected by the small pipe and redirected on top of the second sensor.

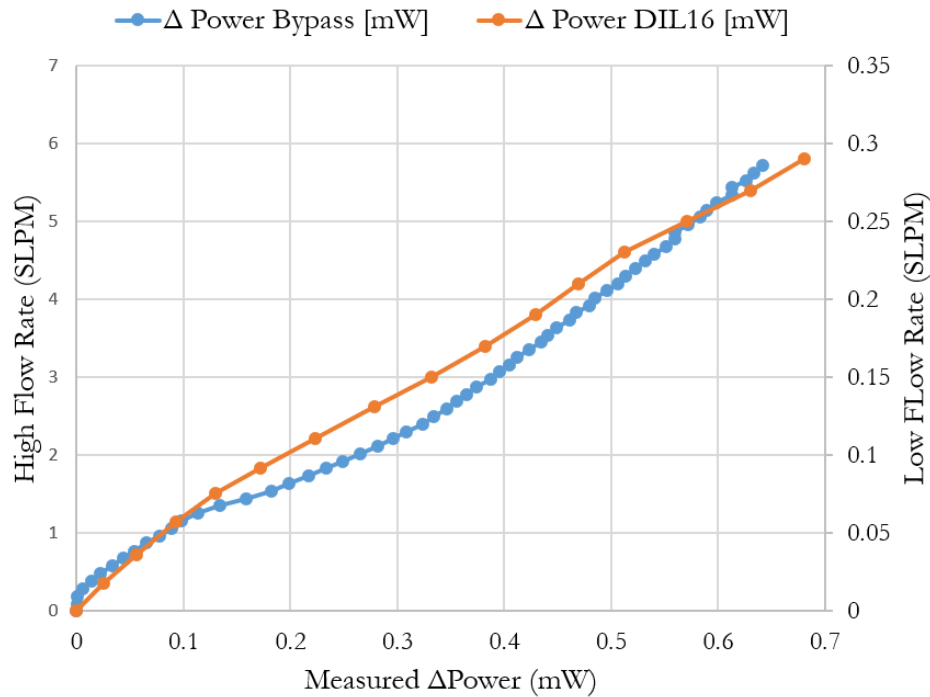


**Figure A.7:** Response comparison from the two sensors, inside the main pipe exposed to slow flow (blue line) and inside the bypass with high flow allowed by the MFCs

The response from the bypass flow sensor is in the range of 0.1 to 0.25 SLPM and is linear, which aids calibration and conversion from power consumption to flow rate. The main channel flow sensor demonstrates a non-standard output in the range of 1 to 3 SLPM, caused by the onset of turbulent flow.

The characterisation experiments demonstrate the bypass chamber successfully reduces the flow across the sensors by a factor of 20. This is sufficient to allow the flow sensor to record accurate flow rates, while remaining within the optimum operating region of the MOX sensors.

## A.3 Conclusions

This section has given insight into one of the projects that was carried out during this thesis. It highlights the importance of accurate, simple sensors that can be implemented in systems of multiple sensors, without creating too much complication for post-processing.

In this case, a flow sensor has been used in conjunction with three gas sensors on the same chip. The response of the metal oxide gas sensors is dependent on the flow rate and in order to compensate for this, a flow sensor is needed in the system for accurate sensing solutions.